



City Research Online

City, University of London Institutional Repository

Citation: Karim, Mohammad (2015). Design and optimization of chalcogenide waveguides for supercontinuum generation. (Unpublished Doctoral thesis, City University London)

This is the accepted version of the paper.

This version of the publication may differ from the final published version.

Permanent repository link: <https://openaccess.city.ac.uk/id/eprint/13592/>

Link to published version:

Copyright: City Research Online aims to make research outputs of City, University of London available to a wider audience. Copyright and Moral Rights remain with the author(s) and/or copyright holders. URLs from City Research Online may be freely distributed and linked to.

Reuse: Copies of full items can be used for personal research or study, educational, or not-for-profit purposes without prior permission or charge. Provided that the authors, title and full bibliographic details are credited, a hyperlink and/or URL is given for the original metadata page and the content is not changed in any way.

Design and optimization of chalcogenide waveguides for supercontinuum generation



Mohammad Rezaul Karim

School of Mathematics, Computer Science and Engineering
City University London

This dissertation is submitted for the degree of
Doctor of Philosophy

City University London

October 2015

I would like to dedicate this thesis to my parents.

Declaration

I hereby declare that except where specific reference is made to the work of others, the contents of this dissertation are original and have not been submitted in whole or in part for consideration for any other degree or qualification in this, or any other university. I grant powers of discretion to the University Librarian to allow this thesis to be copied in whole or in part without further reference to me. This permission covers only single copies made for study purposes, subject to normal conditions of acknowledgement.

Mohammad Rezaul Karim

October 2015

Acknowledgements

Firstly, I would like to thank my supervisor Prof. B M A Rahman for guidance and support during the last three years. His help was invaluable to me during the whole course of research work on chalcogenide waveguides for supercontinuum generation.

Next, I would like to thank all the professional people I become acquainted with during the last three years. Particularly, I am grateful to Prof. Govind P. Agrawal who helped me a lot during his visit to City University London with discussion on various nonlinear effects and resolving different problems arises during numerical simulations on SC generation.

I would like to thank all of my colleagues in the Photonics Modelling Research group for all the help and contributions they have provided me during the three-year course of research work. I express my thanks to the all academic and administration staffs of City University London for conducting and managing this process very smoothly.

I would like to endlessly thank to my parents for guiding and encouraging me all time to keep me in the right path as well as brighten up my future. And thanks to my all other family members and relatives who have given me support in many ways during this course of study.

Finally, and most importantly, I wish to express my gratitude to my wife Selina who has given me continuous support during the whole course of my study. She has completely relieved me of all day to day household related obligations, allowing me to focus completely on research work especially during my thesis writing up period. My warmest thanks and my love go to my daughter Bushra for having patience and for giving me joy during the whole period of study.

Abstract

This research work presents numerical simulations of supercontinuum (SC) generation in optical waveguides based on $\text{Ge}_{11.5}\text{As}_{24}\text{Se}_{64.5}$ chalcogenide (ChG) material. Rigorous numerical simulations were performed using finite-element and split-step Fourier methods in order to optimize the waveguides for wideband SC generation. Through dispersion engineering and by varying dimensions of the 1.8-cm-long ChG nanowires, we have investigated dispersion curves for a number of nanowire geometries and identified a promising one which can be used for generating a SC with 1300 nm bandwidth pumped at 1550 nm with a low peak power of 25 W. It was observed through successive inclusion of higher-order dispersion coefficients during SC simulations that there is a possibility of obtaining spurious results if the adequate number of dispersion coefficients is not considered. We then investigate MIR SC in dispersion-tailored, air-clad, ChG channel waveguide employing either $\text{Ge}_{11.5}\text{As}_{24}\text{S}_{64.5}$ or MgF_2 glass and ChG rib waveguide employing MgF_2 glass for their lower claddings. We study the effect of waveguide parameters on the bandwidth of the SC at the output of 1-cm-long waveguides. Our results show that output can vary over a wide range depending on their design and the pump wavelength employed. At the pump wavelength of $2\ \mu\text{m}$ the SC never extended beyond $4.5\ \mu\text{m}$ for any of our designs. However, SC could be extended to beyond $5\ \mu\text{m}$ for a pump wavelength of $3.1\ \mu\text{m}$. A broadband SC spanning from 2 to $6\ \mu\text{m}$ and extending over 1.5 octave could be generated with a moderate peak power of 500 W at a pump wavelength of $3.1\ \mu\text{m}$ using an air-clad, all-ChG, channel waveguide. We show that SC can be extended even further covering the wavelength ranges $1.8\text{-}7.7\ \mu\text{m}$ and $1.8\text{-}8\ \mu\text{m}$ (> 2 octaves) when MgF_2 glass is used for the lower claddings of ChG channel waveguide and rib waveguide, respectively. By employing the same pump source, we show that SC spectra can cover a wavelength range of $1.8\text{-}11\ \mu\text{m}$ (> 2.5 octaves) in a channel waveguide and $1.8\text{-}10\ \mu\text{m}$ in a rib waveguide employing MgF_2 glass for their lower claddings with a moderate peak power of 3 kW. Finally we present microstructured fibre based design made with same glass to generate SC spectra in the MIR region. Numerical simulations show that such a 1-cm-long fibre can produce a spectrum extending from $1.3\ \mu\text{m}$ to beyond $11\ \mu\text{m}$ (> 3 octaves) with the same pump and peak power applied before. We consider three fibre structures with microstructured air-holes in their cladding and find their optimum designs through dispersion engineering. Among these, equiangular-spiral microstructured fibre is found to be the most promising candidate for generating ultrawide SC in the MIR region.

Table of contents

| | |
|---|-------------|
| List of figures | xiv |
| List of tables | xx |
| List of Acronyms | xxi |
| List of Symbols | xxiv |
| 1 Introduction | 1 |
| 2 Nonlinear optics in optical waveguides | 7 |
| 2.1 Light propagation in optical waveguides | 8 |
| 2.1.1 Maxwell's equations | 8 |
| 2.1.2 Nonlinear pulse propagation equation | 12 |
| 2.2 Linear effects in optical waveguides | 15 |
| 2.2.1 Losses | 15 |
| 2.2.2 Dispersion | 16 |
| 2.3 Nonlinearity in optical waveguides | 18 |
| 2.3.1 Self-phase modulation | 20 |
| 2.3.2 Solitons | 21 |
| 2.3.3 Cross-phase modulation | 23 |
| 2.3.4 Four-wave mixing | 24 |
| 2.3.5 Self-steepening | 25 |
| 2.3.6 Stimulated Raman scattering | 26 |
| 2.3.7 Dispersive waves | 28 |
| 2.4 Summary | 29 |
| 3 Numerical Methods | 31 |
| 3.1 Optical waveguides | 31 |

| | | |
|----------|--|------------|
| 3.2 | Finite-element method | 34 |
| 3.2.1 | The variational approach | 36 |
| 3.2.2 | FE method implementation | 41 |
| 3.3 | Split-step Fourier method | 54 |
| 3.3.1 | SSFM for solving GNLSE | 54 |
| 3.3.2 | SSFM implementation | 57 |
| 3.4 | Summary | 58 |
| 4 | Overview of SC generation | 60 |
| 4.1 | SC generation in bulk media | 61 |
| 4.2 | SC generation in conventional fibres | 62 |
| 4.3 | SC generation in silica microstructured fibres | 64 |
| 4.4 | SC generation using nonsilica fibres | 66 |
| 4.5 | Summary | 71 |
| 5 | SC generation in chalcogenide nanowire | 73 |
| 5.1 | Material properties of ChG glasses | 74 |
| 5.2 | ChG nanowire design | 77 |
| 5.2.1 | Structure of ChG nanowire | 77 |
| 5.2.2 | Aitken extrapolation technique for accuracy testing of FE modal solution | 78 |
| 5.2.3 | Calculation of GVD and higher-order dispersions | 81 |
| 5.2.4 | Accuracy testing of GVD with the variation of FE mesh and data fitting through Taylor series expansion | 84 |
| 5.3 | Simulation parameters for SC generation | 87 |
| 5.4 | Results and discussions | 88 |
| 5.5 | Simulated SC result verification with frequency domain method | 97 |
| 5.6 | Summary | 98 |
| 6 | Mid-infrared SC generation in chalcogenide waveguides | 100 |
| 6.1 | ChG channel and rib waveguides design | 101 |
| 6.1.1 | Geometry of channel and rib waveguides | 101 |
| 6.1.2 | Dispersion engineering of channel waveguides | 102 |
| 6.1.3 | Dispersion tailoring of a rib waveguide | 108 |
| 6.2 | Simulation parameters for MIR SC modelling | 111 |
| 6.3 | Results and discussions | 112 |
| 6.3.1 | Simulation results for channel waveguides pump employing at 2 μm | 112 |

| | | |
|----------|---|------------|
| 6.3.2 | Simulation results for channel waveguides pump employing at $3.1 \mu\text{m}$ | 115 |
| 6.3.3 | Simulation results for a rib waveguide pump employing at $3.1 \mu\text{m}$ | 119 |
| 6.4 | Summary | 124 |
| 7 | Mid-infrared SC generation in chalcogenide microstructured fibres | 126 |
| 7.1 | Microstructured fibres (MoFs) design | 128 |
| 7.1.1 | Structure of MoFs | 128 |
| 7.1.2 | Dispersion tailoring for hexagonal PCF | 129 |
| 7.1.3 | Dispersion tailoring for TC fibre | 132 |
| 7.1.4 | Dispersion tailoring for equiangular spiral PCF | 134 |
| 7.2 | Simulation parameters for SC modelling in ChG MoFs | 138 |
| 7.3 | Results and discussions | 139 |
| 7.3.1 | SC generation in hexagonal PCF | 139 |
| 7.3.2 | SC generation in TC fibre | 141 |
| 7.3.3 | SC generation in ES-PCF | 142 |
| 7.3.4 | Comparison of SC evolution in MoFs output | 142 |
| 7.4 | Summary | 147 |
| 8 | Conclusion and Future work | 149 |
| | Appendix A | 157 |
| | Appendix B | 160 |
| | Author Publications | 165 |
| | References | 167 |

List of figures

| | | |
|-----|--|----|
| 2.1 | Normalized Raman gain for fused silica when pump and stokes wave are copolarized (After [1]) | 26 |
| 3.1 | Schematics of (a) planar (channel) waveguide and (b) PCF with hexagonal symmetry cladding containing air-holes. | 32 |
| 3.2 | Two dimensional elements. | 41 |
| 3.3 | Finite element discretisation of an irregular waveguide cross-section. | 42 |
| 3.4 | Pascal’s triangle for complete polynomials in two dimensions. | 43 |
| 3.5 | Typical two dimensional first order triangular element. | 44 |
| 3.6 | Discretisation of a dielectric waveguide with orthodox and infinite elements. | 53 |
| 3.7 | Schematic diagram of the symmetrized SSFM used for numerical simulations. Waveguide length is divided into a large number of segments of width h and the effect of nonlinearity is included at the mid of the step shown by a dashed line. | 56 |
| 5.1 | Schematic diagram of chalacogenide nanowire. | 77 |
| 5.2 | Dominant H_y field profile of fundamental quasi TE-mode (H_y^{11}) for the nanowire structure of $W = 700$ nm and $H = 500$ nm at a wavelength of 1550 nm; a) Contour, b) Surface, c) H_y field along width, and d) H_y field along thickness of a nanowire. | 79 |
| 5.3 | Variation of n_{eff} of the fundamental quasi-TE mode with the mesh size and improvement realized with the Aitken extrapolation technique. | 81 |
| 5.4 | GVD curves for the fundamental quasi-TE mode calculated from the n_{eff} values for (a) different W and same H and (b) different H and same W . Vertical dotted line represents the wavelength $\lambda = 1550$ nm. | 83 |

| | | |
|------|---|-----|
| 5.5 | GVD for the fundamental quasi-TE mode as a function of wavelength for the nanowire structure with $W = 700$ nm and $H = 500$ nm. The black-solid, red-dashed, and blue-dotted correspond to a mesh size of 200×200 , 300×300 , and 600×600 , respectively. | 85 |
| 5.6 | GVD curves obtained with FE method (black) fitted the Taylor series expansion up to β_8 for the nanowires (a) $W = 775$ nm, $H = 500$ nm and (b) $W = 800$ nm, $H = 500$ nm. | 86 |
| 5.7 | Changes in SC spectra with the successive addition of higher-order dispersion terms pumped at a wavelength of 1550 nm for the nanowire of dimensions $W = 700$ nm and $H = 500$ nm. | 89 |
| 5.8 | Temporal intensity (top), spectral density (middle) and spectrogram (bottom) including terms up to β_3 (left column), up to β_4 (middle column), and up to β_8 (right column) pumped at a wavelength of 1550 nm for the nanowire of dimensions $W = 700$ nm and $H = 500$ nm. | 90 |
| 5.9 | Changes in SC spectra with the successive addition of higher-order dispersion terms pumped at a wavelength of 1550 nm for the nanowire geometry, $W = 775$ nm and $H = 500$ nm. | 92 |
| 5.10 | (a) Temporal and (b) Spectral evolution for 50 fs pulse launched with 25 W peak power pumped at a wavelength of 1550 nm along the length of the nanowire structure, $W = 775$ nm and $H = 500$ nm. | 93 |
| 5.11 | Temporal intensity (top), spectral density (middle) and spectrogram (bottom) including terms up to β_3 (left column), up to β_4 (middle column), and up to β_8 (right column) pumped at a wavelength of 1550 nm for the nanowire geometry, $W = 775$ nm and $H = 500$ nm. | 95 |
| 5.12 | Numerically simulated SC spectra for nanowires with the dispersion curves shown in Fig. 5.4(a) by including dispersion terms up to β_8 at a pump wavelength of 1550 nm. | 96 |
| 5.13 | Numerically simulated SC spectra for nanowire, $W = 775$ nm and $H = 500$ with time domain (SSFM) and frequency domain (Interaction Picture) including dispersion terms up to β_8 at a pump wavelength of 1550 nm with a peak power of 25 W. | 97 |
| 6.1 | Schematic diagram of ChG rib waveguide. | 102 |
| 6.2 | GVD curves for the fundamental quasi-TE mode calculated from n_{eff} for three waveguides geometries employing $\text{As}_{36}\text{S}_{64}$ glass for both the upper and lower claddings. The black solid line curve shows the material dispersion curve for comparison. | 103 |

- 6.3 GVD curves for the waveguide geometries employing two different lower claddings (solid black curve for $\text{Ge}_{11.5}\text{As}_{24}\text{S}_{64.5}$ and red dashed curve for MgF_2) for the fundamental quasi-TE mode (a) at a pump wavelength of $2 \mu\text{m}$ and (b) at a pump wavelength of $3.1 \mu\text{m}$. Vertical dotted line indicates the position of pump wavelength. 105
- 6.4 Dominant field profile for fundamental quasi-TE mode (H_y^{11}) for the ChG channel waveguide geometry, $W = 4 \mu\text{m}$ and $H = 1.6 \mu\text{m}$ employing $\text{Ge}_{11.5}\text{As}_{24}\text{S}_{64.5}$ glass for its lower cladding at a wavelength of 3100 nm ; a) Contour, b) Surface, c) H_y field along width, and d) H_y field along thickness of the waveguide. 106
- 6.5 Dominant field profile for fundamental quasi-TE mode (H_y^{11}) for the channel structure of $W = 5 \mu\text{m}$ and $H = 0.95 \mu\text{m}$ employing MgF_2 for its lower cladding at a wavelength of 3100 nm ; a) Contour, b) Surface, c) H_y field (normalized value) along width, and d) H_y field (normalized value) along thickness of the waveguide. 107
- 6.6 Dominant field profile for fundamental quasi-TE mode (H_y^{11}) for the rib structure of $W = 5 \mu\text{m}$ and $H = 1.1 \mu\text{m}$ employing MgF_2 for its lower cladding at a wavelength of 3100 nm ; a) Contour, b) Surface, c) H_y field (normalized value) along width, and d) H_y field (normalized value) along thickness of the waveguide. 109
- 6.7 GVD curve (solid red line) tailored for the fundamental quasi-TE mode calculated from n_{eff} and dotted black line curve represents the material dispersion (D_M) of $\text{Ge}_{11.5}\text{As}_{24}\text{Se}_{64.5}$ ChG material. Vertical dotted line indicates pump wavelength and the inset shows the spatial profile of the fundamental mode at a wavelength of $3.1 \mu\text{m}$ 110
- 6.8 Simulated SC spectra at a pump wavelength of $2 \mu\text{m}$ for (a) air-clad all-chalcogenide waveguide at peak power from $25, 100, \text{ and } 500 \text{ W}$; (b) air-clad chalcogenide core employing MgF_2 for its lower cladding at the same power levels. 113
- 6.9 Simulated SC spectra at a pump wavelength of $2 \mu\text{m}$ for waveguides with two different lower claddings at a peak power of 500 W only. Black-solid line curve represents the SC spectrum for the waveguide containing $\text{Ge}_{11.5}\text{As}_{24}\text{S}_{64.5}$ glass for its lower cladding and red-dashed line curve represents the spectrum for the structure employing MgF_2 as its lower cladding. 114

- 6.10 Spectral evolution at a pump wavelength of $2 \mu\text{m}$ for (a) air-clad all-chalcogenide waveguide at a peak power of 500 W; (b) air-clad chalcogenide core employing MgF_2 for its lower cladding at the same power level. 115
- 6.11 Simulated SC spectra at a pump wavelength of $3.1 \mu\text{m}$ for (a) air-clad all-chalcogenide waveguide at peak power between 100 W and 3000 W; (b) air-clad chalcogenide core employing MgF_2 for its lower cladding for the same power levels. 116
- 6.12 Simulated SC spectra at a pump wavelength of $3.1 \mu\text{m}$ for (a) waveguides employing with two different lower claddings at a peak power of 500 W only; (b) waveguides with two different lower claddings at peak power of 3000 W only. Black-solid line curve represents the SC spectrum for the waveguide structure containing $\text{Ge}_{11.5}\text{As}_{24}\text{S}_{64.5}$ glass for its lower cladding and red-dashed line curve represents the spectrum for the structure with MgF_2 as its lower cladding. 117
- 6.13 Spectral evolution along the waveguide length at a pump wavelength of $3.1 \mu\text{m}$ for waveguides with (a) $\text{Ge}_{11.5}\text{As}_{24}\text{S}_{64.5}$ and (c) MgF_2 as its lower claddings at a peak power of 500 W only; (b) $\text{Ge}_{11.5}\text{As}_{24}\text{S}_{64.5}$ and (d) MgF_2 as its lower claddings with a peak power of 3000 W only. 118
- 6.14 Simulated SC spectra at a pump wavelength of $3.1 \mu\text{m}$ for rib waveguide with peak power varies between 100 W and 3000 W. 120
- 6.15 Temporal evolution (top), Spectral evolution (middle), and Spectrogram (bottom) at the rib waveguide output pumped at a wavelength of $3.1 \mu\text{m}$ for two different peak power of 500 W (left column) and 3000 W (right column), respectively. 121
- 6.16 GVD curves for the fundamental quasi-TE mode calculated for the waveguide structure employing $\text{Ge}_{11.5}\text{As}_{24}\text{S}_{64.5}$ glass as its lower cladding without (black-solid line curve) and with (red-dotted line curve) adding extra 10 nm layer on the top of the waveguide. 123
- 7.1 Schematic diagrams of ChG MoFs (a) Triangular core (TC) fibre and (b) Equiangular spiral photonic crystal fibre (ES-PCF) geometry used for dispersion optimization. 128
- 7.2 H_x field profile of fundamental mode (H_x^{11}) for the hexagonal PCF structure of $\Lambda = 3 \mu\text{m}$ and $d/\Lambda = 0.8$ at a wavelength of $3.1 \mu\text{m}$; a) Contour, b) Surface, c) H_x field along x-axis, and d) H_x field along y-axis of a H-PCF. 129

| | | |
|------|--|-----|
| 7.3 | Dispersion curves for the ChG hexagonal PCF design (a) for different d/Λ keeping Λ constant; (b) for different Λ with d/Λ constant. Vertical dotted line indicates pump wavelength at $3.1 \mu\text{m}$ | 131 |
| 7.4 | H_x field profile of fundamental quasi-TM (H_x^{11}) mode for triangular core (TC) structure with a base length, $a = 6 \mu\text{m}$ at a wavelength of $3.1 \mu\text{m}$; a) Contour, b) Surface, c) H_x field along x-axis, and d) H_x field along y-axis of a TC fibre. | 133 |
| 7.5 | GVD curves for the ChG triangular core (TC) fibre obtained for base length (a) varies from $6 \mu\text{m}$ to $10 \mu\text{m}$. Vertical dotted line indicates pump wavelength at $3.1 \mu\text{m}$ | 134 |
| 7.6 | H_x field profile of fundamental quasi-TM (H_x^{11}) mode for equiangular spiral PCF structure with first ring spiral radius, $r_0 = 3 \mu\text{m}$, hole radius, $r = 1.32 \mu\text{m}$, and five spiral arms at a wavelength of $3.1 \mu\text{m}$; a) Contour, b) Surface, c) H_x field along x-axis, and d) H_x field along y-axis of a ES-PCF. | 135 |
| 7.7 | Dispersion curves for the ChG equiangular spiral PCF design (a) for different hole radius, r and different spiral arms keeping first ring spiral radius, r_0 constant; (b) for different first ring spiral radius, r_0 different hole radius, r and keeping the number of spiral arm constant. Vertical dotted line indicates pump wavelength. | 136 |
| 7.8 | Output SC pumped at a wavelength of $3.1 \mu\text{m}$ for Hexagonal PCF (a) for the black-line GVD curve shown in Fig. 7.3(a) with peak power variation between 200 W and 3000 W; (b) for the red-line GVD curve shown in Fig. 7.3(a) with power variation between 200 W and 3000 W; (c) for the GVD curves shown in Fig. 7.3(a) with a peak power of 3000 W only. | 140 |
| 7.9 | Output SC pumped at a wavelength of $3.1 \mu\text{m}$ for TC fibre (a) for the red-line GVD curve shown in Fig. 7.5 with peak power variation between 200 W and 3000 W; (b) for the black-line GVD curve shown in Fig. 7.5 with power variation between 200 W and 3000 W; (c) for the GVD curves shown in Fig. 7.5 (red and black line GVD curves only) with a peak power of 3000 W only. | 141 |
| 7.10 | Output SC pumped at a wavelength of $3.1 \mu\text{m}$ for ES-PCF (a) for the red-line GVD curve shown in Fig. 7.7(a) with peak power variation between 200 W and 3000 W; (b) for the blue-line GVD curve shown in Fig. 7.7(a) with power variation between 200 W and 3000 W; (c) for the GVD curves shown in Fig. 7.3(a) (red and blue line GVD curves only) with a peak power of 3000 W only. | 143 |

-
- 7.11 Temporal evolution (left column), Spectral evolution (middle column), and Spectrogram (right column) at the fibre output for three fibres with different hole geometries. Top, middle, and bottom rows correspond to the output spectra shown in Figs. 7.8(a), 7.9(b), and 7.10(b) pumped at a wavelength of $3.1 \mu\text{m}$ with a peak power of 3 kW, respectively. 144
- 7.12 Simulated SC spectra for three different ChG microstructured fibres (a) with higher mode effective area GVD curves in Figs. 7.3(a) (black-line), 7.5 (red-line), and 7.7(a) (red-line); (b) with lower mode effective area GVD curves in Figs. 7.3(a) (red-line), 7.5 (black-line), and 7.7(a) (blue-line) pumped at a wavelength of $3.1 \mu\text{m}$ with a peak power of 3000 W. 146

List of tables

| | | |
|-----|--|-----|
| 5.1 | Sellmeier fitting coefficients | 78 |
| 5.2 | Aitken's extrapolated values calculated using Equation (5.3) for the nanowire, $W = 700$ nm, $H = 500$ nm at a wavelength of 1550 nm. | 80 |
| 6.1 | Sellmeier fitting coefficients | 102 |

List of Acronyms

| | |
|--------------|---|
| ChG | chalcogenide |
| CW | continues wave |
| EDFA | Erbium doped fibre amplifier |
| ES | equiangular spiral |
| FE | finite-element |
| FEM | finite-element method |
| FFT | fast Fourier transform |
| FWHM | full-width-at-half-maximum |
| FWM | four-wave mixing |
| GNLSE | generalized nonlinear Shrödinger equation |
| GVD | group-velocity dispersion |

| | |
|-------------|--------------------------------|
| IFFT | inverse fast Fourier transform |
| IR | infrared |
| MI | modulation instability |
| MIR | mid-infrared |
| PBG | photonic bandgap |
| PCF | photonic crystal fibre |
| SC | supercontinuum |
| S | sulphur |
| Se | selenium |
| SIF | step-index fibre |
| SPM | self-phase modulation |
| SSFM | split-step Fourier method |
| SSFS | soliton self-frequency shift |
| TC | triangular core |

- TOD** third-order dispersion
- TPA** two-photon absorption
- UV** ultraviolet
- ZBLAN** ZrF₄ BaF₂ LaF₃ AlF₃ NaF
- ZDW** zero-dispersion wavelength

List of Symbols

| | |
|--------------------|-----------------------------------|
| A_{eff} | effective mode area |
| c | velocity of light in vacuum |
| k | wavenumber |
| n_{eff} | effective mode index |
| β | propagation constant |
| β_m | higher-order dispersion parameter |
| ε | permittivity |
| λ | wavelength |
| μ | permeability |
| χ | nonlinear susceptibility |
| ϕ_{NL} | nonlinear phase shift |

| | |
|-----------|----------------------------|
| ω | angular frequency |
| Ω | domain discretisation |
| n_2 | nonlinear refractive index |
| α | linear propagation loss |
| d | air-hole diameter |
| Λ | pitch |
| B | magnetic flux density |
| D | electric flux density |
| H | magnetic field intensity |
| E | electric field intensity |
| J | electric current density |
| ρ | dielectric charge density |
| γ | nonlinear coefficient |
| p | penalty factor |

Chapter 1

Introduction

Supercontinuum (SC) generation using nonlinear effects in optical waveguides has been a topic of considerable interest in nonlinear optics over the last decade as its use provides an optical source with properties such as large bandwidth, brightness, high coherence, and potential compactness. When optical pulses propagate through a highly nonlinear waveguide, their temporal as well as spectral evolution are affected not only by a multitude of nonlinear effects but also by the dispersive properties of the waveguide. All nonlinear processes are capable of generating new frequencies within the pulse spectrum. For sufficiently intense pulses, the pulse spectrum becomes so broad that it may extend over a frequency range exceeding 100 THz [1]. Such extreme spectral broadening is referred to as SC generation, a phenomenon first observed in bulk BK7 glass by Alfano and Shapiro in 1970 [2, 3]. Later SC generation in a newly invented photonic crystal fibre (PCF) [4–6] was demonstrated in 2000 by Ranka *et al.* by which spectral broadening could be obtained more than one octave [7]. Subsequently, different types of microstructured fibres [8–12], tapered fibres [13–17], and recently planar waveguides [18–22] have shown immense potential as SC light sources in the mid-infrared (MIR) region and considerable effort has been channelled into making the processes that lead to the broadening of an injected pulse more efficient.

Broadband SC sources have found many applications in the field of telecommunication, molecular fingerprint spectroscopy, bio-imaging, pulse compression, optical coherence tomography, high precision frequency metrology, and optical sensing [23]. There is a strong motivation to fabricate waveguide operating in the molecular fingerprint region of the optical spectrum in the range 2-20 μm both for sensing illicit or dangerous materials via their spectroscopic signatures and for applications such as MIR astronomy. Highly nonlinear waveguides in combination with a mode-locked laser are used to produce such a source through the process called SC generation. The physics behind the process of SC in optical waveguides has been studied since the results of Ranka *et al.* and several attempts have been made to explain generated broad bandwidth [24–26]. SC generation relies on the interplay of various nonlinear effects such as self-phase modulation, cross-phase modulation, soliton dynamics, Raman scattering, and four-wave mixing, and it requires an optical waveguide with suitably designed group velocity dispersion (GVD), including a zero-dispersion wavelength (ZDW) close to the central wavelength of the pump sources.

To generate a SC with a large bandwidth ranging from ultra-violet to mid-infrared region with high brightness, numerous efforts have focused on fused silica fibres. However, the intrinsic transmission window of fused silica makes SC expansion beyond 2.2 μm a challenging task [27] which caused a gradual shift towards other types of glasses that have transmission windows transparent in the long wavelength region. In particular silicon (Si), ZBLAN, tellurite, and chalcogenide were investigated as nonlinear mediums for SC generation. Silicon offers a high Kerr nonlinearity and is attractive for generating SC using silicon-on-insulator (SOI) nanowires [28–30]. Although Si has low losses in the near infrared, it has some disadvantages in the telecommunication band centred at 1550 nm where it is affected by two-photon absorption (TPA) and free-carrier absorption (FCA), both of

which clamp spectral broadening of SC and limit the achievable bandwidth. The nonlinear properties of ZBLAN are approximately same as silica while tellurite is roughly 30 times and chalcogenide can be as much as a factor of thousand times more nonlinear than silica.

In recent years chalcogenide glasses have emerged as promising nonlinear materials in the mid-infrared region extending from 1 to 20 μm . Such glasses have a number of unique properties which make them attractive for fabricating optical waveguides, including low nonlinear absorption, low TPA, no FCA, and fast response time because of the absence of free-carrier effects [31–34]. Chalcogenide glasses contain one or more of the chalcogen elements from group 16 of the periodic table (S, Se, Te but excluding Oxygen) covalently bonded to networks formers such as As, Sb, Ge, Ga, Si and P etc. They are, therefore, composed of relatively weakly bonded heavy elements and this leads to many of their most important optical and physical properties. Relatively low bond energies results in optical gaps in the visible or near infrared (IR) as well as low to moderate glass transition temperatures ($T_g \approx 100\text{-}400^\circ\text{C}$). The low vibrational energies of the bonds extends optical transparency to around 8 μm for sulphides, beyond 14 μm for selenides and beyond 20 μm for tellurites. Their high refractive index (2-3) and broad infrared transparency (1-20 μm) make them attractive for waveguide fabrication in the field of telecommunications, optical sensing, and MIR sciences [35, 36]. A major advantage of the chalcogenide glasses is their large ultrafast third-order nonlinearity. These materials are highly suitable not only for nonlinear applications but also for making compact active and passive devices in the MIR region [37, 38]. A few of these ChG materials such as As_2S_3 , As_2Se_3 , $\text{Ge}_{11.5}\text{As}_{24}\text{S}_{64.5}$ and $\text{Ge}_{11.5}\text{As}_{24}\text{Se}_{64.5}$ glasses are highly suitable for making these type of devices in the MIR region. Amongst them $\text{Ge}_{11.5}\text{As}_{24}\text{Se}_{64.5}$ glass has excellent film-forming properties with high thermal and optical stability under intense illumination [39]. Motivated by such useful properties,

recently interest has grown in designing and optimizing planar waveguides and fibres made from $\text{Ge}_{11.5}\text{As}_{24}\text{Se}_{64.5}$ chalcogenide glass for broadband MIR SC generation by tailoring GVD of the waveguide close to its ZDW which should be located near to the central wavelength of the pump sources.

The work described in this thesis was motivated by the need to explore theoretically the design and optimization of optical planar waveguides and microstructured fibres for SC generation in the MIR regime by utilizing the dispersive and nonlinear properties of the waveguide. To analyse as well as optimize the optical waveguides for such works, a rigorous full-vectorial finite-element (FE) method was used for numerical modeling. To study the formation of SC inside the waveguide, simulations were carried out by solving a generalized nonlinear Schrödinger equation (GNLSE) for an optical pulse evolution along the length of the waveguide by split-step Fourier method. It was thoroughly investigated with rigorous numerical simulations how the SC spectrum can be varied between near-infrared and mid-infrared region through dispersion tailoring of the waveguide and shifting the pump wavelength from near-IR to MIR with low to moderate peak power.

The thesis has been structured as follows:

Chapter 2 reviews the theory of nonlinear optics and introduces the various linear and nonlinear spectral broadening mechanisms that responsible for the generation of SC spectra. For understanding the evolution of optical signal inside the waveguide it is necessary to consider the Maxwell's equations and the generalized nonlinear Schrödinger equation (GNLSE) for modelling the pulse propagation along the length of the waveguide with brief derivation of them. The linear effects including waveguide propagation loss and dispersion and nonlinear phenomena such as self-phase modulation, soliton dynamics, cross-phase modulation, four-wave mixing, stimulated Raman scattering, and dispersive waves generation are discussed briefly.

Chapter 3 presents the numerical methods consists of mainly two parts. First part reviews the light guidance mechanisms of optical waveguides briefly following the details discussion on the full-vectorial finite-element (FE) method used in this work. To study the SC generation by numerical simulation, GNLSE equation has been solved using split-step Fourier method (SSFM) in second part of this chapter.

Chapter 4 presents the brief overview of SC generation. The developments of SC sources employing different types of optical fibres and waveguides made using different nonlinear materials have been presented through reviewing the several literatures published in this exciting research field. Different possibilities raised by the availability of different kinds of optical fibres, waveguides and materials and the diverse applications also have been discussed.

Chapter 5 introduces the results of SC generation in chalcogenide planar waveguides. It has been shown here the FE simulation results of design and optimization of different ChG planar waveguides/nanowires that able to operate between near-IR and MIR SC generation. Accuracy of the results obtained by FE method tested before using those results in SC simulation also shown. A set of ChG nanowires were designed by varying the waveguide transverse dimensions to tailor the GVD close to the ZDW of the nanowires and carried out the SC simulations for all nanowires optimized at a pump wavelength of 1550 nm. From several nanowire geometries shown, one optimized nanowire structure is proposed which is suitable for producing large SC bandwidth. It is shown here that there is a possibility to obtain spurious results if the adequate number of higher-order dispersion coefficients is not considered during numerical simulation and also investigate the role of two ZDWs on SC dynamics.

Chapter 6 presents detailed procedure for design and optimization of ChG planar waveguides for mid-infrared SC generation. To realize sufficient

bandwidth extension in the MIR region, a rectangular channel waveguide and a rib waveguide were designed and optimized at pump wavelengths employed by using air on top and two different types of materials used for their lower claddings. To investigate the effect of pump wavelength on SC extension in the long wavelength edge, simulations have been carried out in ChG channel waveguides at two different pump wavelengths separately. Between the pump wavelengths it was observed sufficient SC bandwidth extension far into the MIR owing to longer pump wavelength employed.

Chapter 7 presents the results of investigation of the SC generation in chalcogenide microstructured fibres (MoFs). After investigating three ChG MoF geometries around the chosen pump wavelength, it is shown the results obtained after dispersion optimization of ChG MoFs with the variation of their structural parameters by FE method. A number of dispersion curves were obtained for ChG triangular core fibre, ChG hexagonal photonic crystal fibre and ChG equiangular spiral photonic crystal fibre by varying their base length, pitch and air-hole diameter and all dispersion curves optimized near the pump wavelength employed. SC simulations were performed including higher-order dispersion coefficients along with other pulse parameters for each microstructured fibre proposed in this chapter separately from which it is demonstrated that the SC bandwidth can be improved with sufficient extension of spectrum in the MIR region by using equiangular spiral PCF than conventional microstructured fibres.

The thesis concludes with Chapter 8 in which it has been summarised the results and discuss the possible directions of future work.

Chapter 2

Nonlinear optics in optical waveguides

The propagation of an electromagnetic (EM) wave or pulse, depends entirely on the medium in which it propagates. In vacuum the pulse can propagate unchanged. When propagating in a medium the EM field interacts with the atoms of the medium. This generally means that the pulse experiences loss and dispersion, where the latter effect occurs because the different wavelength components of the pulse travel at different velocities due to the wavelength dependence of the refractive index. These effects are termed as the linear response of the medium. If the intensity of a pulse is high enough, the medium also responds in a nonlinear way. Most notably the refractive index becomes intensity dependent (Kerr effect) and photons can interact with phonons (molecular vibrations) of the medium (Raman effect). In linear optics, signals are only amplified or attenuated but frequencies remain unchanged, while in nonlinear optics, new frequencies can be generated, and a spectrum of a laser pulse can change drastically during propagation. Such extreme spectral change is referred to as supercontinuum (SC) generation, a phenomenon first observed in bulk BK7 glass by Alfano and Shapiro in 1970 [2]. These effects are the basis for the many spectral broadening mechanisms which will be investigated further in this chapter.

This chapter reviews the basic theory needed to understand results presented in this thesis. Section 2.1 starts with the brief overview of Maxwell's

equations and generalized nonlinear Schrödinger equation (GNLSE) for modelling pulse propagation in optical waveguides. Section 2.2 introduces a few linear effects that occur during pulse propagation inside the optical waveguides. Section 2.3 reviews the various spectral broadening mechanisms responsible for SC generation in the waveguide output.

2.1 Light propagation in optical waveguides

In order to study nonlinear effects related to supercontinuum generation, it is necessary to consider the theory of electromagnetic wave propagation in optical waveguides. A brief overview of the derivation of wave equation starting from Maxwell's equations as well as the derivation of nonlinear pulse propagation equation will be presented in this section.

2.1.1 Maxwell's equations

The evolution of electromagnetic fields inside the optical waveguides can be described by Maxwell's equations. These equations describe the interaction between the electric and magnetic fields that vary in space in a time-dependent manner. The general differential form of Maxwell's equations in homogeneous, lossless dielectric medium is [40]

$$\nabla \times \mathbf{E} = -\frac{\partial \mathbf{B}}{\partial t} \quad (2.1)$$

$$\nabla \times \mathbf{H} = \frac{\partial \mathbf{D}}{\partial t} + \mathbf{J}_f \quad (2.2)$$

$$\nabla \cdot \mathbf{D} = \rho \quad (2.3)$$

$$\nabla \cdot \mathbf{B} = 0 \quad (2.4)$$

where \mathbf{E} is the electric field, \mathbf{H} is the magnetic field, \mathbf{J}_f is the current density, \mathbf{D} is the electric displacement field, \mathbf{B} is the magnetic flux density, and ρ is the free charge density. The fields in the above equations are valid for arbitrary media and connected by the following macroscopic relations

$$\mathbf{D} = \epsilon_0 \mathbf{E} + \mathbf{P} \quad (2.5)$$

$$\mathbf{B} = \mu_0 \mathbf{H} + \mathbf{M} \quad (2.6)$$

where ϵ_0 is the vacuum permittivity, \mathbf{P} is the electric polarization, μ_0 is the vacuum permeability, and \mathbf{M} is the magnetization.

Boundary conditions

To solve the Equations (2.1)-(2.4) for optical waveguides that have usually more than one material medium with several boundaries between the different media, boundary conditions have to be incorporated for continuity of the electric and magnetic fields inside the waveguides. In case of a dielectric medium, one can assume surface charges, $\rho = 0$, $\mathbf{M} = \mathbf{J} = 0$ because optical waveguides are dielectric that do not become magnetized nor do they conduct current.

1. The tangential component of the electric field must be continuous.

$$\mathbf{n} \times (\mathbf{E}_1 - \mathbf{E}_2) = 0 \quad \therefore \mathbf{E}_{t1} = \mathbf{E}_{t2} \quad (2.7)$$

2. The tangential component of the magnetic field must be continuous.

$$\mathbf{n} \times (\mathbf{H}_1 - \mathbf{H}_2) = 0 \quad \therefore \mathbf{H}_{t1} = \mathbf{H}_{t2} \quad (2.8)$$

3. The normal component of the electric flux density must be continuous.

$$\mathbf{n} \cdot (\mathbf{D}_1 - \mathbf{D}_2) = 0 \quad \therefore \mathbf{D}_{n1} = \mathbf{D}_{n2} \quad (2.9)$$

$$\therefore \epsilon_1 \mathbf{E}_{n1} = \epsilon_2 \mathbf{E}_{n2} \Rightarrow \mathbf{E}_{n1} \neq \mathbf{E}_{n2} \quad (2.10)$$

where ϵ_1 and ϵ_2 are the permittivity in medium 1 and 2, respectively. At the medium interface $\epsilon_1 \neq \epsilon_2$.

4. The normal component of the magnetic flux density must be continuous.

$$\mathbf{n} \cdot (\mathbf{B}_1 - \mathbf{B}_2) = 0 \quad \therefore \mathbf{B}_{n1} = \mathbf{B}_{n2} \quad \therefore \mu_1 \mathbf{H}_{n1} = \mu_2 \mathbf{H}_{n2} \quad (2.11)$$

where μ_1 and μ_2 are the relative permeability in medium 1 and 2, respectively and for most nonmagnetic media, $\mu_1 = \mu_2 = 1$.

$$\therefore \mathbf{H}_{n1} = \mathbf{H}_{n2} \quad (2.12)$$

Equation (2.12) implies the equality of the normal component of the magnetic field vectors at the boundary.

In certain cases, one of the two media can be considered, either as a perfect electric conductor (PEC)/electric wall (EW) or a perfect magnetic conductor (PMC)/magnetic wall (MW). When one of the two media becomes a PEC, an electric wall boundary condition is imposed as

$$\mathbf{n} \times \mathbf{E} = 0 \quad \text{or} \quad \mathbf{n} \cdot \mathbf{H} = 0 \quad (2.13)$$

This condition ensures the continuity of the electric field vector, \mathbf{E} while the magnetic field vector, \mathbf{H} vanishes at the boundary.

When one of the two media becomes a PMC, a magnetic wall boundary condition is imposed as

$$\mathbf{n} \times \mathbf{H} = 0 \quad \text{or} \quad \mathbf{n} \cdot \mathbf{E} = 0 \quad (2.14)$$

This condition ensures the continuity of the magnetic field vector, \mathbf{H} while the electric field vector, \mathbf{E} vanishes at the boundary.

In the case of a closed surface, such as the boundary of an optical waveguide, additional boundary conditions are considered. These boundary conditions can be natural, in case where the field decays at the boundary, therefore they can be left free. In some other cases they can be forced, in order to take advantage of the symmetry of the waveguide, to reduce the number of elements in finite-element method (and the order of the matrices). The above boundary conditions can be classified as follows [40, 67]

$$\text{Homogenous Dirichlet} \quad \phi = 0 \quad (2.15)$$

$$\text{Inhomogenous Dirichlet} \quad \phi = k \quad (2.16)$$

$$\text{Homogenous Neumann} \quad \partial\phi/\partial\mathbf{n} = 0 \quad (2.17)$$

where ϕ is a specific component of the vector electric or magnetic field, k is prescribed constant value, and \mathbf{n} is the unit vector normal to the surface.

The Neumann boundary conditions represents the rate of change of the field when it is directed out of the surface and it can be used in the finite-element method to impose the field decay along finite-elements, adjacent to the boundary elements of a waveguide structure.

By applying curl operator on both side of the Equations (2.1) and (2.2) and by inserting Equations (2.5) and (2.6) into the result, the following wave equations can be obtained

$$\nabla^2\mathbf{E} = \epsilon_0\mu\frac{\partial^2\mathbf{E}}{\partial t^2} + \mu\frac{\partial^2\mathbf{P}}{\partial t^2} \quad (2.18)$$

$$\nabla^2 \mathbf{H} = \varepsilon \mu \frac{\partial^2 \mathbf{H}}{\partial t^2} \quad (2.19)$$

where the induced electric polarization \mathbf{P} is related to the electric field \mathbf{E} with dominant linear susceptibility, $\chi^{(1)}$ neglecting all higher-order nonlinear susceptibility given by [1]

$$\mathbf{P} = \varepsilon_0 \left(\chi^{(1)} \cdot \mathbf{E} \right) \quad (2.20)$$

To analyse the Equations (2.18) and (2.19) in frequency domain, replacing the time derivative $\partial/\partial t$ by $j\omega$, the phasor representation of the wave equations are

$$\nabla^2 \mathbf{E} + \omega^2 \varepsilon \mu \mathbf{E} = 0 \quad (2.21)$$

$$\nabla^2 \mathbf{H} + \omega^2 \varepsilon \mu \mathbf{H} = 0 \quad (2.22)$$

Equations (2.21) and (2.22) are homogeneous and represent the scalar wave equations for the electric and magnetic fields. The field components in the solution of these equations are decoupled from each other and are transverse; thus, the longitudinal components are negligible. Each transverse component of the field now satisfies the scalar wave equation independently and it is sufficient to study the evolution of one component alone. The numerical method for obtaining modal solution either of these equations will be discussed in Chapter 3.

2.1.2 Nonlinear pulse propagation equation

To observe different nonlinear effects that are produced with interaction of linear effects during the propagation of optical signal inside the optical waveguides, it is necessary to model the pulse propagation equation which

originates from the wave equation in this chapter and the numerical modelling of this equation for using SC simulation will be presented in Chapter 3.

The electric field of a pulse linearly polarised along the x-axis and propagating in the fundamental mode of an optical waveguide can be written as [1]

$$\mathbf{E}_A(\mathbf{r}, t) = \hat{x}F(x, y)A(z, t) \exp[j(\beta_0 z - \omega_0 t)], \quad (2.23)$$

where $\mathbf{r} = (x, y, z)$, \hat{x} is the polarisation unit vector, $F(x, y)$ describes the transverse field distribution, $A(z, t)$ is the pulse envelope, and β_0 is the mode propagation constant of $\beta(\omega)$ at the centre angular frequency ω_0 of the pulse. \mathbf{E}_A is scaled to the actual electric field \mathbf{E} [V/m] according to $\mathbf{E}_A = \sqrt{\frac{1}{2}\epsilon_0 cn} \mathbf{E}$ where ϵ_0 is the vacuum permittivity, c is the speed of light in vacuum, and n is the refractive index. This ensures that the instantaneous optical power can be calculated as $|A|^2$ which is the power of normalized electrical pulse amplitude A . The change in pulse envelope A as the pulse propagates along the fibre axis z is described by the generalised nonlinear Schrödinger equation (GNLSE) [1]

$$\begin{aligned} \frac{\partial \tilde{A}}{\partial z} = & -\frac{\alpha(\omega)}{2} \tilde{A} + \sum_{m \geq 2} \frac{\beta_m}{m!} [\omega - \omega_0]^m \tilde{A} + j\gamma(\omega) \left(1 + \frac{\omega - \omega_0}{\omega_0} \right) \\ & \times \mathcal{F} \left(A(z, T) \int_{-\infty}^{\infty} R(T) |A(z, T - T')|^2 dT' \right), \end{aligned} \quad (2.24)$$

where \mathcal{F} denotes the Fourier transform and $\tilde{A}(z, \omega)$ is the Fourier transform of $A(z, t)$,

$$\mathcal{F}\{A(z, t)\} = \tilde{A}(z, \omega) = \int_{-\infty}^{\infty} A(z, t) \exp[j(\omega - \omega_0)t] dt \quad (2.25)$$

and the pulse envelope $A(z, T)$ is considered in a retarded time frame $T = t - \beta_1 z$ moving with the group velocity $1/\beta_1$ at the carrier frequency. The dispersion coefficients β_2, β_3, \dots , are defined from the Taylor series expansion

of the mode propagation constant $\beta(\omega)$ [1]

$$\beta(\omega) = \beta_0 + \beta_1(\omega - \omega_0) + \frac{1}{2}\beta_2(\omega - \omega_0)^2 + \frac{1}{6}\beta_3(\omega - \omega_0)^3 + \dots \quad (2.26)$$

where

$$\beta_m(\omega_0) = \left(\frac{d^m \beta}{d\omega^m} \right)_{\omega=\omega_0} \quad m = 0, 1, 2, 3, \dots \quad (2.27)$$

$\alpha(\omega)$ is the linear propagation loss. $\gamma(\omega) = n_2 \omega_0 / [cA_{\text{eff}}(\omega)]$ is the waveguide nonlinear parameter, and A_{eff} is the mode effective area which is defined as [1]

$$A_{\text{eff}}(\omega) = \frac{\left[\int \int_{-\infty}^{\infty} |F(x, y, \omega)|^2 dx dy \right]^2}{\int \int_{-\infty}^{\infty} |F(x, y, \omega)|^4 dx dy} \quad (2.28)$$

Smaller values of A_{eff} enhance the nonlinearity of the waveguide and significantly increase γ , by the strong confinement of field in the core region.

The factor $\left[1 + \frac{\omega - \omega_0}{\omega_0}\right]$ in Equation (2.24) is responsible for self-steepening and is due to the intensity dependence of the group velocity [1].

The propagation Equation (2.24) is often written in the time domain by neglecting the frequency dependence of nonlinear parameter and linear propagation loss [1]

$$\begin{aligned} \frac{\partial}{\partial z} A(z, T) = & -\frac{\alpha}{2} A + \sum_{m \geq 2} \frac{j^{m+1}}{m!} \beta_m \frac{\partial^m A}{\partial T^m} + j \left(\gamma + j \frac{\alpha_2}{2A_{\text{eff}}} \right) \left(1 + \frac{j}{\omega_0} \frac{\partial}{\partial T} \right) \\ & \times \left(A(z, T) \int_{-\infty}^{\infty} R(T') |A(z, T - T')|^2 dT' \right) \end{aligned} \quad (2.29)$$

where α_2 is taken as 9.3×10^{-14} m/W is the two-photon absorption (TPA) coefficient of chalcogenide material [35]. Finally the material response function includes both the instantaneous electronic response (Kerr type) and

the delayed Raman response and has the form

$$R(t) = (1 - f_R)\delta(t) + f_R h_R(t), \quad (2.30)$$

$$h_R(t) = \frac{\tau_1^2 + \tau_2^2}{\tau_1 \tau_2^2} \exp\left(-\frac{t}{\tau_2}\right) \sin\left(\frac{t}{\tau_1}\right). \quad (2.31)$$

where $f_R = 0.031$, $\tau_1 = 15.5$ fs, and $\tau_2 = 230.5$ fs are taken as for chalco-genide material [134, 137, 139].

2.2 Linear effects in optical waveguides

Here we briefly explain different physical linear effects that occur during light propagation inside the optical waveguides.

2.2.1 Losses

Loss/attenuation is an important waveguide parameter which provides a measure of power loss during propagation of optical signals inside the waveguide given by

$$\alpha[\text{dB/m}] = -\frac{10}{L} \log_{10} \left(\frac{P_T}{P_0} \right) \quad (2.32)$$

where P_0 is the power launched at the input of a waveguide of length L and P_T is the transmitted power.

Factors that contribute to the loss spectra of a standard waveguide are material absorption and Rayleigh scattering contributing dominantly [1]. In microstructured fibre based waveguides, two more attenuation mechanisms are occurred such as confinement loss and bend loss [41, 42]. Confinement losses or leakage losses are present in microstructured fibres due to the fact that there are a finite number of air-holes that can be made in the cross-section

of the cladding which results in the PCF guided modes to be leaky [43]. The diameter to pitch ratio in a particular design of microstructured fibre determines how much light leaks from the core into the cladding. The lower the ratio, the more leakage is expected into the cladding. The confinement loss is determined by the waveguide geometry and it has been shown that increasing number of rings in the small core fibre can reduce the fibre loss by improving the confinement of the mode. Typically, including one extra ring of holes during micro-structured fibre design, leads to the reduction of the confinement loss. By careful design, the confinement loss can be made as low as required. Bend loss is caused by bending of the fibre. This is because internal light paths exceeding the critical angle for total internal reflection which mainly depends on wavelength [44]. Theoretically, when the fibre is bent, light propagates outside the bend faster than the inner radius. This is not possible practically and the light is radiated away [43, 45, 46]. Two types of bending occur in micro-structured fibres: macro bending and micro bending. Macro bending is a large scale bending that is visible in which the bend is imposed on optical fibre. The bend region strain affects the refractive index and acceptance angle of the light ray. Micro bending is a small scale bend that is not visible which occurs due to the pressure on the fibre that can be as a result of temperature, tensile stress of force and so forth. It affects refractive index and refracts out the ray of light and thus loss occurs.

2.2.2 Dispersion

When an electromagnetic wave interacts with the bound electrons of a dielectric, the medium response, in general, depends on the optical frequency. This property, referred to as chromatic dispersion, manifests through the frequency dependence of the refractive index. On a fundamental level, the origin of chromatic dispersion is related to the characteristic resonance frequencies at which the medium absorbs the electromagnetic radiation through oscillations

of bound electrons. Far from the medium resonances, the refractive index is well approximated by the Sellmeier equation.

Dispersion plays a critical role in the propagation of short optical pulses because different spectral components associated with the pulse travel at different speeds. Even when the nonlinear effects are not important, dispersion induced pulse broadening can be detrimental for optical communication systems. In the nonlinear regime, the combination of dispersion and nonlinearity can result in a qualitatively different behaviour. By expanding the mode propagation constant β in a Taylor series expansion with respect to the pulse center frequency ω_0 , the effects of dispersion are realized mathematically as

$$\beta(\omega) = n_{\text{eff}} \frac{\omega}{c} = \beta_0 + \beta_1(\omega - \omega_0) + \frac{1}{2}\beta_2(\omega - \omega_0)^2 + \frac{1}{6}\beta_3(\omega - \omega_0)^3 + \dots \quad (2.33)$$

and

$$\beta_m = \left(\frac{d^m \beta}{d\omega^m} \right)_{\omega=\omega_0} \quad m = 0, 1, 2, 3, \dots \quad (2.34)$$

where $\beta_1 = 1/v_g$ implying that the envelope of the pulse moves at group velocity v_g , β_2 represents the group velocity dispersion (GVD) and is responsible for pulse broadening while β_3 is the third-order dispersion (TOD) coefficient. Since it is more common to work in wavelength than in the frequency domain, the group velocity dispersion (GVD), β_2 , is often defined as the dispersion parameter D by the equation

$$D[\text{ps/nm/km}] = \frac{d\beta_1}{d\lambda} = -\frac{2\pi c}{\lambda} \beta_2 = -\frac{\lambda}{c} \frac{d^2 n}{d\lambda^2} \quad (2.35)$$

Nonlinear effects in optical waveguides can manifest qualitatively different behaviours depending on the sign of the GVD parameter. If parameter D is negative ($\beta_2 > 0$), this is the normal dispersion regime where the red components of the pulse travel faster than the blue components, i.e. positive

chirp. Similarly, if D is positive ($\beta_2 < 0$), i.e. anomalous dispersion regime, where the red components of the pulse travel slower than the blue components, i.e. negative chirp. When $D = 0$, which corresponds to the zero-dispersion wavelength (ZDW), all frequency components of the pulse travel at the same speed (to lowest order) and the pulse maintains its original shape. The anomalous dispersion regime is of considerable interest for the study of nonlinear effects because it is the regime that optical waveguides support solitons through a balance between the dispersive and nonlinear effects.

The waveguide dispersion is strongly dependent on the waveguide geometry particularly when its dimension is small compared to the wavelength. In microstructured fibres the waveguide contribution to the chromatic dispersion can be large and is determined by the choice of air-hole diameter (d) and pitch (Λ). For example, by increasing the pitch value, Λ , and decreasing the relative hole size d/Λ , the ZDW can be shifted up to mid-infrared region [27]. By carefully controlling the structural parameters of the microstructured fibre, different dispersion characteristics can be obtained, signifying the unique property of microstructured fibres in tailoring the dispersion characteristics.

2.3 Nonlinearity in optical waveguides

The response of any dielectric to light becomes nonlinear for intense electromagnetic fields, and optical waveguides/fibres are no exception. The origin of nonlinear response is related to the anharmonic motion of bound electrons under the influence of an applied field. As a result, the total polarization \mathbf{P} induced in related to the electric field \mathbf{E} given by Equation (2.9) including higher-order nonlinear susceptibility expressed as [1]

$$\mathbf{P} = \epsilon_0 \left(\chi^{(1)} \cdot \mathbf{E} + \chi^{(2)} : \mathbf{E}\mathbf{E} + \chi^{(3)} : \mathbf{E}\mathbf{E}\mathbf{E} + \dots \right) \quad (2.36)$$

where ϵ_0 is the vacuum permittivity and $\chi^{(j)}$ is j th order susceptibility. In general, $\chi^{(j)}$ is a tensor of rank $j+1$. The linear susceptibility $\chi^{(1)}$ represents the dominant contribution to \mathbf{P} and its effects are taken into account through the refractive index n and the attenuation coefficient α . $\chi^{(2)}$ is the second order nonlinear optical susceptibility which is zero in a material with inversion symmetry (such as silica), so that \mathbf{P}_2 is zero. $\chi^{(3)}$ is the third order nonlinear optical susceptibility.

The lowest order nonlinear effects in optical waveguides originate from the third order susceptibility, such as: nonlinear refraction, third-harmonic generation (THG), four-wave mixing (FWM). Processes such as THG and FWM require phase matching, otherwise they are not efficient and so can in general be ignored. Nonlinear refraction arises from the intensity dependence of refractive index and is given as

$$\tilde{n}(\omega, I) = n(\omega) + n_2 I = n + n_2 |\mathbf{E}|^2 \quad (2.37)$$

where $n(\omega)$ is the linear part which is well approximated by the Sellmeier equation, I is the optical intensity related with the electromagnetic field E , and n_2 is the nonlinear index coefficient related to $\chi^{(3)}$ by the relation

$$n_2 = \frac{3}{8n} \text{Re} \left(\chi_{\chi\chi\chi\chi}^{(3)} \right) \quad (2.38)$$

where the optical field is assumed to be linearly polarized so that only one component $\chi_{\chi\chi\chi\chi}^{(3)}$ of the fourth-rank tensor contributes to the refractive index. Note that nonlinear refraction is always phase matched and so most nonlinear effects originate from nonlinear refraction.

The nonlinear refraction leads to nonlinear effects such as self-phase modulation (SPM) and cross-phase modulation (XPM). These nonlinear effects are elastic which implies that no energy is exchanged between the electromagnetic field and the dielectric medium. Nonlinear effects that result

from inelastic interchange of energy between the electromagnetic field and the medium are stimulated Raman scattering (SRS) and stimulated Brillouin scattering (SBS). The main difference between the two is that optical phonons participate in SRS while acoustic phonons participate in SBS.

2.3.1 Self-phase modulation

The simplest effect due to nonlinear refraction is self-phase modulation (SPM) in which the optical field modulates its own phase. It is due to the intensity dependence of the refractive index in a nonlinear optical medium (Kerr effect), in accordance to Equation 2.37. For the electric field given by its complex amplitude

$$A(t) = A_0 \exp(-j\phi(t)) \quad (2.39)$$

where A_0 is the peak intensity.

The phase of an optical field changes by

$$\phi = (n + n_2|A|^2)k_0L \quad (2.40)$$

The intensity dependence leads to nonlinear phase shift $\phi_{\text{NL}}(t)$ given by

$$\phi_{\text{NL}}(t) = \frac{2\pi}{\lambda} n_2 |A|^2 L \quad (2.41)$$

where L is the propagation distance. SPM creates new frequencies and can lead to the spectral broadening of optical pulses which arises due to the time dependence of the nonlinear phase shift ϕ_{NL} i.e. the instantaneous optical frequency changes across the pulse.

The nonlinear pulse propagation equation (NLSE) with including only SPM by neglecting all other nonlinear effects can be written as [1]

$$\frac{\partial A}{\partial z} = j\gamma|A|^2A \quad (2.42)$$

where dispersive effects are neglected. This equation is obtained by assuming the frequency dependence of n_{eff} and A_{eff} can be ignored by assuming a purely instantaneous material response, ignoring the optical shock effect and ignoring loss.

By multiplication of the complex conjugate A^* and adding the complex conjugate of the obtained result, it can be shown that the power $P = |A|^2$ is a constant with regards to z , and one can derive that the electric field envelope solution is

$$A(z, T) = A(0, T) \exp(j\gamma|A(0, T)|^2 z) = A(0, T) \exp[j\phi(z, T)] \quad (2.43)$$

from which it is seen that the temporal pulse shape $|A|^2$ is unchanged during propagation. The time dependent phase shift $\phi(z, T)$ gives the pulse a frequency chirp $\delta\omega(T) = -\partial\phi/\partial T$ which is negative near the leading edge of the pulse and positive near the trailing edge of the pulse [1] which correspond to a red shift and a blue shift, respectively. SPM is typically observed in the early stages of SC generation.

2.3.2 Solitons

In the previous subsection it was mentioned that SPM alone red-shifts the leading edge of the pulse, while blue-shifting the trailing edge of the pulse. In the additional presence of normal dispersion the red-shifted part of the pulse will propagate faster than the blue-shifted part [1]. This means that the pulse broadens more quickly in time than if only dispersion was present. On the other hand, anomalous dispersion leads to a delay of red-shifted pulse

components and faster propagation of the blue-shifted part of the pulse. SPM thus acts to delay the broadening of a pulse propagating in the anomalous dispersion regime.

It turns out that it is possible for SPM and group-velocity dispersion (GVD) to exactly balance each other so that a pulse can propagate without changing its shape. Adding GVD in SPM Equation (2.42), the unperturbed NLSE can be expressed as

$$\frac{\partial A}{\partial z} = -j\frac{\beta_2}{2}\frac{\partial^2 A}{\partial T^2} + j\gamma|A|^2A \quad (2.44)$$

There is a solution to this equation corresponding to a pulse that does not change its shape upon propagation. It is called the fundamental soliton and can be found directly by assuming a shape preserving solution of the form $A(z, T) = V(T) \exp[j\phi(z, T)]$ and inserting it into Equation (2.44) [1] then one of its possible solution is

$$A(z, T) = \sqrt{P_0} \operatorname{sech}\left(\frac{T}{T_0}\right) \exp\left[\frac{j|\beta_2|}{2T_0^2}z\right] \quad (2.45)$$

where the peak power P_0 and pulse width T_0 is adjusted so that $P_0 = |\beta_2|/(\gamma T_0^2)$, and $\beta_2 < 0$ (or $D > 0$), so dispersion is anomalous. The solution of Equation (2.45) is called a fundamental soliton and it has the property that the power distribution $|A(T)|^2$ does not change during propagation, physically because GVD and SPM counteract each other.

The fundamental soliton is one out of an infinite amount of solutions of Equation (2.24) [1] characterized by the soliton number

$$N = \sqrt{\frac{L_D}{L_{NL}}} = \sqrt{\frac{\gamma P_0 T_0^2}{|\beta_2|}} \quad (2.46)$$

where $L_D = T_0^2/|\beta_2|$ is the dispersion length and $L_{NL} = 1/(\gamma P_0)$ is the nonlinear length. If $L_D \gg L_{NL}$ nonlinear effects will dominate the propagation, while if $L_{NL} \gg L_D$ linear dispersive effects dominate. For the fundamental soliton, the peak power and pulse width is adjusted so that $N = 1$, while if they are adjusted so $N \geq 2$, then a higher order soliton is excited in the waveguide. Higher order solitons do not propagate without changing shape as the fundamental soliton does, but under idealized conditions, as described by Equation (2.24), they change shape in a periodic manner, thereby recovering their initial shape once each period. During SC generation though, the governing equation is the full GNLSE, and the periodic dynamics is lost. An energetic seed laser in the anomalous dispersion regime, can result in a large initial soliton number, and subsequently, the spectrum typically develops through pulse breakup, into a number of fundamental solitons that are often individually distinguishable in a well developed SC spectrum [23, 47].

2.3.3 Cross-phase modulation

The cross-phase modulation (XPM) is another result of Kerr nonlinearity in optical waveguides, which arises from the intensity dependence of the refractive index $n = n_0 + n_2(|\mathbf{E}_1|^2 + |\mathbf{E}_2|^2)$. Two optical pulses at different wavelengths can couple in the process of XPM without any energy transfer between them. XPM is similar to SPM but the origin of spectral broadening is in mutual interaction of the different optical fields of different wavelengths. XPM initiate different nonlinear effects in optical waveguides. For example, in case of normally dispersive fibre with the specially designed dispersion profile (dispersion flattened fibre), the modulation instability occurs as the consequence of XPM. The beneficial applications of XPM modulation include XPM-induced pulse compression, optical switching etc.[1].

XPM plays an important role during the formation of SC spectrum inside the highly nonlinear waveguides. To understand its effects, one has to realize

that, even though the Raman solitons and dispersive waves have widely separated optical spectra, they may still overlap in the time domain. Any temporal overlapping of a Raman soliton with a dispersive wave results in their mutual interaction through XPM. Such a nonlinear interaction can create new spectral components and broaden the spectrum of dispersive waves in an asymmetric fashion which in turn broadens the SC in the short wavelength (anti-stokes) side of the input spectrum [1].

2.3.4 Four-wave mixing

Four wave mixing (FWM) describes a nonlinear process in which four optical waves interact with each other as the consequence of the third order susceptibility $\chi^{(3)}$. Such process is characterized as a parametric effect as it modulates refractive index. The origin of FWM is in the nonlinear response of bound electrons of a material to an electromagnetic field [1].

FWM process involve nonlinear interaction between four optical waves oscillating at frequencies ω_1 , ω_2 , ω_3 , and ω_4 . Generally, there are two types of FWM process. First corresponds to the case in which three photons transfer their energy to a single photon at the frequency $\omega_4 = \omega_1 + \omega_2 + \omega_3$. Second corresponds to the case in which two photons at frequency ω_1 and ω_2 are annihilated, while two photons at frequencies ω_3 and ω_4 are created simultaneously, so that $\omega_3 + \omega_4 = \omega_1 + \omega_2$. The efficiency of FWM depends strongly on the phase matching of the frequency components and consequently relies on dispersion properties of the optical waveguide. The phase matching condition requires matching of the wave vectors, i.e. $\Delta k = 0$. The particularly interesting is degenerate case, in which $\omega_1 = \omega_2$, so that a single input beam can be used to initiate FWM i.e. to generate a stokes and anti-stokes photon

$$2\omega_p = \omega_s + \omega_{as} \quad (2.47)$$

where ω_p , ω_s and ω_{as} are the pump frequency, stoke wave frequency and anti-stoke wave frequency, respectively.

In this case, the phase-matching condition is expressed as

$$\Delta k = (2n_p\omega_p - n_s\omega_s - n_{as}\omega_{as})/c = 0 \quad (2.48)$$

where n is the effective mode index at the frequency ω and c is the speed of light. Note that due to dispersion $n_p \neq n_s$ and so FWM is in general not phase-matched.

Similarly to stimulated Raman scattering (SRS), the process of FWM can be used to convert the input light into light at one or more different frequencies [48]. In comparison with SRS, parametric frequency conversion is more useful as the range of frequencies is broader and both frequency up-conversion as well as down-conversion is possible. The gain coefficient for FWM is larger than for SRS [1] and it can be expected that FWM always dominate over SRS when it is phasematched.

A typical feature of degenerate FWM is that when the pump is in the anomalous dispersion regime, the gain bands are wide and continuously connected across the pump and the gain bands are narrow and separated from the pump when it is in the normal dispersion regime [23]. In the time domain, FWM manifests itself as an instability of the power distribution amplitude as the pulse develops. The term modulation instability (MI) is used for this time domain analogue to FWM.

2.3.5 Self-steepening

Self steepening is a higher order nonlinear effect which results from the intensity dependence of the group velocity. It causes an asymmetry in the SPM broadened spectra of ultrashort pulses as the pulse moves at a lower speed than the wings of the pulse [1]. Therefore, as the pulse propagates inside the waveguide, the peak shifts towards the trailing edge and the trailing

edge becomes steeper with increasing distance. Self steepening of the pulse creates an optical shock and is only important for short pulses.

2.3.6 Stimulated Raman scattering

Raman scattering is a phenomenon that results from stimulated inelastic scattering. On a fundamental level it is related to the scattering of one photon by one of the molecules to a lower frequency photon, while the molecule makes the transition to a higher energy vibrational state. A photon of the incident field (pump) is annihilated to create a photon at a lower frequency (Stokes wave) and a phonon with the right energy and momentum to conserve the energy and the momentum [1]. Stimulated Raman scattering (SRS) is a combination of Raman scattering with stimulated emission, which leads to Raman amplification. The SRS can occur in both directions of a single mode optical waveguide. The initial growth of the stokes wave can be described by the equation

$$\frac{dI_s}{dz} = g_R I_p I_s \quad (2.49)$$

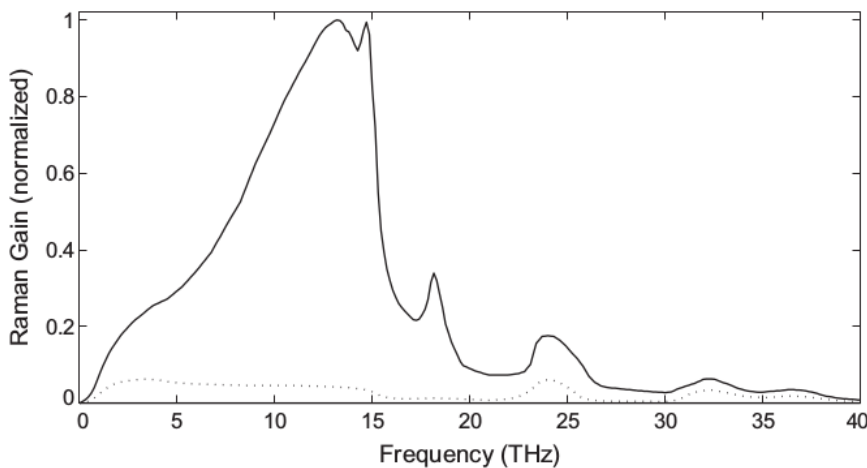


Fig. 2.1 Normalized Raman gain for fused silica when pump and stokes wave are copolarized (After [1])

where g_R is the Raman gain coefficient, I_s is the stokes intensity, while I_p is the pump intensity.

The Raman gain spectrum for silica, $g_R(\Omega)$, where Ω is the frequency difference between the pump and stokes waves, shown in Fig. 2.1, is found to be very broad, extending up to 40 THz with a peak located near 13 THz [48]. As long as the frequency difference Ω lies within the bandwidth of the Raman gain spectrum, the beam launched at the fibre input will be amplified because of the Raman gain. The maximum gain in silica is achieved for the frequency component downshifted by about 13 THz from the pump frequency. SRS exhibits a threshold like behaviour, implying that significant conversion of pump energy to stokes energy occurs when the pump intensity exceeds a threshold level. For a single mode fibre, assuming Lorentzian shape approximation for the Raman gain spectrum, the SRS threshold pump intensity is given by

$$I_p^{\text{th}} \approx 16 \frac{A_{\text{eff}}}{g_R L_{\text{eff}}} \quad (2.50)$$

The threshold pump intensity is inversely proportional to the effective fibre length. Note that the Raman effect in optical waveguides can be used to amplify a weak signal if that signal is launched together with a strong pump such that their frequency difference lies within the bandwidth of Raman gain spectrum [49]. The Raman response time of fused silica is extremely short, it occurs over a time scale of 60-70 fs. When ultrashort pulses are used (≤ 1 ps), which have a wide spectrum, the Raman effect can amplify low frequency pulse components by transferring energy from the high frequency components of the same pulse. Consequently, the spectrum shifts towards the low frequency side as the pulse propagates inside the waveguide (Raman induced frequency shift) [1]. The frequency shift increases linearly along the waveguide and it becomes very large for short pulses.

2.3.7 Dispersive waves

The emission of fundamental solitons is accompanied by a low amplitude temporal pedestal that propagates in a linear regime [50]. Fundamental solitons are susceptible to perturbations such as higher order dispersion and the resultant instability manifests as a nonsoliton radiation (NSR) at a particular frequency [51]. Essentially, a resonance condition involving higher order dispersion terms comes into play and leads to a coherent enhancement of the NSR at a narrow band of frequencies as predicted by the appropriate phasematching condition. This enhanced spectral component (which occurs in the normal dispersion regime of the waveguide) is sometimes also referred to as a Cherenkov radiation or soliton induced resonant emission. Cherenkov radiation is a terminology borrowed from particle physics and it appears when a particle travels faster than the phase velocity of light in the medium [52]. The analog of this effect in optical waveguides is the resonance that occurs between the pulse, which travels at its group velocity, and the dispersive wave resulting in an energy transfer from the soliton to the dispersive wave at a frequency dictated by the appropriate phasematching condition.

The frequency of the dispersive wave that grows because of radiation emitted by the perturbed soliton can be obtained by a simple phasematching argument requiring that the dispersive wave propagate with the same phase velocity as that of the soliton. If ω and ω_s are frequencies of the dispersive wave and of the soliton, respectively, the two phases at a distance z after a delay $t = z/v_g$ are given by [1]

$$\phi(\omega) = \beta(\omega)z - \omega(z/v_g) \quad (2.51)$$

$$\phi(\omega_s) = \beta(\omega_s)z - \omega_s(z/v_g) + \frac{1}{2}\gamma P_s z \quad (2.52)$$

where v_g is the group velocity of the soliton. The last term in Equation (2.52) is due to the nonlinear phase shift occurring only for solitons. The two phases are equal when the following phasematching condition is satisfied

$$\beta(\omega) = \beta(\omega_s) + \beta_1(\omega - \omega_s) + \frac{1}{2}\gamma P_s \quad (2.53)$$

where the relation $v_g = 1/\beta_1$ is used for the solutions of this equation which determine the frequency ω of one or more dispersive waves generated because of soliton perturbation.

The generation of dispersive waves during soliton fission is sensitive to minute details of the dispersion relation $\beta(\omega)$ of the waveguide, and it may be necessary in some situations to include dispersion terms even higher than the fourth order. A numerical approach with multiple higher-order dispersion terms shows that all odd-order terms generate a single NSR peak on the blue or the red side of the carrier frequency of the pulse, depending on the sign of the corresponding dispersion parameter [1]. In contrast, even-order dispersion terms with positive signs always create two NSR peaks on opposite sides of the carrier frequency [1]. It will be shown in details how two NSR produced in a two ZDW waveguide later in Chapter 5.

2.4 Summary

This Chapter gives a theoretical overview of the physics related to the generation of SC that is needed to understand the work presented in this thesis. For an understanding of the linear and nonlinear phenomena as well as their effects during propagation of optical signal inside the waveguide it is necessary to introduce the Maxwell's equations and the GNLSE that governs the propagation of optical field in the waveguide. Brief derivation procedures of the wave equations and the GNLSE equation are also shown. Finally, a few of

the most relevant nonlinear effects and concepts responsible for propagation dynamics of SC generation have been reviewed.

Chapter 3

Numerical Methods

This chapter presents the numerical methods for analyzing the properties of optical waveguides based on the Maxwell's equations and the generalized nonlinear Schrödinger equation (GNLSE) introduced in Chapter 2. Section 3.1 reviews the light guidance mechanisms of optical waveguides briefly. The finite-element (FE) method is used for yielding the linear properties of the optical waveguides in Section 3.2. Finally, Section 3.3 describes split-step Fourier method (SSFM) to solve GNLSE for observing propagation dynamics of optical signal through SC generation in waveguide output.

3.1 Optical waveguides

Before starting with numerical methods, we need to look into the guiding properties of optical waveguides with some examples in brief. There are several kinds of optical waveguides available for different applications, and they are generally divided into two classes depending on the physical guiding mechanism. One class is the index guiding waveguides while the other is photonic bandgap guiding (PBG) waveguides. Among index guiding waveguides, standard step-index fibre (SIF) [53] and photonic crystal fibre (PCF) [5, 7, 54] are prominent. Examples of other waveguides are cobweb lattice [55] and suspended core/wagon-wheel [56, 57] type geometries. Recently, planar ge-

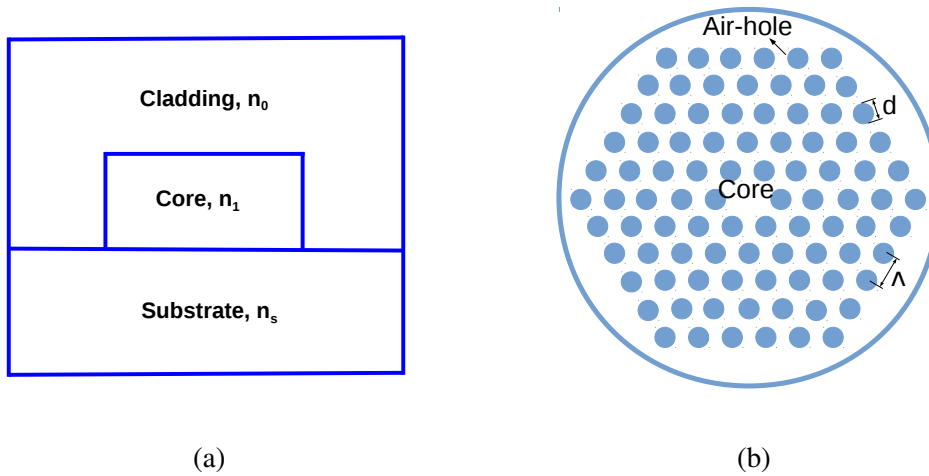


Fig. 3.1 Schematics of (a) planar (channel) waveguide and (b) PCF with hexagonal symmetry cladding containing air-holes.

ometries (rib/channel) are being considered as index guiding waveguides for SC sources owing to scalable, low cost fabrication and the potential for integrated optical chip solutions [21]. An example of PBG guiding waveguides is the hollow core fibres [58].

Standard step-index fibres consist of a cylindrical glass core surrounded by a cladding, with the cladding having a slightly lower index than the core [1]. Planar channel/rib waveguides consist of a square or rectangular core surrounded by a cladding with lower refractive index than that of the core shown in Fig. 3.1(a). Light can be confined in the core due to total internal reflection at the interface between core and cladding in index guiding waveguides [53]. PCF relies on an effective index difference between the solid core and the surrounding cladding containing air-holes for a modified total internal reflection guiding mechanism [54] shown in Fig. 3.1(b). PBG guiding waveguide offers a fundamentally different way of guiding the light in it. The photonic band gap effect makes it possible to guide the light in a hollow air-core, surrounded by a cladding containing air-holes [59, 60].

Optical waveguides analyses imply the process of finding the propagation constants and the field profiles of all the modes that a waveguide can support.

To be able to calculate these propagation characteristics, solutions of the well-known Maxwell's equations are obtained along with the satisfaction of the necessary boundary conditions. Applying the Maxwell's equations may not be an easy task and precise analyses of optical waveguides is generally considered to be a difficult task because of some major reasons such as the optical waveguides may have complex structures, arbitrary refractive index distribution (graded-index optical waveguides or photonic crystal fibres), anisotropic and nonlinear optical materials as well as materials with complex refractive index such as semiconductors and metals. These difficulties are surmounted using various methods of optical waveguide analyses developed. These methods can be broadly classified into two groups, namely the analytical approximation solutions and the numerical solutions. An exact analytical solution can be obtained for step-index two-dimensional optical waveguides (planar waveguides) and step-index fibre (SIF). However, if the waveguide has an arbitrary refractive index distribution such as PCFs and graded-index fibres, then the exact solutions may not be possible. Since we also consider here PCFs that do not have analytical solution, a finite-element based numerical method (FE mode-solver) is used for analyzing all optical waveguides proposed.

Initially the wave equation deduced from Maxwell's equations in Chapter 2 will be solved by finite-element (FE) method for analyzing the transverse field distribution of the optical waveguides. This determines the linear guiding properties of the medium due to the electromagnetic field developed inside the waveguides. Later the dynamical part of the propagation problem will be solved by using the generalized nonlinear Schrödinger equation through split-step Fourier method for the complex electric field envelope development inside the waveguides. Numerical methods used to analyze the properties and modelling of nonlinear medium of interest here are GeAsSe based planar

(rib/channel) waveguides and microstructured fibres (MoFs) for designing broadband mid-infrared SC laser sources.

3.2 Finite-element method

The rapid growth in the millimetre-wave, optical fibre and integrated optics fields has included the use of arbitrarily shaped dielectric waveguides, which in many cases also happened to be arbitrary inhomogeneous and/or arbitrarily anisotropic which do not easily lend themselves to analytical solutions. Therefore many scientists have given their attention to the development of numerical methods to solve such waveguides. Numerical methods may be used to solve Maxwell's equations exactly and the results they provide are accurate enough for the characterisation of most of the devices. Since the advent of computers with large memories, considerable attention has been paid to methods of obtaining numerical solutions of the boundary and initial value problems. These methods are usually evaluated in terms of their generality, accuracy, efficiency and complexity. It is evident from the review articles [61] that every method represents some sort of compromise between these aspects, implying that no method is superior to the others in all aspects. The optimal method should be the one that can solve the problem with acceptable accuracy but requires the minimum effort to implement and run in terms of manpower and computer capacity. The FE method has been the dominant and arguably the most powerful numerical method in computational mechanics for many decades. It has been successfully applied to solve problems encountered in many engineering disciplines such as fluid dynamics, heat conduction, aeronautical, biomechanical and electromagnetics.

The finite-element method is a well established numerical method for the solution of a wide range of guided wave problems. It can be very easily applied not only to optical waveguides of any shape but also to optical waveg-

guides with any refractive index distribution and to those with any anisotropic materials or nonlinear materials. This method is based upon dividing the problem region into a non-overlapping patchwork of polygons, usually triangular elements. The field over each element is then expressed in terms of polynomials weighted by the fields over each element. By applying the variational principle to the system functional, and thereby differentiating the functional with respect to each nodal value, the problem reduces to a standard eigenvalue matrix equation. This is solved using iterative techniques to obtain the propagation constants and the field profiles [64, 68]. The accuracy of the finite element method can be increased by using finer mesh. A number of formulations have been proposed, however, the full vectorial \mathbf{H} -field formulation is the most commonly used and versatile method in modelling optical waveguides due to much easier treatment of the boundary conditions. This method can accurately solve the open type waveguide problems near cut-off region and much better results were obtained by introducing infinite elements to extend the region of explicit field representation to infinity [63]. One drawback associated with this powerful vector formulation is the appearance of spurious or non-physical solutions. Suppression of these spurious solutions can be achieved by introducing a penalty term into the variational expression [65]. In order to eliminate the spurious solutions completely, another approach is employed using the edge elements [62, 68]. In modelling more complex structures, the finite element method is considered to be more flexible than the finite difference method due to the ability of employing irregular mesh. Since this method is used in this work, a more detailed description of the finite element method will be presented next.

Mathematically, the FE method is a numerical technique for obtaining approximate solutions to boundary-value problems and it is the extension of the two classical methods, the Raleigh-Ritz variational formulation and the Galerkin method of weighted residuals. A boundary value problem can be

defined by a governing differential equation in a domain, together with the boundary conditions on the boundary that encloses the domain. In the variational approach the boundary-problem is formulated in terms of variational expressions, referred to as functionals, whose minimum corresponds to the governing differential equations. The approximate solution is obtained by minimising the functional with respect to its variables [66]. The Galerkin method is based on the method of weighted residuals [67] in which the domain of the differential equation is discretized and the solution is approximated by the summation of the unknown solutions of each subdomain weighted by known functionals, relating them to the domain. The overall solution is obtained by minimising the error residual of the differential equation. Variational Formulation, while much less intuitive, is more advantageous as the underlying theory is more involved. Therefore, Variational Formulation is an ideal technique to solve a wide range of electromagnetic problems, which is used in FE method in this thesis.

3.2.1 The variational approach

There are several variational formulations for implementing FE method have been proposed for the analysis of the optical waveguide problem. These can be a scalar form [69], where the electric or magnetic field is expressed only in terms of one component, according to the predominant field component or can be in the vector form, where the electric or magnetic field is expressed in terms of at least two of the constituent field components.

It should be noted that most of the formulations applied in the FE method, yield to a standard eigenvalue equation

$$[A]\{x\} - \lambda[B]\{x\} = 0 \quad (3.1)$$

where $[A]$ and $[B]$ are real symmetric sparse and B is also positive definite. The eigenvalue, λ can be chosen as β^2 or k^2 , depending on the formulation

and the eigenvalues represent the nodal field values of the finite elements. It is desirable for the above matrix equation to be of this canonical form to allow an efficient solution. The scalar field approximation [72] and the vector field [78] both types of variational formulations are described next.

The scalar formulation

The scalar approximation can be applied in situations where the field can be described as predominantly TE or TM and it can be expressed in terms of the longitudinal components of the above modes. It has been used for the solution of homogeneous waveguide problems [70], open boundary problems [71], and for the analysis of the anisotropic waveguides [73]. For the quasi-TE modes over a domain, Ω where the dominant field component is E_x , the formulation can be written as

$$L = \int \int_{\Omega} \left[\left(\frac{\partial E_x}{\partial x} \right)^2 + \left(\frac{\partial E_x}{\partial y} \right)^2 - k_0 n^2 E_x^2 + \beta^2 E_x^2 \right] d\Omega \quad (3.2)$$

where β is the propagation constant, n is the refractive index, and k_0 is the free-space wavenumber.

For the quasi-TM modes, where H_x is the dominant field, the formulation can be written as [69]

$$L = \int \int_{\Omega} \left[\frac{1}{n^2} \left(\frac{\partial H_x}{\partial x} \right)^2 + \frac{1}{n^2} \left(\frac{\partial H_x}{\partial y} \right)^2 - k_0 n^2 H_x^2 + \frac{1}{n^2} \beta^2 H_x^2 \right] d\Omega \quad (3.3)$$

where β , n , and k_0 have their usual meanings defined above.

The vector formulation

For accurate characterization of waveguides where the modes are hybrid in nature and both longitudinal and transverse component exist, vector formulations have to be used. There are various FE method vector formulations using

- The longitudinal electromagnetic (\mathbf{E} and \mathbf{H}) field components;
- The transverse electromagnetic field components;
- The transverse electric field components;
- The transverse magnetic field components;
- The three electric field components;
- The three magnetic field components;
- The six electromagnetic field components;

A vector \mathbf{E} -field formulation based on the three electric field components has been applied in the literature to analyse cylindrical waveguides [80] and optical fibres [76, 81]. This formulation is valid for general anisotropic lossless waveguide problems. However, one must ensure the continuity of the tangential electric field components at the dielectric interface. Further, the natural boundary conditions correspond to a magnetic wall ($\mathbf{n} \times \mathbf{H} = 0$ or $\mathbf{n} \cdot \mathbf{E} = 0$) in the vector \mathbf{E} -field formulation and therefore it is essential to enforce the electric wall ($\mathbf{n} \times \mathbf{E} = 0$) as a boundary condition which is difficult to implement for irregular-shaped structures.

The vector \mathbf{H} -field formulation involves terms of all three magnetic field components, which gives an advantage over all other formulations. This formulation is valid for general anisotropic problems with a non-diagonal permittivity tensor [78, 79]. The natural boundary conditions correspond to those of the electric wall ($\mathbf{n} \times \mathbf{E} = 0$ or $\mathbf{n} \cdot \mathbf{H} = 0$); therefore, boundary conditions do not require to be enforced at the boundaries. Further, in dielectric waveguides, the permeability is always assumed to be that of free space; hence, all the components of are continuous across the dielectric interface which means the variation of the refractive index does not need to impose interface boundary conditions.

The vector \mathbf{H} -field formulation can be written as [40, 78]

$$\omega^2 = \frac{\int (\nabla \times \mathbf{H})^* \cdot \hat{\epsilon}^{-1} \cdot (\nabla \times \mathbf{H}) d\Omega}{\int \mathbf{H}^* \cdot \hat{\mu} \mathbf{H} d\Omega} \quad (3.4)$$

where ω , is the angular frequency, Ω is the waveguide cross-section $\hat{\epsilon}$ and $\hat{\mu}$ are the permittivity and permeability tensors respectively. To obtain the stationary solution of the functional Equation (3.4) this is minimised with respect to each of the variables, which are the unknown nodal field components H_x , H_y and H_z . This minimisation leads to a matrix eigenvalue equation as stated in Equation (3.1), where $[A]$ is a complex Hermitian matrix and $[B]$ is a real symmetric and positive-definite matrix. Because of the general 90° phase difference between the axial and transverse components of \mathbf{H} -field [77], the Hermitian matrix $[A]$ can be transformed to a real symmetric matrix for a lossless problem. In general, the matrices $[A]$ and $[B]$ are quite sparse. The eigenvectors x represents the unknown field components at the nodal points for different modes with λ as their corresponding eigenvalues and also λ is proportional to ω^2 . In order to obtain a solution for a given wavelength, the propagation constant, β value has to be changed iteratively until the output eigenvalue corresponds to that wavelength. By varying β over the wavelength range of interest, it is possible to calculate the dispersion characteristics for the various modes.

However, the above formulation (as well as the \mathbf{E} -field) yields spurious solutions because the divergence condition, $\nabla \cdot \mathbf{H} = 0$ is not satisfied automatically, therefore alternative approaches, such as the penalty coefficient method [63, 75] have been proposed to eliminate those non-physical solutions. This method will be discussed in a later section of this chapter.

Natural boundary condition

The natural boundary condition which is automatically satisfied in the variational formulation is called the natural boundary condition. In variational formulations these can be automatically satisfied, if left free. The scalar functional defined earlier in Equation (3.2) has the continuity of $\partial E_x / \partial \mathbf{n}$ as the natural boundary condition and the functional defined in Equation (3.3) has

the continuity of $(1/n^2)(\partial H_x/\partial \mathbf{n})$ as the natural boundary condition, where \mathbf{n} is the outward normal unit vector.

The vector \mathbf{H} -field formulation described in Equation (3.4) has the natural boundary condition of an electric wall, i.e. $\mathbf{n} \cdot \mathbf{H} = 0$. Therefore, there is no need to force any boundary condition on conducting guide walls. But for regular shaped waveguides and at the symmetric walls (if applicable) the natural boundary condition can be imposed to reduce the matrix size. However, it may be necessary to analyse the structure with complementary symmetry conditions to obtain all the modes, although the exploitation of the symmetry greatly reduces the computational cost.

Spurious solution

As mentioned earlier, solutions to the vector field formulation of Equation (3.4) described can contain some nonphysical or spurious solutions owing to the divergence condition $\nabla \cdot \mathbf{H} = 0$ is not satisfied automatically.

The identification of spurious modes among the physical modes can be difficult. When a set of eigenmodes is computed, sometimes spurious modes can be spotted by their eigenvectors, where the field varies in a random way along the cross-section of the waveguide. The penalty function method, introduced by Rahman and Davies [79], facilitates a way to formally distinguish between physical and spurious modes. The scheme works as follows. The value of $\nabla \cdot \mathbf{H}$ for each eigenvector of interest is calculated over the cross-section and only solutions with a low value of $\nabla \cdot \mathbf{H}$ will be considered as a real modes as an eigenvector of physical mode should satisfy. In order to eliminate the spurious modes, an additional integral is added by introducing penalty coefficient, α , a dimensionless number to the original functional Equation (3.4) which satisfies $\nabla \cdot \mathbf{H} = 0$. The resulting variational expression Equation

(3.4) can be rewritten as

$$\omega^2 = \frac{\iint \left[(\nabla \times \mathbf{H})^* \cdot \hat{\boldsymbol{\epsilon}}^{-1} (\nabla \times \mathbf{H}) + \left(\frac{\alpha}{\boldsymbol{\epsilon}} \right) (\nabla \cdot \mathbf{H})^* (\nabla \cdot \mathbf{H}) \right] d\Omega}{\iint \mathbf{H}^* \cdot \hat{\boldsymbol{\mu}} \mathbf{H} d\Omega}, \quad (3.5)$$

where \mathbf{H} is the full-vectorial magnetic field, * denotes a complex conjugate and transpose, ω^2 is the eigenvalue (ω being the angular frequency), α is the penalty term to eliminate spurious modes and $\hat{\boldsymbol{\epsilon}}$ and $\hat{\boldsymbol{\mu}}$ are the permittivity and permeability tensors, respectively.

3.2.2 FE method implementation

The main steps in the FE method implementation is representing the structure with smaller elements. Therefore, it is necessary to analyse the discretisation of the system domain, the behaviour of the field in each element by using the shape functions and the application of the element and global matrices.

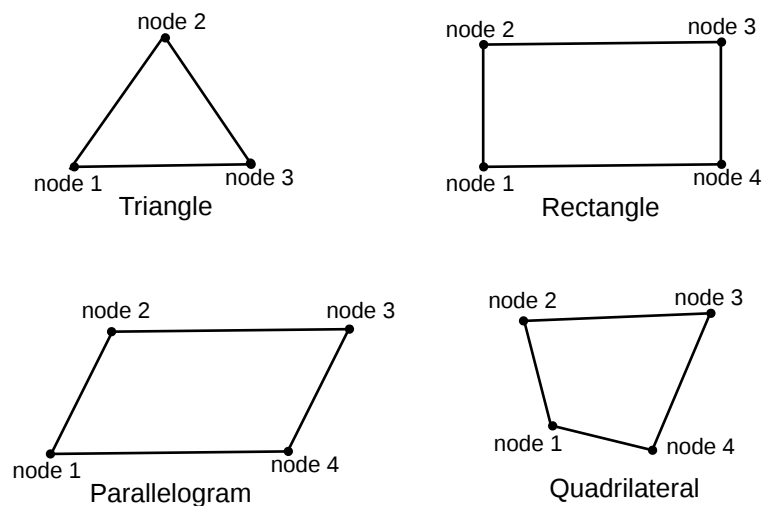


Fig. 3.2 Two dimensional elements.

Domain discretisation

The discretisation of the domain into sub-regions (finite elements) is considered as the initial step in the FE method. The shapes, sizes, number and configurations of the elements have to be chosen carefully such that the original body or domain is simulated as closely as possible without increasing the computational effort needed for the solution. Each element is essentially a simple unit within which the unknown can be described in a simpler manner. There are various types of elements available for use in FE formulations. These elements can be satisfied as one, two and three dimensional elements. When the geometry and material properties can be described in terms of two independent spatial coordinates, the two-dimensional elements shown in Fig. 3.2 can be used. The simplest and indeed the most basic element typically

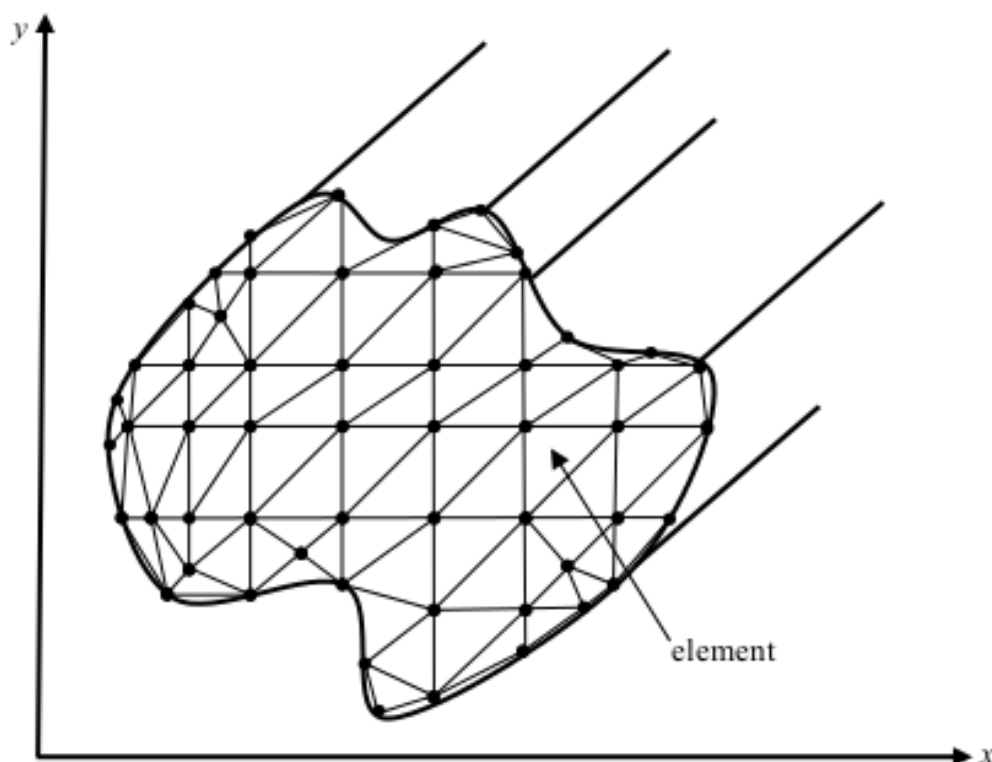


Fig. 3.3 Finite element discretisation of an irregular waveguide cross-section.

considered for two-dimensional analysis is the triangular element. The size of the element also dictates the accuracy of the final solution as higher order elements tend to provide more accurate solutions. A typical representation of an arbitrary waveguide structure using triangular elements is shown in Fig. 3.3.

By dividing the waveguide cross section into triangular elements, the unknown \mathbf{H} is also considered as to be discretised into corresponding sub-regions. These elements are easier to analyse rather than analysing the distribution over the whole cross section. As shown in Fig. 3.3, the transverse plane is covered with a grid of discrete nodes which are the vertices of each triangular element. The values of \mathbf{H} at these nodal points are the basic unknowns. The intersections of the sides of the triangular elements are called the nodal lines.

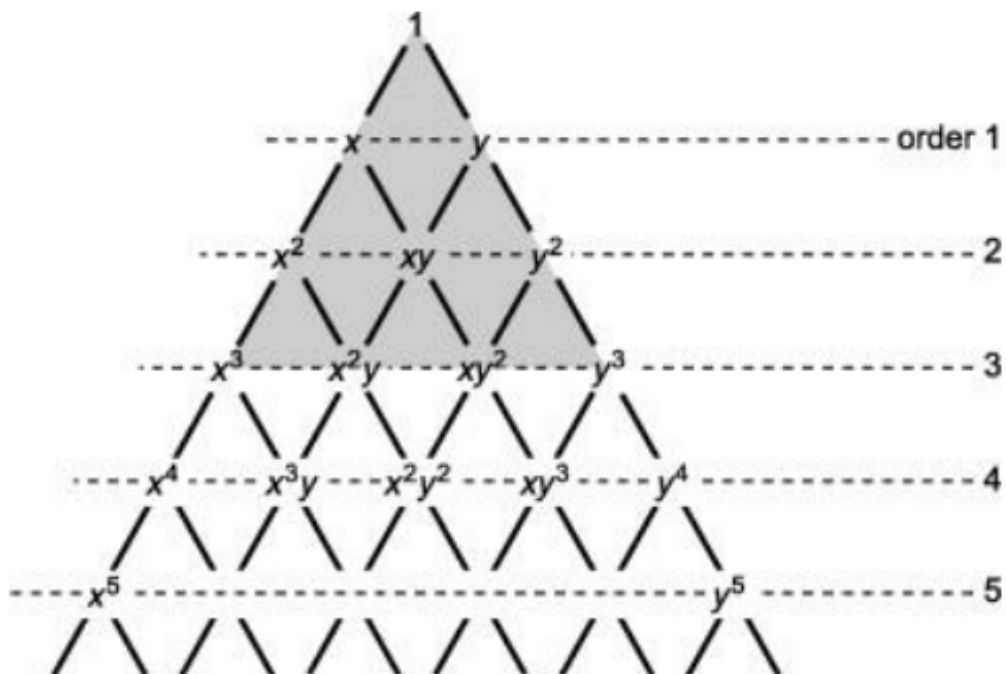


Fig. 3.4 Pascal's triangle for complete polynomials in two dimensions.

Shape function

In two-dimensional problems, the element assumes a linear interpolation between the field values at the vertices of the triangle. Within each element the unknown field \mathbf{H} , is approximated by means of suitably chosen set of polynomials. These functions are called shape functions. For a simple triangular element the interpolation polynomial should include a constant term and both the x and y terms rather than only one of them. The field variable representation within an element should not alter the local co-ordinate system. In order to achieve this geometric isotropy the polynomial should be complete according to Pascal's triangle as shown in Fig. 3.4.

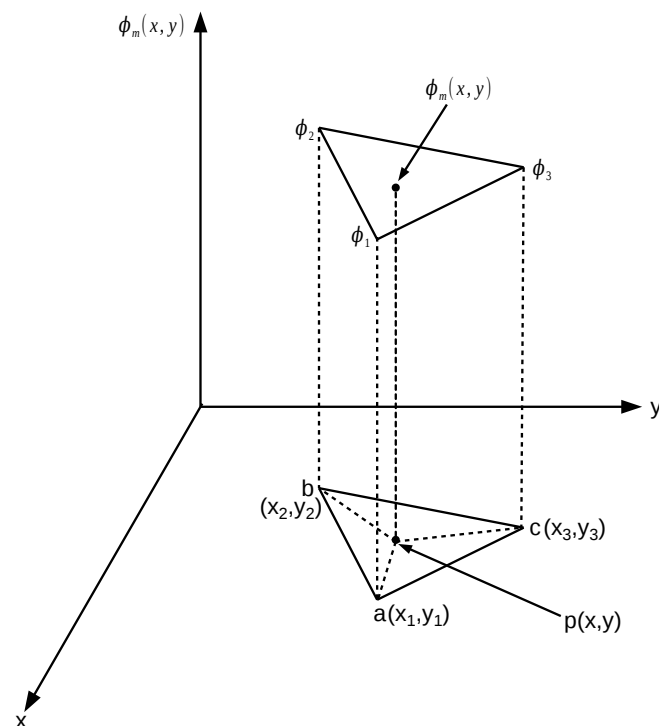


Fig. 3.5 Typical two dimensional first order triangular element.

The final consideration in selecting the order of the interpolation polynomial is to make the total number of terms in the polynomial equal to the

number of nodal degrees of freedom of the element. For example, the first degree polynomial involves three coefficients and so can be expressed in terms of three nodal values at the triangle vertices as shown in Fig. 3.5. The second degree polynomial needs six coefficients and can similarly be expressed in terms of values of six nodes.

The continuous field function $\phi(x,y)$ in the problem domain may be replaced by a set of discrete values ($\phi_i = 1, 2, 3, \dots, m$) where m is the total number of nodes. This function will be continuous across the triangles. To be admissible functions, they must satisfy some specific conditions between the elements; usually the continuity of the field across the boundaries is preferred.

A typical first order triangular element used in finite element discretisation is shown in Fig. 3.5. Inside each first order element, the nodal field values ϕ are interpolated continuously. $N_i(x,y)$ is defined as the shape function and $\phi_m(x,y)$ is defined as the field inside each element.

Thus, using the interpolation function the element field can be written as

$$\phi_m(x,y) = \sum_{i=1}^3 N_i(x,y) \cdot \phi_i \quad i = 1, 2, 3 \quad (3.6)$$

where ϕ_i are the nodal field values. Equation (3.6) can be written in the following matrix form

$$\phi_m(x,y) = [N_1 \quad N_2 \quad N_3] \begin{Bmatrix} \phi_1 \\ \phi_2 \\ \phi_3 \end{Bmatrix} \quad (3.7)$$

Therefore,

$$\phi_m(x,y) = [N] \{ \phi_m \} \quad (3.8)$$

where $[N]$ is the matrix form of the shape function and $\{\phi_m\}$ is the vector corresponding to the element nodal field values at the three nodes of the triangular element.

Linear approximation of the field inside an element is considered in order to obtain the shape function, $N_i(x, y), i = 1, 2, 3$

$$\phi_m(x, y) = a + bx + cy \quad (3.9)$$

where a, b and c are constants.

Equation (3.9) can be written as to satisfy the following condition

$$\phi_m(x_i, y_i) = \phi_i \quad (3.10)$$

Then, the nodal field values ϕ_i can be expressed as

$$\phi_1 \equiv \phi_m(x_1, y_1) = a + bx_1 + cy_1 \quad (3.11)$$

$$\phi_2 \equiv \phi_m(x_2, y_2) = a + bx_2 + cy_2 \quad (3.12)$$

$$\phi_3 \equiv \phi_m(x_3, y_3) = a + bx_3 + cy_3 \quad (3.13)$$

In matrix form:

$$\begin{Bmatrix} \phi_1 \\ \phi_2 \\ \phi_3 \end{Bmatrix} = \begin{bmatrix} 1 & x_1 & y_1 \\ 1 & x_2 & y_2 \\ 1 & x_3 & y_3 \end{bmatrix} \begin{Bmatrix} a \\ b \\ c \end{Bmatrix} \quad (3.14)$$

The constant a, b, c can be determined in terms of ϕ_i as

$$a = \frac{1}{2A_e} [\phi_1(x_2y_3 - x_3y_2) + \phi_2(x_3y_1 - x_1y_3) + \phi_3(x_1y_2 - x_2y_1)] \quad (3.15)$$

$$b = \frac{1}{2A_e} [\phi_1(y_2 - y_3) + \phi_2(y_3 - y_1) + \phi_3(y_1 - y_2)] \quad (3.16)$$

$$c = \frac{1}{2A_e} [\phi_1(x_3 - x_2) + \phi_2(x_1 - x_2) + \phi_3(x_2 - x_1)] \quad (3.17)$$

where A_e is the area of triangular element:

$$\begin{aligned} A_e &= \begin{vmatrix} 1 & x_1 & y_1 \\ 1 & x_2 & y_2 \\ 1 & x_3 & y_3 \end{vmatrix} \\ &= \frac{1}{2} [(x_2y_3 - x_3y_2) + (x_3y_1 - x_1y_3) + (x_1y_2 - x_2y_1)] \end{aligned} \quad (3.18)$$

Substituting the values of a , b , c from Equations (3.15)-(3.17) into Equation (3.9) and rearranging yields

$$\phi_m(x, y) = N_1(x, y) \cdot \phi_1 + N_2(x, y) \cdot \phi_2 + N_3(x, y) \cdot \phi_3 \quad (3.19)$$

or

$$\phi_m(x, y) = [N] \phi_m \quad (3.20)$$

Thus, after meshing the domain into small triangular elements, we can write the unknown field ϕ_m in every element in terms of an interpolation of the field values at each node, given by Equation (3.20). N_i are the shape or interpolation functions and are defined as

$$\{N\}^T = \begin{bmatrix} N_1 \\ N_2 \\ N_3 \end{bmatrix} = \frac{1}{2A_e} \begin{bmatrix} x_2y_3 - x_3y_2 & y_2 - y_3 & x_3 - x_2 \\ x_3y_1 - x_1y_3 & y_3 - y_1 & x_1 - x_3 \\ x_1y_2 - x_2y_1 & y_1 - y_2 & x_2 - x_1 \end{bmatrix} \begin{bmatrix} 1 \\ x \\ y \end{bmatrix} \quad (3.21)$$

where T denotes the transpose. This shape function matrix can also be written as

$$\{N\}^T = \begin{bmatrix} N_1 \\ N_2 \\ N_3 \end{bmatrix} = \frac{1}{2A_e} \begin{bmatrix} a_1 + b_1x + c_1y \\ a_2 + b_2x + c_2y \\ a_3 + b_3x + c_3y \end{bmatrix} \quad (3.22)$$

and $a_i, b_i, c_i, i = 1, 2, 3$ are calculated as

$$a_1 = x_2y_3 - x_3y_2 \quad (3.23)$$

$$b_1 = y_2 - y_3 \quad (3.24)$$

$$c_1 = x_3 - x_2 \quad (3.25)$$

with cycling exchange of $1 \rightarrow 2 \rightarrow 3$ in Equations (3.23)-(3.25).

Consider a typical point $p(x, y)$ inside the linear triangular element in Fig. 3.5. Therefore, the coordinates functions N_i can be expressed in terms of the areas of the triangles as below:

$$N_1 = \frac{\text{area of the sub triangle}(p, b, c)}{\text{area of the full triangle}(a, b, c)} \quad (3.26)$$

N_2 and N_3 can be expressed similarly. Therefore, N_i have the following property:

$$\sum_{i=1}^3 N_i = 1 \quad (3.27)$$

According to Equation (3.27), the value of the shape function N_1 at $a(x_1, y_1)$ is one, and for $b(x_2, y_2)$ and $c(x_3, y_3)$ the value of the shape function N_1 is zero. This is known as the unique first-degree interpolation function

for $a(x_1, y_1)$. Similarly, the shape functions N_2 and N_3 give a value of one at $b(x_2, y_2)$ and $c(x_3, y_3)$, respectively and zero at other nodes.

Formation of element and global matrices

The solution of the optical waveguide by the FE method can be transformed to a standard eigenvalue problem as in Equation (3.1) where matrices $[A]$ and $[B]$ are known as global matrices and consist of the summation of the element matrices for each triangular element of the discretised cross-section of the optical waveguide. In this section, the assembly of the element and global matrices is shown, with respect to the shape functions and the nodal field values of each triangular element, based on the variational formulation. Throughout the procedure, the full \mathbf{H} -field formulation in terms of the three components is assumed and first-order triangular elements are being used. Within each of the triangular elements the three unknown field \mathbf{H} -components H_x , H_y , and H_z of the magnetic field can be represented as follows

$$H_x(x, y) = \begin{bmatrix} N_1 & N_2 & N_3 \end{bmatrix} \begin{bmatrix} H_{x1} \\ H_{x2} \\ H_{x3} \end{bmatrix} \quad (3.28)$$

$$H_y(x, y) = \begin{bmatrix} N_1 & N_2 & N_3 \end{bmatrix} \begin{bmatrix} H_{y1} \\ H_{y2} \\ H_{y3} \end{bmatrix} \quad (3.29)$$

$$H_z(x, y) = \begin{bmatrix} N_1 & N_2 & N_3 \end{bmatrix} \begin{bmatrix} H_{z1} \\ H_{z2} \\ H_{z3} \end{bmatrix} \quad (3.30)$$

where H_{xi}, H_{yi} and H_{zi} for $i = 1, 2, 3$ are the x, y and z components of the magnetic fields at the three-nodes of a triangle. Hence the magnetic field over the element $[\mathbf{H}]_e$ can be described as

$$\begin{aligned}
 [\mathbf{H}]_e &= \begin{bmatrix} H_x(x,y) \\ H_y(x,y) \\ H_z(x,y) \end{bmatrix} \\
 &= \begin{bmatrix} N_1 & N_2 & N_3 & 0 & 0 & 0 & 0 & 0 & 0 \\ 0 & 0 & 0 & N_1 & N_2 & N_3 & 0 & 0 & 0 \\ 0 & 0 & 0 & 0 & 0 & 0 & N_1 & N_2 & N_3 \end{bmatrix} \begin{bmatrix} H_{x1} \\ H_{x2} \\ H_{x3} \\ H_{y1} \\ H_{y2} \\ H_{y3} \\ H_{z1} \\ H_{z2} \\ H_{z3} \end{bmatrix} \quad (3.31)
 \end{aligned}$$

In more compact form, the above equation (3.31) can be expressed as

$$[\mathbf{H}]_e = [N] \{\mathbf{H}\}_e \quad (3.32)$$

where $\{\mathbf{H}\}_e$ is the column vector representing the three components of the nodal field values in the elements and $[N]$ is the shape function matrix.

Using Equation (3.32), the curl of magnetic field vector $(\nabla \times \mathbf{H})_e$ can be applied in order to define this parameter over each element and can be written

as

$$\begin{aligned}
(\nabla \times \mathbf{H})_e &= \nabla \times [N]\{\mathbf{H}\}_e \\
&= \begin{bmatrix} 0 & -\partial/\partial z & \partial/\partial y \\ \partial/\partial z & 0 & -\partial/\partial x \\ -\partial/\partial y & \partial/\partial x & 0 \end{bmatrix} [N]\{\mathbf{H}\}_e \\
&= [Q]\{\mathbf{H}\}_e
\end{aligned} \tag{3.33}$$

where matrix $[Q]$ can be written as

$$\begin{aligned}
[Q] &= \begin{bmatrix} [0] & -\partial[N]/\partial z & \partial[N]/\partial y \\ \partial[N]/\partial z & [0] & \partial[N]/\partial x \\ -\partial[N]/\partial y & \partial[N]/\partial x & [0] \end{bmatrix} \\
&= \begin{bmatrix} [0] & j\beta[N] & \partial[N]/\partial y \\ -j\beta[N] & [0] & -\partial[N]/\partial x \\ -\partial[N]/\partial y & \partial[N]/\partial x & [0] \end{bmatrix}
\end{aligned} \tag{3.34}$$

where, $[0] = [0 \ 0 \ 0]$, $[N] = [N_1 \ N_2 \ N_3]$, $\partial[N]/\partial x = [b_1 \ b_2 \ b_3]$ and $\partial[N]/\partial y = [c_1 \ c_2 \ c_3]$ and the $\partial[N]/\partial x$ and $\partial[N]/\partial y$ are the differentiated form of Equations (3.24) and (3.25).

The vector \mathbf{H} -field formulation can be expressed for an element by substituting Equations (3.32)-(3.33) into Equation (3.4)

$$J_e = \int_{\Omega} \{\mathbf{H}\}_e^T [Q]^* \hat{\epsilon}^{-1} [Q] \{\mathbf{H}\}_e d\Omega - \omega^2 \int_{\Omega} \{\mathbf{H}\}_e^T [N]^T \hat{\mu} [N] \{\mathbf{H}\}_e d\Omega \tag{3.35}$$

where T and $*$ denote a transpose of matrix and the complex conjugate, respectively, and the integration is performed over the waveguide cross-section. In isotropic materials, the permittivity (ϵ) is a scalar value where as tensor permittivity, the ϵ can be represented in terms of the 3×3 inverse matrix format.

The relationship between function, J and the summation of the number of individual elements n over the waveguide cross-section, J_e can be written as

$$J = \sum_{e=1}^n J_e \quad (3.36)$$

By differentiating Equation (3.36) with respect to nodal field values and equating it to zero, the relationship can be obtained

$$\frac{\partial J}{\partial \{\mathbf{H}\}_e} = 0 \quad e = 1, 2, \dots, n \quad (3.37)$$

Therefore, the the eigenvalue equation can be written as

$$[A]\{\mathbf{H}\} - \omega^2[B]\{\mathbf{H}\} = 0 \quad (3.38)$$

where,

$$[A] = \sum_{e=1}^n [A]_e = \sum_{e=1}^n \int_{\Omega} \epsilon^{-1} [Q]^* [Q] d\Omega \quad (3.39)$$

$$[B] = \sum_{e=1}^n [B]_e = \sum_{e=1}^n \int_{\Omega} \mu [N]^T [N] d\Omega \quad (3.40)$$

where $[A]$ and $[B]$ are global matrices, $[A]_e$ and $[B]_e$ denote the element matrices and these matrices derived in Appendix. The $\{\mathbf{H}\}$ matrix consists of all \mathbf{H} -field nodal values of the waveguide cross-section.

The infinite elements

In open-type waveguides the problem domain is represented by filling ortho-dox elements up to a chosen boundary. This simple method is susceptible to significant errors being generated if the boundary is too close, hence requires the consideration of excessively large domains. One solution is to recursively

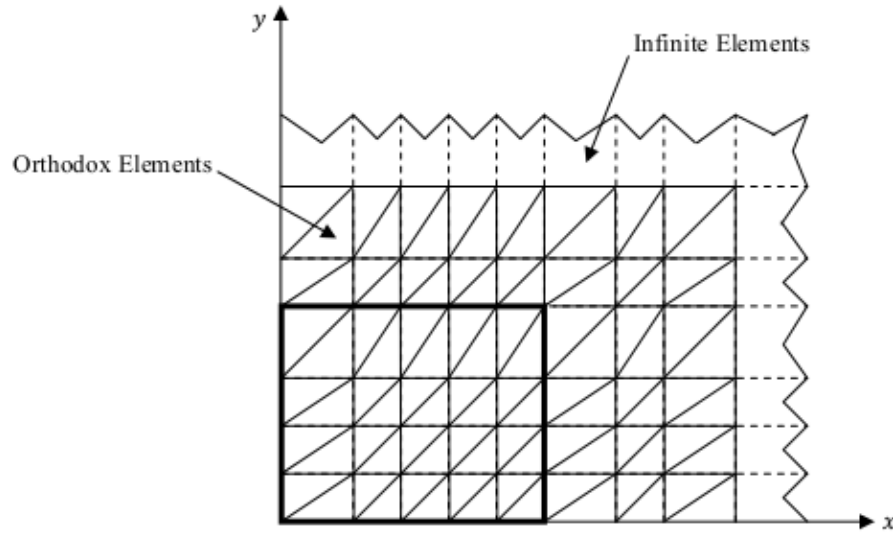


Fig. 3.6 Discretisation of a dielectric waveguide with orthodox and infinite elements.

shift the virtual boundary wall until a criterion for maximum field strength is satisfied. Rahman and Davies [78] presents a rather elegant solution which adds infinite elements along the outer boundary of orthodox elements as shown in Figure 3.6. For a typical rectangular dielectric waveguide problem, a quarter of the structure is discretised into orthodox and infinite elements by assuming two fold symmetry. The advantage of this concept comes from the fact that the computational domain is extended to infinity without increasing the matrix order, thus causing almost no change in the computational complexity.

The shape functions of the infinite elements should decay exponentially in the direction where the field extends to infinity. If an element is extended to infinity in the positive x -direction, the following shape function can be considered

$$N(x, y) = N_y(y) \cdot N_x(x) = N_y(y) \cdot \exp(-x/L_x) \quad (3.41)$$

where L_x is the decay length in the x -direction. L_x represents the decaying behaviour of the field outside the core region and depends on the structure

under consideration, Further, elements can be extended in the y -direction or both directions in a similar pattern to Equation (3.41) [78].

3.3 Split-step Fourier method

The GNLSE [Equation (2.29) in Chapter 2] is a nonlinear partial differential equation that does not generally lend itself to analytic solutions where nonlinear mechanisms such as self-steepening, Raman delayed response, and higher-order dispersions are present. A numerical approach is therefore often necessary for an understanding of the nonlinear effects developed owing to propagation of optical signal inside the optical waveguides [1]. There is a number of different methods have been developed, [82–84], that could be used to solve the GNLSE. The most commonly employed method is the split-step Fourier method (SSFM) [1, 82]. The SSFM is a pseudo-spectral method which is faster by up to two orders of magnitude compared to finite difference methods [1]. For the pulse widths of the order of ps this method is shown to work efficiently and accurately [1, 82]. In this thesis the SSFM is employed to solve the GNLSE for observing SC generation in optical waveguides (Chapter 5-7). A brief description of SSFM will be presented next.

3.3.1 SSFM for solving GNLSE

The SSFM method is based on separating the dispersive and nonlinear effects of the equation from one another. This assumes that over a very small distance these components may be assumed to be independent. Therefore, Equation (2.29) can be expressed in the following form

$$\frac{\partial A}{\partial z} = (\hat{D} + \hat{N})A \quad (3.42)$$

where \hat{D} is linear differential operator that takes into account dispersion and absorption of the medium and \hat{N} is a nonlinear operator that accounts for the effect of waveguide nonlinearities on pulse propagation [1]. These operators are defined as

$$\hat{D} = -\frac{\alpha}{2} + \sum_{m \geq 2} \frac{j^{m+1}}{m!} \beta_m \frac{\partial^m A}{\partial T^m} \quad (3.43)$$

$$\hat{N} = j \left(\gamma + j \frac{\alpha_2}{2A_{\text{eff}}} \right) \left(1 + \frac{j}{\omega_0} \frac{\partial}{\partial T} \right) \left(A(z, T) \int_{-\infty}^{\infty} R(T') |A(z, T - T')|^2 dT' \right) \quad (3.44)$$

Solving Equation (3.42) gives

$$A(z+h, T) = \exp[h(\hat{D} + \hat{N})]A(z, T) \quad (3.45)$$

In general, dispersion and nonlinearity act together along the length of the waveguide. The split-step Fourier method obtains an approximate solution by assuming that in propagating the optical field over a small distance h , the dispersive and nonlinear effects can be assumed to act independently. Suppose, propagation from z to $z+h$ is performed in two steps. In the first step, the nonlinearity acts alone, $\hat{D} = 0$ and in the second step, dispersion acts alone, $\hat{N} = 0$ in Equation (3.42).

The Baker-Hausdorff theorem states that for two non-commuting operators [85]

$$\exp(h\hat{D}) \exp(h\hat{N}) = \exp \left(h(\hat{D} + \hat{N}) + \frac{h^2}{2} [\hat{D}\hat{N} - \hat{N}\hat{D}] + \dots \right) \quad (3.46)$$

By ignoring the h^2 and higher terms in the exponential the following approximation can be made

$$\exp[h(\hat{D} + \hat{N})] \approx \exp(h\hat{D}) \exp(h\hat{N}) \quad (3.47)$$

This will result in the SSFM having an accuracy of approximately second order due to h^2 and higher-terms in the Baker-Hausdorff expansion have been neglected. It should be noted that the nonlinear and dispersive terms do not in fact commute.

Therefore, the solution for the pulse envelope of Equation (3.45) can be expressed as

$$A(z + h, T) \approx \exp(h\hat{D}) \exp(h\hat{N})A(z, T) \quad (3.48)$$

The accuracy of the split-step Fourier method can be improved by variation of Equation (3.48) known as the symmetrised SSFM [86], which has a higher

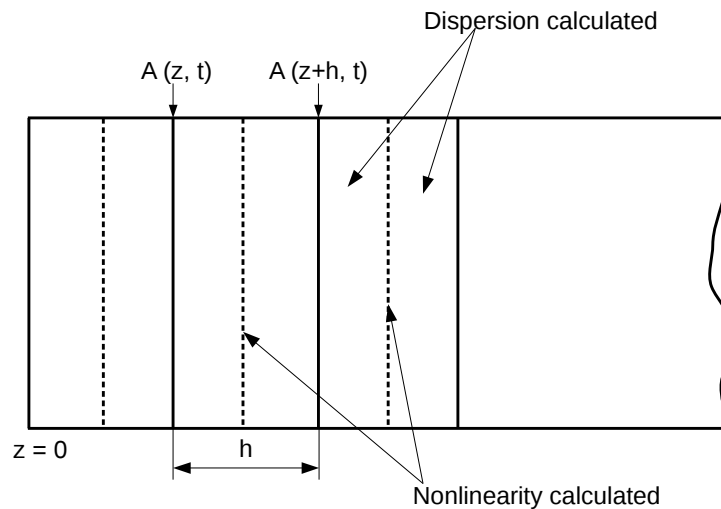


Fig. 3.7 Schematic diagram of the symmetrized SSFM used for numerical simulations. Waveguide length is divided into a large number of segments of width h and the effect of nonlinearity is included at the mid of the step shown by a dashed line.

accuracy. It works by calculating the nonlinear effects in the middle of each step as opposed to the edges as shown in Fig. 3.7. The spatial dependence of the nonlinear term is more accurately described by an integral, where as in Equation (3.48) it was approximated by

$$A(z+h, T) \approx \exp\left(\frac{h}{2}\hat{D}\right) \exp\left(\int_z^{z+h} \hat{N}(\hat{z})d\hat{z}\right) \exp\left(\frac{h}{2}\hat{D}\right) A(z, T) \quad (3.49)$$

The most important advantage of using the symmetrized form is that its accuracy increased to third-order due to applying the Baker-Hausdorff formula twice in Equation (3.49).

The accuracy of the split-step Fourier method can be further improved by evaluating the integral in Equation (3.49) more accurately than approximating it by $h\hat{N}(z)$. A simple approach is to employ the trapezoidal rule and approximate the integral from Equation (3.49) by [1]

$$\int_z^{z+h} \hat{N}(\hat{z})d\hat{z} \approx \frac{h}{2} \left(\hat{N}(z) + \hat{N}(z+h) \right) \quad (3.50)$$

It is necessary to follow an iterative procedure that is initiated by replacing $\hat{N}(z+h)$ by $\hat{N}(z)$ as because $\hat{N}(z+h)$ is unknown at the midsegment located at $z+h/2$. By using Equation (3.49), it can now easily estimate $A(z+h, T)$ which in turn is used to calculate the new value of $\hat{N}(z+h)$. Although the iteration procedure is time consuming, it can still reduce the overall computing time if the step size h can be increased because of the improved accuracy of the numerical algorithm.

3.3.2 SSFM implementation

To simulate SC generation MATLAB was used. The symmetrised SSFM was executed using the code 'SSPROP' [82] (based on the freely available in University of Maryland) in MATLAB. To implement SSFM, the waveguide

length is divided into a large number of segments that need to be spaced equally as shown in Fig. 3.7. The optical pulse is propagated from segment to segment using the prescription of Equation (3.49). The optical field $A(z, T)$ is first propagated for a distance $h/2$ with dispersion using the FFT algorithm [1]. At the midplane $z + h/2$, the field is multiplied by a nonlinear term that represents the effect of nonlinearity over the whole segment length h . Finally, the field is propagated for the remaining distance $h/2$ with dispersion only to obtain $A(z + h, T)$. The nonlinearity is assumed to be lumped at the midplane of each segment by dashed lines as shown in Fig. 3.7.

Taking the Fourier transform of the dispersion terms and the above approximation into account, the program will implement the symmetrised SSFM as follows

$$A(z+h, T) \approx \mathcal{F}^{-1} \left\{ \exp \left(\frac{h}{2} \hat{D}(j\omega) \right) \mathcal{F} \left\{ \exp \left(\int_z^{z+h} \hat{N}(\hat{z}) d\hat{z} \right) \mathcal{F}^{-1} \left\{ \exp \left(\frac{h}{2} \hat{D}(j\omega) \right) \mathcal{F} \{ A(z, T) \} \right\} \right\} \right\} \quad (3.51)$$

3.4 Summary

This chapter gives a theoretical overview of the numerical methods that required to be known for understanding of the work presented in this thesis. The light guiding mechanisms in different kinds of optical waveguides giving emphasis on most extensively used planar waveguides and microstructured fibres have been presented. A finite-element (FE) method based approach using the variational formulation with emphasis giving on vector \mathbf{H} -field formulation has been presented to create the modal solutions of various optical waveguides. Various aspects of the implementation of the FE method including domain discretisation, the use of different scalar and vector formulations, the use of boundary conditions, shape functions and the assembly of element and

global matrices have been discussed including spurious modes elimination technique. Finally, for observing optical signal evolution in the waveguide output, the nonlinear pulse propagation equation (GNLSE) has been solved using split-step Fourier method including the results obtained through modal solutions by FE method.

Chapter 4

Overview of SC generation

The generation of new frequency components with spectral broadening is an inherent feature of nonlinear optics and intensively studied since the early 1960s. When narrowband incident pulses undergo extreme nonlinear spectral broadening to yield a broadband spectrally continuous output then this process is known as SC generation [87]. SC generation was first observed by Alfano and Shapiro in bulk BK7 glass in 1970 [2, 3], and has since been the subject of numerous investigations in a wide variety of nonlinear optical waveguides. The advent of a new class of optical waveguides in the form of the microstructured photonic crystal fibre (PCF) in the late 1990s attracted widespread interest throughout the scientific community, and has led to a revolution in the generation of ultrabroadband high brightness spectra through SC generation [7, 8, 88]. The design freedom of microstructured fibres has allowed SC generation to be observed over a much wider range of source parameters than has been possible with planar waveguides or conventional fibres. For example, experiments have reported SC generation using unamplified input pulses of durations ranging from tens of femtoseconds to several nanoseconds, and even using high power continuous wave sources. SC sources have found numerous applications in the fields of spectroscopy, pulse compression, optical coherent tomography, bio-imaging, frequency metrology, and the design of tunable ultrafast femtosecond laser sources. In

the context of telecommunications, the spectral slicing of broadband SC spectra has also been proposed as a simple way to create multi-wavelength optical sources for dense wavelength division multiplexing (DWDM) applications.

In this chapter, we provide an overview of the nonlinear optics literature relating to the SC generation process. Section 4.1 reviews the work studying SC spectral broadening in bulk media. Section 4.2 devoted to review the SC works on silica microstructured fibres, and then in Section 4.3 reviewed the results obtained in nonsilica fibres and waveguides.

4.1 SC generation in bulk media

SC generation was first observed by Alfano and Shapiro 1970 extending the white light spectrum covering the entire visible range from 400 to 700 nm after launching 5 mJ picosecond pulses at 530 nm in bulk BK7 glass [2, 3]. The bandwidth of SC obtained by the Alfano and Shapiro's experiment was ten-times wider than anything previously reported. It was very interesting that they did not particularly emphasize this aspect in their article where they actually described to the first identification of nonresonant four-photon coupling, i.e., four-wave mixing. Later on Manassah *et al.* coined this phenomenon as 'supercontinuum' [89]. In the meantime, the phenomenon of SC generation was referred to as superbroadening in [90–92].

In 2000, Gaeta has given a consistent explanation based on full three-dimensional simulations of light propagation [93]. The concept proposed by Werncke *et al.* later on accepted that white light continuum generation in bulk material is due to the formation of an optical shock at the back of the pump pulses due to space-time focusing and self-steepening [90]. The role of plasma formation and multiphoton absorption is simply to arrest the collapse of the beam and to prevent the optical breakdown of the material. Self-focusing was found to be the key ingredient to SC generation in bulk

media, as it was commonly observed that the SC threshold coincided with the critical power for catastrophic collapse, usually associated with the formation of self-trapped filaments. SPM enhances in bulk material by beam collapsing which leads to an rapid increase in the peak intensity, but which also gives rise to a range of higher-order nonlinear effects, including self-steepening, space-time focusing, multiphoton absorption, avalanche ionization, and the formation of a free-electron plasma. It is clear that self-trapped filaments may or may not form in the process depending on the pulse duration and on the relative strength of chromatic dispersion, self-focusing, and plasma defocusing[94]. This phenomena is in agreement with all known observations, including the dependence of SC generation on the band gap of the material [95]. Self-focusing, in material with a small band gap, is stopped at lower intensities by free-electron defocusing, preventing the formation of a shock.

SC generation in bulk material is a highly complex process involving an intricate coupling between spatial and temporal effects and required high pump power such as in MW level. SC generation by contrast in optical waveguides such as planar or fibre based geometries involves purely temporal dynamical processes, with the transverse mode characteristics determined only by linear waveguide properties. Therefore, this suggests that a further motivation to study SC generation in planar and microstructured based fibres through dispersion engineering is to clarify the nature of temporal nonlinear propagation effects in order to improve the understanding of the more complex bulk waveguide design.

4.2 SC generation in conventional fibres

The first SC generation in optical fibres was first observed in 1976 by launching 10 ns pulses from a dye laser into a 20-m-long fibre [96]. The SC spectrum extended over 180 nm when the peak power was 1 kW. The pulses with du-

ration of 25 ps were launched into a 15-m-long fibre supporting four modes at the input wavelength of 532 nm in a 1987 experiment [97]. The output spectrum extended over 50 nm because of the combined effects of SPM, XPM, SRS, and FWM. Similar results were observed when single-mode fibres were used [98]. In a 1987 experiment, a 1-km-long single-mode fibre was used in which 830 fs input pulses with 530 W peak power produced a 200 nm wide spectrum at the output end of the fibre [99]. Similar features were obtained later with longer pulses [100, 101].

SC generation in single-mode fibres was used as a practical tool for generating pulse trains at multiple wavelengths simultaneously by launching a single picosecond pulse train at a wavelength near $1.55 \mu\text{m}$ [102–105]. Such a SC source acts as a useful laser for wavelength division multiplexing systems. The pulses with duration of 6 ps at a 6.3 GHz repetition rate with a peak power of 3.8 W which was obtained through amplifying the output of a gain-switched semiconductor laser operating at 1553 nm, were propagated in the anomalous dispersion region of a 4.9-km-long fibre in a experiment [103]. The SC generated was 40 nm wide enough that it could be used to produce 40 WDM channels by filtering the fibre output with an optical filter exhibiting periodic transmission peaks. The resulting 6.3 GHz pulse trains in different channels consisted of nearly transform limited pulses whose widths varied in the range of 5-12 ps. This technique produced a 200 nm wide SC, resulting in a 200 channel WDM source by 1995 [104]. The same technique was used to produce even shorter pulses by enlarging the bandwidth of each transmission peak of the optical filter. In 1997, Morioka *et al.* tuned the variable pulse width in the range of 0.37-11.3 ps by using an arrayed waveguide grating filter. In 1997, a SC source was used to demonstrate data transmission at a bit rate of 1.4 Tb/s using seven WDM channels with 600-GHz spacing [105].

The majority of SC generation studies in conventional fibre focused on the regime where pumping used ultrafast pump pulses. The detailed physics un-

derlying SC generation using longer pump pulses or CW excitation remained a subject of active research. Particularly an important work was reported by [106], where numerical simulations were used to elucidate the relationship between modulation instability, soliton dynamics, and Raman scattering under CW pump conditions. This work highlighted the fact that the SC generation in the anomalous GVD regime using CW pumps also involved soliton dynamics as in the case of pulsed excitation. Although an important physical insight, the lack of suitable high power CW sources somewhat limited follow up experimental studies in this field.

4.3 SC generation in silica microstructured fibres

SC generation is observed in microstructured fibres such as in photonic crystal fibres (PCFs) having a solid core in the center of the structure so that the fibre consists of a region of solid glass surrounded by an array of air-holes running along its length. The effective refractive index of the central region of the PCF is higher than that of the surrounding air-hole region often referred to as the photonic crystal cladding, and guidance occurs through modified total internal reflection [107]. Although this is conceptually similar to the guidance mechanism in conventional fibres, the additional degrees of freedom offered by modifying the hole size and periodicity in such an index-guiding PCF open up possibilities to engineer the waveguide dispersive properties in such ways which simply do not exist in conventional fibres. The total dispersion of PCF can be obtained by combining the both material and waveguide contributions together. The material dispersion for the conventional fibre and PCF are same but the waveguide dispersion are different for both fibres. Owing to high index contrast between core cladding interface, PCF has higher confinement of optical signal inside the core which in turn increases the nonlinearity of the PCF than conventional fibres. The dispersive properties of the PCF can be

adjusted easily by varying the air hole diameter and pitch which is impossible in conventional fibres. Therefore, these two properties have given PCF the superiority for SC generation than standard silica fibres.

In 2000, Ranka *et al.* experimentally reported SC extending from 400 to 1600 nm pumped with 100 fs pulses at 770 nm launched into a 75 cm long section of a silica microstructured fibre exhibiting anomalous dispersion near this wavelength with a peak power of 7 kW [7]. For such a short fibre SC was extremely broad and relatively flat over the entire bandwidth. Similar phenomena were observed in another experiment in the same year in which a 9-cm-long silica tapered PCF with 2 μm core diameter was employed and observed output spectra with 100 fs duration pulses at average power levels ranging between 60 and 380 mW [13]. SC spectra generated using short PCF in 2000 led to an explosion of research activity during the years of 2002 and 2003 in this nascent field [108–113]. The selection of the pump wavelength relative to the ZDW of the fibre was found to be a critical factor for SC generation [108]. Spectral expansion was reduced considerably because higher-order solitons could not form owing to the input pump wavelength fell in the normal GVD region of the fibre. In one experiment in 2002, a Yb-doped fibre laser producing parabolic pulses was used where the pump wavelength employed was exceeded 1000 nm [109]. In another experiment in the same year, femtosecond pulses were launched in the near of the second ZDW of a tapered fibre obtaining SC extending from 1000 to 1700 nm pumped at 1260 nm with 750 pJ of energy [110]. In the same year, a cobweb type 4.1-cm silica PCF with core diameters ranging from 1 to 4 μm was employed for SC generation experimentally by launching pump at a duration of 18 fs. As the PCF core was not perfectly circular, the fibre exhibited some birefringence. The spectral widths of observed SC spectra varied considerably with the polarization angle of incident light with respect to the slow axis of the fibre. In another experiment, a 6-m-long PCF at a pump wavelength of 850 nm

with 200 fs duration of pulses were launched from which it was observed the SC spectra exhibited multiple distinct peaks on the long-wavelength side which corresponded to Raman solitons formed after the fission of a high-order soliton [111]. In 2003, a relatively 600-m-long silica fibre employing 200 fs pulses from a mode-locked erbium fibre laser, a octave spanning SC was obtained from 1100 to 2200 nm experimentally [112]. SC extending from 1000 to 2500 nm was obtained experimentally employing a single 5-m-long highly nonlinear polarization maintaining fibre was used in a 2005 [113].

4.4 SC generation using nonsilica fibres

SC generation is of great theoretical interest as well as having numerous applications in optical frequency metrology, bio-imaging and spectroscopy due to having the creation of broadband spectral components from an intense light pulse passing through a nonlinear medium [23]. The generation of SC in a silica PCF and silica fibre tapers using a Ti:Sapphire laser had a striking impact on this research field [7, 13]. To generate a SC with a large bandwidth ranging from near-infrared to mid-infrared region with high brightness, numerous efforts have focused on fused silica fibres. However, the intrinsic transmission window of fused silica makes SC expansion beyond $2.2 \mu\text{m}$ a challenging task [27] which caused a gradual shift towards other types of glasses that have transmission windows transparent in the long wavelength region. In particular silicon (Si), ZBLAN, tellurite, and chalcogenide were investigated as nonlinear mediums for SC generation. Silicon offers a high Kerr nonlinearity and is attractive for generating SC using silicon-on-insulator (SOI) nanowires [28–30]. Although Si has low losses in the near infrared, it has some disadvantages in the telecommunication band centred at 1550 nm where it is affected by two-photon absorption (TPA) and free-carrier absorption (FCA), both of which clamp spectral broadening of SC and limit the

achievable bandwidth. The nonlinear properties of ZBLAN are approximately same as silica while tellurite is roughly 30 times and chalcogenide can be as much as a factor of thousand times more nonlinear than silica. Nonlinearity when combined with reasonably low TPA makes these glasses highly suited to both SC generation and ultrafast nonlinear switching applications. Fluoride glasses have linear and nonlinear refractive indices similar to those of silica, and ZBLAN has a lower loss than silica in the MIR, which enabled its use in some recent high power SC generation experiment [114]. Heavy metal oxide glasses such as lead silicate, bismuth oxide, tellurite have linear indices in the range 1.8–2.0, nonlinear indices ten times higher than silica, material ZDWs of 2–3 μm . Chalcogenide glasses such as GLS, As_2S_3 have linear indices of 2.2–2.4, and As_2Se_3 , GeAsSe have linear indices 2.4–2.6 where their nonlinear indices significantly greater than those of the oxide glasses and ZDWs larger than 4 μm .

In an experiment in 2003, a 30-cm-long fluoride fibre was pumped with 60 fs pulses and the SC extended in the range 350–1750 nm pumped at 1560 nm with 210 pJ energy where the measured spectra were limited to under 1750 nm because of a limit set by the optical spectrum analyzer employed [115]. It was found that the spectrum extended beyond this limit in 2006 using an infrared HgCdTe detector which could go up to 3000 nm for a fibre that was only 0.57 cm long [116]. In this experiment, 110 fs pulses with a 80 MHz repetition rate at a pump wavelength of 1550 nm were launched into a 2.6 μm core PCF made of Schott SF6 lead-silicate glass for the two different lengths such as 0.57-cm and 70-cm for average launched powers in the range of 1–70 mW, for which nonlinearity coefficient is 10 times larger than that of silica. SC was obtained up to 3000 nm for the highest average power of 70 mW in this experiment. It was found in an experiment in 2006 that the SC could be extended to up to 4500 nm by combining a 1-m-long silica fibre with a few meters long fluoride fibre where the strong absorption exhibited

by the fibres at wavelengths beyond 4500 nm [117]. The largest bandwidth in the range 565-5240 nm was realized in 2009 when a 2-cm-long fluoride fibre was pumped with 180 fs pulses at a wavelength of 1450 nm the average power level of 20 mW [118].

SC generation also have observed in tellurite glass based microstructured fibres. In 2008, the SC spectrum experimentally extended in the range 790-4870 nm measured at the -20 dB below the peak spectral power when 100 fs pulses with 1.9 nJ energy at a 1550 nm wavelength were transmitted through a 0.8-cm-long PCF [119]. In another experiment in the same year, SC could be extended from 900 to 2500 nm in a 9-cm-long microstructured tellurite fibre even with a large effective mode area of $3000 \mu\text{m}^2$ pumped with 120 fs pulses [120]. In an experiment in 2009, SC was observed from visible region to beyond $2.4 \mu\text{m}$ employing a 6-cm-long hexagonal core tellurite PCF pumped using 400 fs pulses at 1557 nm with pulse energies of 0.6 nJ [121].

Recently attention has focused on chalcogenide (ChG) glasses because these glasses exhibit high optical nonlinearities (several hundred times that of silica), are transparent in the MIR region, and can be easily drawn into a fibre form [35]. Clearly, ChG fibres can be used to develop a SC source providing wavelengths beyond $5 \mu\text{m}$, where the propagation losses of silica, ZBLAN, and tellurite fibres become intolerably large. ChG glasses contain the chalcogen elements S, Se, Te, covalently bonded with elements such as Ge, As, Sb and form stable glasses over a wide range of compositions [122]. Their optical properties such as refractive index and nonlinearity can be tuned by the appropriate selection of composition. In general, ChG glasses possess relatively high refractive indices which in turn increases the nonlinear refractive index according to Miller rule. For waveguide fabrication a high refractive index is advantageous and allows strong confinement of light, a reduction in the effective mode area and thus an increased nonlinear response.

The high index contrast also allows the waveguide bend radius to be reduced, which allows more compact integrated photonic devices. ChG glasses can provide MIR transparency up to $14\ \mu\text{m}$ when selenide-based materials are employed [141]. Since GeAsSe glasses have excellent film-forming properties and possess a relatively high third-order nonlinearity, there has been growing interest in using them for designing optical waveguides for broadband MIR SC generation [39]. Their high refractive index (2.4-2.8) allows strong optical field confinement, enabling small form factors in photonic chip design, small waveguide bend radii, as well as enhanced optical intensities for increased nonlinear interaction efficiency. They are also attractive in terms of waveguide fabrication because ChG glass can be drawn into high quality fibre (linear loss of less than 1 dB/m for step-indexed fibre at 1550 nm) [123] or fabricated as a planar waveguide on an oxidised silicon wafer (propagation loss of 0.05 dB/cm) [20]. In one approach, ultrashort pump pulses are launched into a dispersion-engineered planar waveguide. However, this approach suffers from cladding absorption and cut-off of the fundamental mode when an asymmetric structure is employed. A fibre-based device remain attractive because of its ruggedness, excellent beam quality, and relative ease of manufacturing [132]. Microstructured fibres are attractive due to their inherent advantages such as a controllable mode area and desirable dispersion properties achieved through tailoring their structural parameters. PCFs are particularly attractive as they offer significant enhancement of the nonlinear effects owing to a strong mode confinement and easier dispersion management resulting from the use of a cladding containing air holes [142].

Several experimental and theoretical investigations on mid-infrared SC generation were reported in ChG planar waveguides [21, 143–145] and ChG fibres [38, 132, 134, 137, 147–151, 153–156]. In an experiment in 2008, Lamont *et al.* [21] demonstrated SC generation in the range of 1200-1950 nm with a bandwidth of 750 nm launching pulses of 610 fs duration with a peak

power of 68 W in a 6-cm-long dispersion engineered As_2S_3 rib waveguide. Gai *et al.* [143] reported SC generation from 2.9 μm to 4.2 μm in dispersion-engineered As_2S_3 glass rib waveguide (6.6-cm-long) pumped with 7.5 ps duration pulses at a wavelength of 3.26 μm with a pulse peak power of around 2 kW. Yu *et al.* [144] reported SC generation up to 4.7 μm using a 4.7-cm-long As_2S_3 glass rib waveguide employing MgF_2 glass as a substrate and pumped with 7.5 ps duration with a peak power of 1 kW pulses at a wavelength of 3.26 μm . They observed a flat SC extending from 2.5 μm to 7.5 μm in 5-mm-thick bulk sample of $\text{Ge}_{11.5}\text{As}_{24}\text{Se}_{64.5}$ glass pumped with 150 fs duration pulses with up to 20 MW peak power at a wavelength of 5.3 μm . They also reported theoretically that SC could be generated beyond 10 μm in a dispersion-engineered all-chalcogenide $\text{Ge}_{11.5}\text{As}_{24}\text{Se}_{64.5}$ glass rib waveguide pumped with 250 fs duration pulses at a wavelength of 4 μm or longer. Yu *et al.* [145] recently reported the generation of broadband SC spanning from 1.8 μm to 7.5 μm in dispersion-engineered $\text{Ge}_{11.5}\text{As}_{24}\text{Se}_{64.5}$ glass 1-cm-long rib waveguide pumped at 4 μm using 320 fs pulses from a periodically-poled lithium niobate optical parametric amplifier pumped with commercially available mode-locked Yb laser with a peak power of 3260 W. In the case of optical fibres, Salem *et al.* [124] numerically demonstrated MIR SC extending in the range 3.14-6.33 μm by using 8-mm-long tapered As_2S_3 PCF with input pulse energy of 100 pJ pumped at 4.7 μm . Kubat *et al.* [149] reported a approach for generating MIR SC spanning in the range 0.9-9 μm by using concatenated 10-m-long fluoride and 10-cm-long chalcogenide fibres using a Tm fibre laser with a duration of 3.5-ps at a wavelength of 2 μm . For step-index fibre based on As_2S_3 , Hudson *et al.* [38] reported 1.9-octave SC extending from 1.6 μm to 5.9 μm pumped at a wavelength of 3.1 μm with a peak power of 520 kW. Al-Kadry *et al.* [156] reported MIR SC generation from 1.1 μm to 4.4 μm in 10-cm-long As_2Se_3 microwires pumped with 800 fs duration pulses at a wavelength of 1.94 μm with energy

of 500 pJ. Petersen *et al.* [150] used 100 fs pulses at 6.3 μm to generate SC covering the range 1.4-13.3 μm in 85 mm long As_2S_3 step-index fibre with a 16 μm core. Møller *et al.* [151] used a 18-cm-long, low-loss, suspended core $\text{As}_{38}\text{S}_{62}$ fibre and generated a SC spanning from 1.7 to 7.5 μm by pumping this fibre with 320 fs pulses with a peak power of 5.2 kW at a wavelength of 4.4 μm . Yu *et al.* [152] recently reported that a SC extending from 1.8 to 10 μm could be generated in a 11-cm-long, GeAsSe-based fibre using 320 fs pump pulses at a wavelength of 4 μm with a moderate peak power of 3 kW.

The SC generation in As_2S_3 fibres and waveguides has been limited to 5 μm due to their increased losses in the long wavelength region [132, 143, 153]. Although As_2Se_3 chalcogenide glass has its loss edge in the long wavelength region around 16-17 μm , the use of such materials for SC generation has so far been limited owing to high peak power pump sources required in the MIR region [31, 150, 156]. Among all chalcogenide materials, $\text{Ge}_{11.5}\text{As}_{24}\text{Se}_{64.5}$ ChG glass has excellent film-forming properties with high thermal and optical stability under intense illumination [39]. Recently interest has grown in designing and optimizing planar waveguides and microstructured based fibres made from $\text{Ge}_{11.5}\text{As}_{24}\text{Se}_{64.5}$ chalcogenide glass owing to having MIR transparency up to 14 μm for broadband MIR SC generation far into the MIR regime with suitably tailored group-velocity dispersion (GVD), including a zero-dispersion wavelength (ZDW) close to the central wavelength of the pump sources [21, 35].

4.5 Summary

SC sources have been widely available since 1970 and the physics describing its operation has been theoretically and experimentally predicted and identified since the end of the 1980s. It is really quite remarkable that the rapid growth in optical fibre based SC sources development has been commenced

in the last decade. In this chapter initially we have given the short overview of SC generation employing bulk media following the conventional fibres. Then a brief overview on SC generation using silica microstructured fibres has been presented. Finally SC generation employing nonsilica fibres such as fluoride and tellurite fibres have been described following highly nonlinear material such as chalcogenide glasses which are being nowadays considered as a promising platform for the realisation of compact on-chip SC generation. The overview on SC generation described in this chapter gives some indication of how this nonlinear optical processes such as dynamics of SC in optical waveguides has led to this development.

Chapter 5

SC generation in chalcogenide nanowire

Recently chalcogenide (ChG) planar optical waveguides have emerged as the key devices to construct scalable, low cost integrated optical circuits such as supercontinuum (SC) laser sources for numerous applications between near-infrared (IR) and mid-infrared (MIR) regimes [143–145]. Among such planar integrated circuits ChG rectangular channel waveguides have shown promising waveguide design for such applications. ChG waveguide enables the generation of MIR SC to above 10 μm due to its wide transmission window as well as the higher nonlinear refractive index (n_2), depending on the content of sulphur (S) or selenium (Se) used [146–149]. ChG glasses made from series of compound glasses such as As_2S_3 , As_2Se_3 , $\text{Ge}_{11.5}\text{As}_{24}\text{S}_{64.5}$, and $\text{Ge}_{11.5}\text{As}_{24}\text{Se}_{64.5}$ are typically used for optical waveguides fabrication [150–152]. Particularly, the compound $\text{Ge}_{11.5}\text{As}_{24}\text{Se}_{64.5}$ ChG glass has a large ultrafast third-order nonlinearity among other ChG compounds reported which makes it attractive for fabricating planar optical waveguides as laser sources for broadband SC generation. Its high linear refractive index $n \approx 2.6$ and broad infrared transparency beyond 14 μm suggest that compact optical circuit waveguides can be fabricated for near-IR to MIR applications. A high linear refractive index of this glass implies a higher nonlinear refractive index, n_2 which induced from ultrafast third-order (Kerr) nonlinearity which is up to thousand times that of silica, making this ChG glass attractive for all optical

signal processing [35–37]. Owing to having such useful properties, we choose to design and optimize a ChG nanowire through dispersion engineering made from $\text{Ge}_{11.5}\text{As}_{24}\text{Se}_{64.5}$ ChG glass for wideband SC generation.

This chapter presents detailed analysis of chalcogenide nanowire design for SC generation. Section 5.1 briefly reviews the material properties of chalcogenide glasses. Section 5.2 presents the dispersion optimization technique for analyzing two dimensional rectangular waveguides such as chalcogenide nanowires through rigorous numerical simulations by FE mode-solver. To test and verify the results obtained by FE mode-solver, two accuracy testing techniques have also been discussed in this section. Section 5.3 provides the simulations parameters for solving GNLSE numerically to predict SC generation in ChG nanowire output. Section 5.4 describes the results obtained through GNLSE simulations with the propagation dynamics occurred during wideband SC generation by the nanowire geometries optimized through FE mode-solver in earlier section. Section 5.5 shows verification of a SC result obtained through SSFM by frequency domain method. Finally, section 5.6 summarizes the study.

5.1 Material properties of ChG glasses

Chalcogenide glasses are comprised of heavy elements which give them some unique properties for infrared, nonlinear and waveguide optics. They contain one or more of the chalcogen elements from group 16 of the periodic table (S, Se, Te but excluding oxygen) covalently bonded to network formers such as As, Sb, Ge, Gb, Si, or P etc. They are, therefore, composed of relatively weakly bonded heavy elements and this leads to many of their most important optical and physical properties. Relatively low bond energies results in optical gaps in the visible or near IR as well as low to moderate glass transition temperatures ($T_g \approx 100 - 400^\circ\text{C}$). The low vibrational energies of

the bonds extends optical transparency to 8 μm for sulphides to 14 μm for selenides and beyond 20 μm for tellurides although impurities often exist in bulk glasses or films which significantly limit long wavelength transmission. For example 'high purity' chemical elements used for glass fabrication often contain significant quantities of C, O and H and these lead to absorption bands between 1.4 μm and 15 μm . As a consequence, a number of diverse approaches for purifying the starting materials have been developed that can reduce impurity levels to $\approx 10^{-5}\%$ by weight, thus markedly improving infrared transparency [31, 35, 129].

A scenario, how the properties of ChG glasses depend on composition, has emerged from the literatures [35, 125–128] where researchers works have shown substantial improvement of the understanding of the network topology of ternary chalcogenides such as the GeAsSe system. Recent studies comparing the properties of GeAsSe films with those of bulk glass suggest that for some composition films formed by thermal evaporation are also self organized so that they form with chemical bonds indistinguishable from those of the bulk glass [35, 130]. This is in fact quite unusual for ChGs since creating a film by physical vapour deposition onto a cold substrate is a highly non-equilibrium process which results in the film containing large numbers of defect bonds or molecular clusters. As a result it is usual for evaporated ChG films to have different physical properties (band-gap, refractive index, density, etc) from the bulk glass. Thus the self-organizing nature of networks is important for film forming and creates films that have been shown to be thermally stable. This has motivated researchers to study compositions such as $\text{Ge}_{11.5}\text{As}_{24}\text{Se}_{64.5}$ which is an example of a thermally stable nonlinear optical glass suitable for waveguide fabrication.

The structure of GeAsSe ChG glass on the atomic scale is best described as a continuous random network, for which an important parameter is the mean coordination number (MCN) - the sum of the products of the individual

abundance times the valency of the constituent atoms. For common binary ChG glass such as As_2Se_3 , the As-Se network is locally two dimensional with weak van der Waals bonding between the layers. The addition of atoms such as germanium makes the network three dimensional by creating bonds between layers, increasing network rigidity, T_g , strength and hardness. Gai *et al.* reported that glasses from the intermediate phase of the GeAsSe system corresponding to compositions with MCN around 2.45-2.5 should be the best for waveguide fabrication [35, 129, 130]. They demonstrated that films in this range deposited by thermal evaporation have physical properties (refractive index, band gap, density) indistinguishable from those of the bulk glass [35, 130]. In contrast, films with higher (or lower) MCN have quite different properties from the bulk. A consequence is that thermal annealing of films in the region of the intermediate phase does not change their properties whereas outside this region large changes can occur. Therefore it is believed that $\text{Ge}_{11.5}\text{As}_{24}\text{Se}_{64.5}$ ChG glass is a good stable material for waveguide fabrication.

The linear propagation loss of ChG waveguides due to material absorption is almost negligible in short waveguides design. The loss becomes more significant when the waveguide dimensions are reduced to the submicron range. Scattering losses of the optical field at the core-cladding boundary may become more significant only in the transition regions of the tapered fibre waist. To date the smallest planar waveguides/nanowires fabricated from GeAsSe ChG glass have losses around 1.5 dB/cm reported at a wavelength of 1550 nm through process improvements [35]. For larger planar waveguides, the optical losses have reported around 0.05 dB/cm at 1550 nm [20]. This is comparable with the lowest losses achieved in silica planar waveguides and indicate that complex circuits requiring long path lengths are also feasible. Nevertheless, for producing low loss waveguides operating over wide ranges in the MIR, impurity absorption in the glass films must be carefully controlled

to preserve optical transparency which will require careful attention to the purity of the starting materials used to make films and to the processes used to make the devices [35].

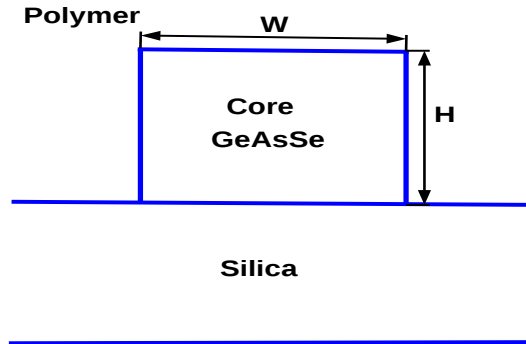


Fig. 5.1 Schematic diagram of chalacogenide nanowire.

5.2 ChG nanowire design

5.2.1 Structure of ChG nanowire

When a thin layer with a slightly increased refractive index is fabricated on top of some crystal or glass, it functions as a planar waveguide. Generally, rectangular planar waveguides consist of a square or rectangular core surrounded by a cladding with lower refractive index than that of the core. A channel waveguide has a guiding structure in the form of a stripe with finite width and thickness. This may be a ridge on top of the cladding structure or an embedded channel. A ridge type ChG nanowire is designed and optimized here which is shown in Fig. 5.1. Five nanowire structures have been optimized here through dispersion tailoring by varying nanowire dimensions at a pump wavelength of 1550 nm intended for applications in the MIR around 3 μm for wideband SC generation.

The schematic diagram of the $\text{Ge}_{11.5}\text{As}_{24}\text{Se}_{64.5}$ ChG nanowire used in our simulations is shown in Fig. 5.1. The wavelength-dependent linear refractive index of $\text{Ge}_{11.5}\text{As}_{24}\text{Se}_{64.5}$ and SiO_2 glasses over the entire wavelength range used in the simulation was obtained using the Sellmeier equation,

$$n(\lambda) = \sqrt{1 + \sum_{j=1}^m \frac{A_j \lambda^2}{\lambda^2 - \lambda_j^2}}, \quad (5.1)$$

Here λ is the wavelength in micrometers. We use the Sellmeier coefficients calculated by fitting smooth curves to the measured refractive index data for the ChG [39] and the SiO_2 [166] glasses. The values of the integer m and the fitting coefficients are given in Table 5.1.

Table 5.1 Sellmeier fitting coefficients

| Material | $\text{Ge}_{11.5}\text{As}_{24}\text{Se}_{64.5}$ [39] | | SiO_2 [166] | |
|----------|---|-------------|----------------------|-------------|
| m | 1 | | 2 | |
| | A_j | λ_j | A_j | λ_j |
| $j = 1$ | 5.78525 | 0.287950 | 0.6961663 | 0.0684043 |
| $j = 2$ | 0.39705 | 30.39338 | 0.4079426 | 0.1539661 |
| $j = 3$ | – | – | 0.8974794 | 9.8961610 |

5.2.2 Aitken extrapolation technique for accuracy testing of FE modal solution

Before evaluating GVD and higher-order dispersion parameters, accuracy of the finite-element modal solutions is tested. It should be noted that the design of optical waveguides for SC generation depends on dispersion parameters, β_m ($m \geq 2$) and β_m depends on mode propagation constant, $\beta_0(\omega)$. So accuracy of any design critically depends on modal solutions of a waveguide. It is well-known that accuracy of numerical solutions depends on several discretization parameters. For our optical waveguides, solution accuracy depends on the number of elements used to represent the waveguide structure. Using the FE

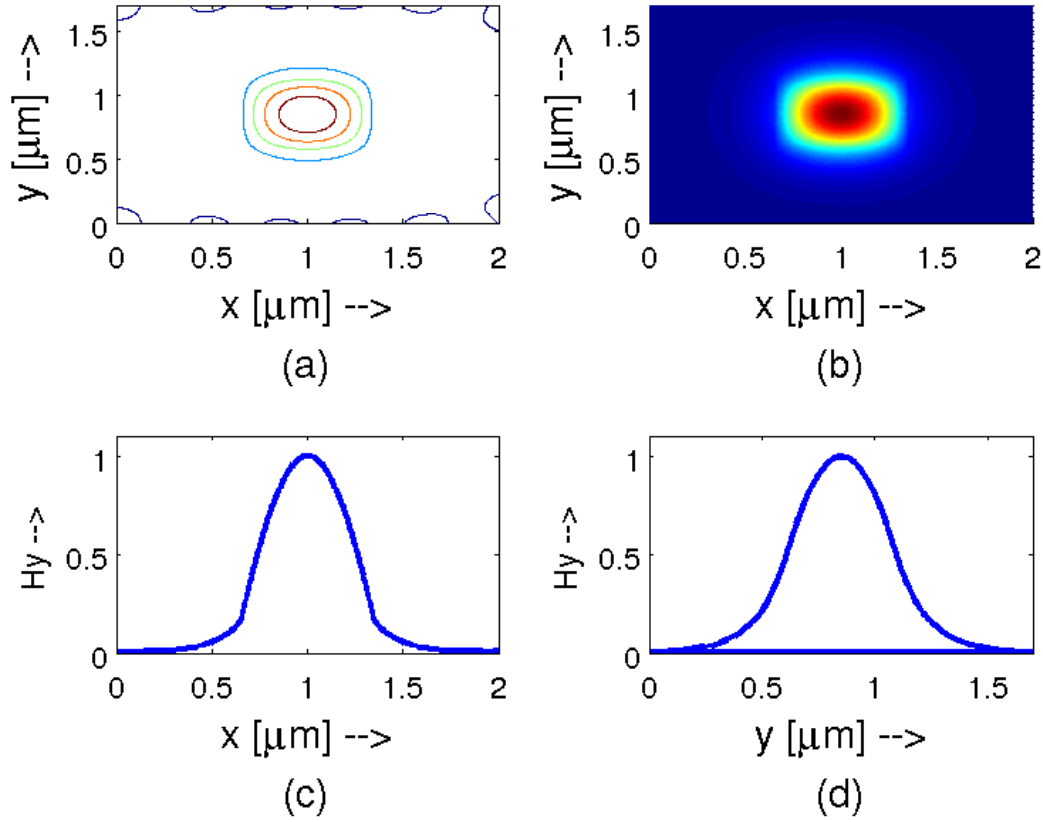


Fig. 5.2 Dominant H_y field profile of fundamental quasi TE-mode (H_y^{11}) for the nanowire structure of $W = 700$ nm and $H = 500$ nm at a wavelength of 1550 nm; a) Contour, b) Surface, c) H_y field along width, and d) H_y field along thickness of a nanowire.

method described in Chapter 3 we have obtained modal solutions from which mode propagation constant $\beta(\omega)$ of the fundamental mode over a range of frequencies are evaluated and calculate the effective index,

$$n_{\text{eff}} = \frac{\beta(\omega)}{2\pi} \lambda \quad (5.2)$$

where λ is the operating wavelength.

Figure 5.2 shows the (H_y^{11}) mode field profile of the fundamental quasi-TE mode with the four different field representations of the nanowire structure, $W = 700$ nm and $H = 500$ nm at a wavelength of 1500 nm. It is apparent from different field representations inside the core as well as along the dimensions

of the structure that the mode is highly confined inside the core of this nanowire. Variation of the effective index, n_{eff} with the number of mesh divisions N used is shown in Fig. 5.3 by a solid black line for the fundamental mode of a waveguide designed with the width and thickness, $W = 700$ nm, $H = 500$ nm and the operating wavelength of 1550 nm. The same value of mesh division, N was used in both the transverse directions. It can be observed that, as N increases, n_{eff} first increases rapidly and then reaches a constant value asymptotically. It should be noted that when a 100×100 mesh is used n_{eff} is accurate to 3rd decimal place, and the accuracy is increased to 4th decimal place when mesh size is increased to 500×500 . A powerful extrapolation technique [133] was used to test the accuracy of modal solution for this nanowire structure. Aitken's procedure [133] extrapolates from three successive values of n_{eff} with a fixed geometric mesh division ratio in both the transverse dimensions of a waveguide:

$$n_{\text{eff}}^{\infty} = n_{\text{eff}(r+1)} - \frac{[n_{\text{eff}(r+1)} - n_{\text{eff}(r)}]^2}{n_{\text{eff}(r+1)} - 2n_{\text{eff}(r)} + n_{\text{eff}(r-1)}}, \quad (5.3)$$

Table 5.2 Aitken's extrapolated values calculated using Equation (5.3) for the nanowire, $W = 700$ nm, $H = 500$ nm at a wavelength of 1550 nm.

| Mesh ($N_x \times N_y$) | n_{eff} | Aitken value (n_{eff}^{∞}) |
|---------------------------|------------------|--|
| 50×50 | 2.20901 | – |
| 100×100 | 2.21377 | – |
| 150×150 | 2.21470 | – |
| 200×200 | 2.21503 | 2.21548 |
| 250×250 | 2.21519 | – |
| 300×300 | 2.21529 | – |
| 400×400 | 2.21536 | 2.21548 |
| 500×500 | 2.21540 | – |
| 600×600 | 2.21543 | 2.21547 |
| 800×800 | 2.21545 | 2.21547 |
| 1000×1000 | 2.21546 | 2.21547 |
| 1200×1200 | 2.21546 | 2.21547 |

We have plotted the Aitken extrapolated values of n_{eff}^{∞} from Table 5.2 in Fig. 5.3 by a red-dashed line. Using Equation (5.3), for instance, we calculate Aitken's value from three successive n_{eff} values of 2.20901, 2.21377, and 2.21503 for mesh divisions, $N_x \times N_y = 50 \times 50, 100 \times 100,$ and $200 \times 200,$ respectively. From these three values, the extrapolated more accurate value is 2.21548. It is possible to get similar accuracy without using Aitken's extrapolation, but it would take a mesh finer than 1000×1000 to obtain it. Figure 5.3 clearly illustrates the convergence of raw FEM results and the advantage of using an extrapolation technique.

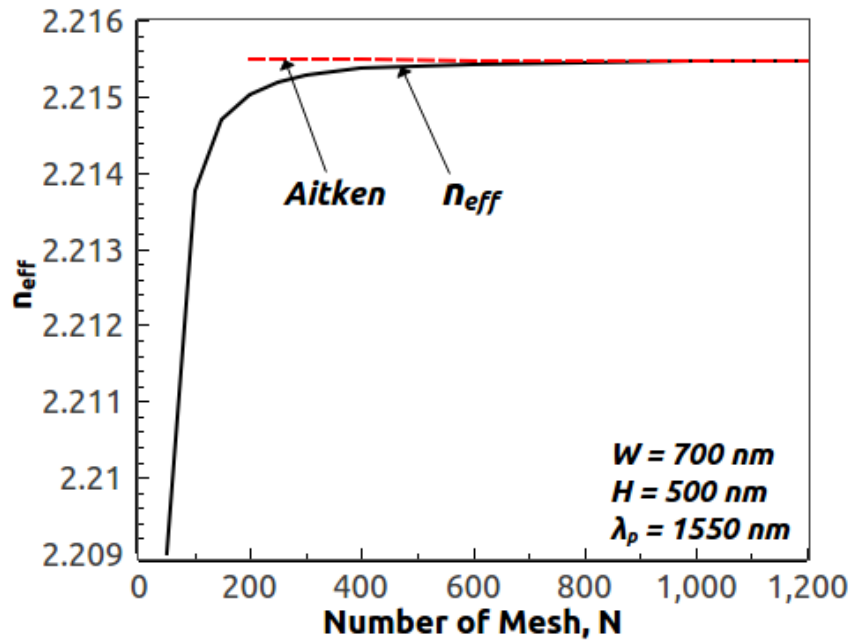


Fig. 5.3 Variation of n_{eff} of the fundamental quasi-TE mode with the mesh size and improvement realized with the Aitken extrapolation technique.

5.2.3 Calculation of GVD and higher-order dispersions

Dispersion of the waveguide plays an important role in determining the SC spectrum. Ideally dispersion near the pump wavelength should be small in magnitude as well as relatively flat in nature [137]. ChG glasses generally have smaller material dispersion than silicon. However, to obtain the ZDW

close to the pump wavelength, relatively larger waveguide dispersion is required to offset the material dispersion, resulting in a waveguide that supports more than one mode. To reduce higher-order modes, a polymer cladding with a refractive index value of 1.51 is often used in place of air cladding [35] as it reduces the index contrast between the core and cladding of the nanowire. As chromatic dispersion of the waveguide manifests through the wavelength dependence of the refractive index $n(\lambda)$ which is approximated by the Sellmeier Equation (5.1), therefore, the GVD parameter of the ChG nanowire can be calculated from the n_{eff} by

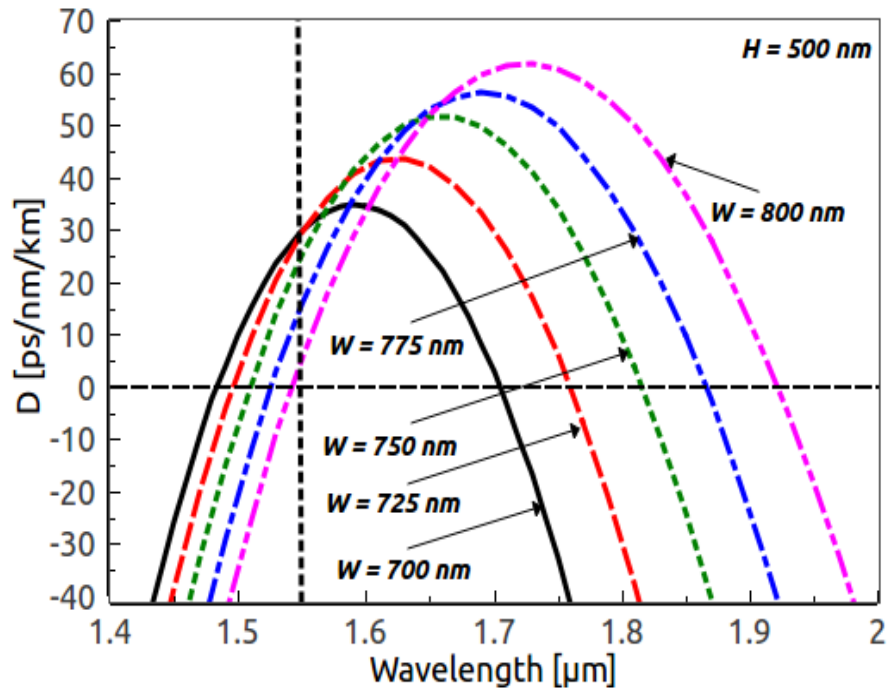
$$D(\lambda) = \frac{d\beta_1}{d\omega} = -\frac{\lambda}{c} \frac{d^2 n_{\text{eff}}}{d\lambda^2} \quad (\text{ps/nm/km}) \quad (5.4)$$

where $\beta_1 = 1/v_g$, v_g is the group velocity of pulse envelop and the third-order dispersion (TOD) can be calculated as

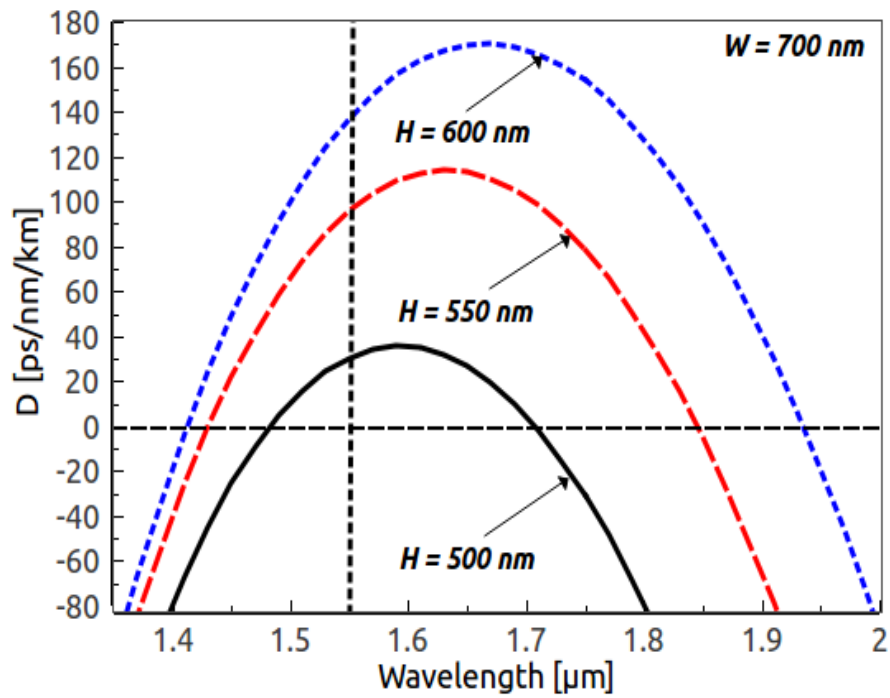
$$\text{TOD} = \frac{dD(\lambda)}{d\omega} \quad (\text{ps}^3/\text{km}) \quad (5.5)$$

The GVD, TOD and subsequently other higher-order dispersion coefficients up to eighth-order are calculated from n_{eff} numerically implemented by finite-difference method. Spectral broadening of a SC mainly depends on these dispersion parameters and the nonlinear coefficient, γ , which in turn depends on the nonlinear refractive index of the material, n_2 and effective mode area of the waveguide. Optimized mode area, A_{eff} can be obtained by using our FE mode-solver [79] and using this A_{eff} a relatively large nonlinear co-efficient can be realized [27].

To realize a ZDW close to the pump wavelength and to make dispersion slightly anomalous at this pump wavelength, the dimension of $\text{Ge}_{11.5}\text{As}_{24}\text{Se}_{64.5}$ nanowires can be adjusted. In one set, thickness of the waveguide is kept constant at 500 nm and its width is varied as shown in Fig. 5.4(a). This figure shows dispersion curves having two ZDWs, with anomalous dispersion



(a)



(b)

Fig. 5.4 GVD curves for the fundamental quasi-TE mode calculated from the n_{eff} values for (a) different W and same H and (b) different H and same W . Vertical dotted line represents the wavelength $\lambda = 1550 \text{ nm}$.

between these two ZDWs but both the peak value and slope of these curves increases as the width is increased. It can be observed from this figure that the 1st ZDW point with a positive slope shifts from left to right, and the 2nd ZDW with a negative slope also shift towards right but with a larger margin when W is increased. In this case the overall anomalous range also increases. Figure 5.4(a) clearly illustrates that the ZDW of the waveguide can be realized close to the pump wavelength by varying the width of that waveguide. In the other set of dispersion curves shown in Fig. 5.4(b), thickness of the waveguide is varied while keeping its width constant at 700 nm. In this case, ZDWs shift in the opposite directions, but the long wavelength one shifts more than the shorter one. It can be observed that the peak value of D increases when H is increased. Figures 5.4(a) and 5.4(b) indicate that the lower ZDW of a waveguide can be made to fall near the pump wavelength by adjusting the waveguide dimensions W and H .

5.2.4 Accuracy testing of GVD with the variation of FE mesh and data fitting through Taylor series expansion

As the dispersion of waveguide depends on n_{eff} which varies with λ , the accuracy of GVD also required testing as well as all higher-order dispersion coefficients calculated from it. Accuracy of the resulting curve is shown in Fig. 5.5 for three different mesh sizes for the same nanowire structure with $W = 700$ nm, $H = 500$ nm. The resulting dispersion curves nearly overlap since they are related to changes in the n_{eff} values rather than their absolute values. At the 1550 nm wavelength, GVD for three different meshes are calculated as 29.60 ps/nm/km, 30.49 ps/nm/km, and 30.94 ps/nm/km, respectively. The small differences among these dispersion values do not result in significant changes in the SC spectrum. However, we have observed through numerical simulations that the third and higher-order dispersion parameters have significant effect on the SC generation. In the following

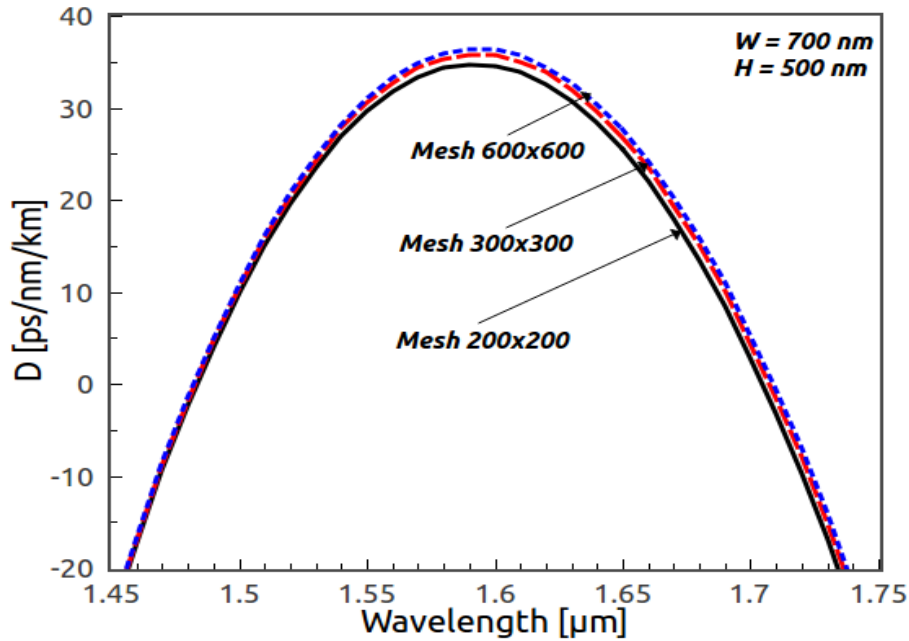
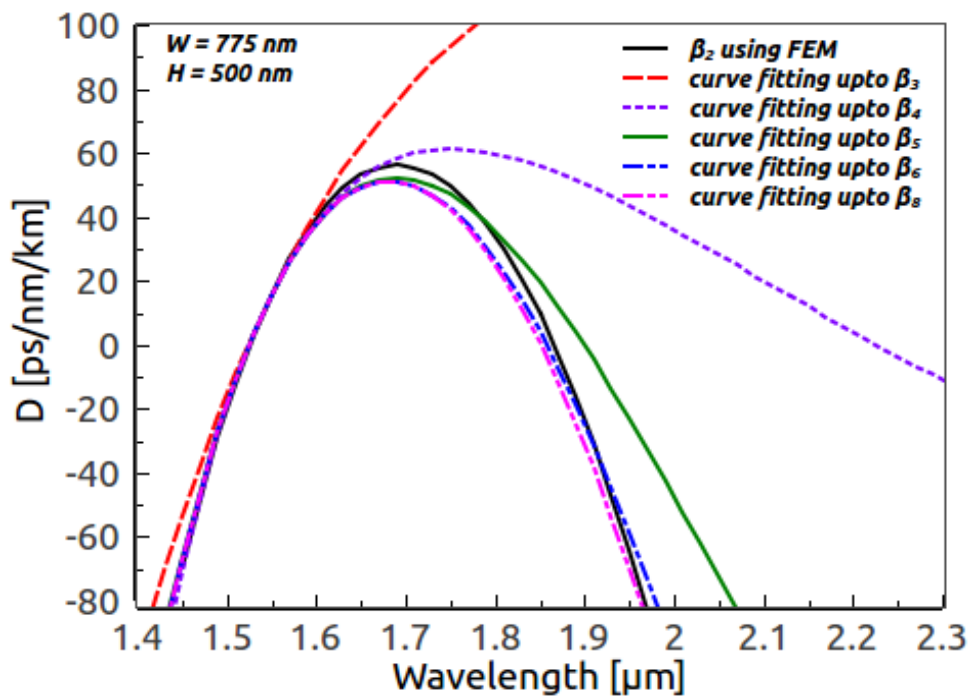


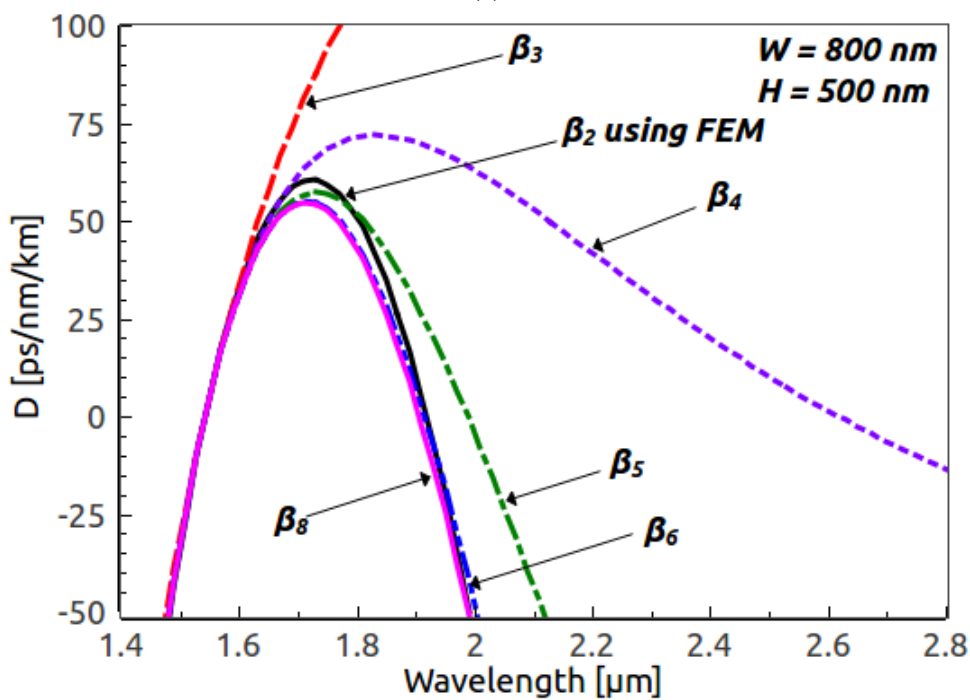
Fig. 5.5 GVD for the fundamental quasi-TE mode as a function of wavelength for the nanowire structure with $W = 700$ nm and $H = 500$ nm. The black-solid, red-dashed, and blue-dotted correspond to a mesh size of 200×200 , 300×300 , and 600×600 , respectively.

numerical results we have used an appropriate mesh size and we are confident about the accuracy of numerically simulated results.

To confirm the accuracy of the GVD coefficients obtained from the FE mode-solver, we plot in Fig. 5.6 the GVD curves for the nanowire structures $W = 775$ nm, $H = 500$ nm and $W = 800$ nm, $H = 500$ nm obtained with the curve fitting method, using the Taylor series expansion and adding successively higher-order dispersion terms. However, as shown in Fig. 5.4, wavelength dependent dispersion $D(\lambda)$ can also be directly calculated over the whole wavelength range; these curves are shown by a black lines in Fig. 5.6. By taking adequate number of higher-order dispersion terms one hopes to mimic the actual wavelength dependent $D(\lambda)$, but when a limited number of higher-order terms are used, the resulting dispersion curve may be very different than the actual one. It is apparent from the Fig. 5.6(a) and 5.6(b) that the GVD curves obtained from curve fitting closely matches with the actual GVDs when dispersion up to eighth-order is included. This gives us confidence in



(a)



(b)

Fig. 5.6 GVD curves obtained with FE method (black) fitted the Taylor series expansion up to β_8 for the nanowires (a) $W = 775$ nm, $H = 500$ nm and (b) $W = 800$ nm, $H = 500$ nm.

claiming that the results obtained by truncating the Taylor series at the β_8 term represent the situation one will observe in actual experiments.

5.3 Simulation parameters for SC generation

To predict the bandwidth of SC in ChG nanowire, the generalized nonlinear Schrödinger equation (GNLSE) is solved numerically by split-step Fourier method (SSFM) as described in Chapter 3. The pulse width is taken to be 50 fs (FWHM) at a pump wavelength of 1550 nm, and the nonlinear refractive index, n_2 of ChG is taken to be 8.6×10^{-18} m²/W at this pump wavelength [35]. The linear propagation loss is taken to be 3.2 dB/cm at a wavelength of 1550 nm [37]. Light propagation in ChG material at a wavelength of 1550 nm is significantly influenced by two-photon absorption (TPA) which is taken to be 9.3×10^{-14} m/W [35]. The delayed Raman response given by the equation in Chapter 2 is estimated with considering fractional delayed Raman response, $f_R = 0.031$, $\tau_1 = 15.5$ fs, and $\tau_2 = 230.5$ fs [134].

To numerically solve GNLSE in SSFM method, we must represent the field on a temporal grid propagate stepwise (Δz) through the length (z) of the waveguide. Therefore, the temporal grid length (T) must be wide enough consisting of a number of smaller time-steps (Δt) so that it can accommodate extreme spectral broadening during pulse propagation containing maximum frequency of the field. For containing maximum frequency in the temporal grid, one must choose a temporal grid spacing (Δt) corresponding to twice the highest frequency and for SC generation this limit is usually on the short wavelength edge. The bandwidth (BW) of spectral window can be calculated as

$$\omega_{\text{BW}} = \frac{2\pi}{\Delta t} = 2\pi c \left(\frac{1}{\lambda_{\text{min}}} - \frac{1}{\lambda_{\text{max}}} \right) \quad (5.6)$$

where c is the velocity of light and λ_{\min} , λ_{\max} are the wavelengths at the short and long wavelength edge of the spectral window, respectively.

As λ_p is the center wavelength of the pulse, therefore, we can calculate λ_{\min} and λ_{\max} from Equation (5.6) as follows:

$$\frac{1}{2\Delta t} = c \left(\frac{1}{\lambda_{\min}} - \frac{1}{\lambda_p} \right) \quad \therefore \lambda_{\min} = \frac{1}{\frac{1}{\lambda_p} + \frac{1}{2c\Delta t}} \quad (5.7)$$

$$\lambda_{\max} = \frac{1}{\frac{1}{\lambda_p} - \frac{1}{2c\Delta t}} \quad (5.8)$$

where Δt is temporal grid spacing and λ_p is the pump wavelength. From Equation (5.8) it is seen that there is a lower limit on Δt which is given by $\Delta t > \lambda_p/(2c)$ in order to avoid negative frequencies in the spectral window. For our case at a pump wavelength of 1550 nm, we obtained minimum Δt of 2.6-fs.

Considering grid point 2^{13} (FFT point) and utilizing the obtained minimum Δt of 2.6-fs, using Equations (5.7) and (5.8) we can calculate $\lambda_{\min} = 777$ nm, $\lambda_{\max} = 24 \mu\text{m}$ and time window is found to be $T = 22$ ps which is wide enough to capture the SC spectrum produced in the output of our ChG nanowire.

5.4 Results and discussions

To study SC generation GNLSE can be solved either in the time domain or in the frequency domain. In this work, we have used time-domain formulation for our simulations using a split-step Fourier method (SSFM), as this is the most commonly reported approach. We verified the result obtained by our SSFM with so called frequency domain 'Interaction Picture' method given in Dudley *et al.* [138] later in this chapter. Initially a waveguide with $W = 700$ nm and $H = 500$ nm is considered for SC generation. This nanowire structure

is selected because the GVD of this structure is nearly flat near the pump wavelength of 1550 nm. Higher-order dispersion coefficients β_m ($m \geq 2$) up to eighth-order (β_2 to β_8) were calculated numerically from the dispersion curve. Our aim here is to study the effect of higher-order dispersion coefficients β_m ($m \geq 2$) terms on the supercontinuum bandwidth, and how the numerically simulated SC spectrum is modified with the inclusion of successive higher-order dispersion terms. Using the FE mode-solver, we obtain $A_{\text{eff}} = 0.28 \mu\text{m}^2$ for our nanowire and this A_{eff} yields $\gamma = 123 \text{ /W/m}$. For numerical simulations a TE polarized 50 fs FWHM secant pulse is launched with the peak power of 25 W. We include wavelength independent propagation loss of 3.2 dB/cm [35] for the 18 mm long nanowire. Simulations have been carried out to test the effect of each higher-order dispersion (β_3 to β_8) terms successively and the generated spectra are shown in Fig. 5.7. With the addition of third-order dispersion term, the SC broadens from 850 nm to 3550 nm (black curve) resulting in a -60 dB bandwidth of around 2700 nm. The

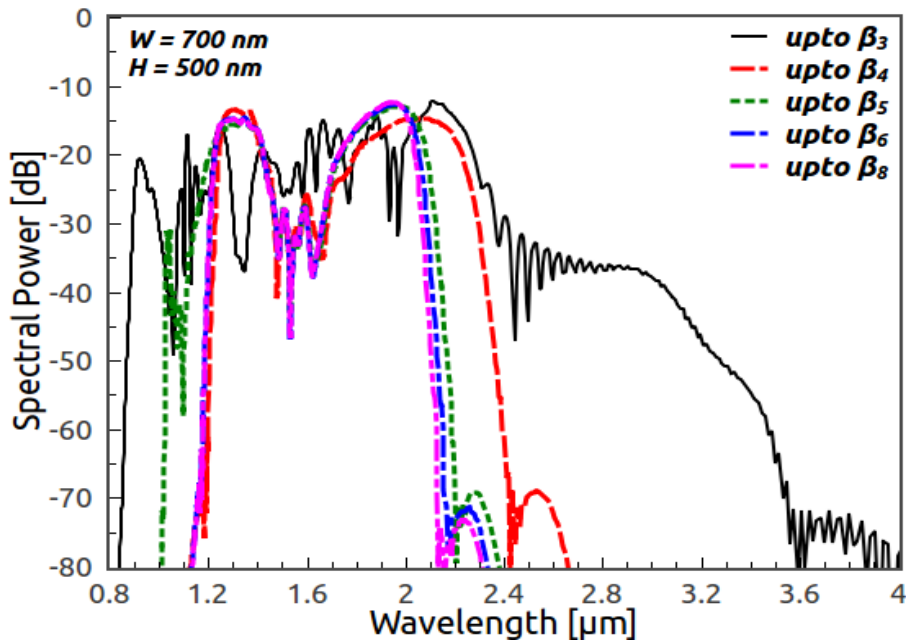


Fig. 5.7 Changes in SC spectra with the successive addition of higher-order dispersion terms pumped at a wavelength of 1550 nm for the nanowire of dimensions $W = 700 \text{ nm}$ and $H = 500 \text{ nm}$.

equivalent -20 dB bandwidth for this case is 1500 nm. However, after the addition of the fourth and other higher-order dispersion coefficients, the SC spectrum becomes narrower. Spectral narrowing converges slowly with the further addition of higher-order dispersion terms, and the spectra with β_m up to 7th and 8th terms are almost identical. For our nanowire structure the final supercontinuum extends from 1200 nm to 2100 nm.

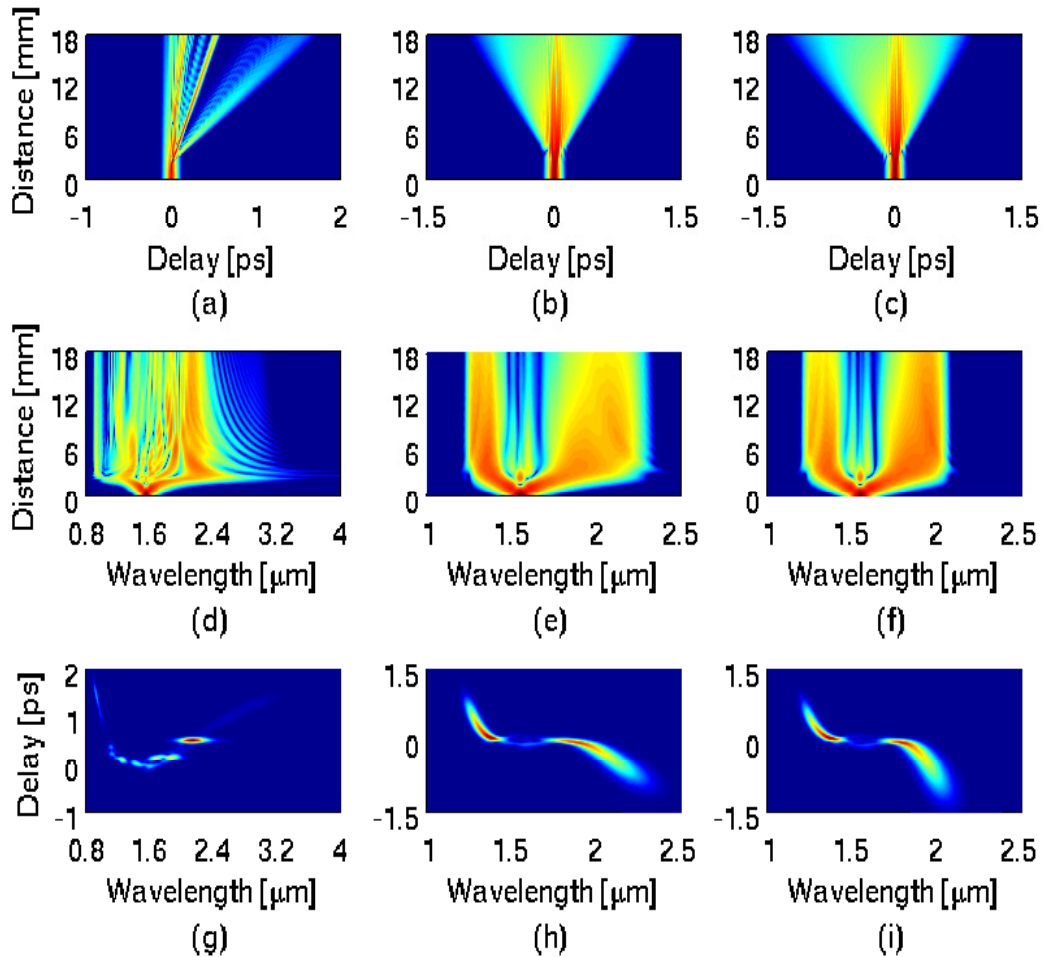


Fig. 5.8 Temporal intensity (top), spectral density (middle) and spectrogram (bottom) including terms up to β_3 (left column), up to β_4 (middle column), and up to β_8 (right column) pumped at a wavelength of 1550 nm for the nanowire of dimensions $W = 700$ nm and $H = 500$ nm.

The dynamics of SC generation is well-known. However, we will here make a numerical investigation of the SC generation broadening process and the influence of Raman contribution with the successive addition of higher-order dispersion parameters for the nanowire structure of $W = 700$ nm and $H = 500$ nm. As the pump lies in the anomalous GVD regime, SC generation is mainly dominated by the soliton fission process. Initially the propagation of the optical pulse is compressed due to the higher-order soliton dynamics. As a result, a broadened spectrum produced from strong temporal contraction and this expanded spectrum touched with the resonant radiation frequency of a dispersive wave on the anti-stoke side. Further propagation now leads to a break-up of the higher-order soliton into a number of fundamental solitons through soliton fission process. For the soliton order, $N_{\text{sol}} = 8.13$, soliton fission occurs at a distance of $L_{\text{fiss}} = 2.6$ mm (Fig. 5.8 (a), (b), and (c)), mainly because of perturbation induced by third and higher-order dispersion parameters. To understand the spectrum broadening process we have considered terms up to β_3 , β_4 , and β_8 separately in the Fig. 5.8. When only third-order dispersion is added, multiple fundamental solitons are produced after the fission, whose spectra shift toward the longer wavelength side (stoke-side) because of intrapulse Raman scattering, producing multiple spectral peaks in the spectrum. In addition, from Fig. 5.8 (a), (d), and (g) it is apparent that each Raman soliton loses some of its energy from which a non-solitonic radiation (NSR) in the form of dispersive wave is also generated but its spectrum lies on the shorter wavelength side (anti-stokes) of the input spectrum. When even-order dispersions such as β_4 , β_8 terms are added, it is well-known that NSR is generated on both sides of the input spectrum that are clearly observed in Fig. 5.8 (b), (e), (h) (addition of dispersion terms up to β_4) and (c), (f), (i) (addition of dispersion terms up to β_8). Since the GVD curve of this nanowire has two ZDWs and a strong NSR is produced in the stoke-side of the SC spectrum right after the second ZDW (located

at around 1710 nm in Fig. 5.4 (a) for the black-solid line curve) of the GVD curve which is only due to the soliton suppression effect. Since the dispersion slope ($dD/d\lambda$) of the GVD curve in the vicinity of the second ZDW is negative, owing to the spectral-recoil effect (soliton suppression) the negative dispersion slope has significantly modified the SC spectrum through the generation of strong redshifted dispersive wave, allowing the SC generation is extended further into the infrared. It is evident from Fig. 5.8 that the final SC depends strongly on how many dispersion terms are included, and one should include higher-order dispersion coefficients as accurately as possible to avoid spurious results. The temporal and spectral differences are also apparent in the spectrogram shown in Fig. 5.8 (bottom row) and the effect of β_3 [Fig. 5.8(g)], β_4 [Fig. 5.8(h)] and β_8 [Fig. 5.8(i)] on SC spectra are clearly observed for our proposed nanowire.

To show sensitivity to the waveguide geometry, we consider another nanowire structure with $W = 775$ nm and $H = 500$ nm, having its ZDW

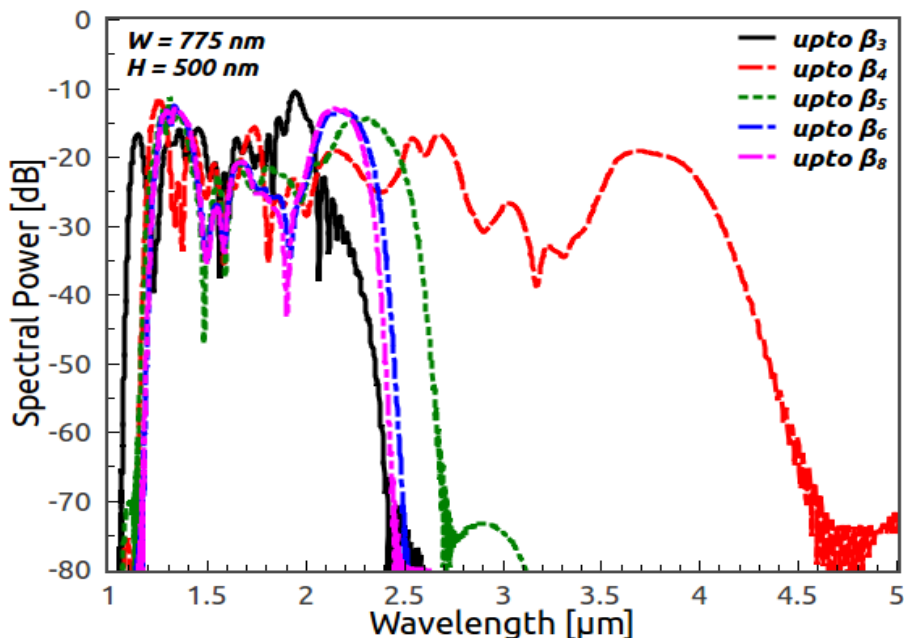
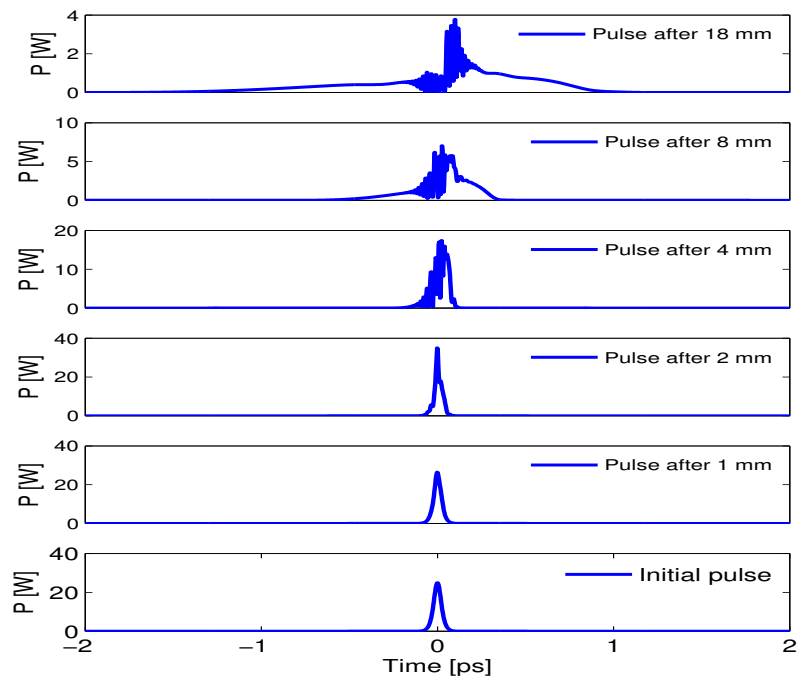
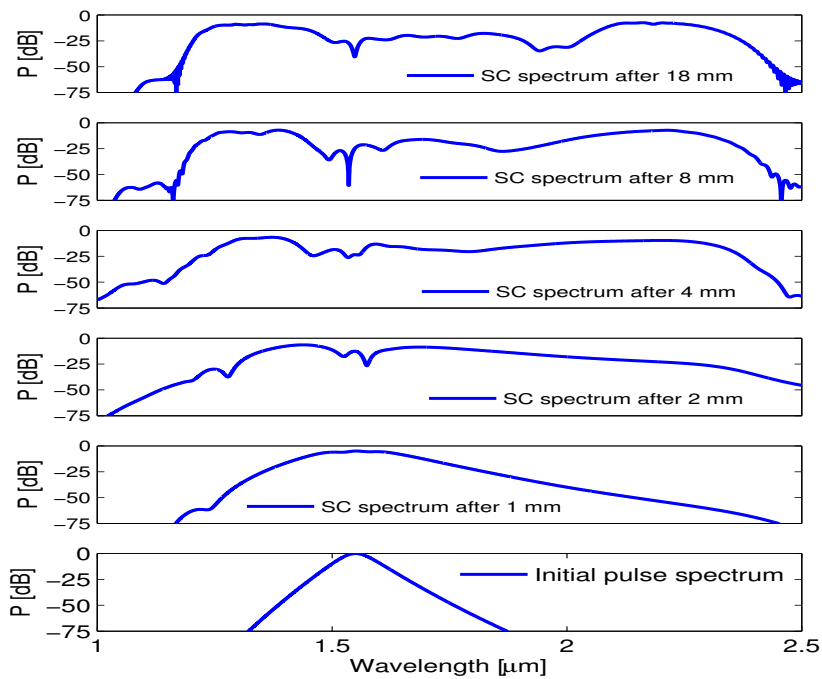


Fig. 5.9 Changes in SC spectra with the successive addition of higher-order dispersion terms pumped at a wavelength of 1550 nm for the nanowire geometry, $W = 775$ nm and $H = 500$ nm.



(a)



(b)

Fig. 5.10 (a) Temporal and (b) Spectral evolution for 50 fs pulse launched with 25 W peak power pumped at a wavelength of 1550 nm along the length of the nanowire structure, $W = 775$ nm and $H = 500$ nm.

closer to the pump wavelength compared to the previous structure. For this waveguide, with $A_{\text{eff}} = 0.31 \mu\text{m}^2$ obtained by the FE technique, $\gamma = 114$ /W/m. After evaluating various dispersion coefficients from dispersion curve and keeping all other parameters the same, we have performed numerical simulations for dispersion terms up to β_8 successively. Figure 5.9 shows the resulting SC spectra and should be compared to Fig. 5.7. Unlike the previous structure interestingly we observe for this nanowire that SC spectrum gets broaden significantly when the β_4 term is added. However, after the addition of fifth and higher-order dispersion terms, SC spectrum again starts to become narrower. In this case, the SC extends from 1200 nm to 2400 nm when third-order dispersion is included, yielding a bandwidth of 1200 nm (1100 nm bandwidth at -20 dB). However, when fourth-order dispersion is added, the SC spectrum broadens up to 4600 nm generating bandwidth of 3400 nm (2950 nm bandwidth at -20 dB). On the other hand, with the addition of fifth and higher-order dispersion terms, spectrum becomes narrower. With the addition of β_8 term, the SC converges and has a final bandwidth of 1200 nm (1150 nm bandwidth at -20 dB). Spectrum obtained with up to β_7 term is not shown in Fig. 5.9 as this is almost identical to that of up to the β_8 term. The effects of successive addition of higher-order dispersion terms corresponding to Fig. 5.9 are also shown through density plots (middle row) and spectrograms (bottom row) in Fig. 5.11.

Figure 5.10 shows the spectral and temporal evolution of 50-fs pulse along the length of ChG nanowire. For the soliton order, $N_{\text{sol}} = 10.74$ and the soliton fission length, $L_{\text{fiss}} = 3.8$ mm, the same phenomena occur after the addition of third-order dispersion. As seen in Fig. 5.10(a) and 5.10(b), initially the pulse undergoes an compression phase while its spectrum broadens because of SPM. However, after 3.8 mm or so, the soliton undergoes the fission process, mainly because of perturbations caused by the β_3 term added, and the pulse break up into multiple fundamental solitons. When the β_4 term is added, the

Raman induced frequency shift (RIFS) reduces gradually as solitons spectra shift towards the second ZDW located at 1865 nm. Since β_3 is positive near the first ZDW but becomes negative near the second ZDW, the change in sign of β_3 changes the frequency associated with NSR generated during soliton fission and the RIFS is completely suppressed near the second ZDW. This phenomena has been called the spectral recoil effect [24,25]. According to energy conservation, as RIFS stops at the second ZDW, because of the

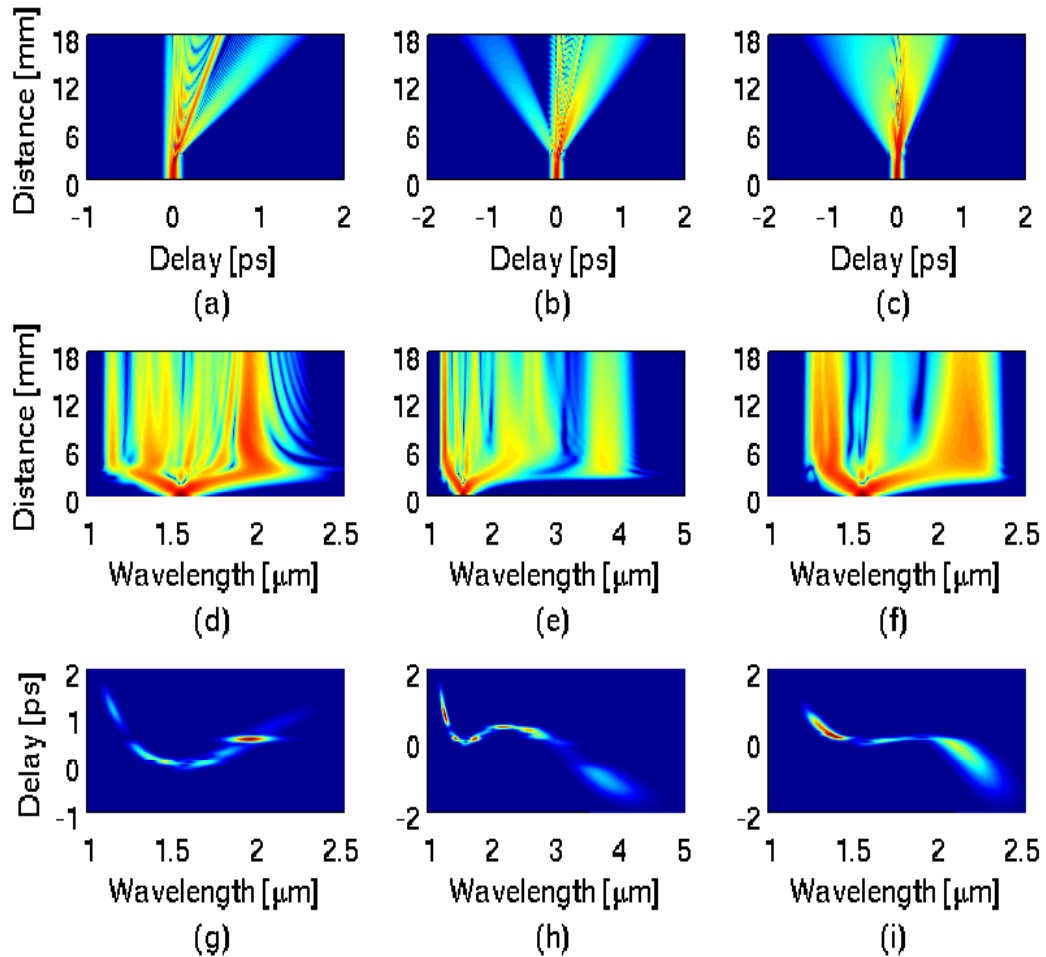


Fig. 5.11 Temporal intensity (top), spectral density (middle) and spectrogram (bottom) including terms up to β_3 (left column), up to β_4 (middle column), and up to β_8 (right column) pumped at a wavelength of 1550 nm for the nanowire geometry, $W = 775$ nm and $H = 500$ nm.

spectral recoil effect soliton loses its energy to NSR that is red-shifted and lies in the infrared region beyond the second ZDW. The red-shifted NSR is mainly responsible for generating much larger SC bandwidth after addition of the β_4 term. This is also evident from spectral density and spectrogram shown in Figs. 5.11(e) and 5.11(h), respectively. This large SC bandwidth reduces considerably after addition of β_5 and higher-order terms. Once again, we note that a premature truncation of the Taylor series can lead to spurious and misleading results.

To study the impact of device geometry, we have carried out rigorous numerical simulations for multiple GeAsSe planar structures whose width varies from 700 to 800 nm, and some of the results were shown in Fig. 5.12. For this set, their GVD curves are shown in Fig. 5.4(a). Dispersion coefficients up to β_8 terms are included for all simulations shown in Fig. 5.12. For the nanowire structure with $W = 800$ nm, $H = 500$ nm which has its ZDW very close to the pump wavelength, it can be observed from

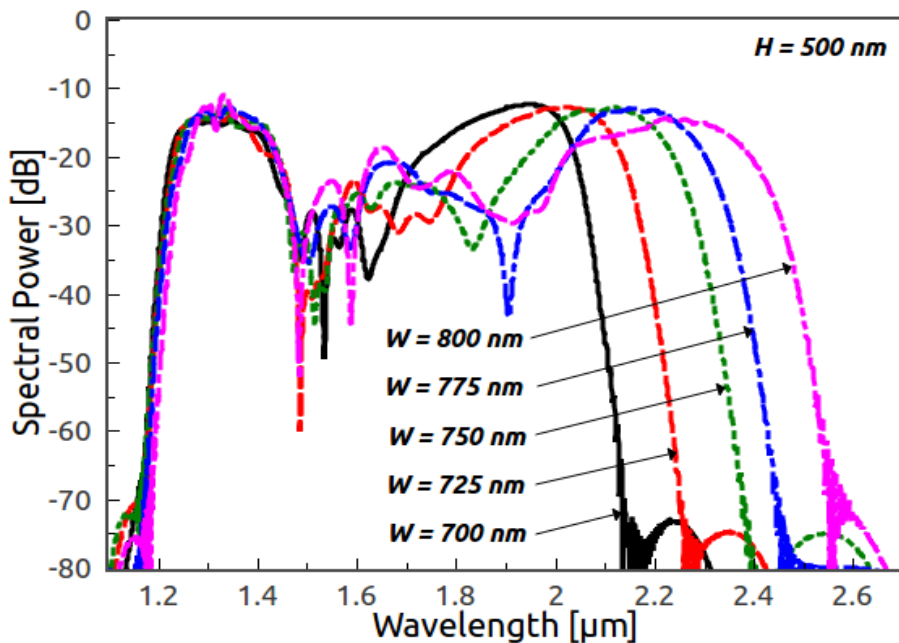


Fig. 5.12 Numerically simulated SC spectra for nanowires with the dispersion curves shown in Fig. 5.4(a) by including dispersion terms up to β_8 at a pump wavelength of 1550 nm.

Fig. 5.12 that the SC extends over 1300 nm (1250 nm bandwidth at -20 dB) covering a wavelength range from 1200 nm to 2500 nm, which is more than the bandwidth achieved by other nanowire structures with widths less than 800 nm.

5.5 Simulated SC result verification with frequency domain method

We have verified one of our SC spectrum obtained through SSFM with the frequency domain 'Interaction Picture' method presented in Dudley *et al.* [138] and the comparison of results obtained by both methods is shown in Fig. 5.13. It can be observed from the result shown in figure that both methods are able to produce nearly same result for SC generation after numerical simulations.

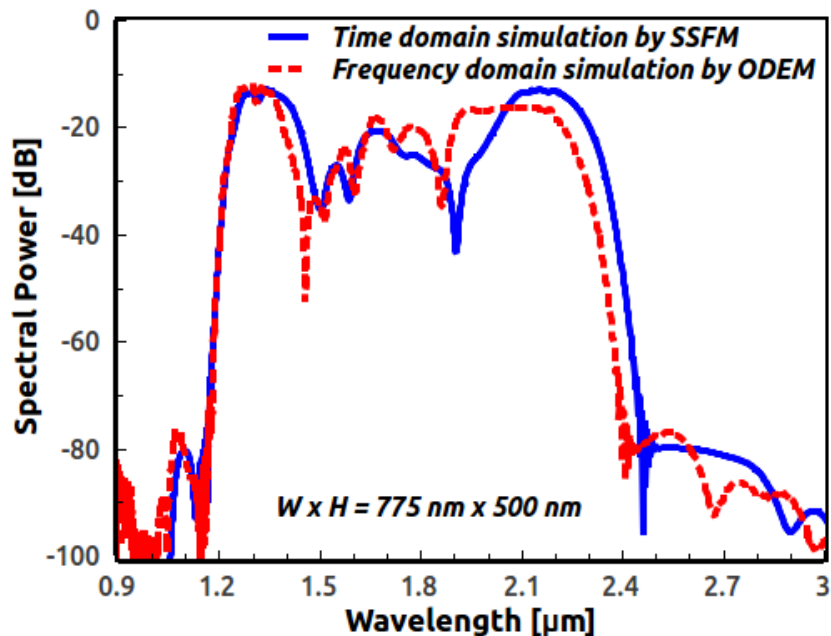


Fig. 5.13 Numerically simulated SC spectra for nanowire, $W = 775$ nm and $H = 500$ nm with time domain (SSFM) and frequency domain (Interaction Picture) including dispersion terms up to β_8 at a pump wavelength of 1550 nm with a peak power of 25 W.

5.6 Summary

In this chapter, a full-vector FE method is used for dispersion tailoring the $\text{Ge}_{11.5}\text{As}_{24}\text{Se}_{64.5}$ ChG nanowire through rigorous numerical simulations. The nanowire designed, by varying its transverse dimensions, in such a way that it exhibits anomalous dispersion near a chosen pump wavelength and can generate broadband supercontinuum at low pump powers. As numerically generated SC spectra critically depend on the dispersion properties of the nanowire, we have discussed how the accuracy of dispersion can be affected with the choice of the mesh divisions used for the FE technique. We have numerically studied SC generation in such nanowire and discussed the effects of higher-order dispersion coefficients from β_3 to β_8 terms on their SC bandwidths. We have designed five nanowire structures with widths considering in the range from 700 to 800 nm keeping the same 500 nm thickness. As seen in Fig. 5.4(a), all of them exhibit anomalous dispersion at a pump wavelength of 1550 nm and all have two ZDWs. We have carried out SC simulations for all five nanowire structures and optimized a design for realizing a wideband SC generation.

Here we highlight the effects of higher-order dispersion coefficients on the SC spectrum and identify changes that occur with addition of each successive dispersion coefficient in numerical simulations. In earlier simulation-based works on SC generation, sometimes the Taylor series expansion has been truncated after the third-order or fourth-order term. We have shown that this may not produce an accurate SC spectrum and more higher-order dispersion terms may need to be included to obtain a reliable SC spectrum. In this work propagation losses for nanowires were taken to be 3.2 dB/cm [35] although such a high loss might not affect a short device design. However, recent work has shown that this loss can be reduced to around 1.5 dB/cm through process improvements [37]. Our conclusions are not affected if this lower value of loss is used for the simulations. Finally we have shown the

comparison between time domain 'split-step Fourier method' and frequency domain 'Interaction Picture' method for one of our earlier result obtained through SSFM. It was found good matching between the results obtained through those methods after numerical simulations for SC generation.

Chapter 6

Mid-infrared SC generation in chalcogenide waveguides

Supercontinuum (SC) generation in mid-infrared (MIR) has increasingly become a focus for research because bright MIR light sources can be used for molecular fingerprint spectroscopy, frequency metrology, optical coherent tomography and microscopy [27, 36]. In recent years, several experimental and theoretical investigations on MIR SC generation were reported in ChG planar waveguides [143–145] and ChG photonic crystal fibres [147, 148]. In our earlier work on SC source design shown in Chapter 5, we demonstrated a low-power broadband SC source with dispersion-tailored $\text{Ge}_{11.5}\text{As}_{24}\text{Se}_{64.5}$ ChG nanowire with polymer on top and silica as the lower claddings [141]. As a silica cladding suffered from severe absorption at wavelengths beyond $3\ \mu\text{m}$, it was not possible to extend the SC spectrum beyond $3\ \mu\text{m}$ with that design. As $\text{Ge}_{11.5}\text{As}_{24}\text{Se}_{64.5}$ ChG glass can provide MIR transparency beyond $14\ \mu\text{m}$, it is possible to design a SC light source using $\text{Ge}_{11.5}\text{As}_{24}\text{Se}_{64.5}$ glass as a core by employing upper and lower claddings with materials that are transparent in the long wavelength edge far into the MIR, and this may open numerous applications inaccessible by the sources limited to $2.5\ \mu\text{m}$. Many previous research works have shown that along with materials transparency in the long wavelength edge, the position of pump wavelength is also an

important factor for the sufficient extension of SC spectrum far into the MIR region. Therefore, to overcome the issues encountered to design a SC source operates in far into the MIR, pump source should be shifted from 1550 nm to long wavelength region at around 3-5 μm and cladding materials should be transparent in the long wavelength edge as well.

This chapter presents detailed design procedure for optimization of ChG rectangular channel and ChG rib waveguides for mid-infrared SC generation. Section 6.1 reviews the waveguide structures with the materials employed as upper and lower claddings mentioning Sellmeier coefficients of them. Section 6.2 discuss the detailed dispersion tailoring for obtaining the ZDW of the proposed waveguides close to the chosen pump wavelengths. Section 6.3 introduces the simulation parameters for numerical modelling of SC generation in MIR regimes. Section 6.4 provides results and discussions and show the effects of pump wavelength in MIR SC on the long wavelength edge. Section 6.5 concludes the study.

6.1 ChG channel and rib waveguides design

6.1.1 Geometry of channel and rib waveguides

The schematic diagrams of the $\text{Ge}_{11.5}\text{As}_{24}\text{Se}_{64.5}$ ChG channel waveguides used for dispersion optimization was shown in Fig. 5.1 in Chapter 5 and ChG rib waveguide is shown in Fig. 6.1. We have employed $\text{As}_{36}\text{S}_{64}$ or air as a top cladding and $\text{As}_{36}\text{S}_{64}$ or $\text{Ge}_{11.5}\text{As}_{24}\text{S}_{64.5}$ or MgF_2 as a lower cladding instead of polymer and silica during ChG channel waveguides design. Air and MgF_2 glass are employed as upper and lower claddings when rib waveguide design for MIR SC generation. The wavelength-dependent linear refractive index of core and claddings materials over the entire wavelength range used in the simulation was obtained using the Sellmeier Equation (5.1) given in Chapter 5. As the Sellmeier coefficients of $\text{Ge}_{11.5}\text{As}_{24}\text{Se}_{64.5}$ glass mentioned

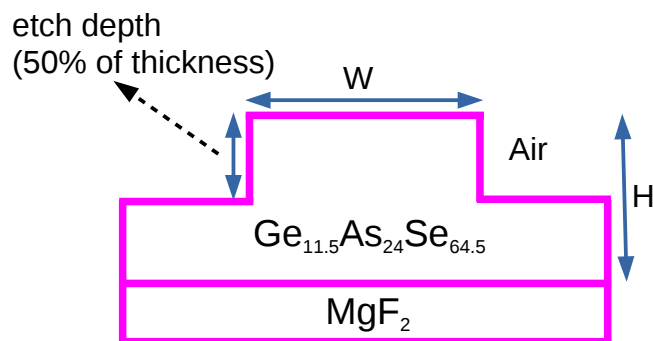


Fig. 6.1 Schematic diagram of ChG rib waveguide.

Table 6.1 Sellmeier fitting coefficients

| Material | Ge _{11.5} As ₂₄ S _{64.5} [39] | | MgF ₂ [166] | |
|----------|--|-------------|------------------------|-------------|
| m | 1 | | 2 | |
| | A_j | λ_j | A_j | λ_j |
| $j = 1$ | 4.18011 | 0.316790 | 0.487557080 | 0.04338400 |
| $j = 2$ | 0.35895 | 22.77018 | 0.398750310 | 0.09461442 |
| $j = 3$ | – | – | 2.312035300 | 23.7936040 |

in Chapter 5, we only provide here the Sellmeier coefficients for the lower cladding materials such as Ge_{11.5}As₂₄S_{64.5} [39] and MgF₂ [166] glasses. The fitting coefficients are given in Table 6.1.

6.1.2 Dispersion engineering of channel waveguides

The design of an optical waveguide for SC generation depends on GVD and higher-order dispersion parameters. The accuracy of dispersion parameters depend on how accurately calculates the mode propagation, $\beta(\omega)$ for the fundamental mode through FE modal solutions. Therefore, accuracy of any design critically depends on the accuracy of modal solutions of a waveguide. For our the channel waveguides proposed here, we represent the all waveguide structures with 360,000 first order triangular elements across the transverse dimensions to obtain higher accuracy modal solutions. A powerful

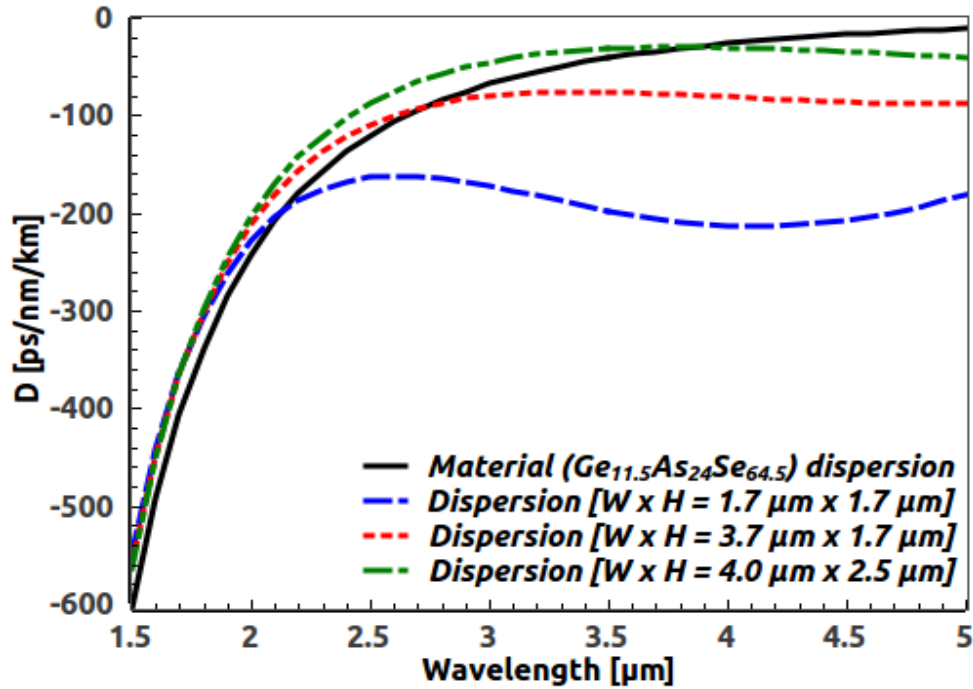


Fig. 6.2 GVD curves for the fundamental quasi-TE mode calculated from n_{eff} for three waveguides geometries employing $\text{As}_{36}\text{S}_{64}$ glass for both the upper and lower claddings. The black solid line curve shows the material dispersion curve for comparison.

extrapolation technique that was used in previous chapter also applied here to test the accuracy of modal solution for this waveguide structure. We tested the FE results by Aitken's extrapolation through convergence between the raw FEM results and extrapolated values as the number of elements increased. Using our FE mode-solver we have obtained modal solutions from which mode propagation constant $\beta(\omega)$ of the fundamental mode over a range of frequencies are evaluated and calculate the effective index from the mode propagation constant obtained through modal solutions. We also tested the GVD curves obtained through FE mode-solver by the data fitting method applying Taylor series expansion. It was observed good matching between the two which made us confident about the GVD curve obtained through FE mode-solver.

As the MIR SC generation requires the cladding as well as core materials of a waveguide to be transparent at long wavelengths, we first choose a channel

waveguide fabricated using all chalcogenide materials with a rectangular core made of $\text{Ge}_{11.5}\text{As}_{24}\text{Se}_{64.5}$ glass and using $\text{As}_{36}\text{S}_{64}$ glass for both the upper and lower claddings, whose refractive index of 2.37 at $1.55 \mu\text{m}$ provides an index contrast of 0.3. By varying waveguide dimensions for realizing ZDW in the range of $2\text{-}4 \mu\text{m}$ or longer, we numerically calculated GVD for three different structures as a function of wavelength for the fundamental quasi-TE mode and plot them with material dispersion in Fig. 6.2. It can be observed from this figure that the material dispersion, shown by a solid black line, remains normal for the wavelength range $1.5 \mu\text{m}$ to $5 \mu\text{m}$, considered here. The total dispersion curve for a waveguide with, $W = 4 \mu\text{m}$ and $H = 2.5 \mu\text{m}$ is shown by the green dot-dashed line, and it follows the material dispersion curve quite closely. As the waveguide dimension is reduced, waveguide dispersion becomes larger. However, total dispersion curves shown by red dotted and blue dashed lines for structures with, $W = 3.7 \mu\text{m}$, $H = 1.7 \mu\text{m}$ and $W = 1.7 \mu\text{m}$, $H = 1.7 \mu\text{m}$, respectively. Gai *et al.* [35] have analyzed buried channel waveguide using $\text{As}_{36}\text{S}_{64}$ as upper and lower claddings with a square core geometry, $W = 1.7 \mu\text{m}$ and $H = 1.7 \mu\text{m}$ and obtained the total dispersion of around -500 ps/nm/km after dispersion tailoring with obtaining polarization independent losses of around 0.2 dB/cm at a wavelength of 1550 nm . After dispersion engineering, we have obtained total dispersion of around -490 ps/nm/km for the same channel waveguide structure at a wavelength of 1550 nm which can be observed from Fig. 6.2. After increasing the width and thickness of a structure to $W = 4.0 \mu\text{m}$ and $H = 2.5 \mu\text{m}$, total dispersion of the waveguide still remains normal (-40 ps/nm/km) at $3.1 \mu\text{m}$ and continues to remain normal over a wide range of wavelengths exceeding $5 \mu\text{m}$. It appears unlikely that a waveguide can be designed to have anomalous dispersion in this wavelength range by employing such a lower index contrast cladding material such as $\text{As}_{36}\text{S}_{64}$ glass.

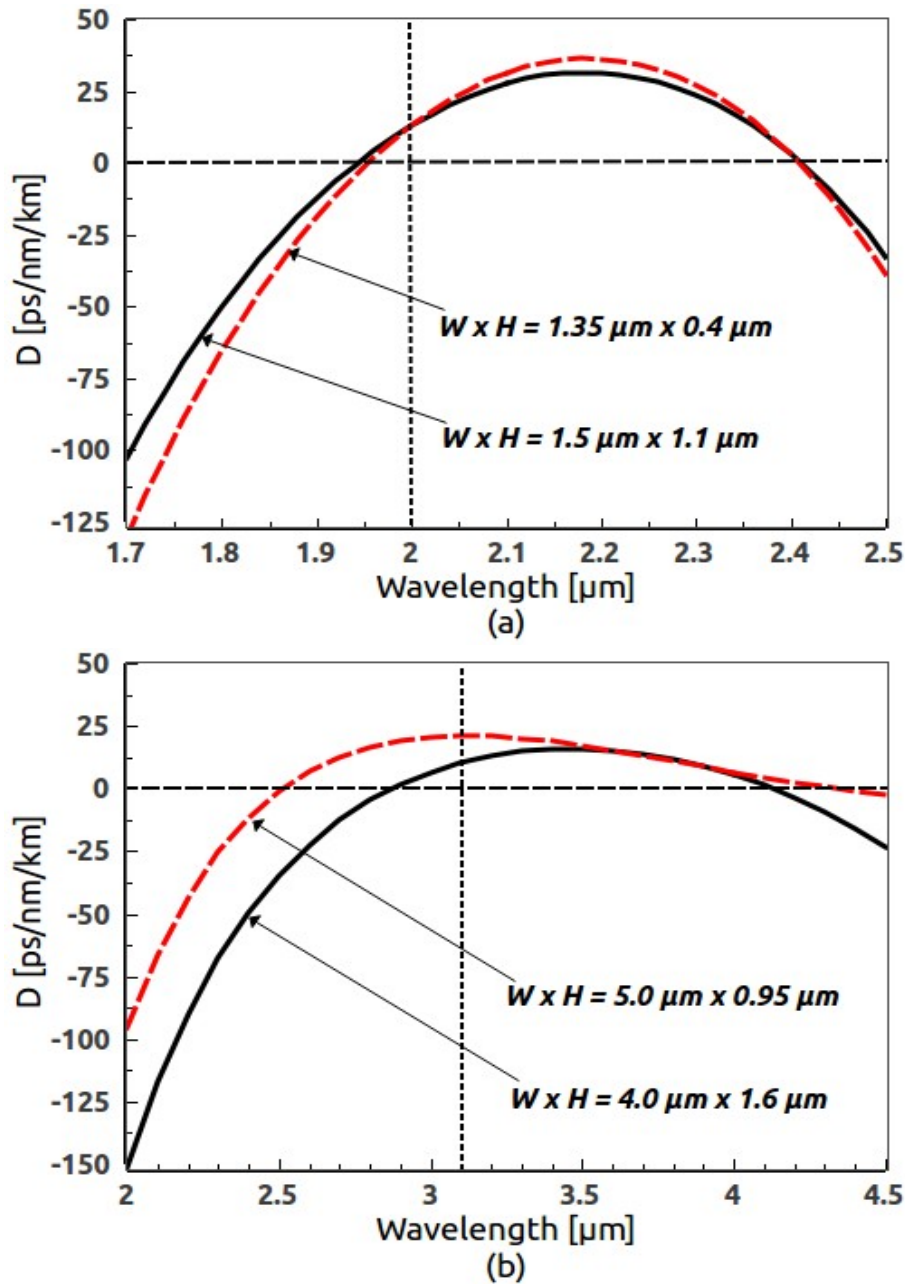


Fig. 6.3 GVD curves for the waveguide geometries employing two different lower claddings (solid black curve for $\text{Ge}_{11.5}\text{As}_{24}\text{S}_{64.5}$ and red dashed curve for MgF_2) for the fundamental quasi-TE mode (a) at a pump wavelength of $2 \mu\text{m}$ and (b) at a pump wavelength of $3.1 \mu\text{m}$. Vertical dotted line indicates the position of pump wavelength.

For realizing anomalous dispersion around the pump wavelength, cladding materials with larger index contrast than the $\text{As}_{36}\text{S}_{64}$ glass are required. To realize the ZDW between $2 \mu\text{m}$ and $4 \mu\text{m}$, we have chosen two different channel

waveguides by replacing upper cladding with air and lower cladding with either $\text{Ge}_{11.5}\text{As}_{24}\text{S}_{64.5}$ glass or MgF_2 glass, respectively. With $\text{Ge}_{11.5}\text{As}_{24}\text{S}_{64.5}$ glass as the lower clad, index contrast increases to ~ 0.4 but with MgF_2 glass this value increases significantly to 1.3. To obtain the ZDWs of both designs close to the pump wavelength of $2 \mu\text{m}$ and to make GVDs slightly anomalous at these wavelengths, we optimized the dimensions of the waveguides. Similarly, another set waveguides were optimized for the longer pump wavelength of $3.1 \mu\text{m}$. Figures 6.3(a) and 6.3(b) show the GVD curves obtained for two

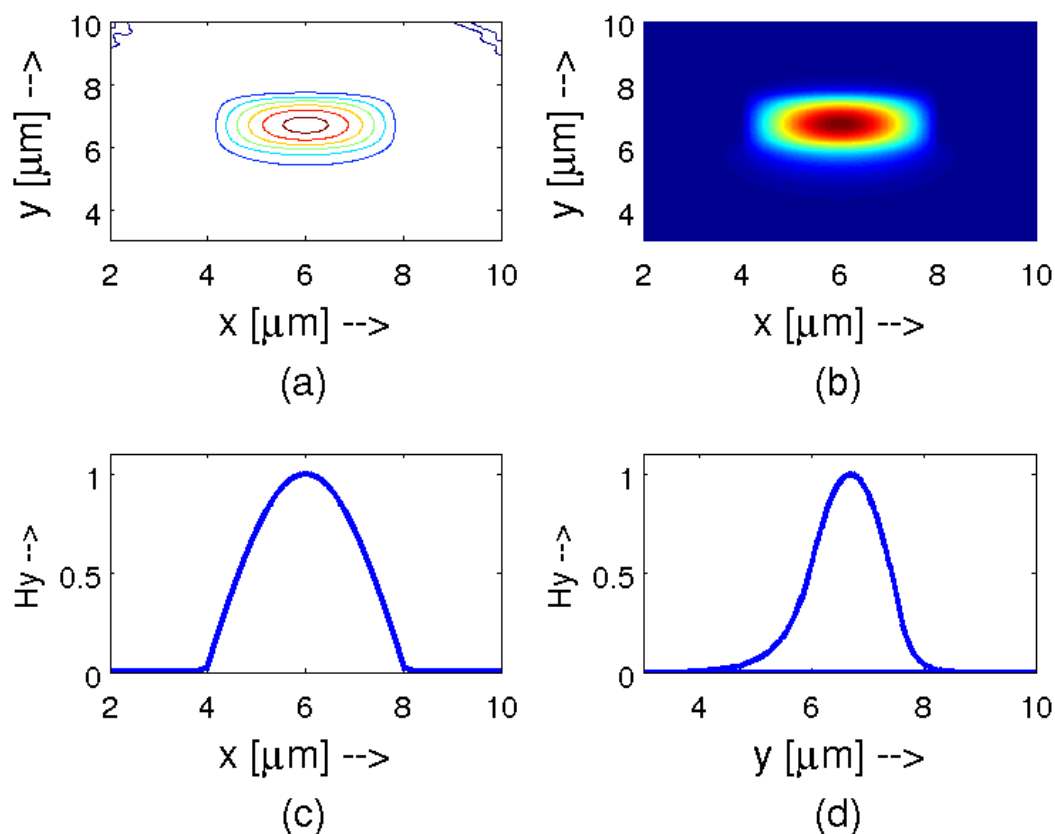


Fig. 6.4 Dominant field profile for fundamental quasi-TE mode (H_y^{11}) for the ChG channel waveguide geometry, $W = 4 \mu\text{m}$ and $H = 1.6 \mu\text{m}$ employing $\text{Ge}_{11.5}\text{As}_{24}\text{S}_{64.5}$ glass for its lower cladding at a wavelength of 3100 nm ; a) Contour, b) Surface, c) H_y field along width, and d) H_y field along thickness of the waveguide.

different waveguide geometries optimized to work at the pump wavelengths of $2 \mu\text{m}$ and $3.1 \mu\text{m}$, respectively.

Figures 6.4 and 6.5 show the H_y field profile of the fundamental quasi-TE mode (H_y^{11}) of the ChG channel waveguides at a pump wavelength of $3.1 \mu\text{m}$ for two different geometries proposed here. Figure 6.4 shows the field profile for the structure, $W = 4 \mu\text{m}$ and $H = 1.6 \mu\text{m}$ employing $\text{Ge}_{11.5}\text{As}_{24}\text{S}_{64.5}$ glass for its lower cladding and Fig 6.5 shows the field profile of the structure, $W = 5 \mu\text{m}$ and $H = 0.95 \mu\text{m}$ employing MgF_2 for its lower cladding. It is apparent from the figures that the different field representations inside the core as well

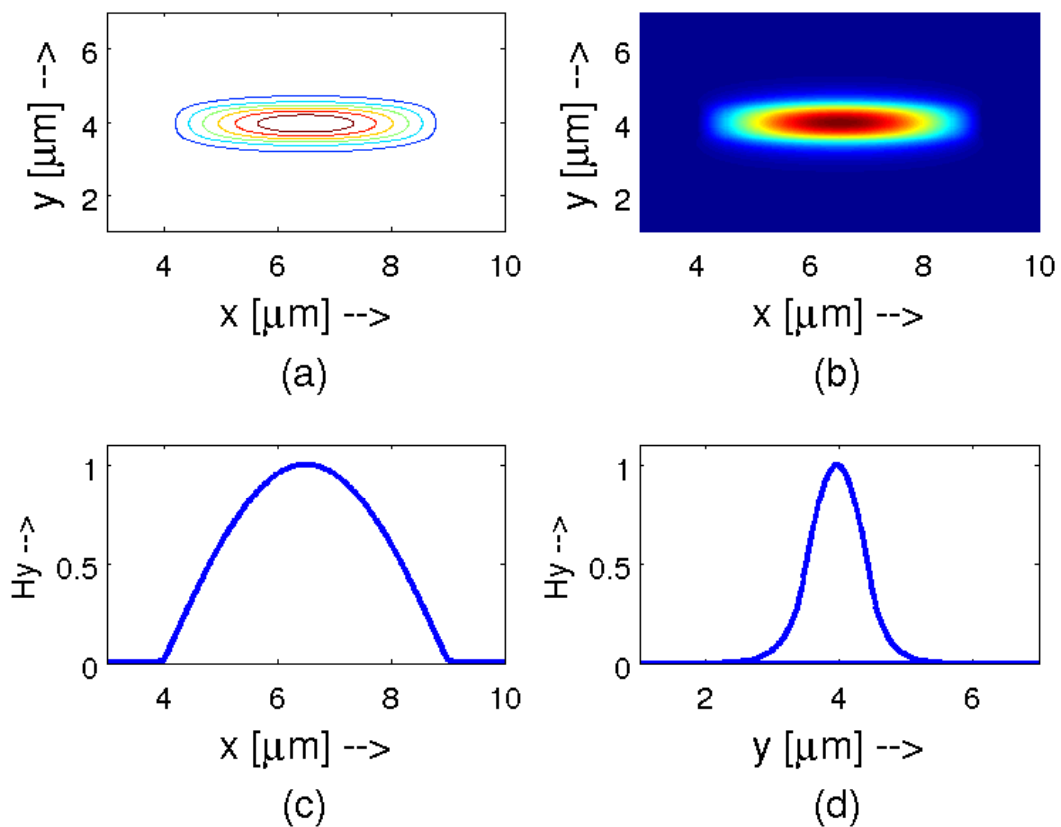


Fig. 6.5 Dominant field profile for fundamental quasi-TE mode (H_y^{11}) for the channel structure of $W = 5 \mu\text{m}$ and $H = 0.95 \mu\text{m}$ employing MgF_2 for its lower cladding at a wavelength of 3100 nm ; a) Contour, b) Surface, c) H_y field (normalized value) along width, and d) H_y field (normalized value) along thickness of the waveguide.

as along the transverse dimensions of the structures that the mode is highly confined inside the channel waveguide for its lower cladding containing MgF_2 than the waveguide for its lower cladding containing $\text{Ge}_{11.5}\text{As}_{24}\text{S}_{64.5}$ glass. From Fig. 6.4(d), it is seen that owing to using lower index contrast material as a lower cladding for this structure, a large portion of field is penetrated into the lower cladding which is increased with the wavelength and eventually increases the mode area (A_{eff}) of this waveguide. In contrast, the field is highly confined along the thickness (Fig. 6.5(d)) for the other structure due to using larger index contrast material for its lower cladding which gives lower A_{eff} than the earlier structure. The field variations along the width of the either waveguide geometry is remained symmetrical which can be observed from Figs. 6.4(c) and 6.5(c).

6.1.3 Dispersion tailoring of a rib waveguide

To tailor the rib waveguide for obtaining GVD curve, we represent the waveguide structure with 360,000 first order triangular elements across the transverse dimensions to obtain higher accuracy modal solutions as before. We tested the FE results by Aitken's extrapolation through convergence between the raw FEM results and extrapolated values as the number of elements increased. Using the FE mode-solver we have obtained modal solutions from which mode propagation constant $\beta(\omega)$ of the fundamental mode over a range of wavelengths are calculated. Inset of Fig. 6.6 shows the field profile of the fundamental quasi-TE mode of the ChG rib waveguide at a pump wavelength of $3.1 \mu\text{m}$ for the waveguide geometry, $W = 5 \mu\text{m}$ and $H = 1.1 \mu\text{m}$ employing air as upper and MgF_2 glass for its lower claddings. It is apparent from the figure that the field representation inside the core as well as along the transverse dimensions of the structures that the mode is highly confined inside the rib waveguide owing to using large index contrast cladding material. As the mode field is highly confined along the thickness due to using

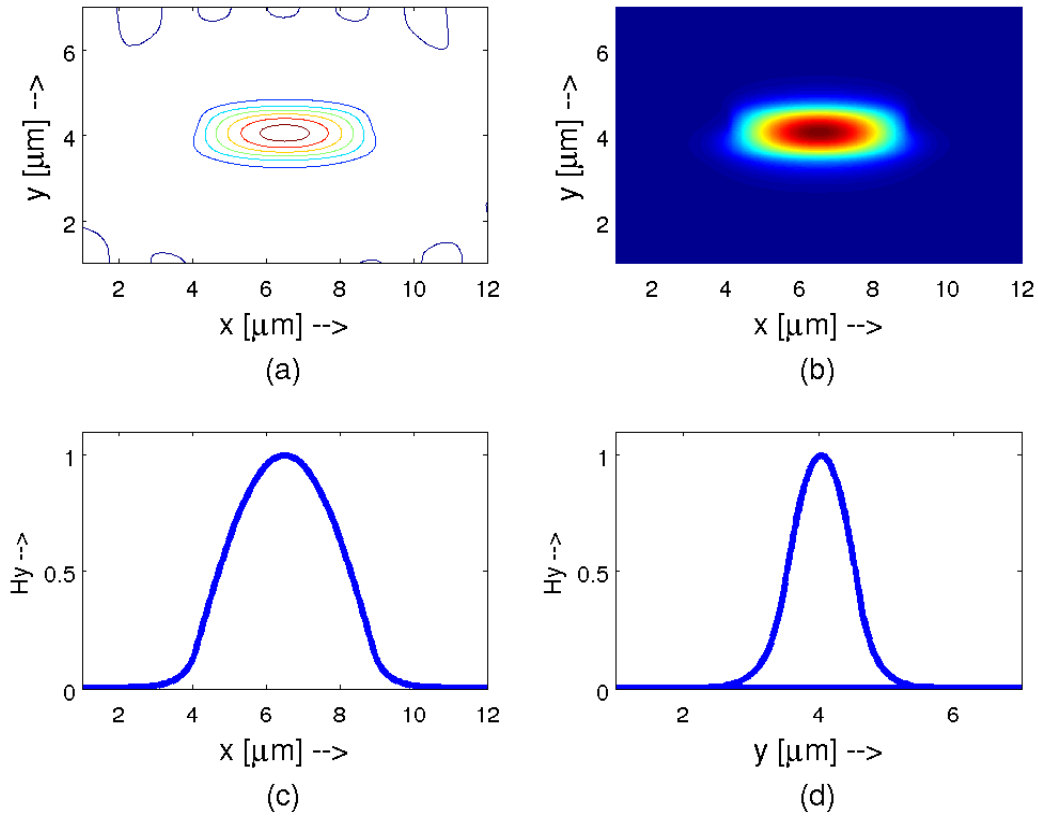


Fig. 6.6 Dominant field profile for fundamental quasi-TE mode (H_y^{11}) for the rib structure of $W = 5 \mu\text{m}$ and $H = 1.1 \mu\text{m}$ employing MgF_2 for its lower cladding at a wavelength of 3100 nm; a) Contour, b) Surface, c) H_y field (normalized value) along width, and d) H_y field (normalized value) along thickness of the waveguide.

larger index contrast material for its lower cladding resulting in lower A_{eff} which, in turn, increases nonlinearity of the waveguide. The spatial profile of the fundamental mode, shown as an inset of Fig. 6.6, exhibits excellent field confinement to the central core region which thus enables an enhanced nonlinear interaction.

Since the MIR SC generation requires the cladding as well as core materials of a waveguide to be transparent at long wavelengths, we designed and optimized a rib waveguide made using air as upper cladding and MgF_2 glass as lower cladding, whose refractive index of 1.33 at $3.1 \mu\text{m}$ provides an index contrast of 1.3. By varying waveguide dimensions for realizing

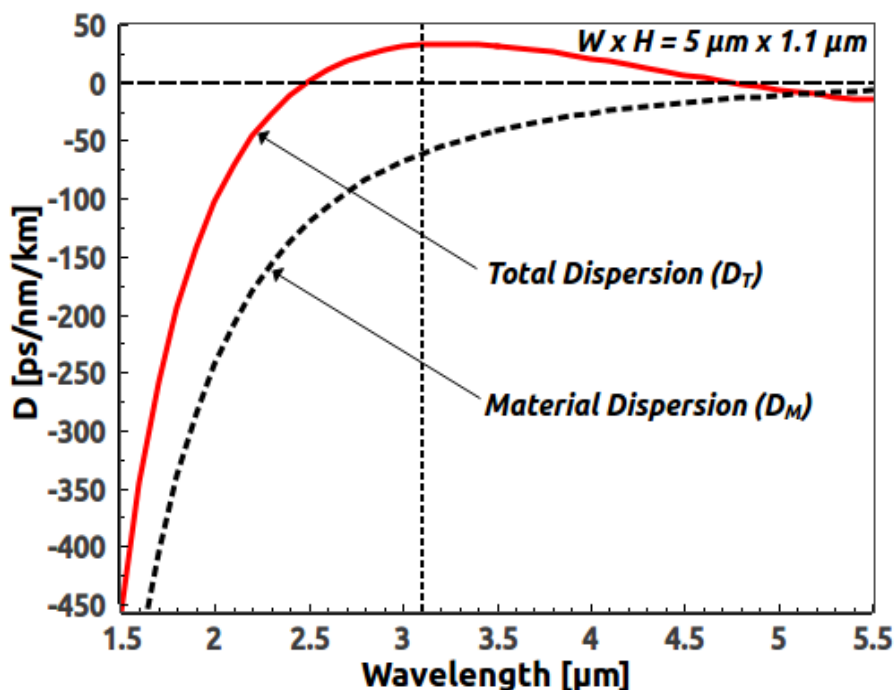


Fig. 6.7 GVD curve (solid red line) tailored for the fundamental quasi-TE mode calculated from n_{eff} and dotted black line curve represents the material dispersion (D_M) of $\text{Ge}_{11.5}\text{As}_{24}\text{Se}_{64.5}$ ChG material. Vertical dotted line indicates pump wavelength and the inset shows the spatial profile of the fundamental mode at a wavelength of $3.1 \mu\text{m}$.

ZDW around the pump wavelength, we numerically calculated GVD for this structure as a function of wavelength for the fundamental quasi-TE mode and plot it with material dispersion in Fig. 6.7. It can be observed from this figure that the material dispersion, shown by a dotted black line, remains normal for the wavelength range $1.5 \mu\text{m}$ to $5.5 \mu\text{m}$, considered here but the total dispersion curve, shown by a solid red line, reached to the anomalous dispersion region between the $2.5 \mu\text{m}$ (1st ZDW) and $4.8 \mu\text{m}$ (2nd ZDW) due to tailoring dispersion through the variation of transverse dimensions of the rib waveguide. The GVD value estimated at the pump wavelength is around 32 ps/nm/km . Due to asymmetric waveguide structure, this waveguide geometry supports propagation of the fundamental quasi-TE mode up to the cut-off wavelength beyond $12 \mu\text{m}$.

6.2 Simulation parameters for MIR SC modelling

For modelling MIR SC in ChG channel waveguides designed and optimized in earlier section, the GNLSE is solved through SSFM as described in Chapter 3. We carry out simulations for two different structures of ChG channel waveguides and a rib waveguide assuming that the input pulse excites the fundamental quasi-TE mode for two pump sources at wavelength of $2 \mu\text{m}$ and $3.1 \mu\text{m}$, respectively. A sech pulse of 150 fs duration (FWHM) at a pump wavelength of $2 \mu\text{m}$ was launched including a wavelength-independent propagation loss of 2.5 dB/cm [39] for our 1-cm-long rectangular channel waveguides. For achieving sufficient extension of SC in the MIR, we next perform simulations for the another set of ChG geometries that were optimized at a pump wavelength of $3.1 \mu\text{m}$ assuming input pulse excites the fundamental quasi-TE mode with pulse duration of 85 fs and repetition rate of 160 kHz [157] taking wavelength independent loss of 0.5 dB/cm [39]. The TPA and delayed Raman response are taken as considered in Chapter 5. Since the actual n_2 of ChG glasses has not been measured in the MIR region, so its measured value at $1.55 \mu\text{m}$ [35] was reduced by a factor of two at the pump wavelength of $3.1 \mu\text{m}$ [145].

The minimum time-step (Δt) is calculated according to the procedure described in Chapter 5 at a wavelength of $2 \mu\text{m}$ and $3.1 \mu\text{m}$ as 3.3 fs and 5.2 fs, respectively. Considering grid point 2^{13} (FFT point) at a wavelength of $2 \mu\text{m}$ and $3.1 \mu\text{m}$ and using the minimum time-step obtained accordingly, we can calculate the time window as 27 ps and 43 ps that are wide enough to capture the SC spectrum produced in the output of the waveguides at a pump wavelengths of $2 \mu\text{m}$ and $3.1 \mu\text{m}$, respectively. The minimum wavelength edge for the spectral window in both pumps are calculated by using Equation (5.7) in Chapter 5 as $1 \mu\text{m}$ and $1.56 \mu\text{m}$, respectively.

6.3 Results and discussions

As we know, among many other factors, the extension of SC in the long wavelength edge depends on the position of pump source employed. To study SC in the MIR regimes and to know the effect of pump wavelength on SC extension in the long wavelength region, we have carried out simulations in our dispersion optimized channel waveguides at a wavelength of $2\ \mu\text{m}$ and $3.1\ \mu\text{m}$, separately. We proposed here two rectangular channel waveguides with air as top cladding and either $\text{Ge}_{11.5}\text{As}_{24}\text{S}_{64.5}$ glass or MgF_2 glass as its lower cladding material. Both waveguides optimized by dispersion tailoring at wavelengths of $2\ \mu\text{m}$ and $3.1\ \mu\text{m}$ and their GVD curves are shown in Fig. 6.3. We also optimized a rib waveguide employing MgF_2 as a lower cladding at a pump wavelength of $3.1\ \mu\text{m}$. Before carrying out SC simulations, we have performed some accuracy testing procedure such as FE modal solution accuracy and GVD parameters testing accuracy. However, as these accuracy testing methods described in detail in Chapter 5, we did not show it here further. In earlier chapter we found spurious results owing to the addition of insufficient number of higher-order dispersion coefficients during numerical simulations for SC generation. Therefore we calculate and add up to 10^{th} order dispersion during SC simulations.

6.3.1 Simulation results for channel waveguides pump employing at $2\ \mu\text{m}$

For studying SC generation at a pump wavelength of $2\ \mu\text{m}$, we consider a waveguide containing a core of dimensions $W = 1.5\ \mu\text{m}$ and $H = 1.1\ \mu\text{m}$ with air and $\text{Ge}_{11.5}\text{As}_{24}\text{S}_{64.5}$ glass as upper and lower claddings, respectively. Another geometry has a core with $W = 1.35\ \mu\text{m}$ and $H = 0.4\ \mu\text{m}$ but MgF_2 glass as the lower cladding. We optimized both of these waveguides by dispersion engineering and their dispersion curves were shown in Fig. 6.3(a). Using

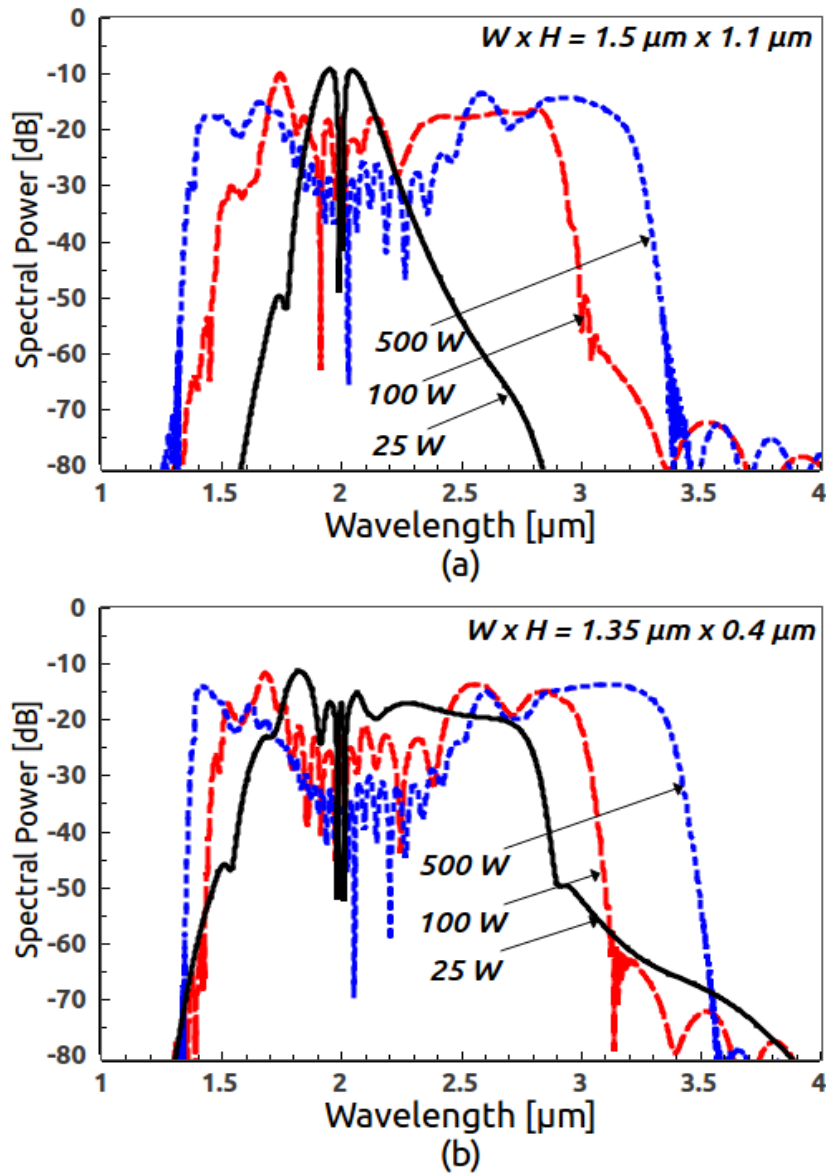


Fig. 6.8 Simulated SC spectra at a pump wavelength of 2 μm for (a) air-clad all-chalcogenide waveguide at peak power from 25, 100, and 500 W; (b) air-clad chalcogenide core employing MgF_2 for its lower cladding at the same power levels.

FE mode-solver, we obtain $A_{\text{eff}} = 1.09 \mu\text{m}^2$ which yields $\gamma = 24.79 \text{ /W/m}$ for the structure with $\text{Ge}_{11.5}\text{As}_{24}\text{S}_{64.5}$ lower cladding and significantly lower $A_{\text{eff}} = 0.51 \mu\text{m}^2$ which yields $\gamma = 53.39 \text{ /W/m}$ for the structure with MgF_2 lower cladding (provides higher index contrast) at a pump wavelength of 2 μm . The GVD parameter calculated at the pump wavelength for both waveg-

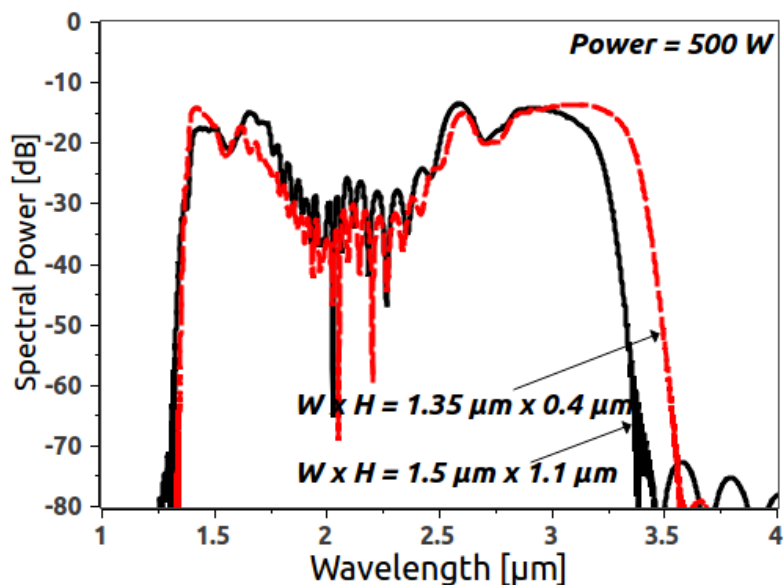


Fig. 6.9 Simulated SC spectra at a pump wavelength of $2 \mu\text{m}$ for waveguides with two different lower claddings at a peak power of 500 W only. Black-solid line curve represents the SC spectrum for the waveguide containing $\text{Ge}_{11.5}\text{As}_{24}\text{S}_{64.5}$ glass for its lower cladding and red-dashed line curve represents the spectrum for the structure employing MgF_2 as its lower cladding.

guides has a value of 13 ps/nm/km. These waveguides supported propagation of the fundamental TE mode up to the cut-off wavelength near $3.1 \mu\text{m}$ for the air-clad all-ChG structure and around $4 \mu\text{m}$ for the structure employing MgF_2 glass as lower cladding. A sech pulse of 150 fs duration (FWHM) was launched with peak power between 25 W and 500 W for numerical simulations. We included a wavelength-independent propagation loss of 2.5 dB/cm [39] for our 1-cm-long rectangular channel waveguides. Figure 6.8 shows the predicted SC spectra for the two waveguides at three different power levels at a pump wavelength of $2 \mu\text{m}$. In the case of 100 W input power the SC spectrum extends from $1.5 \mu\text{m}$ to around $3 \mu\text{m}$, producing a -30 dB bandwidth of 1500 nm for the waveguide using $\text{Ge}_{11.5}\text{As}_{24}\text{S}_{64.5}$ glass for its lower cladding. At the same power level the SC spectrum extends from $1.4 \mu\text{m}$ to around $3.1 \mu\text{m}$ producing a -30 dB bandwidth of 1700 nm for the waveguide with MgF_2 glass for its lower cladding. After increasing

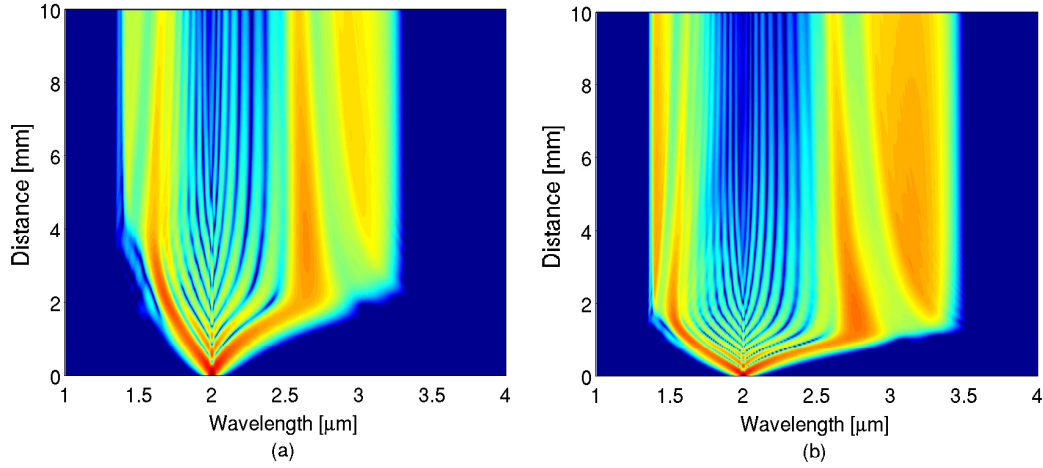


Fig. 6.10 Spectral evolution at a pump wavelength of $2 \mu\text{m}$ for (a) air-clad all-chalcogenide waveguide at a peak power of 500 W; (b) air-clad chalcogenide core employing MgF_2 for its lower cladding at the same power level.

input peak power level at 500 W, the SC spectra broadened from $1.3 \mu\text{m}$ to $3.3 \mu\text{m}$ (output bandwidth of 2000 nm) and from $1.3 \mu\text{m}$ to $3.5 \mu\text{m}$ (output bandwidth of 2200 nm) for these two waveguides, respectively. The spectral evolution plots corresponding to Fig. 6.9 at a peak power level of 500 W are shown in Fig. 6.10. It is apparent that a larger output bandwidth can be realized by using a waveguide employing MgF_2 glass for its lower cladding. The reason behind this bandwidth enhancement solely related to the higher index contrast between the core and cladding materials when MgF_2 glass is used for the lower cladding. However, it was not possible to extend the SC spectrum to beyond $3.5 \mu\text{m}$ by using a pump wavelength of $2 \mu\text{m}$.

6.3.2 Simulation results for channel waveguides pump employing at $3.1 \mu\text{m}$

We have found that at the pump wavelength of $2 \mu\text{m}$ the SC never extended beyond $4.5 \mu\text{m}$ for any of our designs. Therefore, to extend the SC in the MIR

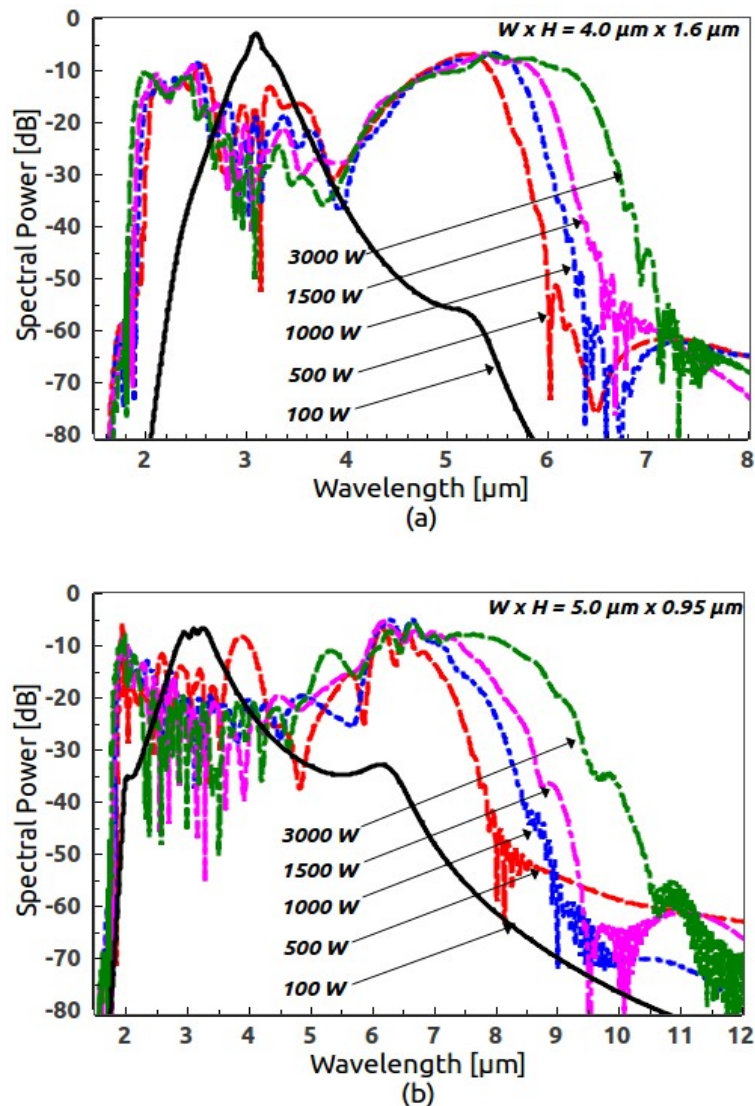


Fig. 6.11 Simulated SC spectra at a pump wavelength of $3.1 \mu\text{m}$ for (a) air-clad all-chalcogenide waveguide at peak power between 100 W and 3000 W; (b) air-clad chalcogenide core employing MgF_2 for its lower cladding for the same power levels.

regime, we need to shift the pump wavelength toward longer wavelengths [144]. We employ a pump wavelength of $3.1 \mu\text{m}$ since such a pump source has been realized at a repetition rate of 160 kHz [157]. Using 85 fs duration pulses at a wavelength of $3.1 \mu\text{m}$, we focus on a waveguide with $W = 4 \mu\text{m}$ and $H = 1.6 \mu\text{m}$ with $\text{Ge}_{11.5}\text{As}_{24}\text{S}_{64.5}$ glass for its lower lower cladding. The second waveguide structure had $W = 5 \mu\text{m}$ and $H = 0.95 \mu\text{m}$ but employed

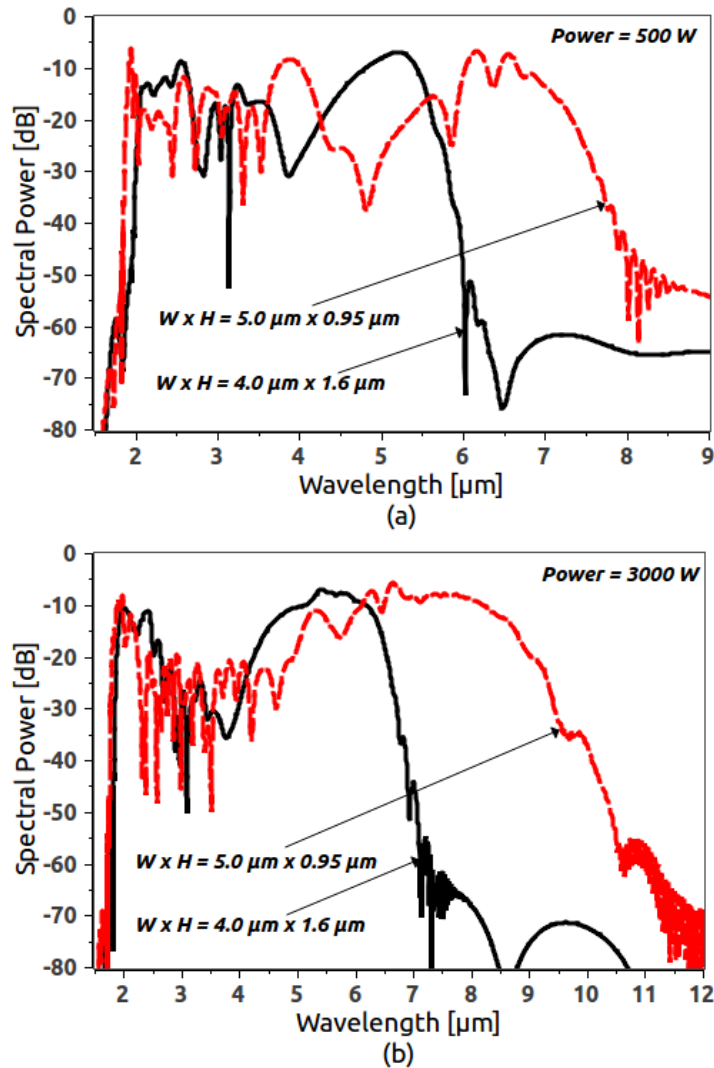


Fig. 6.12 Simulated SC spectra at a pump wavelength of $3.1 \mu\text{m}$ for (a) waveguides employing with two different lower claddings at a peak power of 500 W only; (b) waveguides with two different lower claddings at peak power of 3000 W only. Black-solid line curve represents the SC spectrum for the waveguide structure containing $\text{Ge}_{11.5}\text{As}_{24}\text{S}_{64.5}$ glass for its lower cladding and red-dashed line curve represents the spectrum for the structure with MgF_2 as its lower cladding.

MgF_2 glass for its lower cladding. Using the FE mode-solver, we obtain $A_{\text{eff}} = 4.25 \mu\text{m}^2$ and $\gamma = 2.05 \text{ /W/m}$ for the first structure and $A_{\text{eff}} = 3.32 \mu\text{m}^2$ and $\gamma = 2.63 \text{ /W/m}$ for the second structure. The GVD parameter calculated at the pump wavelength for these waveguides has values of 10.22 ps/nm/km and 21 ps/nm/km, respectively. These waveguides supported propagation of

the fundamental TE mode up to the cut-off wavelength around $6.5 \mu\text{m}$ for the air-clad all-ChG structure and beyond $12 \mu\text{m}$ for the structure employing MgF_2 as lower cladding.

After evaluating higher-order dispersion terms up to tenth-order from GVD curves shown in Fig. 6.3(b), we performed numerical simulations for SC generation in both the waveguide geometries at a power level between 100 W and 3000 W. The dispersion length, $L_D = T_P^2 / |\beta_2|$ for the 85 fs pump pulse for these two structures is 45 mm and 28 mm and the nonlinear length, $L_{NL} = 1/\gamma P$

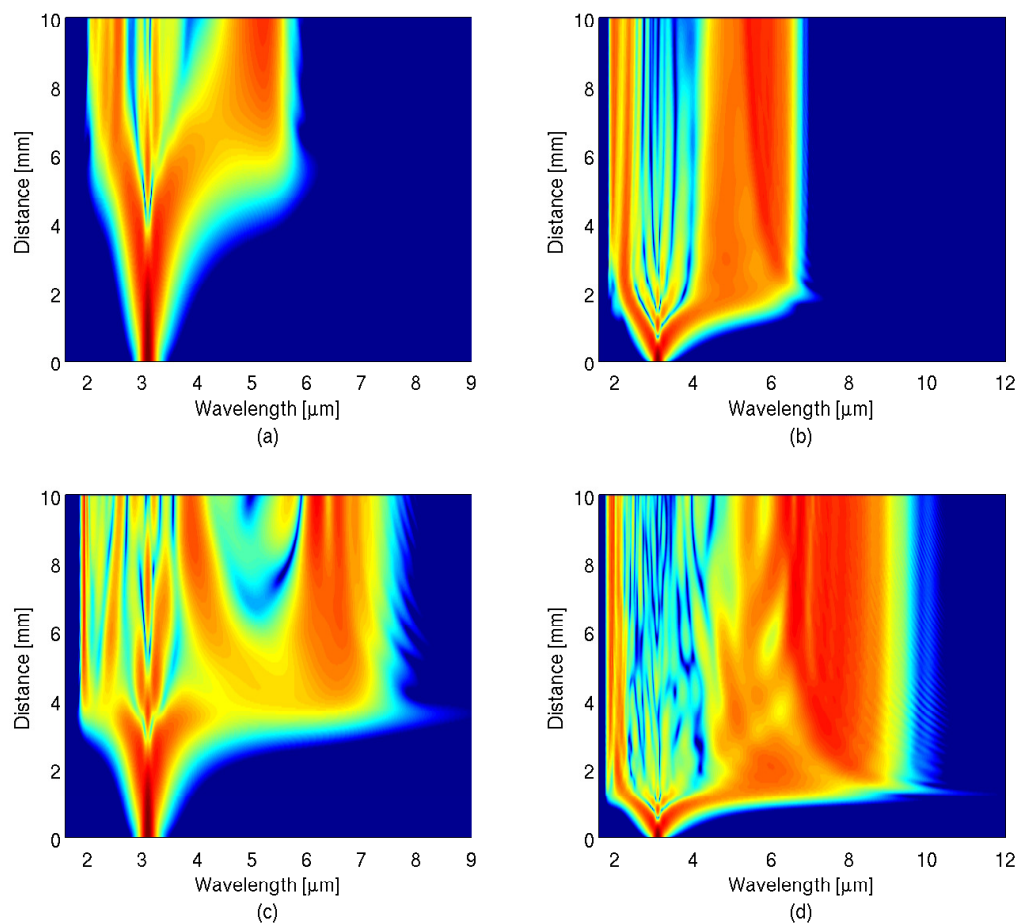


Fig. 6.13 Spectral evolution along the waveguide length at a pump wavelength of $3.1 \mu\text{m}$ for waveguides with (a) $\text{Ge}_{11.5}\text{As}_{24}\text{S}_{64.5}$ and (c) MgF_2 as its lower claddings at a peak power of 500 W only; (b) $\text{Ge}_{11.5}\text{As}_{24}\text{S}_{64.5}$ and (d) MgF_2 as its lower claddings with a peak power of 3000 W only.

at a peak power of 500 W is 0.98 mm and 0.76 mm, respectively. The soliton order, $N = \sqrt{L_D/L_{NL}}$ was 7 and 6 for the two waveguides, respectively, and the soliton fission length, $L_{fiss} \approx L_D/N$ was found to be 6.6 mm and 4.1 mm, respectively. Figure 6.11 shows the predicted spectra at various power level up to 3000 W for the two waveguide geometries at a pump wavelength of 3.1 μm . The spectral evolution plots corresponding to Fig. 6.12(a) and 6.12(b) are shown in Fig. 6.13. It is observed from Fig. 6.13 that the SC generation is dominated by soliton fission, which results in many short pulses generated through the soliton fission process whose spectra shifted towards the long wavelength side of the input spectrum. Raman-induced frequency shift (RIFS) is reducing gradually as solitons moved towards the second ZDWs located near 4.15 μm and 4.4 μm for the two waveguide geometries, respectively. Due to the spectral recoil effect [135, 136], RIFS were completely suppressed near the second ZDWs. At the same time, nonsolitonic radiation in the form of dispersive wave is produced at a wavelength that lies beyond the second ZDW. For the waveguide geometry employing $\text{Ge}_{11.5}\text{As}_{24}\text{S}_{64.5}$ glass as a lower cladding, it can be observed from Fig. 6.13 that the SC extends over 4 μm covering a wavelength range from 2 μm to 6 μm and for the structure employing MgF_2 as a bottom cladding, the SC extends over 6 μm covering a wavelength range from 1.8 μm to around 7.7 μm both at a peak power of 500 W. By increasing power level up to 3000 W, one can generate a SC spectrum that extends from 2 μm to 7 μm producing a bandwidth of 5 μm for the first waveguide and bandwidth of 9.2 μm (> 2.5 octave) for the second waveguide employing MgF_2 glass as its lower cladding.

6.3.3 Simulation results for a rib waveguide pump employing at 3.1 μm

To predict SC generation in our proposed rib waveguide, we have calculated higher-order dispersion terms up to 10th order and the effective mode area was

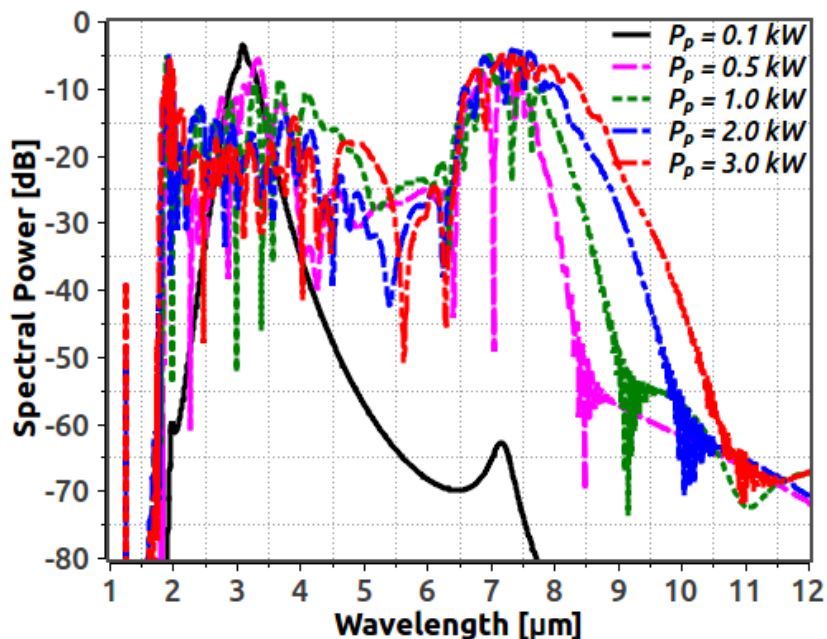


Fig. 6.14 Simulated SC spectra at a pump wavelength of $3.1 \mu\text{m}$ for rib waveguide with peak power varies between 100 W and 3000 W.

evaluated numerically by using our FE mode-solver which is $A_{\text{eff}} = 3.86 \mu\text{m}^2$, yielding a nonlinear coefficient of $\gamma = 2.26 \text{ W}^{-1}/\text{m}$ at the pump wavelength of $3.1 \mu\text{m}$. We have carried out numerical simulations launching a TE polarized 85-fs FWHM secant pulse pumped at a wavelength of $3.1 \mu\text{m}$ for peak power levels between 100 W and 3000 W and the results are shown in Fig. 6.14. The SC spectrum extends farther into the long-wavelength region with increasing pump power as expected. For the largest peak power of 3000 W, SC extended up to $10 \mu\text{m}$ at a spectral power level of -30 dB from the peak. However, SC extended more than two octave covering the wavelength range $1.8\text{--}8 \mu\text{m}$ for relatively low peak power of 500 W.

The spectra shown in Fig. 6.14 does not reveal how the SC evolves inside the waveguide. The left and right columns in Fig. 6.15 present the temporal evolution, spectral evolution, and spectrogram of pump pulses along the 1-cm length of the waveguide for the peak power levels of 500 W and 3000 W, respectively. The dispersion lengths of the 85-fs pump pulse in these

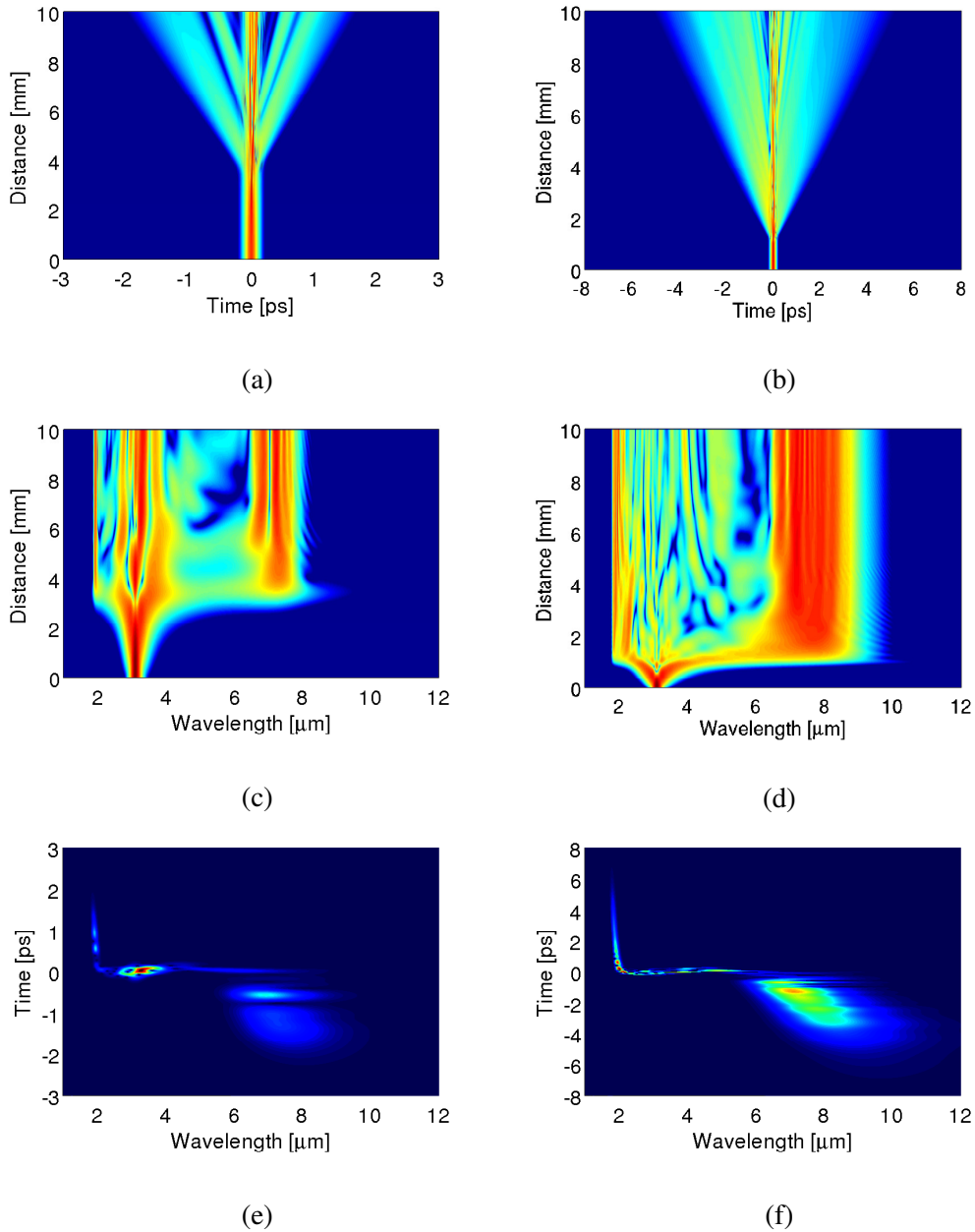


Fig. 6.15 Temporal evolution (top), Spectral evolution (middle), and Spectrogram (bottom) at the rib waveguide output pumped at a wavelength of $3.1 \mu\text{m}$ for two different peak power of 500 W (left column) and 3000 W (right column), respectively.

power level is $L_D = 14.1 \text{ mm}$ and the corresponding nonlinear lengths at a peak power of 0.5 and 3 kW are $L_{NL} = 0.15$ and 0.89 mm , respectively. These values correspond to soliton orders $N = \sqrt{L_D/L_{NL}}$ of about 4 and 10 for the peak power levels 500 and 3000 W, respectively. In both cases, SC

formation is mainly dominated by the soliton fission process occurring at a distance of 1.4 mm (left column) and 3.5 mm (right column) shown in Fig. 6.15. The dynamics behind the SC generation has been already described for channel waveguides above. Since the GVD curve of our proposed rib waveguide also has two ZDWs, a strong NSR is produced in the stoke-side of the SC spectrum right after the second ZDW (located at around $4.8 \mu\text{m}$) of the GVD curve which is only due to the soliton suppression effect. As the dispersion slope ($dD/d\lambda$) of the GVD curve in the vicinity of the second ZDW is negative, owing to the spectral-recoil effect (soliton suppression), the negative dispersion slope has significantly modified the SC spectrum through the generation of strong redshifted dispersive wave, allowing the SC generation is extended further into the MIR regime up to $8 \mu\text{m}$ (Fig. 6.15(a) and 6.15(c) in left column) and $10 \mu\text{m}$ (Fig. 6.15(b) and 6.15(d) in right column) for the peak powers of 500 W and 3000 W, respectively. The temporal and spectral differences are also apparent in the spectrogram shown in Fig. 6.15 (bottom row) and the SC extension beyond $8 \mu\text{m}$ [Fig. 6.15(e)] and $10 \mu\text{m}$ [Fig. 6.15(f)] are clearly observed for our proposed rib waveguide design with a peak power of 500 W and 3000 W, respectively.

There may be a disadvantage for ChG waveguides fabricated using MgF_2 glass for the lower cladding owing to its fragility. This problem becomes severe for long waveguides but is manageable for short waveguides around 1-cm-long [144]. Ma *et al.* [39] have shown experimentally that, if the top surface of the waveguides made from chalcogenide materials is left uncoated, the bare waveguide surface becomes rapidly contaminated by absorbing water and hydrocarbons from surrounding environment, resulting in increased losses. To prevent the surface contamination, a thin 10-nm protective coating layer of fluoro-polymer may be placed on top of the waveguide geometries. For this study, we have tested numerically the effect of placing of such a thin layer and found that the dispersions at a pump wavelength of $3.1 \mu\text{m}$ for

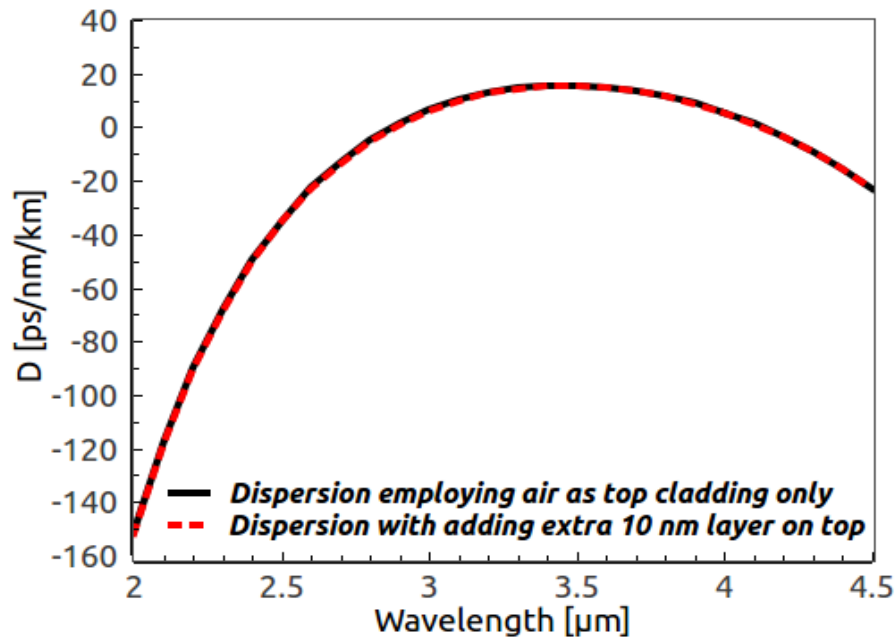


Fig. 6.16 GVD curves for the fundamental quasi-TE mode calculated for the waveguide structure employing $\text{Ge}_{11.5}\text{As}_{24}\text{S}_{64.5}$ glass as its lower cladding without (black-solid line curve) and with (red-dotted line curve) adding extra 10 nm layer on the top of the waveguide.

the two waveguides used in our work was 9.85 ps/nm/km (10.23 ps/nm/km without coating) and 21.68 ps/nm/km (21 ps/nm/km without coating). Such relatively small changes in the β_2 value do not produce noticeable changes on the SC generated at the waveguide output. Figure 6.16 shows dispersion calculated for the waveguide employing $\text{Ge}_{11.5}\text{As}_{24}\text{S}_{64.5}$ glass as its lower cladding without and with adding extra 10 nm layer coating on the top of the waveguide from which it can be observed that both dispersion curves merged and following the same path with a very little difference. As we did not obtain significant difference between the dispersion curves calculated for this waveguide structure, we measured the dispersion value of the other structure at a pump wavelength only.

Recently Yu *et al.* [145] proposed an air-clad rib waveguide whose core was made with $\text{Ge}_{11.5}\text{As}_{24}\text{Se}_{64.5}$ glass and whose lower cladding was made with $\text{Ge}_{11.5}\text{As}_{24}\text{S}_{64.5}$ glass. They were able to generate SC covering the wavelength range 1.8-7.5 μm when pumped with an optical parametric amplifier

at 4 μm with a peak power of 3260 W. By rigorous numerical simulations, it is shown here that MIR SC can be generated with dispersion-engineered air-clad rectangular channel waveguide employing the same materials and covering the wavelength range of 1.9-7 μm by employing a pump source at a wavelength of 3.1 μm with a peak power of 3000 W. It is observed from Figs. 6.12 and 6.14 that MIR SC can be extended in the long wavelength regime up to 11 μm with channel waveguide and 10 μm with rib waveguide employing MgF_2 glass for their lower cladding when pumped with the same power and pump source although MgF_2 glass would be expected to absorb beyond 9 μm [39].

6.4 Summary

In this chapter we have discussed the possibility of producing a broadband MIR SC in $\text{Ge}_{11.5}\text{As}_{24}\text{Se}_{64.5}$ ChG waveguides extending beyond 11 μm which was not possible to achieve by ChG nanowire designed in Chapter 5. We have numerically demonstrated MIR SC generation by using dispersion-engineered, air-clad, channel and rib waveguides designed and optimized such that they use either $\text{Ge}_{11.5}\text{As}_{24}\text{S}_{64.5}$ ChG glass or MgF_2 glass for its lower cladding material. The SC is generated with the waveguides proposed here by using pump pulses with low to moderate peak power at wavelength near 2 μm and 3.1 μm , separately. Although the nonlinear parameter has larger values at a pump wavelength of 2 μm , the SC spectra were extended only over 1.3-3.3 μm and 1.3-3.5 μm , respectively even at the highest but moderate peak power of 500 W for the two proposed structures.

To extend SC to beyond the 5 μm , it is necessary to choose a longer pump wavelength around 3-5 μm . To realize the ZDW of the waveguide around this wavelength the core size of the waveguide must be increased which increases the effective mode area and hence reduces the nonlinear parameter. The

only solution is to increase the peak power of the input pulse toward MW levels which can damage the input facet of the waveguide. Considering these factors, we designed and optimized an air-clad rectangular channel waveguide by employing either $\text{Ge}_{11.5}\text{As}_{24}\text{S}_{64.5}$ or MgF_2 glass for its lower cladding material and a rib waveguide employing MgF_2 glass as its lower cladding choosing pump at a wavelength of $3.1 \mu\text{m}$ such that broadband SC could be generated at moderate peak power levels. We have also discussed the disadvantage of bare waveguide design owing to surface contamination from surrounding environment. After placing a protective coating on the surface which does not produce noticeable changes on SC results have also been discussed.

Using pump source at a wavelength of $3.1 \mu\text{m}$ with a relatively low peak power of 500 W we obtained a SC spectrum extended over 1.5 octave and covering the wavelength range from $2\text{-}6 \mu\text{m}$ with an air-clad all-ChG structure. However, when we used an optimized waveguide using MgF_2 glass for its lower cladding using same pump power, the SC spectrum extended over more than two-octaves covered a wavelength ranges $1.8\text{-}7.7 \mu\text{m}$ and $1.8\text{-}8 \mu\text{m}$ for a channel waveguide and a rib waveguide, respectively. We have also found that, MIR SC can be extended over in the wavelength range $1.9\text{-}7 \mu\text{m}$ and $1.8\text{-}11 \mu\text{m}$ with a moderate peak power of 3000 W when the air-clad channel waveguide is designed with a $\text{Ge}_{11.5}\text{As}_{24}\text{Se}_{64.5}$ glass core and employs $\text{Ge}_{11.5}\text{As}_{24}\text{S}_{64.5}$ or MgF_2 glass for its lower cladding, respectively.

Chapter 7

Mid-infrared SC generation in chalcogenide microstructured fibres

SC sources operating in the mid-infrared (MIR) wavelength range have attracted much attention because of their numerous applications in the MIR sciences [31]. Most of the earlier theoretical and experimental investigations on SC generation mainly focused on fibre based geometries, particularly photonic crystal fibre (PCF), in which the dispersion could be easily engineered due to strong confinement associated with the air-holes. Although strong confinement can be achieved in silica PCF, the low nonlinearity of silica necessitates kilowatt peak powers for SC generation. Moreover, as silica suffered from severe absorption at wavelengths beyond $2.2 \mu\text{m}$, it was not possible to extend the SC far into the MIR by using silica based structures. Recently, efforts have focused on increasing the optical fibre nonlinearity by using nonlinear glasses and the chalcogenide (ChG) glasses are particularly attractive as these glasses can have optical nonlinearities several thousand times that of silica, and also transparent in the MIR, and can be easily drawn into optical fibres. Therefore, ChG fibre can be used to obtain an SC laser source beyond $5 \mu\text{m}$ where the propagation loss of silica, ZBLAN, and tellurite fibres becomes severely large.

ChG glasses can provide MIR transparency up to 14 μm when selenide-based materials are employed [141]. Since GeAsSe glasses have excellent film-forming properties and possess a relatively high third-order nonlinearity, there has been growing interest in designing and optimizing waveguides made from these materials and using them for broadband MIR SC generation [39]. Recently a number of experimental and theoretical investigations on MIR SC generation was reported and a few of which were ChG planar waveguides [143–146] and ChG fibres [38, 147–152]. In one approach, ultrashort pump pulses are launched into a dispersion-engineered planar waveguide. However, this approach suffers from cladding absorption and cut-off of the fundamental mode when an asymmetric structure is employed. A fibre-based device remain attractive because of its ruggedness, excellent beam quality, and relative ease of manufacturing [132]. Microstructured fibres (MoFs) are seen as potentially important specialized optical waveguides due to their inherent advantages arising from their modal properties such as controllable mode area and their dispersion properties which are achieved through tailoring their structural parameters. Photonic crystal fibres (PCFs) are particularly attractive as they offer significant enhancement of the nonlinear effects owing to a strong mode confinement and easier dispersion management resulting from the use of a cladding containing air holes [142].

This chapter presents the detailed design and optimization of three different chalcogenide microstructured fibres (MoFs) such as conventional hexagonal photonic crystal fibre (H-PCF), triangular/suspended core (TC) fibre, and equiangular spiral photonic crystal fibre (ES-PCF) through dispersion engineering with comparative studies for MIR SC generation. Section 7.1 presents MoFs structures. Section 7.2 discusses the dispersion tailoring of MoFs proposed here. Section 7.3 reviews simulation parameters for numerical modelling. Section 7.4 presents the results and discussions with comparative

analysis among microstructured fibres proposed. Section 7.5 summarizes the study.

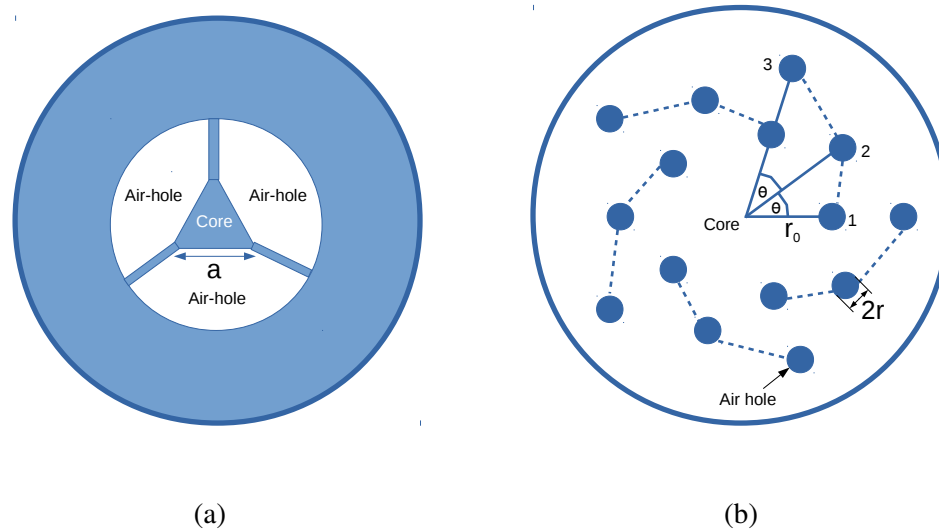


Fig. 7.1 Schematic diagrams of ChG MoFs (a) Triangular core (TC) fibre and (b) Equiangular spiral photonic crystal fibre (ES-PCF) geometry used for dispersion optimization.

7.1 Microstructured fibres (MoFs) design

7.1.1 Structure of MoFs

The schematic diagram of the $\text{Ge}_{11.5}\text{As}_{24}\text{Se}_{64.5}$ ChG hexagonal PCF used for numerical modelling was shown in Fig. 3.1 (b) in Chapter 3. Its air holes follow conventional hexagonal symmetry with the central air-hole missing and consists of five rings of air-holes. The schematic diagram of triangular/suspended core ChG fibre is shown in Fig. 7.1(a) which cladding contains three large air-holes resulting a triangular shaped core. The schematic diagram of ChG equiangular spiral PCF is shown in Fig. 7.1(b) which consists of five spiral arms with cladding containing three ring air-holes. The wavelength-dependent linear refractive index of core materials over the entire

wavelength range used in the simulation was obtained using the Sellmeier Equation (5.1) given in Chapter 5.

7.1.2 Dispersion tailoring for hexagonal PCF

We have seen in Chapters 5 and 6 that the design of an optical waveguide for SC generation depends on dispersion parameters and the accuracy of GVD and higher-order dispersion parameters depends on how accurately calculates

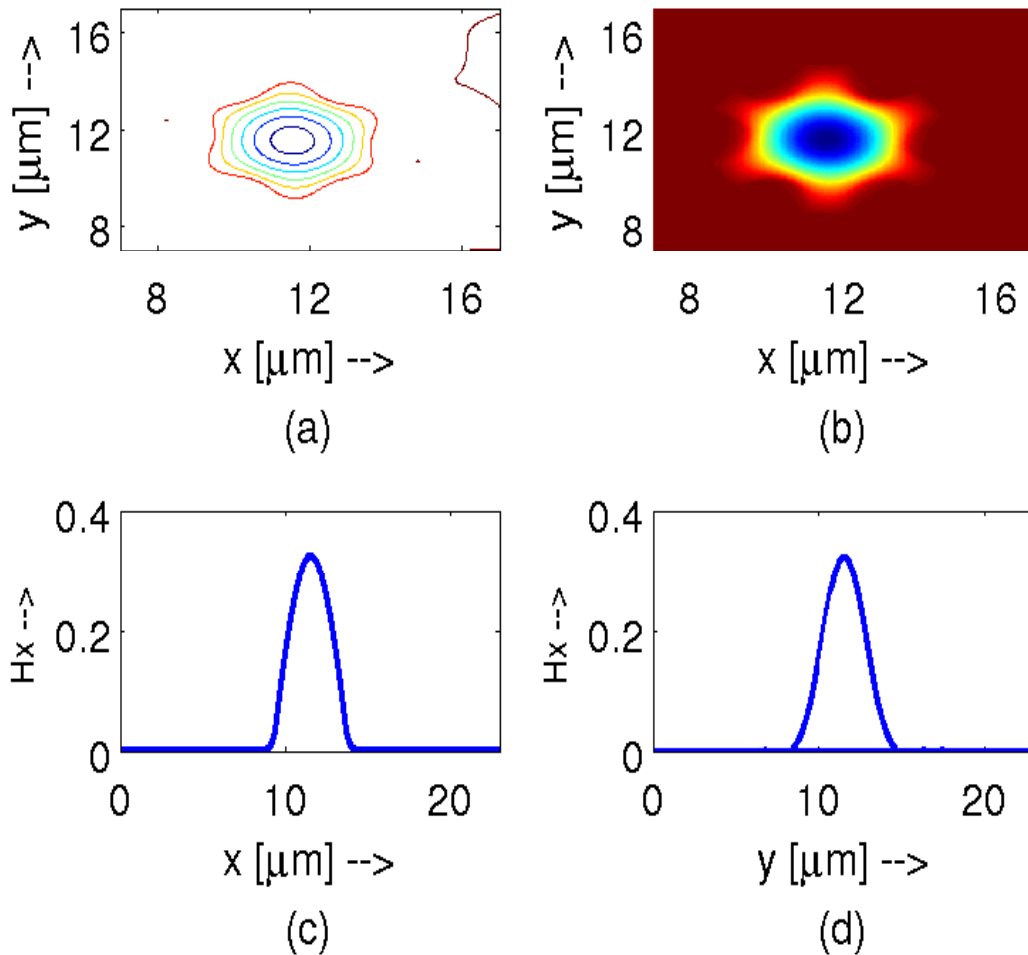
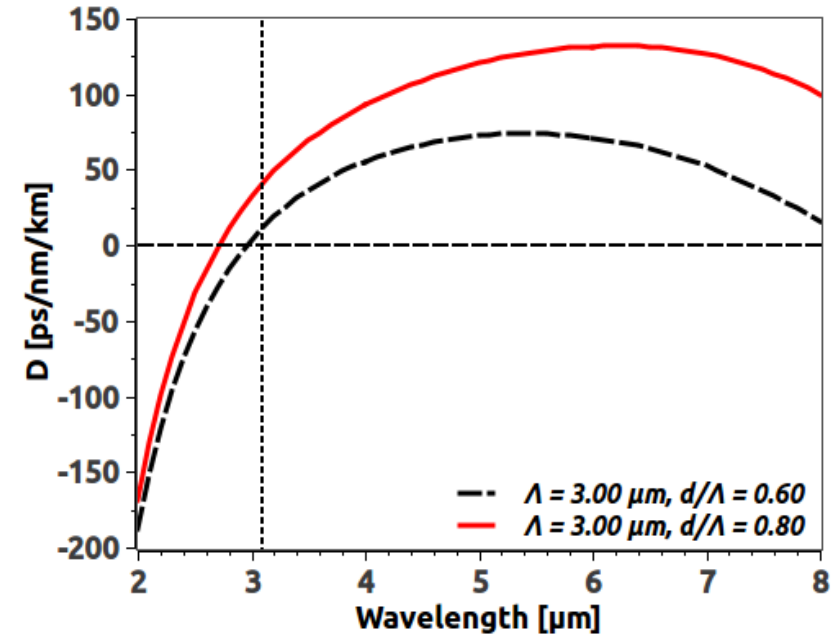


Fig. 7.2 H_x field profile of fundamental mode (H_x^{11}) for the hexagonal PCF structure of $\Lambda = 3 \mu\text{m}$ and $d/\Lambda = 0.8$ at a wavelength of $3.1 \mu\text{m}$; a) Contour, b) Surface, c) H_x field along x -axis, and d) H_x field along y -axis of a H-PCF.

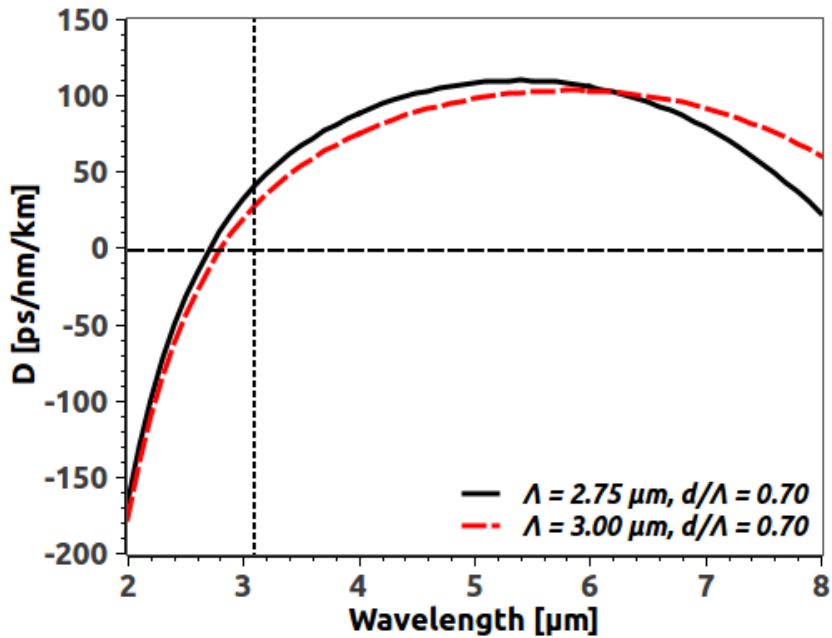
the mode propagation, $\beta(\omega)$ for the fundamental mode through finite-element modal solutions. Therefore, accuracy of any design critically depends on the accuracy of modal solutions of a waveguide. For our H-PCF, we represent the waveguide structure with 360,000 first order triangular elements to obtain higher accuracy modal solutions. A powerful extrapolation technique [133] was used to test the accuracy of modal solution for this PCF structure. Using the FE method described in Chapter 3 we have obtained modal solutions from which mode propagation constant $\beta(\omega)$ of the fundamental mode over a range of frequencies are evaluated and calculate the effective index from the mode propagation constant obtained through modal solutions. Figure 7.2 shows the H_x field profile of the fundamental (H_x^{11}) mode with the four different field representations of the H-PCF structure with $\Lambda = 3 \mu\text{m}$ and $d/\Lambda = 0.8$ at a wavelength of $3.1 \mu\text{m}$. The spatial profile of the fundamental mode, shown in Fig. 7.2(b), exhibits excellent field confinement to the central core region, enabling enhanced nonlinear interaction.

As discussed in earlier chapters, a broadband MIR SC source can be obtained by using a pump wavelength close to the ZDW of the waveguide. Several techniques have been used to shift the ZDW of $\text{Ge}_{11.5}\text{As}_{24}\text{Se}_{64.5}$ ChG material (which is located near $7 \mu\text{m}$) toward shorter wavelengths [27, 147, 148]. Here, we have designed and optimized $\text{Ge}_{11.5}\text{As}_{24}\text{Se}_{64.5}$ ChG PCF structure with micro-structuring the air holes in the claddings. It is easier to fine tune/adjust ZDW over a much wider wavelength range compared to that of planar waveguides and conventional fibres. In order to shift the ZDW of a ChG fibre near $3.1 \mu\text{m}$ with a small value of anomalous dispersion at the pump wavelength, we tailored a conventional hexagonal PCF and obtained GVD curves are shown in Fig. 7.3. Its air holes follow hexagonal symmetry with the central air hole missing. Both the diameter (d) and pitch (Λ) of the air-hole array can be varied to engineer PCF's dispersion properties. Through a rigorous numerical procedure, we obtain two sets of dispersion curves

for our proposed H-PCF structure. Figure 7.3(a) shows how the dispersion curve $D(\lambda)$ changes when the air-hole diameter to pitch ratio, d/Λ is varied



(a)



(b)

Fig. 7.3 Dispersion curves for the ChG hexagonal PCF design (a) for different d/Λ keeping Λ constant; (b) for different Λ with d/Λ constant. Vertical dotted line indicates pump wavelength at $3.1 \mu\text{m}$.

while keeping the pitch, Λ constant. Figure 7.3(b) shows the situation in which the Λ is changed while keeping the ratio d/Λ constant. In the case of air-hole diameter (d) variation, ZDW of the dispersion curves changes with increasing or lowering the GVD value at the pump wavelength of the dispersion curve which in turn enhancing or decreasing the nonlinearity of PCF as the effective mode area changes. On the other hand, ZDW of the dispersion curve moves near to the pump wavelength with lowering the GVD value if the Λ of that PCF increases which in turn decreases nonlinearity of the PCF. It can be observed in Fig. 7.3(a) that the separation between two ZDWs (anomalous dispersion region) of a GVD curve becomes wider for higher ratio of d/Λ with increasing dispersion value at the pump wavelength. In contrast, two ZDWs of a GVD curve move to left or right with the variation of Λ shown in Fig. 7.3(b). It is apparent from the figure that a ChG H-PCF can be designed to exhibit relatively small anomalous dispersion over a wide wavelength range extending from $2.7 \mu\text{m}$ to beyond $8 \mu\text{m}$.

7.1.3 Dispersion tailoring for TC fibre

To calculate GVD and higher-order dispersion coefficients accurately, we represent our proposed triangular core structure with 360,000 first order triangular elements for obtaining the mode propagation constant, $\beta(\omega)$ for the fundamental mode by FE mode-solver. The simulated fundamental mode-field profile of the fundamental quasi-TM mode at a wavelength of $3.1 \mu\text{m}$ is shown in Fig. 7.4 when the triangular core base, $a = 6 \mu\text{m}$. In this case H_x field was dominant and it is seen from the figure that field along the x-axis of the TC fibre shows symmetric (Fig. 7.4(c)) while along the y-axis of the fibre, the field shows asymmetric (Fig. 7.4(d)). It can be observed from field-profile that the mode is tightly confined inside the core enabling good nonlinear interaction. Now the effective index, n_{eff} for this TC structure can be calculated from the $\beta(\omega)$ obtained by FE mode-solver up to the wavelength

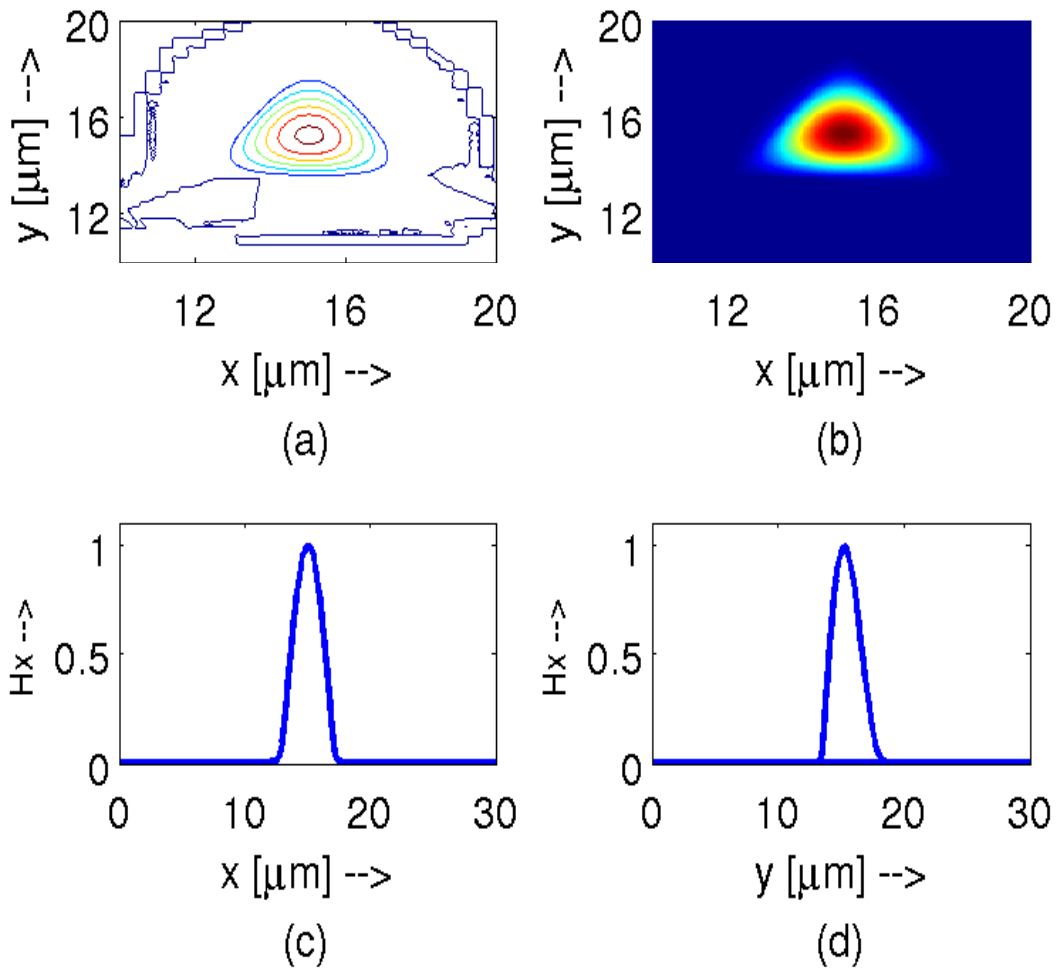


Fig. 7.4 H_x field profile of fundamental quasi-TM (H_x^{11}) mode for triangular core (TC) structure with a base length, $a = 6 \mu\text{m}$ at a wavelength of $3.1 \mu\text{m}$; a) Contour, b) Surface, c) H_x field along x -axis, and d) H_x field along y -axis of a TC fibre.

of interest. In order to shift the ZDW of a ChG TC fibre near $3.1 \mu\text{m}$ with a small value of anomalous dispersion at the pump wavelength, we optimized a MoF structure by adjusting its base, a . We tailored this structure for a number of its base lengths from $6 \mu\text{m}$ to $10 \mu\text{m}$ and obtained GVD curves are shown in Fig. 7.5. It can be seen from this figure that ZDW of the dispersion curve moves towards the right with lowering the GVD value at a pump wavelength as the base length of fibre increased and all dispersion

curves show a bit sloppy in nature compare with the GVD curves obtained for H-PCF. Therefore, it is not easier to control dispersion properties of TC fibre as desired by varying of its only one structural parameter (base length of TC fibre).

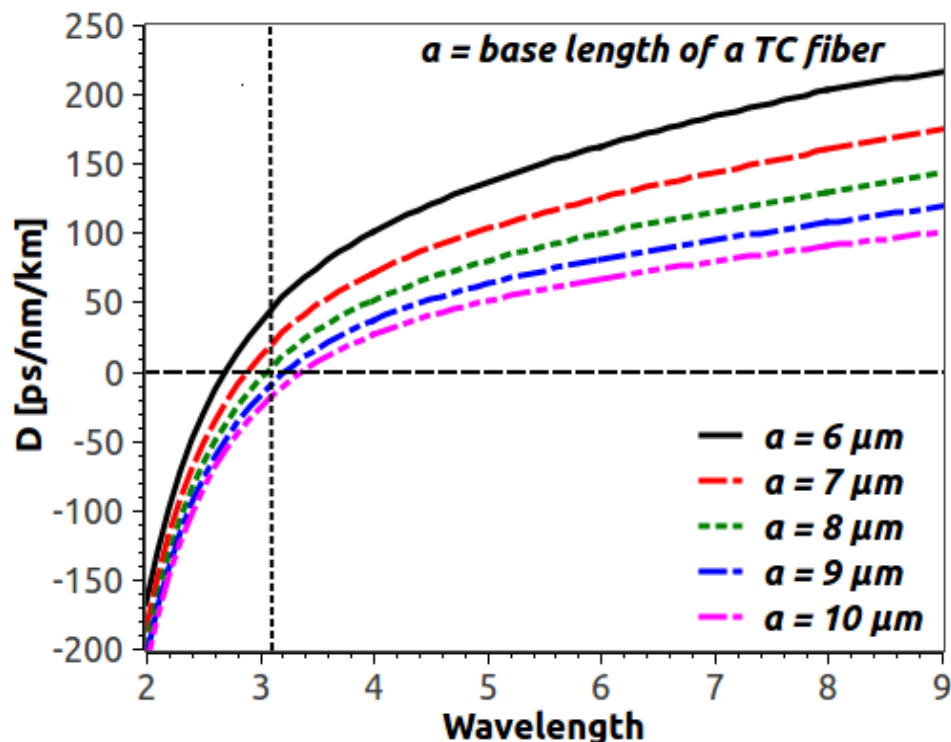


Fig. 7.5 GVD curves for the ChG triangular core (TC) fibre obtained for base length (a) varies from $6 \mu\text{m}$ to $10 \mu\text{m}$. Vertical dotted line indicates pump wavelength at $3.1 \mu\text{m}$.

7.1.4 Dispersion tailoring for equiangular spiral PCF

The equiangular spiral (ES) microstructured fibre we propose here is a modification of the ES-PCF reported in [158–160]. Figure 7.1(b) shows the five arm air-hole arrangement in the ES-PCF and the equation for obtaining spiral pitch (Λ_s) of this design in polar coordinates is,

$$\Lambda_s = r_0 e^{\theta \cot \alpha}, \quad (7.1)$$

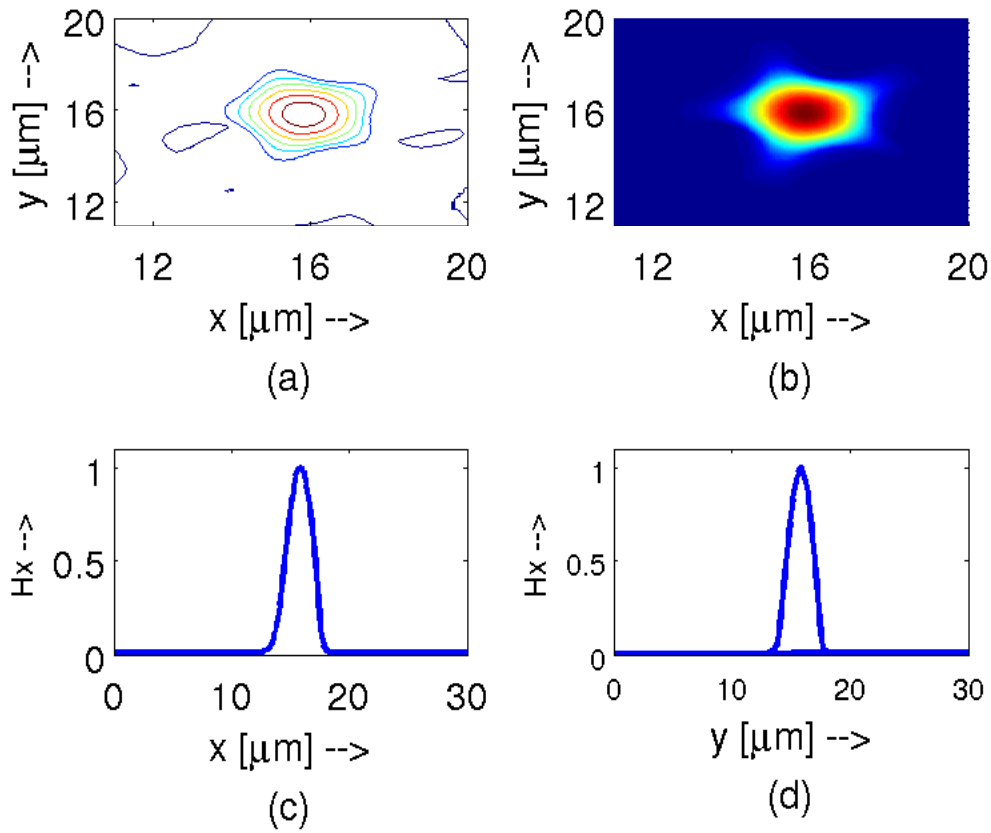
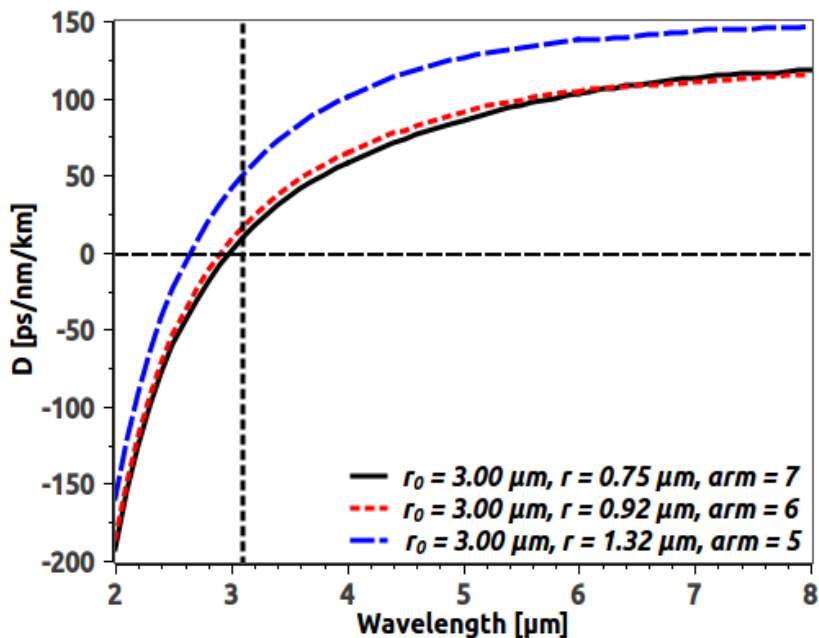


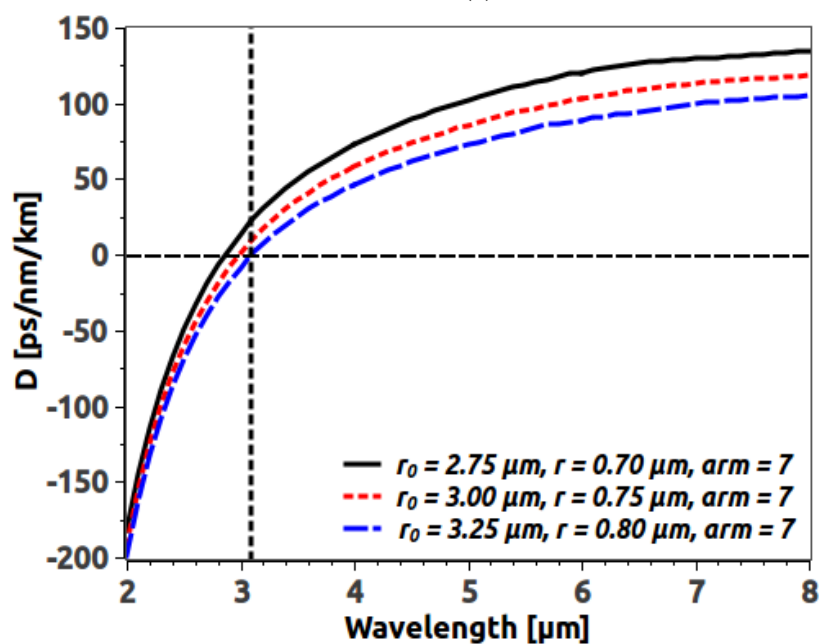
Fig. 7.6 H_x field profile of fundamental quasi-TM (H_x^{11}) mode for equiangular spiral PCF structure with first ring spiral radius, $r_0 = 3 \mu\text{m}$, hole radius, $r = 1.32 \mu\text{m}$, and five spiral arms at a wavelength of $3.1 \mu\text{m}$; a) Contour, b) Surface, c) H_x field along x-axis, and d) H_x field along y-axis of a ES-PCF.

where r_0 is the spiral radius which is a distance between the centre of the structure and the centre of air-holes in first ring, θ is the angular increment between two successive air-holes in the same arm, Λ_s is the spiral pitch between the centre of any air-hole and the the centre of the structure, and α is the angle between the tangent and the radial line.

Finally we designed and optimized an ES-PCF and obtained two sets of GVD curves as shown in Fig. 7.7(a) and 7.7(b) from mode propagation constant obtained by our FE mode-solver. We represent our proposed ES-PCF structure with 360,000 first order triangular elements as H-PCF and TC fibre



(a)



(b)

Fig. 7.7 Dispersion curves for the ChG equiangular spiral PCF design (a) for different hole radius, r and different spiral arms keeping first ring spiral radius, r_0 constant; (b) for different first ring spiral radius, r_0 different hole radius, r and keeping the number of spiral arm constant. Vertical dotted line indicates pump wavelength.

and evaluate $\beta(\omega)$ up to the wavelength range of interest. Aitken extrapolation technique has been used to verify the accuracy of the results obtained by FE the mode-solver. The spatial mode-field profile of the fundamental quasi-TM mode is shown in Fig. 7.6 which exhibits excellent field confinement inside the central core region enabling excellent nonlinear interaction. The ES-PCF parameters used for dispersion tailoring are 3 air-hole ring, 5 to 7 spiral arm with spiral radius, $r_0 = 2.75$ to $3.00 \mu\text{m}$, spiral angle, $\theta = 27^\circ$ to 36° , and hole radius, $r = 0.75$ to $1.32 \mu\text{m}$, respectively. Figure 7.7(a) shows GVD curves with varying air-hole radius, r and number of arms while keeping spiral radius, r_0 constant. In other set shown in Fig. 7.7(b), GVD curves obtained in a situation by changing r_0 and r while keeping number of arms constant. In ES-PCF, there are four parameters (r_0 , r , θ , and number of spiral arms) which can be varied for tailoring the dispersion curve and can be obtained better dispersion properties than H-PCF and TC fibre. Therefore, it is easier to tailor a design of an ES-PCF by varying any one or more than one parameter at a time and can be obtained ZDW around the pump wavelength with higher confinement and flattened dispersion than conventional H-PCF (where only two parameters such as Λ and d can be varied) and TC fibre (where only base length can be varied). The air-holes of each ring in ES-PCF are revolved with respect to the previous ring which effectively stops the field spreading into the regions between air-holes and tightly confined in the core region. During ES-PCF design, as next spiral pitch, Λ_s varies with initial spiral radius, r_0 , angular progression, θ , and the tangent angle, α , there are possibilities to occur air-hole merging if the structural parameters for the ES-PCF are not chosen correctly. So, we adopted hole merging check during simulations. For our design, GVD curves shown in Fig. 7.7(a), we maintain minimum separation between air-holes is 265 nm and average air-holes separation is $4.66 \mu\text{m}$ for blue-line curve. For red-line dispersion curve shown in Fig. 7.7(a), the minimum separation between air-holes is obtained around

254 nm and average air-holes separation is obtained around $3.96 \mu\text{m}$. In our design, as we used the five spiral arms where designer typically use six or more than six spiral arms, we can obtain good confinement using our design by increasing air-hole radius with reducing number of arms than the earlier design reported in [160].

7.2 Simulation parameters for SC modelling in ChG MoFs

To predict SC far into the MIR region using the ChG MoFs tailored in earlier sections, the GNLSE is solved by SSFM as described in Chapter 3. We carry out simulations for three different optimized ChG MoF structures assuming that the input pulse excites the fundamental mode using pump at a wavelength of $3.1 \mu\text{m}$. To obtain sufficient SC extension in the MIR, a sech pulse of 85 fs duration (FWHM) with repetition rate of 160 kHz [157] at this pump wavelength was launched including a wavelength-independent linear propagation loss of 0.5 dB/cm [39] for our 1-cm-long microstructured fibres. The TPA and delayed Raman response are assumed as considered in Chapter 5. As the actual n_2 of ChG glasses has not been measured in the MIR region, so its measured value at $1.55 \mu\text{m}$ [35] was reduced by a factor of two at the pump wavelength of $3.1 \mu\text{m}$ [145].

The minimum time-step (Δt) was calculated according to the procedure described in Chapter 5 at a wavelength $3.1 \mu\text{m}$. Assuming grid point 2^{13} (FFT point) at a wavelength of $3.1 \mu\text{m}$ and using the minimum time-step obtained accordingly, we can calculate the time window as 43 ps which is wide enough to capture the SC spectrum produced in the output of the waveguides.

7.3 Results and discussions

To study the formation of SC inside the waveguide, we model the pulse evolution in the MoFs with a generalized nonlinear Schrödinger equation (GNLSE) presented in Chapter 2. Before the SC simulation, it is important to consider the damage threshold of ChG material. GeAsSe based glass has the lowest damage threshold at an average power density of 30 kW/cm². The damage threshold increases significantly when selenium-based glass is progressively replaced with the sulphide-based glass [152]. Even then, the ChG fibre core could be damaged if the peak intensity of pump pulses reaches 30 GW/cm² or the average power density at the input facet of the MoF exceeds 100 kW/cm². Paying attention with these factors, we designed our GeAsSe microstructured fibres for MIR SC generation such that the required peak power of pump pulses is at most 3 kW. For SC simulation we utilize the GVD curves shown in Fig. 7.3(a), Fig. 7.5 (black and red-line curves only), and 7.7(a) (blue and red-line curves only) for our three optimized MoFs structures.

7.3.1 SC generation in hexagonal PCF

Initially we have carried out SC simulation for hexagonal PCF. Using FE mode-solver, the A_{eff} for H-PCF is obtained as 6.83 (red-line curve in Fig. 7.3(a)) and 9.36 μm^2 (black-line curve in Fig. 7.3(a)), yielding $\gamma = 1.28$ and 0.93 W^{-1}/m and $D \approx 41$ and 12 ps/nm/km. Evaluating higher-order dispersion terms up to 10th order at a pump wavelength from the GVD curves shown in Fig. 7.3 for $\Lambda = 3.00 \mu\text{m}$, $d/\Lambda = 0.6$ and 0.8, we performed numerical simulations for the peak power levels between 200 W and 3000 W, and the results are shown in Fig. 7.8. For the largest peak power of 3000 W, the SC spectrum at the H-PCF output extends up to 7 μm (for black-line GVD curve shown in 7.3(a)) and 8 μm (for red-line GVD curve shown

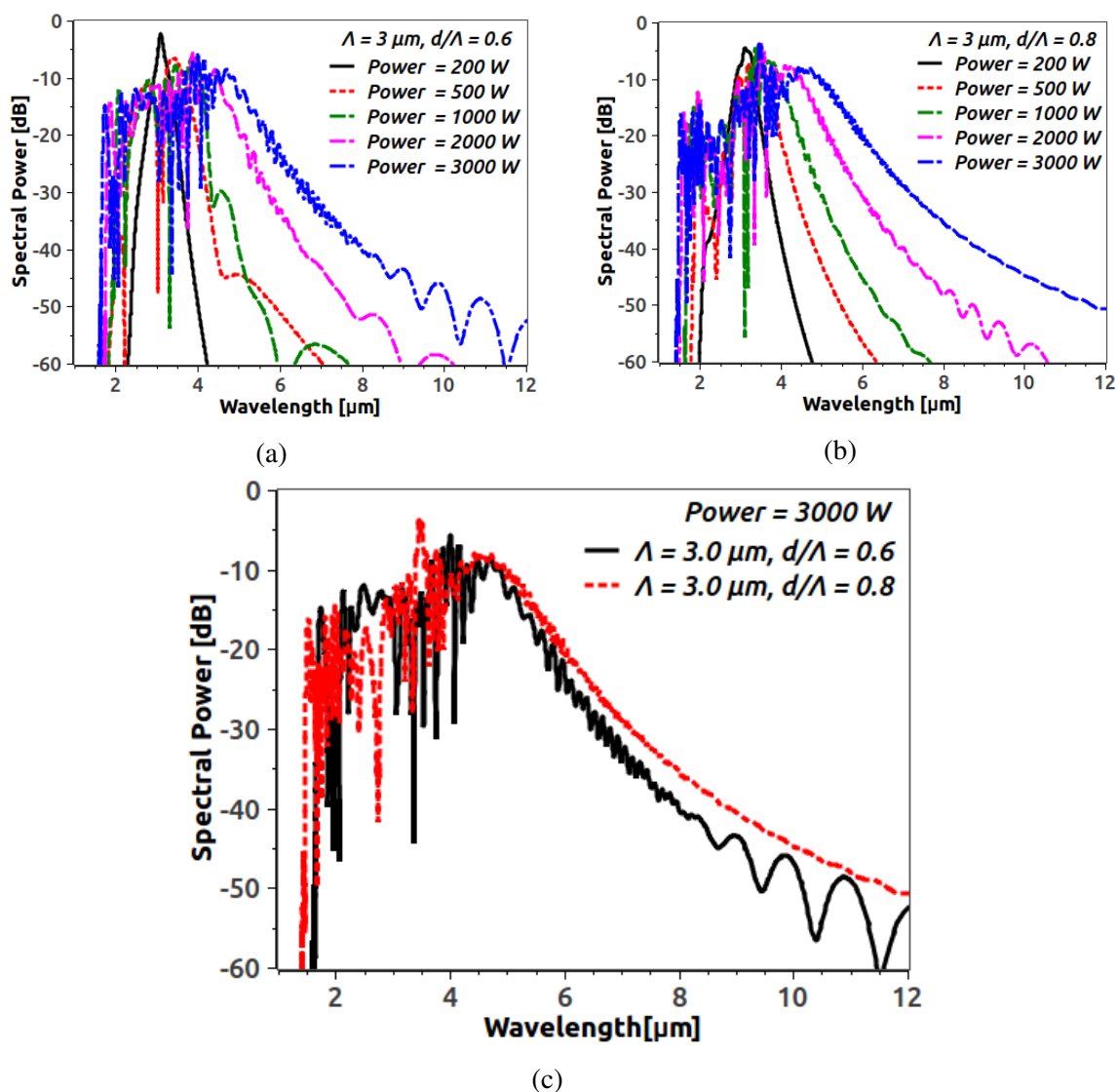


Fig. 7.8 Output SC pumped at a wavelength of $3.1 \mu\text{m}$ for Hexagonal PCF (a) for the black-line GVD curve shown in Fig. 7.3(a) with peak power variation between 200 W and 3000 W; (b) for the red-line GVD curve shown in Fig. 7.3(a) with power variation between 200 W and 3000 W; (c) for the GVD curves shown in Fig. 7.3(a) with a peak power of 3000 W only.

in Fig.7.3(a)). Figure 7.8(c) shows the comparative SC output spectra of dispersion curves shown in Fig. 7.3(a) from which it can be observed that SC spectrum for lower mode area GVD curve gets broaden than other one though the GVD value of higher mode area dispersion curve approaches near to the ZDW of that dispersion curve.

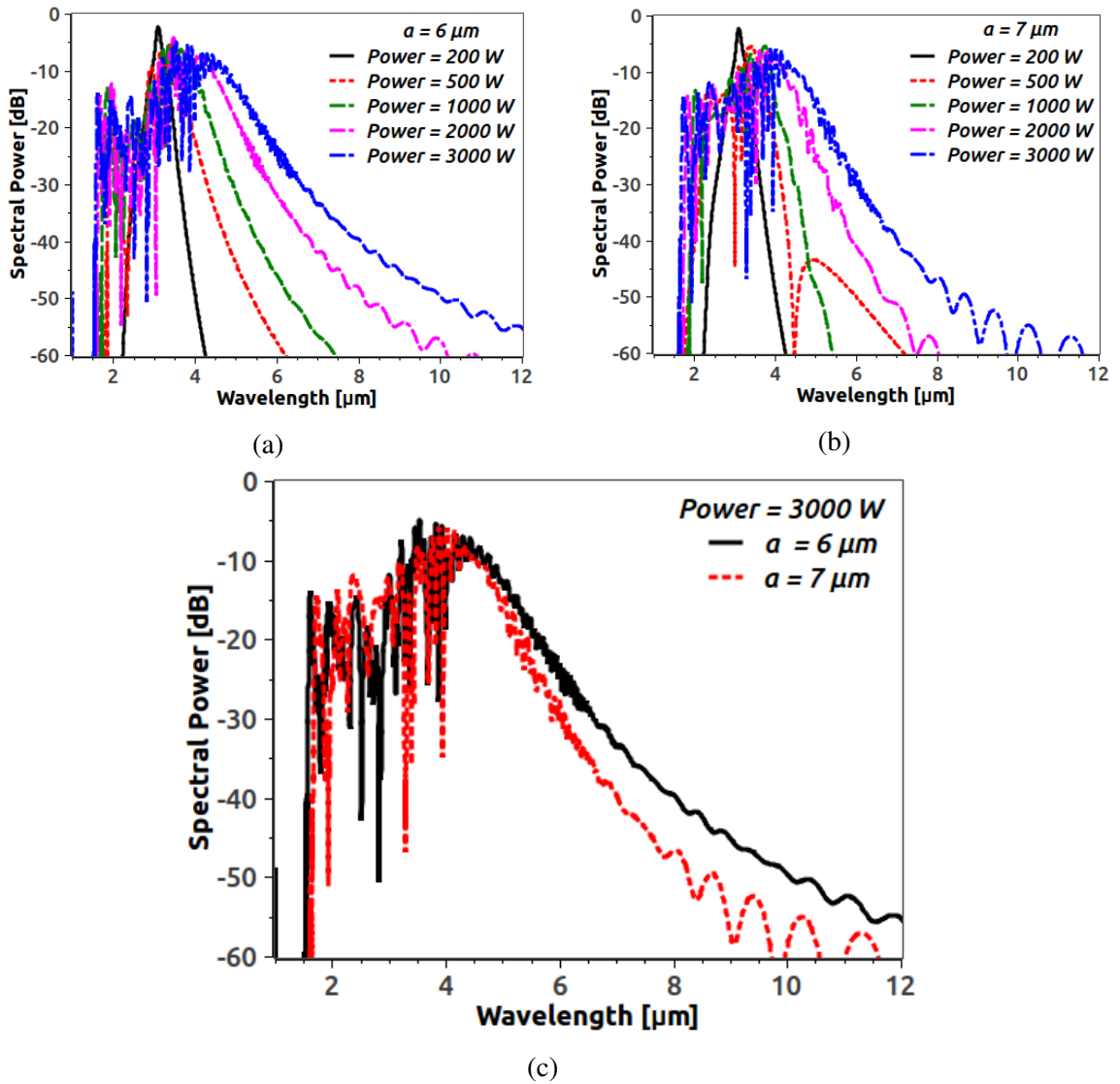


Fig. 7.9 Output SC pumped at a wavelength of $3.1 \mu\text{m}$ for TC fibre (a) for the red-line GVD curve shown in Fig. 7.5 with peak power variation between 200 W and 3000 W; (b) for the black-line GVD curve shown in Fig. 7.5 with power variation between 200 W and 3000 W; (c) for the GVD curves shown in Fig. 7.5 (red and black line GVD curves only) with a peak power of 3000 W only.

7.3.2 SC generation in TC fibre

Next, we consider triangular core (TC) fibre for SC generation. Similarly, the effective mode-area of TC fibre are obtained as $A_{\text{eff}} = 7.06$ (red-line curve in Fig. 7.5) and $9.41 \mu\text{m}^2$ (black-line curve in Fig. 7.5), resulting in a nonlinear coefficient $\gamma = 1.24$ and $0.93 \text{ W}^{-1}/\text{m}$ and $D \approx 44$ and 20

ps/nm/km, respectively, at the pump wavelength of $3.1 \mu\text{m}$. Using higher-order dispersion terms up to tenth order at a pump wavelength of $3.1 \mu\text{m}$ for the red-solid curve shown in Fig. 7.5 for base length, $a = 6$ and $7 \mu\text{m}$, we have carried out numerical simulations for power levels between 200 and 3000 W, and the results are shown in Fig. 7.9. For the largest peak power of 3000 W, the SC spectrum at the MoF output extends up to 7.5 (for black-line GVD curve) and $6.5 \mu\text{m}$ (for red-line GVD curve) and the output SC bandwidth are calculated at a power level of -30 dB from the peak. SC spectrum also gets broaden here for lower mode area dispersion curve although the dispersion value of higher mode area GVD curve approaches near to ZDW (shown in Fig. 7.9(c)).

7.3.3 SC generation in ES-PCF

Finally we consider the equiangular spiral PCF for SC generation. The mode-area for the ES-PCF are achieved as $A_{\text{eff}} = 6.12 \mu\text{m}^2$ (blue-line GVD curve in Fig. 7.7(a)) and $8.94 \mu\text{m}^2$ (red-line curve in Fig. 7.7(a)) resulting $\gamma = 1.42$ and $0.98 \text{ W}^{-1}/\text{m}$ and $D \approx 50$ and $17 \text{ ps}/\text{nm}/\text{km}$ at the pump wavelength of $3.1 \mu\text{m}$. After evaluating dispersion terms up to 10^{th} order from the GVD curves shown in Fig. 7.7, a sech pulse of 85-fs (FWHM) duration with a repetition rate of 160 kHz were applied for numerical simulation with a peak power variation between 200 W and 3000 W. The spectral evaluation of ES-PCF for this power range are shown in Fig. 7.10 in which SC spectrum clearly extends beyond the $11 \mu\text{m}$ (> 3 octave) (for blue-line GVD curve) and extends up to $7 \mu\text{m}$ (for red-line GVD curve) with a largest peak power of 3000 W.

7.3.4 Comparison of SC evolution in MoFs output

To study how the SC evolves along the MoFs length, we present here the evolution of pulse spectra over the entire MoFs length of 1-cm for the lower

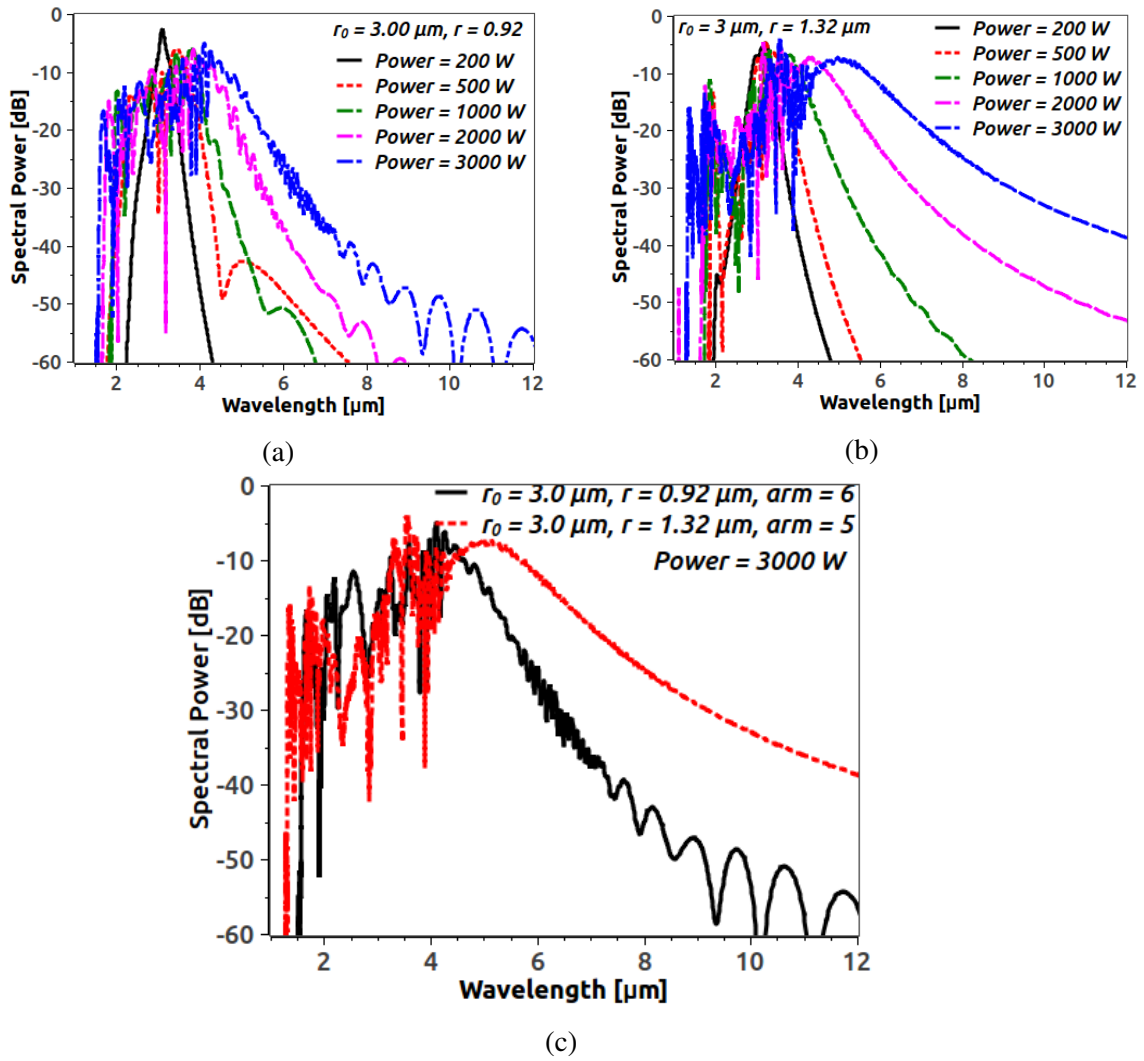


Fig. 7.10 Output SC pumped at a wavelength of $3.1 \mu\text{m}$ for ES-PCF (a) for the red-line GVD curve shown in Fig. 7.7(a) with peak power variation between 200 W and 3000 W; (b) for the blue-line GVD curve shown in Fig. 7.7(a) with power variation between 200 W and 3000 W; (c) for the GVD curves shown in Fig. 7.3(a) (red and blue line GVD curves only) with a peak power of 3000 W only.

effective mode area dispersion curves shown in Figs. 7.3(a) (red-line), 7.5 (black-line), and 7.7(a) (blue-line). For the GVD curves mentioned above, the dispersion lengths of 85-fs pump pulse are $L_D = 11.1$, 10.2, and 9.1 mm, the nonlinear lengths at a peak power of 3 kW is $L_{NL} = 0.26$, 0.27, and 0.23 mm, resulting in a soliton orders $N = \sqrt{L_D/L_{NL}} \approx 7$, 6, and 6 for the H-PCF, TC fibre and ES-PCF, respectively. As the pump lies in the anomalous GVD

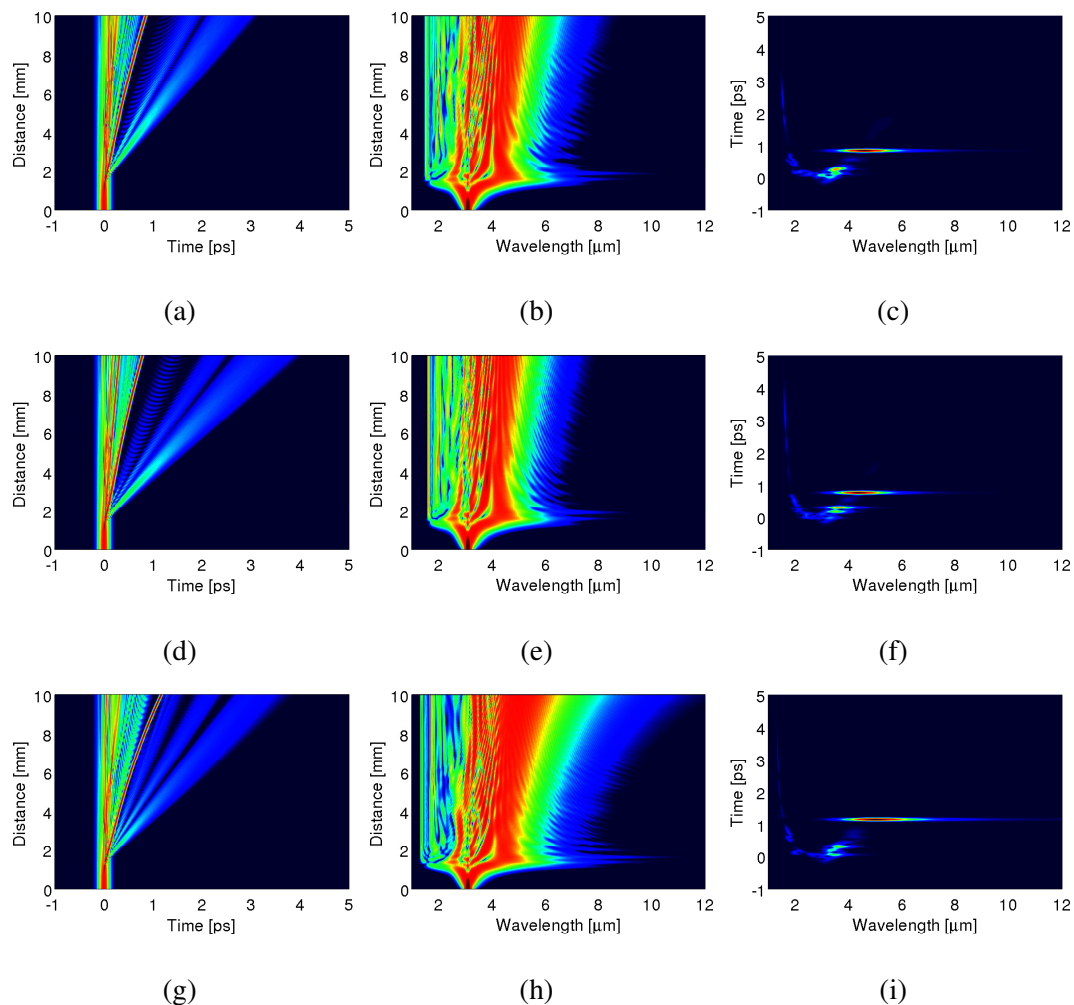
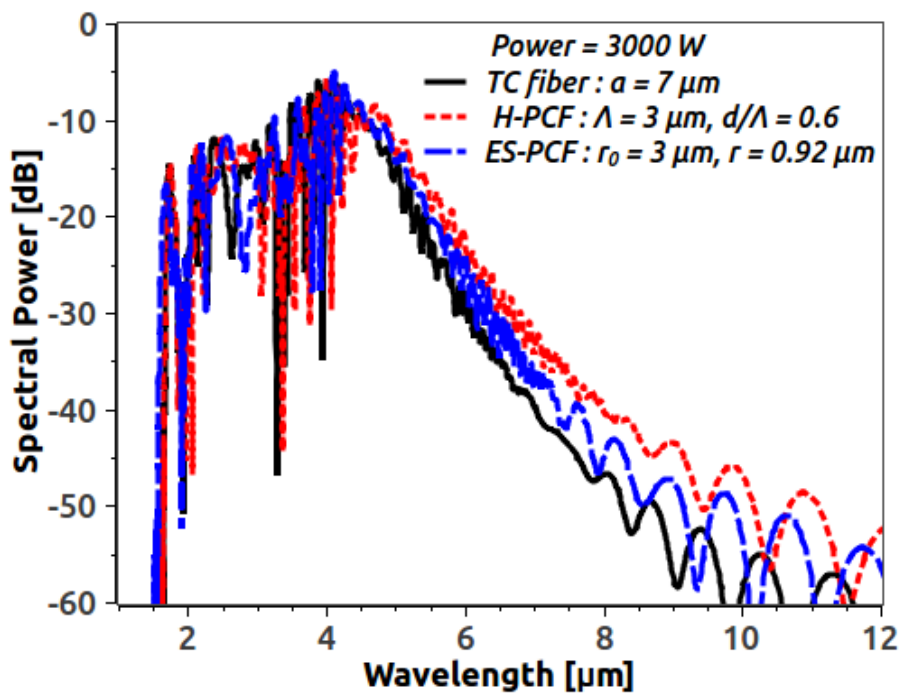


Fig. 7.11 Temporal evolution (left column), Spectral evolution (middle column), and Spectrogram (right column) at the fibre output for three fibres with different hole geometries. Top, middle, and bottom rows correspond to the output spectra shown in Figs. 7.8(a), 7.9(b), and 7.10(b) pumped at a wavelength of $3.1 \mu\text{m}$ with a peak power of 3 kW, respectively.

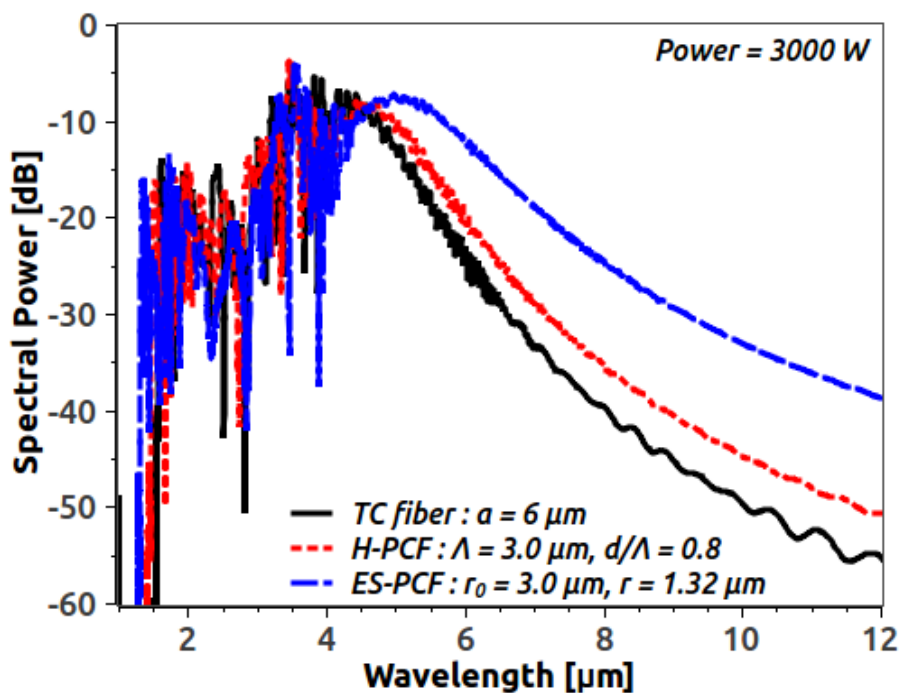
regime, SC generation is mainly dominated by the soliton-fission process. For the soliton order of 7, 6, and 6 fission occurs at a distance of 1.7 mm, 1.7 mm, and 1.5 mm, respectively, which can be observed from temporal evolution shown in Fig. 7.11 (left column), and corresponding number of fundamental solitons are produced after the fission, whose spectra shift toward the long-wavelength side owing to intrapulse Raman scattering, producing multiple spectral peaks in the spectra seen in Fig. 7.11 (middle column). One can also observe that non-solitonic radiation in the form of a dispersive wave

is also generated at a wavelength around first ZDWs of the above mentioned GVD curves lying in the normal dispersion regime of our ChG MoFs. It can be observed from Fig. 7.11 (bottom row) that the SC extends over more than three octaves covering a wavelength range from 1.3 to 11 μm for our proposed ES-PCF design. The temporal and spectral differences are also apparent in the spectrogram shown in Fig. 7.11 (right column) and the SC extension beyond the 11 μm is clearly observed from Fig. 7.11(i) for our proposed ES-PCF design.

Finally it has been shown comparative spectral evolutions of ES-PCF with the variation of its structural parameters as well as with other microstructured fibres proposed in this chapter. Figure 7.10(c) shows the spectral evolution of the GVD curve obtained in Fig. 7.7(a) with two different structural parameters of ES-PCF. SC bandwidth can be extended beyond 11 μm at a peak power of 3000 W by tailoring a dispersion curve as shown Fig. 7.7(a) (blue-line) for an ES-PCF structure with 5 spiral arms of all identical air-holes using air-hole radius, $r = 1.32 \mu\text{m}$ and initial spiral pitch length, $r_0 = 3.00 \mu\text{m}$. After increasing an arm with reducing air-hole to $0.92 \mu\text{m}$ keeping the separation between air-holes above the fabrication tolerance, we tailored a GVD curve as shown Fig. 7.7(a) (red-line) and obtained SC evolution for this dispersion curve shown in Fig. 7.10(c) (black-line curve) where it can be observed that SC spectrum is significantly reduced when the number of spiral arms increased. Usually when ES-PCF is designed employing six arms with identical air-holes it behaves like a conventional PCF. Figure 7.12(b) shows the comparative spectral evolution among the microstructured fibres considered here and it can be observed from the figure that by choosing similar parameters with tailoring identical GVD parameter for each microstructured fibre, the SC bandwidth can be extended up to 11 μm for an ES-PCF at a peak power of 3 kW which is higher than the bandwidth obtained by the other MoFs. Therefore, from Fig. 7.12(b), it is clear that by reducing an air-hole from the first ring of



(a)



(b)

Fig. 7.12 Simulated SC spectra for three different ChG microstructured fibres (a) with higher mode effective area GVD curves in Figs. 7.3(a) (black-line), 7.5 (red-line), and 7.7(a) (red-line); (b) with lower mode effective area GVD curves in Figs. 7.3(a) (red-line), 7.5 (black-line), and 7.7(a) (blue-line) pumped at a wavelength of $3.1 \mu\text{m}$ with a peak power of 3000 W.

conventional PCF following the design algorithm of equiangular spiral we can optimize an ES-PCF by which it is possible to improve the SC output bandwidth significantly than can be obtained by traditional microstructured fibres. It can also be observed from this figure that the largest SC spectrum extension occurs for our proposed ES-PCF design and the lowest extension occurs for the TC fibre. It is also apparent from these Fig. 7.12(a) (higher mode area SC spectra) and 7.12(b) (lower mode area SC spectra) that SC spectrum gets broaden for lower mode-area dispersion curve obtained for every microstructured fibre proposed. Microstructured fibre based on this geometry can be easily fabricated from soft glasses by the extrusion technique [158], or even by the stacking technique[159].

7.4 Summary

In this chapter, by using numerical simulations it is demonstrated the use of dispersion-engineered ChG MoFs allows us to generate ultra-broadband SC spectra in the MIR region. As a specific example, we considered a quasi PCF (ES-PCF) made with $\text{Ge}_{11.5}\text{As}_{24}\text{Se}_{64.5}$ glass and optimized its dispersive properties by varying the number of spiral arms and diameter of air holes used for the cladding. Using pump pulses at a wavelength of $3.1 \mu\text{m}$ with a relatively low peak power of 3 kW, we obtained a SC spectrum covering a wavelength range from $1.3 \mu\text{m}$ to beyond $11 \mu\text{m}$ (> 3 octave). We also optimized here TC fibre and conventional H-PCF and used them for SC generation. Among three different microstructured fibres, ES-PCF design has shown lower mode effective area which in turn increases the nonlinearity of ES-PCF and shows good dispersion characteristics with relatively flattened dispersion than others. The key feature of ES-PCF based waveguide design with cladding containing air-holes over the planar waveguides and conventional fibres is that ChG MoF has no cladding absorption like ChG planar

waveguides and ChG step-index fibres in the long wavelength edge of the broadband SC spectrum. By increasing the pump power, or shifting the pump wavelength to around 4-5 μm with adjusting ES-PCF design parameters, or by adjusting both while paying attention to the damage threshold limit of ChG glass, it should be possible to extend the SC to beyond 14 μm with our proposed $\text{Ge}_{11.5}\text{As}_{24}\text{Se}_{64.5}$ chalcogenide ES-PCF. Moreover, the ability of the ES-PCF structure to effectively control more than two parameters simultaneously gives it a significant advantage over conventional MoF/PCF design.

Chapter 8

Conclusion and Future work

The objective of this research was to study the design and optimization of supercontinuum (SC) sources employing highly nonlinear chalcogenide (ChG) material for wideband SC generation between near-infrared and mid-infrared regime. This was accomplished in two stages. ChG planar waveguides and microstructured optical fibres were considered for designing such SC sources which could be used for near infrared to mid-infrared applications. The waveguides proposed for designing SC sources were optimized by applying rigorous numerical procedure such as the finite-element (FE) approach and the results obtained by this approach have been utilized for numerically solving the generalized nonlinear Schrödinger equation (GNLSE) by split-step Fourier method (SSFM) to study broadband SC generation.

Initially SC generation in $\text{Ge}_{11.5}\text{As}_{24}\text{Se}_{64.5}$ ChG nanowires was studied considering pump source at a wavelength of 1550 nm with a low peak power of 25 W. A full-vectorial FE method is used for dispersion tailoring the ChG nanowires through rigorous numerical simulations. The nanowires were optimized, by varying their transverse dimensions, in such a way that they exhibits anomalous dispersion near the chosen pump wavelength. To obtain GVD coefficient for our proposed ChG nanowires at a pump wavelength, we use our FE mode-solver to obtain the propagation constants of the fundamental mode over a wide range of wavelengths. To calculate the effective mode

index, which is used for calculating GVD and various higher-order dispersion coefficients, we utilize the mode propagation constant obtained by our FE mode-solver. To examine the accuracy of the FE modal solution of our ChG nanowires, we tested the FEM results by Aitken's extrapolation through convergence between the raw FEM results and extrapolated values as the number of mesh elements increased along the transverse dimensions of the nanowires. As group velocity dispersion (GVD) which is a linear effect interacting with nonlinearity of the waveguide plays an important role in producing the broadband SC in the ChG nanowire output, the accuracy of numerically calculated GVD parameters were tested for different number of elements used along the transverse dimensions of nanowires. Five nanowires were specifically designed and all of them exhibit anomalous dispersion at a pump wavelength having two ZDWs. SC simulations were carried out for all five nanowires and find out an optimized design from them for realizing a wideband SC generation. It is highlighted the effects of higher-order dispersion coefficients on the SC spectrum and identifies changes that occur with addition of each successive higher-order dispersion coefficient in numerical simulations. In earlier simulation-based works on SC generation, sometimes the Taylor series expansion has been truncated after the third-order or fourth-order term. It has been shown that this may not produce an accurate SC spectrum and more higher-order dispersion terms may need to be included to obtain a reliable SC spectrum.

During nanowire design we employ polymer and silica as upper and lower claddings, respectively. Such nanowires were optimized at a pump wavelength of $1.55 \mu\text{m}$ with a low peak power of 25 W. To extend the SC into MIR region, pump wavelength need to be shifted around 3-4 μm region. As the silica cladding suffers severe absorption after 3 μm , it was not possible to obtain long wavelength extension of SC by shifting pump wavelength in the long wavelength region for that design. Therefore, for producing a

broadband MIR SC in $\text{Ge}_{11.5}\text{As}_{24}\text{Se}_{64.5}$ ChG channel waveguides, the upper and lower claddings were replaced by air and either $\text{Ge}_{11.5}\text{As}_{24}\text{S}_{64.5}$ or MgF_2 glass for its lower cladding material, respectively. We initially optimized these structures for employing pump at a wavelength of $2\ \mu\text{m}$. Although the nonlinear parameter has larger values at a pump wavelength, the SC spectra were extended only over $1.3\text{-}3.3\ \mu\text{m}$ and $1.3\text{-}3.5\ \mu\text{m}$, respectively even at the highest but moderate peak power of $500\ \text{W}$ for the two proposed structures. To extend SC to beyond the $5\ \mu\text{m}$, it is necessary to choose a longer pump wavelength around $3\text{-}4\ \mu\text{m}$. To realize the ZDW of the waveguide around this wavelength, the core size of the waveguide must be increased which increases the effective mode area and hence reduces the nonlinear parameter. The only solution is to increase the peak power of the input pulse toward MW levels which can damage the input facet of the waveguide. Paying attention with these factors, we designed and optimized an air-clad rectangular channel waveguide either employing $\text{Ge}_{11.5}\text{As}_{24}\text{S}_{64.5}$ or MgF_2 glass as its lower cladding and choose a pump at a wavelength of $3.1\ \mu\text{m}$ such that broadband SC could be generated at moderate peak power levels. We have also optimized an air-clad rib waveguide employing MgF_2 glass as its lower cladding at a wavelength of $3.1\ \mu\text{m}$. We have discussed the disadvantage of bare waveguide design owing to surface contamination from surrounding environment. After placing a protective coating on the surface which does not produce noticeable changes on SC results have also been discussed. Using pump source at a wavelength of $3.1\ \mu\text{m}$ with a relatively low peak power of $500\ \text{W}$ we obtained a SC spectrum extended over 1.5 octave and covering the wavelength range from $2\text{-}6\ \mu\text{m}$ with an air-clad all-ChG structure. However, when we used an optimized waveguide using MgF_2 glass for its lower cladding, the SC spectrum extended over more than two-octaves covered a wavelength ranges $1.8\text{-}7.7\ \mu\text{m}$ and $1.8\text{-}8\ \mu\text{m}$ for a rectangular channel and a rib waveguide, respectively. We have also found

that, MIR SC can be extended over in the wavelength range 1.9-7 μm and 1.8-11 μm with a moderate peak power of 3000 W when the air-clad channel waveguide is designed with a $\text{Ge}_{11.5}\text{As}_{24}\text{Se}_{64.5}$ glass core and employs either $\text{Ge}_{11.5}\text{As}_{24}\text{S}_{64.5}$ or MgF_2 glass for its lower cladding, respectively. SC can be extended up to 10 μm using the rib waveguide by employing same pump with a modest peak power of 3000 W as well.

We have demonstrated in earlier theoretical investigation on chalcogenide based planar waveguides for extending SC far into the mid-infrared regime, but the longest wavelength reached was limited owing to cladding absorption of asymmetric nature of planar waveguide design. Microstructured fibres based design still attracts researcher much attention to employ them for mid-infrared SC generation due to having them no cladding absorption in the long wavelength edge and can be fabricated them easily. In our theoretical study, we show that the use of microstructured fibres instead of planar and conventional fibres can overcome this limitation and SC spectrum can be extended far into the mid-infrared regime. In this thesis, we have demonstrated numerically that the use of dispersion-engineered ChG microstructured fibres should allow one to generate an ultra-broadband SC in the MIR region that extends beyond 11 μm . We considered three fibre geometries based on $\text{Ge}_{11.5}\text{As}_{24}\text{Se}_{64.5}$ glass and optimized the dispersive properties of resulting fibres by varying the design parameters associated with each geometry. We found that the ES-PCF geometry is superior to other two geometries because it provides more control over fibre's dispersive properties. Microstructured fibre based on this geometry can be easily fabricated from soft glasses by the extrusion technique [158], or even by the stacking technique [159]. Using pump pulses at a wavelength of 3.1 μm with a relatively low peak power of 3 kW, we obtained a SC spectrum covering a wavelength range from 1.3 μm to beyond 11 μm (>3 octaves). The ES-PCF design resulted in a lower mode effective area (which increases the nonlinear parameter) and shows flatter

dispersion than the other two geometries we studied. The key feature of the ES-PCF based design is that the cladding containing air-holes is made of the same material as the core. As a result, the ChG microstructured fibres do not suffer from cladding absorption that has limited the performance of ChG planar waveguides and ChG step-index fibres. Therefore, we have shown a novel design which is a modification of conventional hexagonal photonic crystal fibre which has the ability to effectively control more than one parameter simultaneously gives it a significant advantage over conventional microstructured fibre design.

To extend the long wavelength edge of SC far into the MIR region, we numerically investigated the chalcogenide planar waveguides by which it was possible to extend the SC spectrum beyond $11 \mu\text{m}$. The long wavelength edge of a SC developing in a chalcogenide planar waveguides are determined by the long wavelength absorption edge as well as cladding absorption due to cut-off of those asymmetric waveguides design. We then moved to focus on microstructured based fibres design as these type of fibres can have more control over their structural parameters for optimizing optical properties in comparison to planar waveguides and conventional fibres. We investigated three different microstructured fibres based on microstructuring their cladding containing air-holes. After optimizing them for obtaining with suitable dispersion properties based on their structural parameters variation, we proposed one novel design from them by which it was also possible to obtain SC extension beyond $11 \mu\text{m}$ by applying same pump source with same peak power applied during planar waveguides design. The advantage of microstructured based fibre design is that there is no possibility to occur cladding absorption as the cladding was made by periodic arrangement of microstructuring the air-holes in the same ChG material running along the length during the fibre design.

There has been considerable progress to fabricate low loss planar optical waveguides employing chalcogenide glasses for SC generation over the past decade. The creation of very small waveguides keep the optical field inside the waveguide so tightly that it effectively enhance the intensity of the field and thereby increasing the nonlinear response of the device. Normally ChG waveguides are fabricated on oxidized silicon wafers for near infrared applications. However, due to rapidly increasing absorption from the silica bottom cladding in the long wavelength region oxidized silicon wafers need to be replaced. Sulphide (S) based composition such as GeAsS and MgF₂ also can be employed as substrate materials which have longer transparency than oxidized silicon wafers. The latter substrate has the advantage of providing a larger index contrast between the core and substrate which helps to keep power into the core region enhancing nonlinear interaction of the waveguide. Gai *et al.* reported GeAsSe and GeAsS ChG glasses can be prepared by conventional melt quenching technique from purified starting materials [35]. Two methods became popular among several methods exists for ChG waveguide fabrication. These are lift-off technique and dry (plasma) etching technique. Using dry etching technique, thin films can be deposited via thermal evaporation onto oxidized silicon wafers or MgF₂ wafers using an Angstrom Engineering deposition system. Different type of structures such as channel/rib waveguide can be prepared by using this method. Ma *et al.* reported that the core layer using Ge_{11.5}As₂₄Se_{64.5} ChG material can be evaporated directly onto oxidized silicon wafer or MgF₂ substrate by thermal evaporation technique [39]. The ChGs core layer was then dry etched using an inductively coupled plasma reactive ion etcher. By using wet chemical stripping and oxygen/argon plasma, the residual photo resist layer can be removed. The top surface of the waveguides can be either left uncoated or can be covered with a 10-nm layer of fluoro-polymer which is deposited at high CHF₃ pressure and gas flow after oxygen plasma cleaning of the wave-

uide surface. In case of chalcogenide microstructured fibres, stack and draw technique and extrusion technique can be used for such kind of waveguides fabrication.

The results obtained in this study are very promising though they are solely based on numerical predictions. The next step in this line of research would be the experimental validation of results obtained through numerical simulations. It is also possible to improve numerical model developed for SC generation. Some of the assumptions can be replaced by more rigorous theoretical or empirical findings. During numerical simulations, wavelength independent propagation losses were considered throughout this work for SC generation. To predict better results, wavelength dependent propagation loss could be included in numerical simulations. Simulation of SC generation places high demands on numerical accuracy, which makes efficient high-order methods attractive. During implementing split-step Fourier method, for achieving such accuracy, a higher-order method such as a fourth-order Runge-Kutta would be preferable instead of using a trapezoidal rule for the integration. In order to minimize the computational effort it is possible to implement adaptive step size control in the program which would enable less steps to be taken overall and would be more accurate.

As most of the earlier theoretical and experimental investigations were facing difficulties to extend the SC far into the MIR region owing to severe cladding absorption in the long wavelength edge using ChG planar waveguides and ChG step-index fibre, the alternatives were to use ChG microstructured fibres for MIR SC extension in the long wavelength edge. Although hexagonal and equiangular photonic crystal fibres can be optimized by tailoring their dispersion characteristics for producing SC up to MIR, it is not possible to obtain the extension beyond $11 \mu\text{m}$ by using the designs proposed in this thesis due to peak power limited by damage threshold of ChG material at a pump wavelength of $3.1 \mu\text{m}$. Therefore, by shifting the pump

wavelength to beyond $4\ \mu\text{m}$, tailoring the hexagonal and equiangular spiral PCF around the pump wavelength, it should be possible to extend the SC to beyond $14\ \mu\text{m}$ using $\text{Ge}_{11.5}\text{As}_{24}\text{Se}_{64.5}$ ChG glass microstructured photonic crystal fibres. As equiangular spiral PCF has more control over its structural parameters than hexagonal PCF, long wavelength extension of the SC into MIR region could be easily achieved by using equiangular spiral PCF than conventional microstructured fibre.

The results demonstrated for MIR SC generation in Chapter 7 with ES-PCF were shown promising one as this microstructured fibre has shown excellent control over its structural parameters for dispersion optimization. Further numerical studies of SC generation using tapered fibre could potentially improve the MIR SC generation in the long wavelength edge. Nonlinear effects can be enhanced by tapering optical fibres and particularly by tapering microstructured fibre. In order to achieve better control of the dispersion, microstructured fibre with tapering through controlling of its structural parameters could be chosen for extending the SC far into the MIR regime. Particularly, a few specific but crucial numerical investigations regarding to the spectral flatness and coherence properties of the SC could be carried out in future, which were not investigated here.

Appendix A

A.1 Pulse parameters

Gaussian pulse

The electric field envelop of a laser pulse (phase free or chirp free) is

$$A(T) = \sqrt{P_0} \exp\left(-\frac{T^2}{2T_0^2}\right), \quad (\text{A.1})$$

with pulse energy E is given by

$$E = \int_{-\infty}^{\infty} |A(T)|^2 dT = \sqrt{\pi} P_0 T_0 \approx 1.06 P_0 T_{\text{FWHM}}. \quad (\text{A.2})$$

T_0 is the half-width at $1/e$ -power, related to the power FWHM by

$$T_{\text{FWHM}} = 2\sqrt{\ln 2} T_0 \approx 1.665 T_0. \quad (\text{A.3})$$

The Fourier transform of a Gaussian pulse is also a Gaussian with a FWHM power spectral width of

$$\Delta\nu_{\text{FWHM}} = \frac{2\ln 2}{\pi T_{\text{FWHM}}} \approx \frac{0.44}{T_{\text{FWHM}}}, \quad (\text{A.4})$$

$$\Delta\lambda_{\text{FWHM}} \approx \frac{\lambda_0^2}{c} \Delta\nu_{\text{FWHM}} \approx 0.44 \frac{\lambda_0^2}{T_{\text{FWHM}}}, \quad (\text{A.5})$$

The average power P_{av} is

$$P_{\text{av}} = Ef = \sqrt{\pi}P_0T_0f \approx 1.06P_0T_{\text{FWHM}}f, \quad (\text{A.6})$$

where f is the repetition rate.

Hyperbolic-secant pulse

The electric field envelop (phase free) of a laser pulse is

$$A(T) = \sqrt{P_0} \operatorname{sech}\left(\frac{T}{T_0}\right), \quad (\text{A.7})$$

$$T_{\text{FWHM}} = 2 \ln(1 + \sqrt{2})T_0 \approx 1.763T_0, \quad (\text{A.8})$$

$$P_{\text{av}} = 2P_0T_0f \approx 1.13P_0T_{\text{FWHM}}f. \quad (\text{A.9})$$

A.2 Scaling of the electric field

The electric field of an electromagnetic wave is given by [1]

$$\mathbf{E}(\mathbf{r}, t) = \mathbf{E}_0(\mathbf{r}, t) \exp[j(\beta_0 z - \omega_0 t)], \quad (\text{A.10})$$

The intensity of this electromagnetic wave is given by

$$I(\mathbf{r}, t) = \frac{n}{2} \sqrt{\frac{\epsilon_0}{\mu_0}} |\mathbf{E}_0(\mathbf{r}, t)|^2, \quad (\text{A.11})$$

where μ_0 is the vacuum permeability.

From Eq. (2.24) and the scaling relation $\mathbf{E}_A = \sqrt{\frac{1}{2}\epsilon_0 cn}\mathbf{E}$ one has:

$$|\mathbf{E}_0(\mathbf{r}, t)|^2 = \frac{2}{\epsilon_0 cn} |F(x, y)A(z, t)|^2 = \frac{2}{\epsilon_0 cn} |F(x, y)|^2 |A(z, t)|^2, \quad (\text{A.12})$$

The optical power is then found by integrating over the intensity in the xy plane:

$$\begin{aligned} P(z, t) &= \int \int I(\mathbf{r}, t) \, dx dy \\ &= \frac{n}{2} \sqrt{\frac{\epsilon_0}{\mu_0}} |A(z, t)|^2 \int \int |F(x, y)|^2 \, dx dy \\ &= |A(z, t)|^2 \int \int |F(x, y)|^2 \, dx dy, \end{aligned} \quad (\text{A.13})$$

From this equation it is seen that if $F(x, y)$ is normalized so that $\int \int |F(x, y)|^2 \, dx dy = 1$, then the optical power can be calculated as

$$P(z, t) = |A(z, t)|^2. \quad (\text{A.14})$$

Appendix B

Element matrix $[A]_e$

In Eq. (3.39) the matrix $[A]$ has matrices $[Q]$ and $[Q]^*$ which can be written as:

$$[Q] = \begin{bmatrix} [0] & -\frac{\partial[N]}{\partial z} & \frac{\partial[N]}{\partial y} \\ \frac{\partial[N]}{\partial z} & [0] & \frac{\partial[N]}{\partial x} \\ -\frac{\partial[N]}{\partial y} & \frac{\partial[N]}{\partial x} & [0] \end{bmatrix} \quad (\text{B.1})$$

Replacing $\frac{\partial}{\partial z}$ by $-j\beta$, $[Q]$ matrix can be obtain as follows:

$$[Q] = \begin{bmatrix} [0] & j\beta[N] & \frac{\partial[N]}{\partial y} \\ -j\beta[N] & [0] & \frac{\partial[N]}{\partial x} \\ -\frac{\partial[N]}{\partial y} & \frac{\partial[N]}{\partial x} & [0] \end{bmatrix} \quad (\text{B.2})$$

Consequently, $[Q]^*$ can be obtain as:

$$[Q]^* = \begin{bmatrix} [0] & j\beta[N]^T & \frac{\partial[N]^T}{\partial y} \\ -j\beta[N]^T & [0] & \frac{\partial[N]^T}{\partial x} \\ -\frac{\partial[N]^T}{\partial y} & \frac{\partial[N]^T}{\partial x} & [0] \end{bmatrix} \quad (\text{B.3})$$

where $[N]$ and $j\beta[N]$ are defined as:

$$[N] = [N_1 \ N_2 \ N_3] \quad (\text{B.4})$$

$$j\beta[N] = [j\beta N_1 \ j\beta N_2 \ j\beta N_3] \quad (\text{B.5})$$

The element matrix $[A]_e$ from Eq. (3.39) can be evaluated as:

$$\begin{aligned} [A]_e &= \int_{\Omega} \frac{1}{\varepsilon} [Q]^* [Q] d\Omega \\ &= \frac{1}{\varepsilon} \int_{\Omega} \begin{bmatrix} \beta^2 [N]^T [N] - \frac{\partial [N]^T}{\partial [y]} \frac{\partial [N]}{\partial y} & -\frac{\partial [N]^T}{\partial [y]} \frac{\partial [N]}{\partial x} & -j\beta [N]^T \frac{\partial [N]}{\partial x} \\ \frac{\partial [N]^T}{\partial [x]} \frac{\partial [N]}{\partial y} & \beta^2 [N]^T [N] + \frac{\partial [N]^T}{\partial [x]} \frac{\partial [N]}{\partial x} & -j\beta [N]^T \frac{\partial [N]}{\partial y} \\ -j\beta \frac{\partial [N]^T}{\partial x} [N] & -j\beta \frac{\partial [N]^T}{\partial y} [N] & \frac{\partial [N]^T}{\partial [y]} \frac{\partial [N]}{\partial y} - \frac{\partial [N]^T}{\partial [x]} \frac{\partial [N]}{\partial x} \end{bmatrix} d\Omega \end{aligned} \quad (\text{B.6})$$

Now the integrating the individual function inside the matrix will result:

$$\begin{aligned} 1^{\text{st}} \text{ term} &= \frac{1}{\varepsilon} \int_{\Omega} \left(\beta^2 [N]^T [N] - \frac{\partial [N]^T}{\partial [y]} \frac{\partial [N]}{\partial y} \right) d\Omega \\ &= \frac{1}{\varepsilon} \int_{\Omega} \left(\beta^2 \begin{bmatrix} N_1 \\ N_2 \\ N_3 \end{bmatrix} [N_1 \ N_2 \ N_3] - \begin{bmatrix} \frac{\partial N_1}{\partial y} \\ \frac{\partial N_2}{\partial y} \\ \frac{\partial N_3}{\partial y} \end{bmatrix} \begin{bmatrix} \frac{\partial N_1}{\partial y} & \frac{\partial N_2}{\partial y} & \frac{\partial N_3}{\partial y} \end{bmatrix} \right) d\Omega \\ &= \frac{1}{\varepsilon} \int_{\Omega} \left(\beta^2 \begin{bmatrix} N_1^2 & N_1 N_2 & N_1 N_3 \\ N_1 N_2 & N_2^2 & N_2 N_3 \\ N_1 N_3 & N_2 N_3 & N_3^2 \end{bmatrix} - \begin{bmatrix} \left(\frac{\partial N_1}{\partial y}\right)^2 & \frac{\partial N_1}{\partial y} \frac{\partial N_2}{\partial y} & \frac{\partial N_1}{\partial y} \frac{\partial N_3}{\partial y} \\ \frac{\partial N_1}{\partial y} \frac{\partial N_2}{\partial y} & \left(\frac{\partial N_2}{\partial y}\right)^2 & \frac{\partial N_1}{\partial y} \frac{\partial N_3}{\partial y} \\ \frac{\partial N_1}{\partial y} \frac{\partial N_3}{\partial y} & \frac{\partial N_2}{\partial y} \frac{\partial N_3}{\partial y} & \left(\frac{\partial N_3}{\partial y}\right)^2 \end{bmatrix} \right) d\Omega \end{aligned} \quad (\text{B.7})$$

Element matrix $[B]_e$

In Eq. (3.40) the matrix $[B]$ has matrices $[N]$ and $[N]^T$ which can be written as:

$$[N] = \begin{bmatrix} [N] & [0] & [0] \\ [0] & [N] & [0] \\ [0] & [0] & [N] \end{bmatrix} \quad (\text{B.8})$$

$$[N]^T = \begin{bmatrix} [N]^T & [0]^T & [0]^T \\ [0]^T & [N]^T & [0]^T \\ [0]^T & [0]^T & [N]^T \end{bmatrix} \quad (\text{B.9})$$

where $[N]$ and $[N]^T$ are defined as:

$$[N] = [N_1 \quad N_2 \quad N_3] \quad (\text{B.10})$$

$$[N]^T = \begin{bmatrix} N_1 \\ N_2 \\ N_3 \end{bmatrix} \quad (\text{B.11})$$

The element matrix $[B]_e$ from Eq. (3.40) can be evaluated as:

$$\begin{aligned} [B]_e &= \int_{\Omega} \mu [N]^T [N] d\Omega \\ &= \mu \int_{\Omega} \begin{bmatrix} [N]^T [N] & [0]^T [0] & [0]^T [0] \\ [0]^T [0] & [N]^T [N] & [0]^T [0] \\ [0]^T [0] & [0]^T [0] & [N]^T [N] \end{bmatrix} d\Omega \end{aligned} \quad (\text{B.12})$$

Now the integrating the individual shape function inside the matrix will result:

$$\begin{aligned} \int_{\Omega} [N]^T [N] d\Omega &= \int_{\Omega} \begin{bmatrix} N_1 \\ N_2 \\ N_3 \end{bmatrix} \times [N_1 \ N_2 \ N_3] d\Omega \\ &= \begin{bmatrix} \int_{\Omega} N_1^2 d\Omega & \int_{\Omega} N_1 N_2 d\Omega & \int_{\Omega} N_1 N_3 d\Omega \\ \int_{\Omega} N_2 N_2 d\Omega & \int_{\Omega} N_2^2 d\Omega & \int_{\Omega} N_2 N_3 d\Omega \\ \int_{\Omega} N_3 N_1 d\Omega & \int_{\Omega} N_3 N_2 d\Omega & \int_{\Omega} N_3^2 d\Omega \end{bmatrix} \end{aligned} \quad (\text{B.13})$$

The evaluation of the integrations of the shape functions in Eqs. (B.7) and (B.13) for a triangular element;

$$\int_{\Omega} N_1^i N_2^j N_3^k d\Omega = \frac{i! j! k! 2!}{(i+j+k+2)!} A_e, \quad (\text{B.14})$$

where A_e is the area of the triangular element.

Therefore, the following integral can be obtained:

$$\int_{\Omega} N_1^2 d\Omega = \int_{\Omega} N_2^2 d\Omega = \int_{\Omega} N_3^2 d\Omega = \frac{A_e}{6}, \quad (\text{B.15})$$

$$\int_{\Omega} N_1 N_2 d\Omega = \int_{\Omega} N_2 N_3 d\Omega = \int_{\Omega} N_1 N_3 d\Omega = \frac{A_e}{12}, \quad (\text{B.16})$$

$$\int_{\Omega} d\Omega = A_e. \quad (\text{B.17})$$

From Eq. (B.7) some of the elements of the $[9 \times 9]$ A_e matrix can be written as:

$$[A]_{e(1,1)} = \frac{1}{\varepsilon} \int_{\Omega} \left(\beta^2 N_1^2 - \left(\frac{\partial N_1}{\partial y} \right)^2 \right) d\Omega = \frac{1}{\varepsilon} \left[\frac{\beta^2 A_e}{6} - c_1^2 A_e \right], \quad (\text{B.18})$$

$$[A]_{e(1,2)} = \frac{1}{\varepsilon} \int_{\Omega} \left(\beta^2 N_1 N_2 - \frac{\partial N_1}{\partial y} \frac{\partial N_2}{\partial y} \right) d\Omega = \frac{1}{\varepsilon} \left[\frac{\beta^2 A_e}{12} - c_1 c_2 A_e \right], \quad (\text{B.19})$$

$$[A]_{e(1,3)} = \frac{1}{\varepsilon} \int_{\Omega} \left(\beta^2 N_1 N_3 - \frac{\partial N_1}{\partial y} \frac{\partial N_3}{\partial y} \right) d\Omega = \frac{1}{\varepsilon} \left[\frac{\beta^2 A_e}{12} - c_1 c_3 A_e \right], \quad (\text{B.20})$$

$$[A]_{e(1,4)} = \frac{1}{\varepsilon} \int_{\Omega} -\frac{\partial N_1}{\partial x} \frac{\partial N_1}{\partial y} d\Omega = -\frac{1}{\varepsilon} b_1 c_1 A_e. \quad (\text{B.21})$$

From Eq. (B.13) some of the elements of the $[9 \times 9]$ B_e matrix can be written as:

$$[B]_{e(1,1)} = \mu \int_{\Omega} N_1^2 d\Omega = \mu \frac{A_e}{6}, \quad (\text{B.22})$$

$$[B]_{e(1,2)} = \mu \int_{\Omega} N_1 N_2 d\Omega = \mu \frac{A_e}{12}, \quad (\text{B.23})$$

$$[B]_{e(1,3)} = \mu \int_{\Omega} N_1 N_3 d\Omega = \mu \frac{A_e}{12}, \quad (\text{B.24})$$

$$[B]_{e(1,4)} = 0. \quad (\text{B.25})$$

Author Publications

Journal papers

- **M. R. Karim**, B. M. A. Rahman, and G. P. Agrawal, “Dispersion engineered $\text{Ge}_{11.5}\text{As}_{24}\text{Se}_{64.5}$ nanowire for supercontinuum generation: A parametric study”, *Optics Express*, vol. 22(25), pp. 31029–31040, Dec. 2014.
- **M. R. Karim**, B. M. A. Rahman, and G. P. Agrawal, “Mid-infrared supercontinuum generation using dispersion engineered $\text{Ge}_{11.5}\text{As}_{24}\text{Se}_{64.5}$ chalcogenide channel waveguide”, *Optics Express*, vol. 23(5), pp. 6903–6914, Mar. 2015.
- **M. R. Karim**, B. M. A. Rahman, Y. O. Azabi, A. Agrawal, and G. P. Agrawal, "Ultra-broadband mid-infrared supercontinuum generation through dispersion engineering of chalcogenide microstructured fibres", *Journal of Optical Society of America B*, 32(11), pp. 2343-2351, Nov. 2015.
- **M. R. Karim** and B. M. A. Rahman, "Ultra-broadband mid-infrared supercontinuum Generation in chalcogenide rib waveguide", Accepted for publications in *Journal of Optical and Quantum Electronics*.

Conference papers

- **M. R. Karim** and B. M. A. Rahman, "Mid-infrared supercontinuum generation using $\text{Ge}_{11.5}\text{As}_{24}\text{Se}_{64.5}$ chalcogenide rib waveguide", in international Workshop on *Optical Wave and Waveguide Theory and Numerical Modelling (OWTNM)*, London, UK, Apr. 17-18, 2015.

- **M. R. Karim**, B. M. A. Rahman, and Govind P. Agrawal, "A broadband mid-infrared supercontinuum generation using $\text{Ge}_{11.5}\text{As}_{24}\text{Se}_{64.5}$ channel waveguide", in proceedings *Integrated Photonics Research, Silicon and Nano Photonics (IPR)*, OSA, Boston, Massachusetts, USA, Jun. 27-29, 2015.

OPTICS & PHOTONICS NEWS (OPN)

- One of our published research result [Karim *et al.* *Opt. Exp.* **23**(5), 6903 (2015)] recently referred in optics and photonics news (OPN) of July/August 2015 as "**Extending the spectrum: In the mid-infrared**" in *Materials and Photonics: Some Recent Developments*, pp. 32-39, compiled by Valerie C. Coffey.

References

- [1] G. P. Agrawal, *Nonlinear Fiber Optics 5th ed.*, Academic press, San Diego, California, 2013.
- [2] R. R. Alfano and S. L. Shapiro, "Emission in the region 4000 to 7000 Å via four-photon coupling in glass," *Phys. Rev. Lett.*, **24**(11), pp. 584–587, 1970.
- [3] R. R. Alfano and S. L. Shapiro, "Observation of self-phase modulation and small-scale filaments in crystals and glasses," *Phys. Rev. Lett.*, **24**(11), pp. 592–594, 1970.
- [4] T. A. Birks, P. J. Roberts, P. St. J. Russell, D. M. Atkin, and T. J. Shepherd, "Full 2D photonic bandgaps in silica/air structures," *Elect. Lett.*, **31**, pp. 1941–1943, 1995.
- [5] J. C. Knight, T. A. Birks, P. St. J. Russell, and D. M. Atkin, "All-silica single-mode optical fibre with photonic crystal cladding," *Opt. Lett.*, **21**, pp. 1547–1549, 1996.
- [6] J. C. Knight, T. A. Birks, P. St. Russell, and J. P. De-Sandro, "Properties of photonic crystal fibre and effective index model," *J. Opt. Soc. Am. B*, **15**, pp. 748–752, 1998.
- [7] J. K. Ranka, R. S. Windeler, and A. J. Stentz, "Visible continuum generation in air-silica microstructure optical fibres with anomalous dispersion at 800 nm," *Opt. Lett.*, **25**, pp. 25–27, 2000.
- [8] P. St. J. Russell, "Photonic-crystal fibres," *Science*, **299**(5605), pp. 358–362, 2003.
- [9] G. Chang, T. B. Norris, and H. G. Winful, "Optimization of supercontinuum generation in photonic crystal fibres for pulse compression," *Opt. Lett.*, **28**, pp. 546–548, 2003.

- [10] K. M. Hilligsoe, T. V. Andersen, H. N. Paulsen, C. K. Nielsen, K. Molmer, S. Keiding, R. Kristiansen, K. P. Hansen, and J. J. Larsen, "Supercontinuum generation in a photonic crystal fibre with two zero dispersion wavelengths," *Opt. Exp.*, **12**, pp. 1045–1054, 2004.
- [11] W. J. Wadsworth, N. Joly, J. C. Knight, T. A. Birks, F. Biancalana, and P. St. J. Russell, "Supercontinuum and four-wave mixing with Q-switched pulses in endlessly single-mode photonic crystal fibre," *Opt. Exp.*, **12**, pp. 299–308, 2004.
- [12] P. St. J. Russell, "Photonic-crystal fibres," *J. Lightwave Technol.*, **24**(12), pp. 4729–4749, 2006.
- [13] T. A. Birks, W. J. Wadsworth, and P. St. J. Russell, "Supercontinuum generation in tapered fibres," *Opt. Lett.*, **25**(19), pp. 1415–1417, 2000.
- [14] X. Liu, C. Xu, W. Knox, J. Chandalia, B. Eggleton, S. Kosinski, and R. Windler, "Soliton self-frequency shift in a short tapered air-silica microstructure fibre," *Opt. Lett.*, **26**(6), pp. 358–360, 2001.
- [15] W. J. Wadsworth, A. Ortigosa-Blanch, J. C. Knight, T. A. Birks, T. P. M. Man, and P. St. J. Russell, "Supercontinuum generation in photonic crystal fibres and optical fibre tapers: a novel light source," *J. Opt. Soc. Am. B*, **19**, pp. 2148–2155, 2002.
- [16] P. Falk, M. H. Frosz, and O. Bang, "Supercontinuum generation in a photonic crystal fibre with two zero-dispersion wavelengths tapered to normal dispersion at all wavelengths," *Opt. Exp.*, **13**(19), pp. 7535–7540, 2005.
- [17] F. Poletti, K. Furusawa, Z. Yusoff, P. Petropoulos, N. G. R. Broderick, T. M. Monro, and D. J. Richardson, "Nonlinear tapered holey fibres with high SBS threshold and controlled dispersion," *J. Opt. Soc. Am. B*, **24**(9), pp. 2185–2194, 2007.
- [18] N. D. Psaila, R. R. Thomson, H. T. Bookey, S. X. Shen, N. Chiodo, R. Osellame, G. Cerullo, A. Jha, and A. K. Kar, "Supercontinuum generation in an ultrafast laser inscribed chalcogenide glass waveguide," *Opt. Exp.*, **15**, pp. 15776–15781, 2007.

- [19] M. R. E. Lamont, C. M. Sterke, and B. J. Eggleton, "Dispersion engineering of highly nonlinear As_2S_3 waveguides for parametric gain and wavelength conversion," *Opt. Exp.*, **15**(15), pp. 9458–9463, 2007.
- [20] S. J. Madden, D. Y. Choi, D. A. Bulla, A. V. Rode, B. Luther-Davies, V. G. Ta'eed, M. D. Pelusi, and B. J. Eggleton, "Long, low loss etched As_2S_3 chalcogenide for all-optical signal regeneration," *Opt. Exp.*, **15**(22), pp. 14414–14421, 2007.
- [21] M. R. E. Lamont, B. Luther-Davies, D. Y. Choi, S. Madden, and B. J. Eggleton, "Supercontinuum generation in dispersion engineered highly nonlinear ($\gamma = 10 \text{ /W/m}$) As_2S_3 chalcogenide planar waveguide," *Opt. Exp.*, **16**(19), pp. 14938–14944, 2008.
- [22] F. Luan, M. D. Pelusi, M. R. E. Lamont, D. Y. Choi, S. Madden, B. Luther-Davies, and B. J. Eggleton, "Dispersion engineered As_2S_3 planar waveguides for broadband four-wave mixing based wavelength conversion of 49 Gb/s signals," *Opt. Exp.*, **17**(5), pp. 3514–3520, 2009.
- [23] J. M. Dudley, G. Genty, and S. Coen, "Supercontinuum generation in photonic crystal fibre," *Rev. Mod. Phys.*, **78**, pp. 1135–1184, 2006.
- [24] S. Coen, A. H. L. Chau, R. Leonhardt, J. D. Harvey, J. C. Knight, W. J. Wadsworth, and P. St. J. Russell, "Supercontinuum generation by stimulated Raman scattering and parametric four-wave mixing in photonic crystal fibres," *J. Opt. Soc. Am. B*, **19**(4), pp. 753–764, 2002.
- [25] J. M. Dudley, L. Provino, N. Grossard, H. Maillotte, R. S. Windeler, B. J. Eggleton, and S. Coen, "Supercontinuum generation in air-silica microstructured fibres with nano second and femtosecond pulse pumping," *J. Opt. Soc. Am. B*, **19**(4), pp. 765–771, 2002.
- [26] J. Herrmann, U. Griebner, N. Zhavoronkov, A. Husakou, D. Nickel, J. C. Knight, W. J. Wadsworth, P. St. J. Russell, and G. Korn, "Experimental evidence for supercontinuum generation by fission of higher-order solitons in photonic crystal fibres," *Phy. Rev. Lett.*, **88**(17), 173901, 2002.
- [27] J. Hu, C. R. Menyuk, L. B. Shaw, J. S. Sanghera, and I. D. Aggarwal, "Maximizing the bandwidth of supercontinuum generation in As_2Se_3 chalcogenide fibres," *Opt. Exp.*, **18**(3), pp. 6722–6739, 2010.

- [28] L. Yin, Q. Lin, and G. P. Agrawal, "Soliton fission and supercontinuum generation in silicon waveguides," *Opt. Lett.*, **32**(4), pp. 391–393, 2007.
- [29] I. W. Hsieh, X. G. Chen, J. I. Dadap, N. C. Panoiu, and R. M. Osgood, Jr., "Ultrafast-pulse self-phase modulation and third-order dispersion in Si photonic wire-waveguides," *Opt. Exp.*, **14**(25), pp. 12380–12387, 2006.
- [30] I. W. Hsieh, X. G. Chen, X. P. Liu, J. I. Dadap, N. C. Panoiu, C. Y. Chou, F. N. Xia, W. M. Green, Y. A. Vlasov, and R. M. Osgood, Jr., "Supercontinuum generation in silicon photonic wires," *Opt. Exp.*, **15**(23), pp. 15242–15249, 2007.
- [31] B. J. Eggleton, B. Luther-Davies, and K. Richardson, "Chalcogenide photonics," *Nat. Photonics*, **5**, pp. 141–148, 2011.
- [32] D. Yeom, E. C. Mägi, M. R. E. Lamont, M. A. F. Roelens, L. Fu, and B. J. Eggleton, "Low-threshold supercontinuum generation in highly nonlinear chalcogenide nanowires," *Opt. Lett.*, **33**(7), pp. 660–662, 2008.
- [33] D. D. Hudson, S. A. Dekker, E. C. Mägi, A. C. Judge, S. D. Jackson, E. Li, J. S. Sanghera, L. B. Shaw, I. D. Aggarwal, and B. J. Eggleton, "Octave spanning supercontinuum in an As_2S_3 taper using ultralow pump pulse energy," *Opt. Lett.*, **36**(7), pp. 1122–1124, 2011.
- [34] D. D. Hudson, E. C. Mägi, A. C. Judge, S. A. Dekker, and B. J. Eggleton, "Highly nonlinear chalcogenide glass micro/nanofibre devices: Design, theory, and octave-spanning spectral generation," *Opt. Commun.*, **285**, pp. 4660–4669, 2012.
- [35] X. Gai, T. Han, A. Prasad, S. Madden, D. Y. Choi, R. Wang, D. Bulla, and B. Luther-Davies, "Progress in optical waveguides fabricated from chalcogenide glasses," *Opt. Exp.*, **18**(25), pp. 26635–26646, 2010.
- [36] I. D. Aggarwal and J. S. Sanghera, "Development and applications of chalcogenide glass optical fibres at NRL," *J. Optoelectron. Adv. Mater.*, **4**(3), pp. 665–678, 2002.
- [37] X. Gai, S. Madden, D. Y. Choi, D. Bulla, and B. Luther-Davies, "Dispersion engineered $\text{Ge}_{11.5}\text{As}_{24}\text{Se}_{64.5}$ nanowires with a nonlinear parameter

- of $136 \text{ W}^{-1}\text{m}^{-1}$ at 1550 nm," *Opt. Exp.*, **18**(18), pp. 18866–18874, 2010.
- [38] D. D. Hudson, M. Baudisch, D. Werdehausen, B. J. Eggleton, and J. Biegert, "1.9 octave supercontinuum generation in a As_2S_3 step-index fibre driven by mid-IR OPCPA," *Opt. Lett.*, **39**(19), pp. 5752–5755, 2014.
- [39] P. Ma, D. Y. Choi, Y. Yu, X. Gai, Z. Yang, S. Debbarma, S. Madden, and B. Luther-Davies, "Low-loss chalcogenide waveguides for chemical sensing in the mid-infrared," *Opt. Exp.*, **21**(24), pp. 29927–29937, 2013.
- [40] B. M. A. Rahman and A. Agrawal, *Finite Element Modelling Methods for Photonics*, Artech house, London, 2013.
- [41] H. Ebendorff-Heidepriem, K. Furusawa, D. R. Richardson, and T. M. Monro, "Fundamentals and applications of silica and non-silica holey fibres," *Proc. SPIE*, Photonics West, San Jose, 2004.
- [42] V. Finazzi, T. M. Monro, and D. J. Richardson, "Small core silica holey fibres: nonlinearity and confinement loss trade-off," *J. Opt. Soc. Am. B*, **20**(7), pp. 1427–1436, 2003.
- [43] F. Poli, A. Cucinotta, and S. Seller, *Photonic crystal fibres: properties and applications*, Dordrecht, Springer, 2007.
- [44] J. C. Baggett, T. M. Monro, J. R. Hayes, V. Finazzi, and D. J. Richardson, "Improving bending losses in holey fibres," in *Proceedings of OFC*, Anaheim, 2005.
- [45] J. P. Goure and I. Verrier, *Optical Fibre Devices*, Cornwall, MPG Books Ltd, 2002.
- [46] G. P. Agrawal, *Applications of Nonlinear Fiber Optics*, Academic press, New York, 2008.
- [47] A. V. Husakou and J. Herrmann, "Supercontinuum generation, four-wave mixing, and fission of higher-order solitons in photonic crystal fibres", *J. Opt. Soc. Am. B*, **19**, pp. 2171–2182, 2002.

- [48] R. H. Stolen, J. P. Gordon, W. J. Tomlinson, and H. A. Haus, "Raman response function of silica-core fibres," *J. Opt. Soc. Am. B*, **6**(6), pp. 1159-1166, 1989.
- [49] K. J. Blow and D. Wood, "Theoretical description of transient stimulated Raman scattering in optical fibres," *IEEE J. Quan. Elect.*, **25**, pp. 2665-2673, 1989.
- [50] N. Akhmediev and M. Karlsson, "Cherenkov radiation emitted by solitons in optical fibres", *Phy. Rev. A*, **51**, pp. 2602-2607, 1995.
- [51] P. K. A. Wai, C. R. Menyuk, H. H. Chen, and Y. C. Lee, "Soliton at the zero group dispersion wavelength of a single-mode fibre", *Opt. Lett.*, pp. 628-630, 1987.
- [52] P. K. A. Wai, H. H. Chen, and Y. C. Lee, "Radiations by solitons at the zero group dispersion wavelength of single-mode optical fibres", *Phy. Rev. A*, **41**, pp. 426-439, 1990.
- [53] K. Okamoto, *Fundamentals of Optical Waveguides 2nd ed.*, Academic press, Elsevier, 2006.
- [54] T. A. Birks, J. C. Knight, and P. St. J. Russell, "Endlessly single mode photonic crystal fibre", *Opt. Lett.*, vol. 22, pp. 961-963, 1997.
- [55] W. Wadsworth, A. Witkowska, S. Leon-Saval, and T. Birks, "Hole inflation and tapering of stock photonic crystal fibres", *Opt. Exp.*, **13**, pp. 6541-6549, 2005.
- [56] M. El-Amraoui, G. Gadret, J. C. Jules, J. Fatome, C. Fortier, I. Skripatchev, Y. Messaddeq, J. Troles, L. Brilland, W. Gao, T. Suzuki, Y. Ohishi, and F. Smektala, "Microstructured chalcogenide optical fibres from As₂S₃ glass: towards new IR broadband sources", *Opt. Exp.*, **18**, pp. 26655-26665, 2010.
- [57] J. H. V. Price, T. M. Monro, H. Ebendorff-Heidepriem, F. Poletti, P. Horak, V. Finazzi, J. Y. Y. Leong, P. Petropoulos, J. C. Flanagan, G. Brambilla, X. Feng, and D. J. Richardson, "Mid-IR supercontinuum generation from nonsilica microstructured optical fibres", *IEEE J. Sel. Top. in Quan. Elect.*, **13**, pp. 738-749, 2007.

- [58] J. Lagsgaard, "Mode profile dispersion in the generalised nonlinear Schrödinger equation", *Opt. Exp.*, **15**, pp. 16110–16123, 2007.
- [59] J. C. Knight, J. Broeng, T. A. Birks, and P. St. J. Russell, "Photonic band gap guidance in optical fibres", *Science* 282(5393), pp. 1476–1478, 1998.
- [60] F. Benabid, J. C. Knight, G. Antonopoulos, and P. St. J. Russell, "Stimulated Raman scattering in hydrogen-filled hollow-core photonic crystal fibre", *Science* 298(5592), pp. 399–402, 2002.
- [61] K. S. Chiang, "Review of numerical and approximate methods for the modal analysis of general optical dielectric waveguides," *Opt. Quantum Electron.*, **26**(3), pp. S113-S134, 1994.
- [62] A. Bossavit and I. Mayergoyz, "Edge-elements for scattering problems," *IEEE Trans. Microw. Theory*, **25**(4), pp. 2816-2821, 1989.
- [63] B. M. A. Rahman and J. B. Davies, "Finite-element analysis of optical and microwave waveguide problems," *IEEE Trans. Microw. Theory*, **32**(1), pp. 20–28, 1984.
- [64] B. M. A. Rahman and J. B. Davies, "Finite-element solution of integrated optical waveguides," *J. Lightwave Technol.*, **2**(5), pp. 682–688, 1984.
- [65] B. M. A. Rahman and J. B. Davies, "Penalty function improvement of waveguide solution by finite elements," *IEEE Trans. Microw. Theory*, **32**(8), pp. 922-928, 1984.
- [66] J. M. Jin, *The Finite Element Method in Electromagnetics*, New York,, Wiley, 1993.
- [67] J. B. Davies, *Numerical Techniques for Microwave and Millimetre-wave Passive Structures*, New York, Wiley, 1989.
- [68] M. Koshiba and K. Inoue, "Simple and efficient finite-element analysis of microwave and optical waveguides," *IEEE Trans. Microw. Theory*, **40**(2), pp. 371-377, 1992.
- [69] N. Mabaya, P. Lagasse, and P. Vandenbulcke, "Finite element analysis waveguides of optical," *IEEE Trans. Microw. Theory*, **29**(6), pp. 600-605, 1981.

- [70] P. Daly, "Finite element approach to propagation in elliptical and parabolic waveguides," *Int. J. Numer. Methods Eng.*, **20**(4), pp. 681-688, 1984.
- [71] R. Wu and C. Chen, "A scalar variational conformal mapping technique for weakly guiding dielectric waveguides," *IEEE J. Quan. Elect.*, **22**(5), pp. 603-609, 1986.
- [72] M. Koshiba, K. Hayata, and M. Suzuki, "Approximate scalar finite element analysis of anisotropic optical waveguides," *Elect. Lett.*, **18**, pp. 411-413, 1982.
- [73] M. Koshiba, K. Hayata, and M. Suzuki, "Approximate scalar finite-element analysis of anisotropic optical waveguides with off-diagonal elements in a permittivity tensor," *IEEE Trans. Microw. Theory*, **32**(6), pp. 587-593, 1984.
- [74] M. Koshiba, K. Hayata, and M. Suzuki, "Finite-element formulation in terms of the electric-field vector for electromagnetic waveguide problems," *IEEE Trans. Microw. Theory*, **33**(10), pp. 900-905, 1984.
- [75] M. Koshiba, K. Hayata and M. Suzuki, "Improved finite-element formulation in terms of the magnetic field vector for dielectric waveguides." *IEEE Trans. Microw. Theory*, **33**(3), pp. 227-233, 1984.
- [76] M. Koshiba, K. Hayata, and M. Suzuki, "Vector E-field finite element analysis of dielectric optical waveguides," *App. Opt.*, **25**, pp. 10-11, 1986.
- [77] A. Konard, "High-order triangular finite elements for electromagnetic waves in anisotropic media," *IEEE Trans. Microw. Theory*, **25**(5), pp. 353-360, 1977.
- [78] B. M. A. Rahman and J. B. Davies, "Finite element analysis of optical and microwave waveguide problems," *IEEE Trans. on Microw. Theory and Techn.*, **32**, pp. 20-28, 1984.
- [79] B. M. A. Rahman and J. B. Davies, "Penalty-function improvement of waveguide solution by finite elements," *IEEE Trans. Microw. Theory and Techn.*, **32**, pp. 922-928, 1984.

- [80] W. J. English, "Vector variational solutions of inhomogeneously loaded cylindrical waveguide structures," *IEEE Trans. on Microw. Theory and Techn.*, **19**, pp. 9-18, 1971.
- [81] J. Katz, "Novel solution of 2-D waveguides using the finite element method," *App. Opt.*, **21**, pp. 2747-2750, 1982.
- [82] T. E. Murphy, *Simulation software split-step Fourier propagation software (SSPROP)*, University of Maryland, 2006, www.photonics.umd.edu/software/ssprop.
- [83] P. L. Francois, "Nonlinear propagation of ultrashort pulses in optical fibres: total field formulation in the frequency domain", *J. Opt. Soc. Am. B*, **8**(2), pp. 276-293, 1996.
- [84] I. Cristiani, R. Tediosi, L. Tartara, and V. Degiorgio, "Dispersive wave generation by solitons in microstructured optical fibres", *Opt. Exp.*, **78**, pp. 124-135, 2003.
- [85] G. H. Weiss and A. A. Maradudin, "The Baker-Hausdorff formula and a problem in crystal physics", *J. Math. Phys.*, **3**, pp. 771-777, 1962.
- [86] J. A. Fleck, J. R. Morris, and M. D. Feit, "Time-dependent propagation of high energy laser beams through the atmosphere", *Appl. Phys. A*, **10**, pp.129-160, 1976.
- [87] N. Bloembergen, "Nonlinear optics: Past, present, and future," *IEEE J. Sel. Top. Quantum Electron.*, **6**, pp. 876-880, 2000.
- [88] J. C. Knight, "Photonic crystal fibres," *Nature*, **424**, pp. 847-851, 2003.
- [89] J. T. Manassah, P. P. Ho, A. Katz, and R. R. Alfano, "Ultrafast super-continuum laser source," *Photonics Spectra*, **18**, pp. 53-59, 1984.
- [90] W. Werncke, A. Lau, M. Pfeiffer, K. Lenz, H. J. Weigmann, and C. D. Thuy, "An anomalous frequency broadening in water," *Opt. Commun.*, **4**, pp. 413-415, 1972.
- [91] N. Bloembergen, "The influence of electron plasma formation on super-broadening in light filaments," *Opt. Commun.*, **8**, pp. 285-288, 1973.

- [92] R. L. Fork, C. V. Shank, C. Hirlimann, R. Yen, and W. J. Tomlinson, "Femtosecond white-light continuum pulses," *Opt. Lett.*, **8**, pp. 1–3, 1983.
- [93] A. L. Gaeta, "Catastrophic collapse of ultrashort pulses," *Phys. Rev. Lett.*, **84**, pp. 3582–3585, 2000.
- [94] N. Akozbek, M. Scalora, C. M. Bowden, and S. L. Chin, "White-light continuum generation and filamentation during the propagation of ultra-short laser pulses in air," *Opt. Commun.*, **191**, pp. 353–362, 2001.
- [95] A. Brodeur and S. L. Chin, "Band-gap dependence of the ultrafast white-light continuum," *Phys. Rev. Lett.*, **80**, pp. 4406–4409, 1998.
- [96] C. Lin and R. H. Stolen, "New nanosecond continuum for excited-state spectroscopy," *Appl. Phys. Lett.*, **28**, pp. 216–218, 1976.
- [97] P. L. Baldeck and R. R. Alfano, "Intensity effects on the stimulated four photon spectra generated by picosecond pulses in optical fibers," *J. Lightwave Technol.*, **5**, pp. 1712–1715, 1987.
- [98] B. Gross and J. T. Manassah, "Supercontinuum in the anomalous group-velocity dispersion region," *J. Opt. Soc. Am. B*, **9**, pp. 1813–1818, 1992.
- [99] P. Beaud, W. Hodel, B. Zysset, and H. P. Weber, "Ultrashort pulse propagation, pulse breakup, and fundamental soliton formation in a single-mode optical fiber," *IEEE J. Quantum Electron.*, **23**, pp. 1938–1946, 1987.
- [100] M. N. Islam, G. Sucha, I. Bar-Joseph, M. Wegener, J. P. Gordon, and D. S. Chemla, "Femtosecond distributed soliton spectrum in fibers," *J. Opt. Soc. Am. B*, **6**, pp. 1149–1158, 1989.
- [101] I. Ilev, H. Kumagai, K. Toyoda, and I. Koprnikov, "Highly efficient wideband continuum generation in a single-mode optical fiber by powerful broadband laser pumping," *Appl. Opt.*, **35**, pp. 2548–2553, 1996.
- [102] T. Morioka, K. Mori, and M. Saruwatari, "More than 100-wavelength-channel picosecond optical pulse generation from single laser source using supercontinuum in optical fibres," *Electron. Lett.*, **29**, pp. 862–864, 1993.

- [103] T. Morioka, K. Mori, S. Kawanishi, and M. Saruwatari, "Multi-WDM-channel, Gbit/s pulse generation from a single laser source utilizing LD-pumped supercontinuum in optical fibers," *IEEE Photon. Technol. Lett.*, **6**, pp. 365-368, 1994.
- [104] T. Morioka, K. Uchiyama, S. Kawanishi, S. Suzuki, and M. Saruwatari, "Multiwavelength picosecond pulse source with low jitter and high optical frequency stability based on 200 nm supercontinuum filtering," *Electron. Lett.*, **31**, pp. 1064-1066, 1995.
- [105] S. Kawanishi, H. Takara, K. Uchiyama, I. Shake, O. Kamatani, and H. Takahashi, "1.4 Tbit/s (200 Gbit/s×7 ch) 50 km optical transmission experiment," *Electron. Lett.*, **33**, pp. 1716-1717, 1997.
- [106] E. A. Golovchenko, P. V. Mamyshev, A. N. Pilipetskii, and E. M. Dianov, "Mutual influence of the parametric effects and stimulated Raman scattering in optical fibers," *IEEE J. Quantum Electron.*, **26**, pp. 1815–1820, 1990.
- [107] T. A. Birks, J. C. Knight, and P. St. J. Russell, "Endlessly single-mode photonic crystal fiber," *Opt. Lett.*, **22**, pp. 961–963, 1997.
- [108] G. Genty, M. Lehtonen, H. Ludvigsen, J. Broeng, and M. Kaivola, "Spectral broadening of femtosecond pulses into continuum radiation in microstructured fibers," *Opt. Exp.*, **10**, pp. 1083-1098, 2002.
- [109] J. H. V. Price, W. Belardi, T. M. Monro, A. Malinowski, A. Piper, and D. J. Richardson, "Soliton transmission and supercontinuum generation in holey fiber, using a diode pumped Ytterbium fiber source," *Opt. Exp.*, **10**, pp. 382-387, 2002.
- [110] J. M. Harbold, F. O. Ilday, F. W. Wise, T. A. Birks, W. J. Wadsworth, and Z. Chen, "Long-wavelength continuum generation about the second dispersion zero of a tapered fiber," *Opt. Lett.*, **27**, pp. 1558-1560, 2002.
- [111] A. Ortigosa-Blanch, J. C. Knight, and P. St. J. Russell, "Pulse breaking and supercontinuum generation with 200-fs pump pulses in photonic crystal fibers," *J. Opt. Soc. Am. B*, **19**, pp. 2567-2572, 2002.
- [112] J. W. Nicholson, M. F. Yan, P. Wisk, J. Fleming, F. DiMarcello, E. Monberg, A. Yablon, C. Jorgensen, and T. Veng, "All-fiber, octave-spanning supercontinuum," *Opt. Lett.*, **28**, pp. 643-645, 2003.

- [113] J. Takayanagi, N. Nishizawa, H. Nagai, M. Yoshida, and T. Goto, "Generation of high-power femtosecond pulse and octave-spanning ultrabroad supercontinuum using all-fiber system," *IEEE Photon. Technol. Lett.*, **17** (1), pp. 37-39, 2005.
- [114] C. Xia, M. Kumar, M. Y. Cheng, R. S. Hegde, M. N. Islam, A. Galvanauskas, H. G. Winful, F. L. Terry, M. J. Freeman, M. Poulain, and G. Maze, "Power scalable mid-infrared supercontinuum generation in ZBLAN fluoride fibers with up to 1.3 watts time-averaged power," *Opt. Exp.*, **15**, pp. 865–871, 2007.
- [115] H. Hundertmark, D. Kracht, D. Wandt, C. Fallnich, V. V. R. K. Kumar, A. K. George, J. C. Knight and P. St. J. Russel, "Supercontinuum generation with 200 pJ laser pulses in an extruded SF6 fiber at 1560 nm," *Opt. Exp.*, **11**, pp. 3196-3201, 2003.
- [116] F. G. Omenetto, N. A. Wolchover, M. R. Wehner, M. Ross, A. Efimov, A. J. Taylor, V. V. Kumar, A. K. George, J. C. Knight, N. Y. Joly, and P. S. Russell, "Spectrally smooth supercontinuum from 350 nm to 3 μm in subcentimeter lengths of soft-glass photonic crystal fibers," *Opt. Exp.*, **14**, pp. 4928–4934, 2006.
- [117] C. Xia, M. Kumar, O. P. Kulkarni, M. N. Islam, F. L. Terry, Jr., M. J. Freeman, M. Poulain, and G. Mazé, "Mid-infrared supercontinuum generation to 4.5 μm in ZBLAN fluoride fibers by nanosecond diode pumping," *Opt. Lett.*, **31**(17), pp. 2553–2555, 2006.
- [118] G. Qin, X. Yan, C. Kito, M. Liao, C. Chaudhari, T. Suzuki, and Y. Ohishi, "Ultrabroadband supercontinuum generation from ultraviolet to 6.28 μm in a fluoride fiber," *Appl. Phys. Lett.*, **95**(16), pp. 161103, 2009.
- [119] P. Domachuk, N. A. Wolchover, M. Cronin-Golomb, A. Wang, A. K. George, C. M. B. Cordeiro, J. C. Knight, and F. G. Omenetto, "Over 4000 nm bandwidth of Mid-IR supercontinuum generation in subcentimeter segments of highly nonlinear tellurite PCFs," *Opt. Exp.*, **16**, pp. 7161-7168, 2008.
- [120] X. Feng, W. H. Loh, J. C. Flanagan, A. Camerlingo, S. Dasgupta, P. Petropoulos, P. Horak, K. E. Frampton, N. M. White, J. H. V. Price, H.

- N. Rutt, and D. J. Richardson, "Single mode tellurite glass holey fiber with extremely large mode area for infrared nonlinear applications," *Opt. Exp.*, **16**, pp. 13651, 2008.
- [121] M. Liao, C. Chaudhari, G. Qin, X. Yan, T. Suzuki, and Y. Ohishi, "Tellurite microstructure fibers with small hexagonal core for supercontinuum generation," *Opt. Exp.*, **17**(14), pp. 12174–12182, 2009.
- [122] J. S. Sanghera, L. B. Shaw, L. E. Busse, V. Q. Nguyen, P. C. Pureza, B. C. Cole, B. B. Harbison, I. D. Aggarwal, R. Mossadegh, F. Kung, D. Talley, D. Roselle, and R. Miklos, "Development and infrared applications of chalcogenide glass optical fibers," *Fiber and Integrated Optics*, **19**, pp. 251–274, 2000.
- [123] R. E. Slusher, G. Lenz, J. Hodelin, J. Sanghera, L. B. Shaw, and I. D. Aggarwal, "Large Raman gain and nonlinear phase shifts in high-purity As₂Se₃ chalcogenide fibers," *J. of Opt. Soc. of Am. B*, **21**, pp. 1146–1155, 2004.
- [124] A. B. Salem, R. Cherif, and M. Zghal, "Development Tapered As₂S₃ chalcogenide photonic crystal fiber for broadband mid-infrared supercontinuum generation," *Frontiers in Optics 2011/Laser Science XXVII OSA Technical Digest (Optical Society of America, 2011)*, paper FMG6, doi:10.1364/FIO.2011.FMG6.
- [125] J. C. Phillips, "Topology of covalent non-crystalline solids I: short-range order in chalcogenide alloys," *J. Non-Cryst. Solids*, **34**(2), pp. 153–181, 1979.
- [126] M. F. Thorpe, "Continuous deformations in random networks," *J. Non-Cryst. Solids*, **57**(3), pp. 355–370, 1983.
- [127] K. Tanaka, "Structural phase transitions in chalcogenide glasses," *Phys. Rev. B Condens. Matter*, **39**(2), pp. 1270–1279, 1989.
- [128] P. Boolchand, D. G. Georgiev, and B. Goodman, "Discovery of the intermediate phase in chalcogenide glasses," *J. Optoelect Mat.*, **3**(3), pp. 70–720 (2001).
- [129] A. Prasad, C. J. Zha, R. P. Wang, A. Smith, S. Madden, and B. Luther-Davies, "Properties of Ge_xAs_ySe_{1-x-y} glasses for all-optical signal processing," *Opt. Exp.*, **16**(4), pp. 2804–2815, 2008.

- [130] D. A. P. Bulla, R. P. Wang, A. Prasad, A. V. Rode, S. J. Madden, and B. Luther-Davies, "On the properties and stability of thermally evaporated Ge-As-Se thin films," *Appl. Phys., A Mater. Sci. Process.*, **96**(3), pp. 615–625, 2009.
- [131] C. Choudhari, M. Liao, T. Suzuki, and Y. Ohishi, "Chalcogenide core tellurite cladding composite microstructured fibre for nonlinear applications," *J. Lightwave Technol.*, **30**(13), pp.2069–2076, 2012.
- [132] L. B. Shaw, R. R. Gattass, J. S. Sanghera, and I. D. Aggarwal, "All-fiber mid-IR supercontinuum source from 1.5 to 5 μm ," *Proc. SPIE*, **7914** (79140P), pp. 1–5, 2011.
- [133] B. M. A. Rahman and J. B. Davies, "Vector- H finite element solution of GaAs/GaAlAs rib waveguides," in *Proc. IEE*, **132**(6), pp. 349–353, 1985.
- [134] N. Granzow, M.A. Schmidt, W. Chang, L. Wang, Q. Coulombier, J. Troles, P. Toupin, I. Hartl, K. F. Lee, M. E. Fermann, L. Wondraczek, and P. St. J. Russell, "Mid-infrared supercontinuum generation in As_2S_3 "nano-spike" step index waveguide," *Opt. Exp.*, **21**(9), pp. 10969–10977, 2013.
- [135] D. V. Skryabin, F. Laun, J. C. Knight, and P. St. J. Russel, "Soliton self-frequency shift cancellation in photonic crystal fibres," *Science*, **301**, pp. 1705–1708, 2003.
- [136] F. Biancalana, D. V. Skryabin, and A. V. Yulin, "Theory of the soliton self-frequency shift compensation by resonant radiation in photonic crystal fibres," *Physical Review E*, **70**, 016615, 2004.
- [137] W. Gao, M. E. Amraoui, M. Liao, H. Kawashima, Z. Duan, D. Deng, T. Cheng, T. Suzuki, Y. Messaddeq, and Y. Ohishi, "Mid-infrared supercontinuum generation in a suspended-core As_2S_3 chalcogenide microstructured optical fibre," *Opt. Exp.*, **21**(8), pp. 9573–9583, 2013.
- [138] J. M. Dudley and J. R. Taylor, *Supercontinuum Generation in Optical fibres*, Cambridge University press, 2010.
- [139] N. Granzow, S. P. Stark, M. A. Schmidt, A. S. Tverjanovich, L. Wondraczek, and P. St. J. Russell, "Supercontinuum generation in

- chalcogenide-silica step-index fibres," *Opt. Exp.*, **19**(21), pp. 21003–21010, 2011.
- [140] J. M. Dudley and J. R. Taylor, "Ten years of nonlinear optics in photonic crystal fibre," *Nat. Photonics*, **3**, pp. 85–90, 2009.
- [141] M. R. Karim, B. M. A. Rahman, and G. P. Agrawal, "Dispersion engineered $\text{Ge}_{11.5}\text{As}_{24}\text{Se}_{64.5}$ nanowire for supercontinuum generation: A parametric study," *Opt. Exp.*, **22**(25), pp. 31029–31040, 2014.
- [142] J. Fatome, C. Fortier, T. N. Nguyen, T. Chartier, F. Smektala, K. Messaad, B. Kibler, S. Pitois, G. Gadret, C. Finot, J. Troles, F. Desevedavy, P. Houizot, G. Renversez, L. Brilland, and N. Traynor, "Linear and nonlinear characterizations of chalcogenide photonic crystal fibres," *J. Lightwave Technol.*, **27**(11), pp. 1707–1715, 2009.
- [143] X. Gai, D. Choi, S. Madden, Z. Yang, R. Wang, and B. Luther-Davies, "Supercontinuum generation in the mid-infrared from a dispersion-engineered As_2S_3 glass rib waveguide," *Opt. Lett.*, **37**(18), pp. 3870–3872, 2012.
- [144] Y. Yu, X. Gai, T. Wang, P. Ma, R. Wang, Z. Yang, D. Choi, S. Madden, and B. Luther-Davies, "Mid-infrared supercontinuum generation in chalcogenides," *Opt. Mater. Exp.*, **3**(8), pp. 1075–1086, 2013.
- [145] Y. Yu, B. Zhang, X. Gai, P. Ma, D. Choi, Z. Yang, R. Wang, S. Debarma, S. J. Madden, and B. Luther-Davies, "A broadband, quasi-continuous, mid-infrared supercontinuum generated in a chalcogenide glass waveguide," *Laser Photonics Rev.*, pp. 1–7, 2014.
- [146] M. R. Karim, B. M. A. Rahman, and G. P. Agrawal, "Mid-infrared supercontinuum generation using dispersion-engineered $\text{Ge}_{11.5}\text{As}_{24}\text{Se}_{64.5}$ chalcogenide channel waveguide," *Opt. Exp.*, **23**(5), pp. 6903–6914, 2015.
- [147] R. J. Weiblen, A. Docherty, J. Hu, and C. R. Menyuk, "Calculation of the expected bandwidth for a mid-infrared supercontinuum source based on As_2S_3 chalcogenide photonic crystal fibres," *Opt. Exp.*, **18**(25), pp. 26666–26674, 2010.

- [148] C. Wei, X. Zhu, R. A. Norwood, F. Seng, and N. Peyghambarian, "Numerical investigation on high power mid-infrared supercontinuum fibre lasers pumped at 3 μm ," *Opt. Exp.*, **21**(24), pp. 29488–29504, 2013.
- [149] I. Kubat, C. R. Petersen, U. V. Møller, A. B. Seddon, T. M. Benson, L. Brilland, D. Mechin, P. M. Moselund, and O. Bang, "Thulium pumped mid-infrared 0.9-9 μm supercontinuum generation in concatenated fluoride and chalcogenide glass fibres," *Opt. Exp.*, **22**(4), pp. 3959–3967, 2014.
- [150] C. R. Petersen, U. Møller, I. Kubat, B. Zhou, S. Dupont, J. Ramsay, T. Benson, S. Sujecki, M. Abdel-Moneim, Z. Tang, D. Furniss, A. Seddon, and O. Bang, "Mid-infrared supercontinuum covering the 1.4-13.3 μm molecular fingerprint region using ultra-high NA chalcogenide step-index fibre," *Nat. Photonics*, **8**, pp. 830–834, 2014.
- [151] U. Møller, Y. Yu, I. Kubat, C. R. Petersen, X. Gai, L. Brilland, D. Mechin, C. Caillaud, J. Troles, B. Luther-Davies, and O. Bang, "Multi-milliwatt mid-infrared supercontinuum generation in a suspended core chalcogenide fibre," *Opt. Exp.*, **23**(3), pp. 3282–3291, 2015.
- [152] Y. Yu, X. Gai, C. Zhai, S. Qi, W. Guo, Z. Yang, R. Wang, D. Choi, S. Madden, and B. Luther-Davies, "1.8-10 μm mid-infrared supercontinuum generation in a step-index chalcogenide fiber using low peak pump power," *Opt. Lett.*, **40**(6), pp. 1081–1084, 2015.
- [153] A. Marandi, C. W. Rudy, V. G. Plotnichenko, E. M. Dianov, K. L. Vodopyanov, and R. L. Byer, "Mid-infrared supercontinuum generation in tapered chalcogenide fiber for producing octave spanning frequency comb around 3 μm ," *Opt. Exp.*, **20**(22), pp. 24218–24225, 2012.
- [154] I. Savelii, O. Mouawad, J. Fatome, B. Kibler, F. Desevedavy, G. Gadret, J. C. Jules, P. Y. Bony, H. Kawashima, W. Gao, T. Kohoutek, T. Suzuki, Y. Ohishi, and F. Smektala, "Mid-infrared 2000-nm bandwidth supercontinuum generation in suspended-core microstructured Sulphide and Tellurite optical fibres," *Opt. Exp.*, **20**(24), pp. 27083–27093, 2012.
- [155] I. Kubat, C. S. Agger, U. Moller, A. B. Seddon, Z. Tang, S. Sujecki, T. M. Benson, D. Furniss, S. Lamarini, K. Scholle, P. Fuhrberg, B. Napier,

- M. Farries, J. Ward, P. M. Moselund, and O. Bang, "Mid-infrared supercontinuum generation to $12.5\ \mu\text{m}$ in large NA chalcogenide step-index fibres pumped at $4.5\ \mu\text{m}$," *Opt. Exp.*, **22**(16), pp. 19169–19182, 2014.
- [156] A. Al-Kadry, M. E. Amraoui, Y. Messaddeq, and M. Rochette, "Two octaves mid-infrared supercontinuum generation in As_2Se_3 microwires," *Opt. Exp.*, **22**(25), pp. 31131–31137, 2014.
- [157] F. Silva, D. R. Austin, A. Thai, M. Baudisch, M. Hemmer, D. Faccio, A. Couairon, and J. Biegert, "Multi-octave supercontinuum generation from mid-infrared filamentation in a bulk crystal," *Nat. Commun.*, **3**(807), pp. 1–5, 2012.
- [158] A. Agrawal, N. Kejalakshmy, B. M. A. Rahman, and K. T. V. Grattan, "Soft glass equiangular spiral photonic crystal fiber for supercontinuum generation" *IEEE Photonics Technol. Lett.*, **21**(22), pp. 1722–1724, 2009.
- [159] A. Agrawal, Y. O. Azabi, and B. M. A. Rahman, "Staking the equiangular spiral" *IEEE Photonics Technol. Lett.*, **25**(3), pp. 291–294, 2013.
- [160] A. Agrawal, M. Tiwari, Y. O. Azabi, V. Janyani, B. M. A. Rahman, and K. T. V. Grattan, "Ultrabroad supercontinuum generation in a tellurite equiangular spiral photonic crystal fiber" *J. of Modern Opt.*, **60**(12), pp. 956–962, 2013.
- [161] J. H. Kim, M. Chen, C. Yang, J. Lee, S. Yin, P. Ruffin, E. Edwards, C. Brantley, and C. Luo, "Broadband IR supercontinuum generation using single crystal sapphire fibres," *Opt. Exp.*, **16**(6), pp. 4085–4093, 2008.
- [162] B. Kuyken, X. Liu, R. M. Osgood Jr., R. Baets, G. Roelkens, and W. M. J. Green, "Mid-infrared to telecom-band supercontinuum generation in highly nonlinear silicon-on-insulator wire waveguides," *Opt. Exp.*, **19**(21), pp. 20172–20181, 2011.
- [163] O. P. Kulkarni, V. V. Alexander, M. Kumar, M. J. Freeman, M. N. Islam, F. L. Terry Jr., M. Neelakandan, and A. Chan "Supercontinuum generation from 1.9 to $4.5\ \mu\text{m}$ in ZBLAN fibre with high average power generation beyond $3.8\ \mu\text{m}$ using a thulium-doped fibre amplifier," *J. Opt. Soc. Am. B*, **28**(10), pp. 2486–2498, 2011.

- [164] M. Liao, W. Gao, T. Cheng, X. Xue, Z. Duan, D. Deng, H. Kawashima, T. Suzuki, and Y. Ohishi, "Five-octave-spanning supercontinuum generation in fluoride glass," *App. Phy. Exp.*, **6**(032503), pp. 1–3, 2013.
- [165] E. A. Anashkina, A. V. Andrianov, M. Y. Koptev, S. V. Muravyev, and A. V. Kim, "Towards mid-infrared supercontinuum generation with germano-silicate fibres," *IEEE J. of Sel. Top. in Quan. Elect.*, **20**(5), 7600608, 2014.
- [166] M. Bass, G. Li, and E. V. Stryland, *Hand Book of Optics Vol-IV 3rd ed.*, The McGraw-Hill, New York, 2010.
- [167] J. Andreasen, A. Bhal, and M. Kolesik, "Spatial effects in supercontinuum generation in waveguides," *Opt. Exp.*, **22**(21), pp. 25756–25767, 2014.
- [168] C. Chaudhari, T. Suzuki, and Y. Ohishi "Design of zero chromatic dispersion chalcogenide As_2S_3 glass nanofibres," *J. Lightwave Technol.*, **27**(12), pp. 2095–2099, 2009.